ELECTRON PARAMAGNETIC RESONANCE STUDIES OF DEFECTS IN SINGLE CRYSTALS OF BARIUM OXIDE AND CALCIUM TUNGSTATE

by

P. Weightman B.A.

Being a thesis
submitted to the University of Keele
for the Degree of Doctor of Philosophy

Department of Physics,
University of Keele,
Keele, Staffordshire.

October, 1970.

ABSTRACT

E.P.R. studies are reported of point defects in single crystals of BaO and neutron irradiated $CaWO_4$.

BaO : An Mn^{2+} spectrum, unique to blue crystals of BaO, has been studied at X and Q band frequencies. It arises from an axial defect with a large zero-field splitting, the principal axis of which lies along a <111> direction. The angular dependence of the Q band spectrum in the <110> and <111> planes and the spectra observed along <111> and <110> directions at X band, may be described by the spin hamiltonian:

$$\mathcal{H} = \beta.\underline{H}.\underline{g}.\underline{S} + \underline{S}.\underline{D}.\underline{S} + \underline{I}.\underline{A}.\underline{S}$$

with $g_{||} = 2.0017$, $g_{\perp} = 2.0013$, $D = 0.0778$ cms^{-1}, $A_{||} = 67.5 \times 10^{-4}\text{cms}^{-1}$ and $A_{\perp} = 68.5 \times 10^{-4}$ cms^{-1}. By analogy with previous work on the Alkali-Halides the spectrum is attributed to an Mn^{2+} ion occupying an off centre lattice site.

A broad, temperature sensitive, background absorption has also been found to be unique to blue crystals. The previously reported spectrum of Gd^{3+} has been observed in blue, green and transparent crystals together with a single line, 40 gauss wide, at $g = 2.0054$. Optical Microscopy studies revealed the presence of cubic inclusions ($\sim 10\mu$) in all crystals.

$\underline{CaWO_4}$: Three prominent absorption spectra, observed in $CaWO_4$ after heavy neutron irradiation, have been investigated together with a previously reported spectrum due to Mn^{2+}.

The A spectrum consists of a group of narrow lines arising from an $S = 3/2$ centre located at four sites in the structure. The angular variation of the spectrum may be described by:

$$\mathcal{H} = \beta\underline{S}.\underline{g}.\underline{H} + \underline{S}.\underline{D}.\underline{S}$$

where the $\underline{g}$ and $\underline{D}$ tensors are non-coincident and have principal values: $g_z = 2.048$, $g_y = 2.007$, $g_x = 2.004$, $D_1 = 4.32 \times 10^{-4}\text{cms}^{-1}$, $D_2 = 0.31 \times 10^{-4}\text{cms}^{-1}$ and $D_3 = -4.63 \times 10^{-4}\text{cms}^{-1}$. It is proposed that the spectrum arises from O^+ located at an interstitial site.

The B spectrum has not been investigated in detail but consists of a complex group of lines, the four most prominent of which have a similar width, intensity and spectral position to the A lines.

The C spectrum appears to high field and is very sensitive to temperature. Besides unidentified lines it is composed, at liquid nitrogen temperature, of two species, termed α and β, each of which may be described by:-

$$\mathcal{H} = \beta\underline{S}.\underline{g}.\underline{H} + \underline{S}.\underline{A}.\underline{(I_1} + \underline{I_2})$$

with $g_1 = 1.811$, $g_2 = 1.785$ and $g_3 = 1.497$ for α and $g_1 = 1.774$, $g_2 = 1.766$ and $g_3 = 1.429$ for β. Both centres have identical hyperfine structure arising from the 14% abundant W^{183} at two equivalent sites:-

$A_{\parallel} = 167.4 \times 10^{-4}\text{cms}^{-1}$ and $A_{\perp} = 87.4 \times 10^{-4}\text{cms}^{-1}$ with $I_1 = \pm\frac{1}{2}$ or 0 and $I_2 = \pm\frac{1}{2}$ or 0. It is suggested that these spectra arise from related oxygen deficient species located on two adjacent WO_4^{2-} complexes along <100> directions.

ACKNOWLEDGMENTS

The author would like to express his thanks to the following:

Professor D.J.E. Ingram for the provision of research facilities in his department.

Dr. B. Henderson for his encouragement, advice and general supervision.

Dr. D.E. Dugdale for his supervision and assistance in the final year of this work.

Professor L.V. Holroyd of the University of Missouri for the provision of Barium Oxide crystals and his assistance in the X band work on this material.

Dr. D.G. Holloway for his general advice and in particular his assistance with the X ray and Optical aspects of this work.

Dr. R.D. Dowsing of the Department of Computer Science, University of Swansea, for his aid and advice on computational matters.

Miss K.B. Davies for her care and patience in typing this thesis.

Mr. M. Cheney for the photographic work.

All other members of the Physics Department for their help and cooperation.

The staff of the Computer Centre for their assistance and permission to operate the University Computer.

The Science Research Council for a maintenance grant.

CONTENTS

Chapter VI (Continued)

INTRODUCTION

Electron Paramagnetic Resonance (E.P.R.) is a very specific spectroscopic technique which is used to investigate the detailed structure of systems containing electrons with unpaired spins. Owing to the wide variety of such systems in nature e.p.r. has been applied with success in many fields and has yielded valuable information about the electronic structure of matter in forms as diverse as organic free radicals and gases. Since the energy levels occupied by electrons are determined by the symmetry and strength of the potential in which they move, e.p.r. gives an insight into the immediate environment of the unpaired electron on an atomic scale.

From its very beginning e.p.r. has been particularly useful as a technique for exploring the nature of defect structures in solids. The majority of non-metallic solid materials, if they could be obtained in a pure and ideally structured form, would have all the electrons from their component atoms paired in the bonding and hence would be quite unresponsive to e.p.r. However such ideals of purity and structure are seldom, if ever, realised in practice and actual materials contain defects of various kinds. These defects often contain unpaired electrons and it is this paramagnetism which may be exploited by e.p.r. and used to determine the structure of defects and the nature of their immediate surroundings in the solid.

In the work reported in this thesis e.p.r. has been used to investigate the nature of paramagnetic defects in single crystals of Barium Oxide and Calcium Tungstate. Chapters I and II give a brief review of the basic theory of e.p.r. and of the electronic structure of point defects in insulators. An account of the experimental apparatus and techniques employed in the work reported here is given in Chapter III. Chapter IV is concerned with describing the nature of the two materials studied and also surveys previous work. The results of the e.p.r. studies of these materials are presented and discussed in Chapters V (Barium Oxide) and VI (Calcium Tungstate).

CHAPTER I

BASIC THEORY OF ELECTRON PARAMAGNETIC RESONANCE

In electron paramagnetic resonance transitions are observed between the energy levels of electrons with unpaired spins. Since electrons are charged particles possessing angular momentum they will have associated magnetic moments. The net magnetic moment of an electron will depend upon the angular momentum associated with it in the energy state it occupies. If the total angular momentum of an electron, or collection of electrons is $\underline{J}$ and the associated magnetic moment is $\underline{\mu}$ the two vectors may be taken as parallel and the relationship between them expressed as

$$\underline{\mu} = -\gamma\underline{J} \tag{1.1}$$

where γ is a scalar termed the gyromagnetic ratio. γ is a constant for a particular energy state but varies from state to state as the amount of angular momentum attributed to the electron changes.

1.1 Quantum Mechanical Description of Resonance

Quantum mechanics considers $\underline{\mu}$ and $\underline{J}$ as vector operators and the concept of two such operators being parallel is taken to mean that their matrix elements between the quantised energy states of the system are linearly related. The interaction between the electron and an applied magnetic field can be represented by the hamiltonian

ENERGY LEVELS OF A FREE Mn^{2+} ION IN A MAGNETIC FIELD

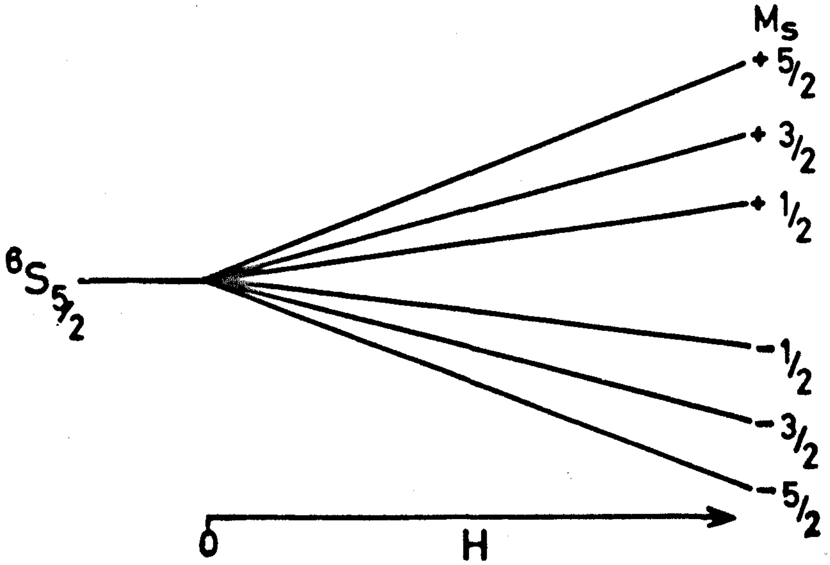

FIGURE 1·1

THE CLASSICAL LARMOR PRECESSION

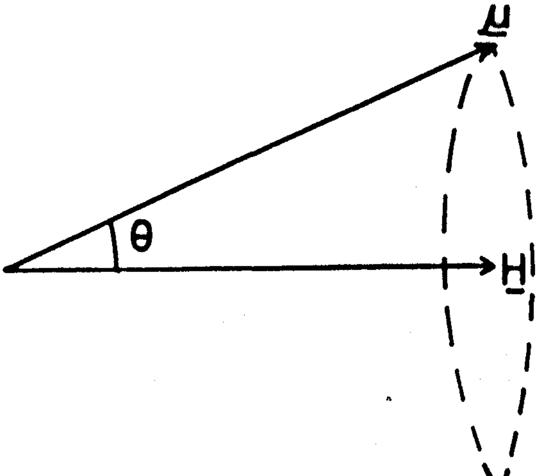

FIGURE 1·2

$$\mathcal{H} = -\underline{\mu}.\underline{H} \qquad (1.2)$$

The angular momentum and consequently the energy levels of the electron are assumed to be quantised in the magnetic field. If we define a dimensionless angular momentum operator $\underline{S}$ by

$$\underline{J} = \hbar\underline{S} \qquad (1.3)$$

then $\underline{S}^2$ has (2S+1) eigenvalues, S,(S-1),(S-2),.....,-S, which are either integer or half integer. Any component of $\underline{S}$ such as S_z commutes with $\underline{S}^2$ and may have simultaneous eigenvalues with it.

Assuming the field, of magnitude H_o, is applied along the z direction then (1.2) becomes

$$\mathcal{H} = \gamma\hbar H_o S_z \qquad (1.4)$$

The eigenvalues of this hamiltonian are the eigenvalues of S_z multiplied by the scalar $\gamma\hbar H_o$. Thus the allowed energies of the electron are

$$E = \gamma\hbar H_o M_s \qquad (1.5)$$

$M_s = S,(S-1),....,-S.$

Figure 1-1 shows the energy levels for an $\underline{S} = 5/2$ state such as the ground state of the free Mn^{2+} ion. It can be seen that the separation of the levels depends linearly on the magnitude of H and the figure suggests the possibility of observing transitions between the spin energy levels of the electronic system. It is transitions of this kind that are observed in e.p.r.

To cause transitions between these levels an interaction must fulfil two conditions:-

1) To satisfy the conservation of energy the interaction must be time dependent and of such an angular frequency ω that

$$\hbar\omega = \Delta E \tag{1.6}$$

where ΔE is the energy difference between the initial and final states of the electron making the transition.

2) The interaction must 'mix' the electron wavefunctions of the initial and final states. Quantum mechanically this condition requires the perturbation operator of the interaction to have non-zero matrix elements between the initial and final states.

The coupling most commonly used to produce magnetic resonance is an alternating magnetic field applied at right angles to the static field. If the alternating field has a frequency ω and an amplitude H_x we get a perturbing term in the hamiltonian of

$$\mathcal{H}_{\text{pert}} = \gamma\hbar H_x S_x \cos\omega t \tag{1.7}$$

It can be seen from Appendix I that the operator $\underline{S}_x$, which in quantum mechanical formalism can be written as $\frac{1}{2}(S_+ + S_-)$, only has non-zero matrix elements between states that differ by ±1 in their M_s values. Thus the allowed transitions are given by the selection rule $\Delta M_s = \pm 1$ and will have energies

$$\Delta E = \gamma\hbar H_o \tag{1.8}$$

or alternatively

$$\Delta E = g\beta H_o \tag{1.9}$$

where the Bohr magneton $\beta = \frac{e\hbar}{2mc}$ is the magnetic moment associated with unit angular momentum and g is the spectroscopic splitting factor. Effectively g represents the total angular momentum of the state including both spin and orbital contributions. For a pure spin state g = 2.0023 and deviations from this value are attributed to the admixture of orbital angular momentum into the state by such mechanisms as the spin-orbit coupling.

From (1.6) and (1.8) it can be seen that resonance will occur when

$$\omega = \gamma H_o \qquad (1.10)$$

This condition can also be derived from classical theory and although resonance is essentially a quantum mechanical effect the classical treatment gives a useful insight into its dynamic or transient aspects. For this reason a brief description of the classical viewpoint will be given here.

1.2 Classical Treatment of the Motion of an Isolated Spin

In classical terms the applied field $\underline{H}$ will produce a torque on the magnetic moment $\underline{\mu}$ equal to $\underline{\mu} \times \underline{H}$. Since the electron also possesses angular momentum the equation of its motion can be found by equating the torque and the rate of change of angular momentum.

$$\frac{d\underline{J}}{dt} = \underline{\mu} \times \underline{H} \qquad (1.11)$$

since $\underline{\mu} = -\gamma\underline{J}$

$$\frac{d\underline{\mu}}{dt} = \gamma\underline{H} \times \underline{\mu} \qquad (1.12)$$

This equation, which holds even when H is time dependent, indicates that the change in $\underline{\mu}$ at any instant of time is perpendicular to both $\underline{\mu}$ and $\underline{H}$. As illustrated in Figure 1.2 the electron will behave rather like a gyroscope and in the absence of 'frictional forces' its magnetic moment will precess around $\underline{H}$, the angle θ remaining constant. This classical precession frequency is termed the Larmor frequency and has a magnitude γH_o which is equal to the angular frequency required for magnetic resonance absorption as derived from quantum mechanics (equation 1.10).

As indicated earlier the means of achieving a resonance is to apply an oscillating magnetic field at right angles to $\underline{H}$. The effect of this oscillating field $\underline{H}\,(t) = 2H_1 \cos \omega t$ can be analysed by regarding it as a combination of two oppositely rotating components

$$\begin{aligned} \underline{H}_R(t) &= H_1(\underline{i} \cos \omega t + \underline{j} \sin \omega t) \\ \underline{H}_L(t) &= H_1(\underline{i} \cos \omega t - \underline{j} \sin \omega t) \end{aligned} \qquad (1.13)$$

One component will rotate in the same sense as $\underline{\mu}$ whereas the other will rotate in the opposite sense and consequently near resonance will have little effect on the system. Thus considering only $\underline{H}_R$ and making use of (1.12)

$$\frac{d\underline{\mu}}{dt} = \gamma(H_o\underline{k} + H_R(t)) \times \underline{\mu} \qquad (1.14)$$

The time dependence of $\underline{H}_R(t)$ can best be considered by expressing (1.14) in a coordinate system $\underline{i}'$, $\underline{j}'$, $\underline{k}'$ which rotates about the $\underline{k}$ direction of the $\underline{i}$, $\underline{j}$, $\underline{k}$ system with an angular frequency ω_z, where ω_z is the component of ω along H_o. This transformation to a rotating frame changes the form of (1.14), the relation between the time derivatives of $\underline{\mu}$ in the two

THE MOTION OF THE ROTATING FRAME

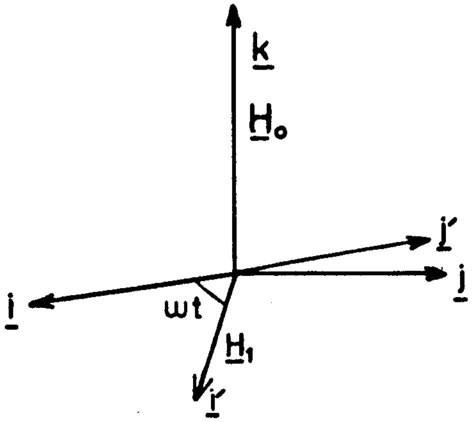

(a)

THE MOTION OF $\underline{\mu}$ IN THE ROTATING FRAME

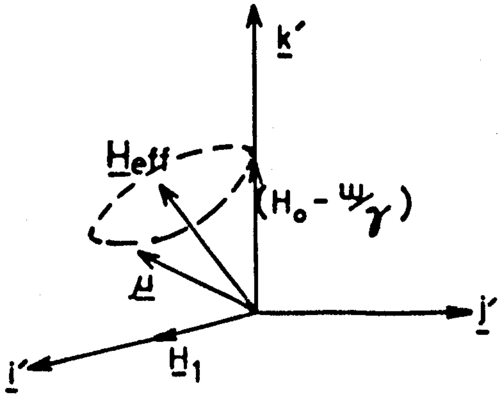

(b)

FIGURE 1·3

frames being given by (Rutherford p.13)

$$\frac{d\underline{\mu}}{dt} = \frac{d\underline{\mu}}{dt'} + \underline{\omega} \times \underline{\mu} \qquad (1.15)$$

Thus (1.14) becomes

$$\frac{d\mu}{dt'} = \gamma\left[\underline{k}(H_o - \frac{\omega_z}{\gamma}) + H_1\underline{i}\right] \times \mu \qquad (1.16)$$

or

$$\frac{d\mu}{dt'} = \gamma\underline{H}_{effective} \times \underline{\mu} \qquad (1.17)$$

which predicts that in the rotating frame the moment acts as though it experienced a static magnetic field

$$\underline{H}_{effective} = \underline{k}(H_o - \frac{\omega}{\gamma}) + H_1\underline{i} \qquad (1.18)$$

and consequently it will precess in a cone of fixed angle about the direction of $\underline{H}_{effective}$ with an angular frequency $\gamma H_{effective}$ as illustrated in Figure 1.3b.

In the absence of any friction forces to dissipate its angular momentum the motion of $\underline{\mu}$ will be periodic. When the resonance condition is fulfilled $H_{eff} = H_1\underline{i}$ and the magnetic moment will precess about $\underline{H}_1$ moving periodically from a position having a net moment parallel to $\underline{H}_o$ to one having a net moment in opposition to $\underline{H}_o$. When viewed from the laboratory frame it can be seen that the magnetisation is continuously changing its orientation with respect to the large static field and the energy absorbed from the rotating field in changing the spin orientation from parallel to anti-parallel is recovered as the spin turns back. Thus this analysis predicts that there will be no net absorption but a

ENERGY LEVEL SPLITTING OF AN S=1/2 STATE IN A MAGNETIC FIELD

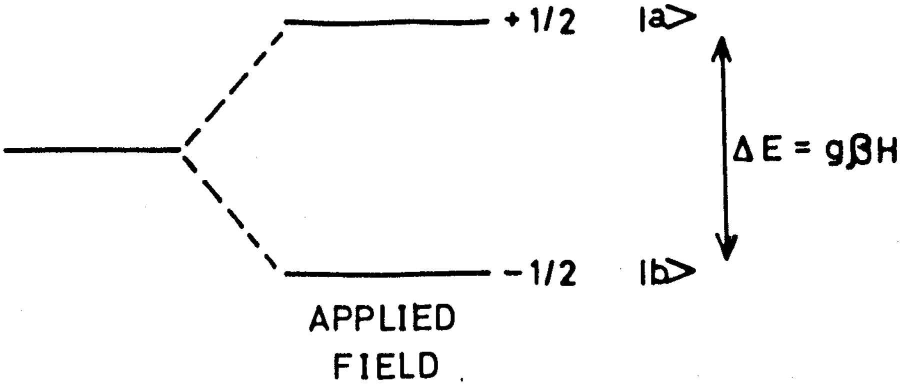

FIGURE 1·4

continuous absorption and remission of radiation from the oscillating field. In practice a net absorption does occur and this is attributable to the interactions between the spins and between the spins and their environment. Thus at this point it is profitable to leave the classical approach and considerations of an isolated spin and to take account of the interactions between electrons and between the electron and its environment.

1.3 Spin Lattice Relaxation and Thermal Equilibrium

Suppose that a macroscopic solid containing N electrons in spin states $S = \frac{1}{2}$ is placed in a magnetic field. The spin energy levels will be quantised by the magnetic field and their degeneracy removed as shown in Figure 1.4. Initially one would expect there to be as many electrons in the upper state $|a\rangle$ as in the lower state $|b\rangle$ and if the electrons were not coupled in any way to their environment this situation would persist. However there is a coupling of the electron spins to the total energy level system of the solid and this causes the electrons to make transitions between the spin states. Thermodynamic considerations indicate that the effect of these transitions will be to relate the distribution of energy between the spin states to the overall distribution of energy in the solid. A dynamic equilibrium and a population difference between the two states will be established which will be related to the energy separation of the two states and the overall temperature of the solid.

In thermal equilibrium the ratio of the number of electrons in the upper state N_a^o to the number in the lower state N_b^o will be given by Boltzmann's law

$$\frac{N_a^o}{N_b^o} = e^{-g\beta H/kT} \qquad (1.19)$$

The process by which this equilibrium is established is called spin-lattice relaxation, the term lattice being taken to refer to all the degrees of freedom of the system not directly concerned with spin.

It is a necessary corollary of the above that the transition probability for an electron making a radiationless jump from the upper to the lower state, W_{ab}, is more favourable than for the reverse jump W_{ba}. The rate of change of the population of state $|a>$ will be given by:-

$$\frac{dN_a}{dt} = N_b W_{ba} - N_a W_{ab} \qquad (1.20)$$

In thermal equilibrium $\frac{dN_a}{dt} = 0$

and $\frac{N_b^o}{N_a^o} = \frac{W_{ab}}{W_{ba}}$

thus by (1.19)

$$\frac{W_{ab}}{W_{ba}} = e^{g\beta H/kT} \qquad (1.21)$$

If the population difference between the two states is n

$$\begin{aligned} n &= N_b - N_a \\ N &= N_b + N_a \end{aligned} \qquad (1.22)$$

and from (1.20)

$$\frac{dn}{dt} = -n(W_{ba} + W_{ab}) + N(W_{ab} - W_{ba})$$

or

$$\frac{dn}{dt} = -\frac{(n - n_o)}{T_1} \qquad (1.23)$$

in which the population difference in thermal equilibrium

$$n_o = N\frac{(W_{ab} - W_{ba})}{(W_{ba} + W_{ab})} \qquad (1.24)$$

and

$$\frac{1}{T_1} = (W_{ba} + W_{ab})$$

T_1 has the dimensions of time and is called the spin-lattice relaxation time. It is a measure of the time taken for energy to be transferred between the spin system and the other degrees of freedom of the solid, i.e. for the spin system to reach thermal equilibrium. Its magnitude is inversely proportional to the strength of the coupling of the electron spins to the lattice.

1.4 Spin-Spin Relaxation and the shape of the Resonance Line

E.P.R. absorption lines have a finite width which is determined by the interactions between the electrons and their environment.
The concept of spin-lattice relaxation implies that the spin states have a finite lifetime and consequently, by the uncertainty principle, there will be a degree of indefiniteness in the energy separation of these states. This uncertainty will make a contribution to the line width of the transition which will be inversely proportional to the spin-lattice

relaxation time T_1. Spin lattice broadening is homogeneous in that it broadens the resonance from every paramagnetic centre in a macroscopic sample equally. There are other broadening mechanisms which vary the relative energy of the spin levels over the sample and consequently produce slight shifts in the resonance observed from different centres. This spreading of the resonance is termed inhomogeneous broadening and the most important process involved is the dipolar interaction of the electron spin with other spins, electron and nuclear, within its vicinity. Such processes are characterised by a relaxation time T_2, the spin-spin or more generally the transverse relaxation time.

The shape of the resonance line is described empirically by a frequency distribution function $g(\omega)$ which reflects how the energy absorption varies near resonance. $g(\omega)$ is normalised to unit area:-

$$\int_0^\infty g(\omega)d \quad = \quad 1$$

The two most common line shapes are:-

$$\underline{\text{Lorentzian}} \qquad g(\omega - \omega_o) \;=\; \frac{T_2}{\pi} \; \frac{1}{\left[1 + T_2{}^2(\omega - \omega_o)^2\right]} \qquad (1.25)$$

This is characteristic of a damped oscillatory motion and has a width at half height of $\frac{2}{T_2}$.

$$\underline{\text{Gaussian}} \qquad g(\omega - \omega_o) \;=\; \frac{T_2}{\sqrt{2\pi}} \; e^{-\frac{1}{2}T_2{}^2(\omega-\omega_o)^2} \qquad (1.26)$$

where the width at maximum slope is $\frac{2}{T_2}$.

1.5 The Absorption of Energy

Consider the application of an oscillating field of frequency ν to a macroscopic paramagnetic specimen placed in a magnetic field H. Provided the energy of the radiation field corresponds to the energy separation of the spin states transitions will be induced between them. From (1.6) and (1.9) this requires:-

$$h\nu = g\beta H \tag{1.27}$$

Time dependent perturbation theory predicts that the rate at which the r.f. field causes transitions between the two levels $|a\rangle$ and $|b\rangle$ is given by:-

$$P_{ab} = \frac{2\pi}{\hbar^2} |\langle b| \mathcal{H}_{pert}|a\rangle|^2 g(\omega - \omega_o) \tag{1.28}$$

where P_{ab} is the transition probability or number of transitions induced per second, $\langle b| \mathcal{H}_{pert}|a\rangle$ is the matrix element of the perturbation between the two states, $g(\omega - \omega_o)$ is the shape function of the resonance about ω_o the angular frequency at resonance.

It may be noted that for transitions to occur $\langle b| \mathcal{H}_{pert}|a\rangle$ must be non-zero, i.e. the perturbation must mix the states.

The transitions caused by the r.f. field are called stimulated transitions and since $|\langle b| \mathcal{H}_{pert}|a\rangle|^2 = |\langle a| \mathcal{H}_{pert}|b\rangle|^2$ the probabilities for an upward and a downward transition are equal. One will thus only observe a net absorption of power if the spin lattice relaxation mechanism is efficient in producing a net population difference between the two states.

Considering an $S = \frac{1}{2}$ system (Figure 1.4) and denoting the transition probabilities by

$$P_{ab} = P_{ba} = P$$

then the rate of change of the population of state $|a>$ due to the r.f. field is:-

$$\frac{dN_a}{dt} = N_b P - N_a P$$

$$\frac{dN_a}{dt} = + Pn$$

By (1.22), $N_a = \frac{1}{2}(N - n)$ and since $\frac{dN}{dt} = 0$, i.e. the total number of spins is constant,

$$\frac{1}{2}\frac{dn}{dt} = -Pn \qquad (1.29)$$

Thus the rate of change of the population difference is given by

$$n = n_o\ e^{-2Pt} \qquad (1.30)$$

where n_o is the initial population difference.

The rate of absorption of energy from the r.f. field is given by:-

$$\frac{dE}{dt} = N_a\ P_{ab}(E_b - E_a) + N_b\ P_{ba}(E_a - E_b)$$

or

$$\frac{dE}{dt} = nP\Delta E \qquad (1.31)$$

From (1.30)

$$\frac{dE}{dt} = n_o e^{-2Pt}\Delta E \qquad (1.32)$$

Equation (1.32) implies the exponential decay of the population difference and thus the eventual disappearance of the resonance line, an effect which is termed saturation. However this analysis has so far ignored the effect of spin lattice relaxation which by inducing radiationless transitions from the upper to the lower state will maintain the population difference required for the observation of a continuous resonance absorption. Thus including the effects of spin lattice relaxation (1.23) with the r.f. perturbation (1.29)

$$\frac{dn}{dt} = -2Pn - \frac{(n - n_o)}{T_1}$$

so that at equilibrium when spin lattice relaxation balances resonant absorption and $\frac{dn}{dt} = 0$

$$n = \frac{n_o}{1 + 2PT_1}$$

(1.31) thus becomes

$$\frac{dE}{dt} = \frac{n_o P\Delta E}{1 + 2PT_1} \qquad (1.33)$$

We have now to include the broadening of the resonance line by spin-spin relaxation. As indicated earlier, the spin-spin relaxation mechanisms make the transition probability a function of frequency $P(\omega)$ giving the absorption line a definite shape. Thus

$$\frac{dE}{dt} = \frac{n_o P(\omega)\Delta E}{(1 + 2P(\omega)T_1)} \qquad (1.34)$$

$(1 + 2P(\omega)T_1)$ is termed the saturation factor and it depends upon both the lifetimes and the energy spread of the spin levels. Saturation will not occur if $2P(\omega)T_1 << 1$ and since $P(\omega)$ is proportional to the square of the amplitude of the r.f. field it is usual to operate at low power levels.

We are now in a position to calculate the power absorbed by electrons making transitions between the spin levels of our $S = \frac{1}{2}$ system. Combining (1.7) with (1.28) the transition probability becomes

$$P(\omega) = \frac{2\pi}{\hbar^2} \left|\left<-\tfrac{1}{2}\right|\gamma\hbar H_x S_x \cos \omega t\left|+\tfrac{1}{2}\right>\right|^2 g(\omega - \omega_o)$$

Writing $S_x = \frac{1}{2}(S_+ + S_-)$ and using the rules of quantum mechanical operators (Appendix I)

$$P(\omega) = \frac{\gamma^2 \pi H_x}{2} g(\omega - \omega_o)$$

Assuming a Lorentzian line shape (1.25) the absorption of power becomes

$$\frac{dE}{dt} = \frac{n_o \gamma^2 H_x{}^2 T_2 \Delta E}{2(1 + T_2{}^2 \Delta\omega^2)\left[1 + \dfrac{T_1 \gamma^2 H_x{}^2 T_2}{(1 + T_2{}^2 \Delta\omega^2)}\right]}$$

since $\Delta E = h\nu$

$$\frac{dE}{dt} = \frac{n_o \gamma^2 H_x{}^2 T_2 h\nu}{2(1 + T_2{}^2 \Delta\omega^2 + \gamma^2 T_1 T_2 H_x{}^2)} \qquad (1.35)$$

Since $n_o = \dfrac{N(W_{ab} - W_{ba})}{(W_{ba} + W_{ab})}$

we can expand the exponential of (1.21) and on neglecting second order terms this approximates to

$$n_o = \frac{Ng\beta H}{2kT}$$

The static susceptibility for a two level system

$$\chi_o = \frac{Ng^2\beta^2}{4kT}$$

and (1.35) becomes

$$\frac{dE}{dt} = \frac{\chi_o H_x{}^2 T_2 \omega\omega_o}{(1 + T_2{}^2\Delta\omega^2 + \gamma^2 T_1 T_2 H_x{}^2)}$$

At the centre of the resonance $\omega = \omega_o$ and for an unsaturated line

$$\left(\frac{dE}{dt}\right)_{Max} = \chi_o H_x{}^2 T_2 \omega_o{}^2 \qquad (1.36)$$

1.6 Magnetic Susceptibility

Equation (1.36) is an expression for the power absorbed in resonance derived by considering the rate at which transitions are induced by the radiation field. It is useful to compare this expression with one developed by considering the paramagnetic susceptibility χ of the whole specimen. χ is usually defined by:-

$$\underline{M}_x = \chi \underline{H}_x \qquad (1.37)$$

where $\underline{M}_x$ is the magnetisation vector induced by $\underline{H}_x$. For slowly varying H_x, M_x will be parallel to $\underline{H}_x$ since the mechanisms of reorientation will have time to act.

As the frequency ω is increased $\underline{M}_x$ will become out of phase with $\underline{H}_x$ and χ will decrease. By analogy with phase lag in A.C. theory this situation can be represented by considering χ to be complex

$$\chi = \chi' - \underline{i}\chi'' \qquad (1.38)$$

Thus the radio frequency field induces a magnetisation

$$M_x = 2\chi' H_1 \cos \omega t + 2\chi'' H_1 \sin \omega t$$

The energy of a magnetic dipole in a field H_x is $H_x.\frac{dM}{dt}$ per unit volume, per sec. Thus over one cycle

$$E = \int_0^{2\pi/\omega} H(\frac{dM}{dt})\, dt$$

and the average rate of absorption of energy is

$$\frac{dE}{dt} = \frac{\omega}{2\pi}\int_0^{2\pi/\omega} 4H_x{}^2\omega(\chi''\cos^2\omega t - \chi'\sin\omega t\cos\omega t)dt$$

and

$$\frac{dE}{dt} = 2\omega\chi''H_x \tag{1.39}$$

The rate of absorption of energy depends on only the complex component of the susceptibility. Combining (1.36) with (1.39)

$$\text{Max } \chi'' = \frac{\chi_o\omega_oT_2}{2} \tag{1.40}$$

Thus for microwave frequencies $\omega_o \sim 10^{10}$rad.sec^{-1} and with $T_2 \sim 10^{-7}$ sec,

$$\chi'' \sim 10^3\chi_o$$

consequently the resonance technique of detecting paramagnetism is very sensitive and improves with frequency.

References

Carrington, A. and MaLachlan, A.D., 'Introduction to Magnetic Resonance' (Harper and Row) 1967.

Ingram, D.J.E., 'Spectroscopy at Radio and Microwave Frequencies' (Butterworths) 1967.

Orton, J.W., 'Electron Paramagnetic Resonance' (Iliffe) 1968.

Pake, G.E., 'Paramagnetic Resonance' (Benjamin) 1962.

Rutherford, D.E., 'Classical Mechanics' Chap. 1, (Oliver & Boyd) 1960.

Slichter, C.P., 'Principles of Magnetic Resonance' (Harper & Row) 1964.

CHAPTER II

ELECTRONIC STRUCTURE OF POINT DEFECTS IN INSULATORS

To observe e.p.r. it is necessary to have a specimen containing electrons with unpaired spins. However the bonding between the constituent atoms of the majority of insulating solids is such as to lead to a cancelling of the spin angular momentum of the valence electrons and thus produce a diamagnetic situation. In pure ionic bonding each atom is considered to ionise into a closed shell configuration and thus have no residual electronic spin or orbital momentum. A similar result holds for covalent bonding but here it is the pairing of the valence electrons in the shared orbitals between atoms that is responsible for the cancellation of the spin angular momentum. Even though the bonding in a particular insulator is rarely either of these extremes and is best thought of as involving proportions of ionicity and covalency there is no relaxation of the paired spin arrangement for the majority of its electrons.

However the presence of defects in the crystal structure of such materials may give rise to unpaired electrons and hence to centres from which e.p.r. can be observed. Moreover the concentration of centres required to give an observable e.p.r. signal is quite small (10^{11} spins/cc for a 1 gauss linewidth or 1 atom in 10^{12}) and it is usually possible to treat such signals as being due to a collection of discrete non-interacting point defects. Such point defects are loosely classified as extrinsic, by which are meant impurities, or intrinsic. Intrinsic defects are defects in the structure of the material such as broken bonds, vacant lattice sites or interstitial atoms and it can be shown on thermodynamic grounds that some intrinsic defects will always be present in crystals at finite temperatures. The concentration and nature of intrinsic defects in a crystal will depend upon the conditions under which it was grown and its subsequent history. An imbalance of constituents in the melt will produce nonstoichiometric ~~nonstociometric~~ crystals containing interstitials and vacancies whilst exposure to radiation and heat treatment may disrupt the atomic arrangements of properly formed crystals and change the nature of defects already present. From the point of view of e.p.r. the most important extrinsic defects in crystals are transition metal ions. Transition metal ions are characterised by having incompletely filled orbitals within the orbitals of the valence electrons and it is from unpaired electrons in these states that resonance is observed.

To treat e.p.r. centres rigorously in theoretical terms would require the setting up and solution of the full Schrödinger equation for all the atoms and centres in the crystal. As such a fundamental treatment is impractical, various alternative approaches have been made to calculate the energy level structure of e.p.r. centres, which will have different degrees of validity depending upon the nature of the centre under consideration. Transition metal impurities are usually treated in terms of Ligand Field theory in which the positive ion is considered to occupy a potential well formed by the nearest neighbour negative ions or ligands of the host. This approach includes considerations of the overlap of electron orbitals and covalency. A special case of Ligand Field theory, and one which has achieved considerable success, is Crystal Field theory.

The technique here is to approximate the ligands to point charges and to determine the energy level structure of the positive ion in terms of the overall symmetry of the field produced by these point charges. A brief account of crystal field theory will be given here and a more thorough treatment can be found in Low (1960) and Murrell, Kettle and Teddar (1965, Ch. 13).

E.P.R. centres which arise from broken bonds or electrons trapped at vacant lattice sites are not susceptible to analysis in terms of Crystal Field theory as the electrons cannot be considered to belong essentially to a single atom, but rather as being shared between several atoms. Consequently these centres are best treated in terms of Molecular Orbital theory, an outline of which will be given in a later section.

2.1 Crystal Field Theory

Crystal Field theory assumes that the most important determinant of the electron energy levels and wavefunctions of an ion in a solid is the nature of the ion itself. The technique is to consider the various interactions in an ion one by one in decreasing order of magnitude and to insert the crystal field perturbation at an appropriate point in the development. Consequently it is usual to begin by considering the Hamiltonian of the free ion.

2.1.1 The free ion Hamiltonian

The most important terms in the free ion Hamiltonian in decreasing order are:

$$\mathcal{H} = \sum_{i=1}^{N}\left[\frac{\nabla i^2}{2m} - \frac{Ze^2}{r_i}\right] + \sum_{i>j}^{N}\frac{e^2}{r_{ij}} + \sum_{\substack{i=1\\j=1}}^{N} a_{ij}\,\underline{\ell}_i\cdot\underline{s}_j \tag{2.1}$$

The first term represents the kinetic energy of the N electrons and the coulomb force between them and the nucleus. The second term expresses the coulomb repulsion between electrons and the last term represents the magnetic coupling that will occur between their spin, s, and orbital, ℓ, angular momenta. It is not possible to solve the wave equation associated with this Hamiltonian exactly (this is a manifestation of the many body problem) and consequently various approximations are used in determining the electron wave functions, ψ, and energies. The central field approximation recognises that the first term is much larger than the others and taking advantage of its spherical symmetry considers each electron to move independently in a spherically symmetric potential well modified by a spherical 'screening' effect from the other electrons. This form of potential assures the separation of variables in the wave equation and each electron will have a well defined angular momentum. It is still necessary, however, to determine the radial dependence of the individual electron eigenfunctions and indeed to specify the exact potential $V_i(r)$ seen by each electron. This problem is solved by the Self Consistent Field (S.C.F.) method in which initial 'guesses' for the V_i and ψ_i are substituted into the Schrödinger equation for each electron. These equations are then solved by numerical integration to yield new forms for the ψ_i's. The new forms of ψ_i are used to determine new V_i and the process is repeated again and again until a self consistent solution is achieved. It can be shown that wavefunctions derived in this way will satisfy the condition derived from the calculus of variations (Eisberg 1963, p.278) that the wavefunction for the ground state of a system will always give an absolute minimum of energy:-

$$E = \int \psi \mathcal{H} \psi = \text{Min}$$

Following Hartree (Tinkham 1964) the initial forms chosen for the wavefunctions in the S.C.F. approach are products of one electron orbital wave functions. Later modifications by Fock to make the initial forms antisymmetric and allow for the fact that electrons are indistinguishable particles improved slightly on the Hartree functions. Having determined the one-electron central field eigenstates it is possible to describe the ground state of the ion by specifying which states must be filled in order to minimise the total energy and also satisfy the exclusion principle. Such a description is called a configuration.

For a configuration that does not consist entirely of closed shells it is necessary to consider how the spin and orbital angular momenta of the one electron states will be coupled together and. how the energies of these various coupled states, or Terms, will be split by the inter-electronic coulomb repulsion. In the Russel-Saunders coupling scheme, applicable to the lighter atoms, the individual orbital momenta $\underline{\ell}_i$ are assumed to couple separately and form a total orbital quantum number $\underline{L}$. A similar coupling of spin momenta produces a total spin quantum number $\underline{S}$.

$$\underline{L} = \sum_i \underline{\ell}_i$$
$$\underline{S} = \sum_i \underline{s}_i \qquad (2.2)$$
$$\underline{J} = \underline{L} + \underline{S}$$

The high degree of degeneracy within a configuration prevents the use of perturbation theory to calculate the new eigenstates and consequently the matrix of $\Sigma\frac{e^2}{r_{ij}}$ must be diagonalised directly. Fortunately it is possible to perform a considerable amount of initial factorisation of this matrix by making use of the group theoretical properties of angular momentum. Since we are still ignoring spin orbit coupling the Hamiltonian is invariant not only under rotation of the coordinates of the whole atom, but also under separate rotations of orbital and spin coordinates. Thus $\mathcal{H}$ commutes with $\underline{J}$, $\underline{L}$ and $\underline{S}$ and it is possible to choose simultaneous eigenvalues for these operators. A theorem of group theory (Tinkham p.80) shows that the matrix elements of $\mathcal{H}$ between states with different $\underline{J}$, $\underline{L}$ or $\underline{S}$ or different M_J, M_L or M_S values will be zero since these quantum numbers label the irreducible representations of the angular moment group of the configuration and their rows. Consequently by choosing as basis functions combinations of one electron wavefunctions which are already angular momentum eigenfunctions we can considerably simplify the matrix.

Unfortunately all the angular momentum operators that commute with $\mathcal{H}$ do not commute with each other and it is possible to simultaneously diagonalise only four of them. To be consistent with Russel-Saunders coupling, we assign good quantum numbers to $\underline{L}$, $\underline{S}$, $\underline{M}_L$ and $\underline{M}_S$.

Although group theory allows the determination of the nature of the splitting up of the configuration into terms by the electronic coulomb repulsion, it gives no indication of the energy separation between terms or of the nature of the ground term. To solve this last problem recourse is usually made to the semi-empirical Hund's rules in which the term with maximum $\underline{L}$ value consistent with maximum $\underline{S}$ value is assumed to lie lowest. The energy separation between terms is of the order of the inter-atomic coulomb energy - a few electron volts.

We are now in a position to consider the effect of the remaining term in the free ion hamiltonian, the spin orbit coupling, on the energies of the various terms. However, as the crystal field V_c is often of the same order or larger than the spin orbit coupling, we will proceed first to an evaluation of its effect on the hamiltonian. It may be noted however that as $\underline{L}$ and $\underline{S}$ are good quantum numbers, then for the ground term $\sum_{ij} a_{ij} \ell_i s_j$ may be written as $\lambda \underline{L}.\underline{S}$, where λ, the spin orbit coupling constant, has a definite value for a given term.

2.1.2 The crystal potential V_c

As a general rule, and as our analysis so far has demonstrated, it is simpler to achieve a description of the energy levels and splittings of an ion in a crystalline field by treating successive terms in the hamiltonian as perturbations on a state determined by the previous terms. This method requires that the relative magnitude of the various interactions be known and further, that the hamiltonian can be written in such a way that successive terms differ in their effects by roughly an order of magnitude. Inclusion of the crystal field however presents the difficulty that its position relative to other terms in the hamiltonian hierarchy depends very much on the particular situation envisaged. An investigation of the experimental data reveals that the strengths of the various crystalline fields fall into three groups which are generally categorised as follows:-

(a) Weak Field $\lambda \underline{L}.\underline{S} \gg V_c$

The Stark splittings by the electronic charges of the crystal field are less than the spin orbit splittings and consequently $\underline{J}$ will still be a useful quantum number. This is a situation typified by the rare earth elements in which the paramagnetic electrons lie in the 4f orbitals well shielded from the effects of the lattice.

(b) Medium Field $\sum_i \frac{e^2}{r_{ij}} > V_c > \lambda \underline{L}.\underline{S}$

This is the situation that usually prevails for the elements of the 3d transition group and is the designation appropriate to the studies reported here. The splittings produced by V_c are of the same order or slightly less than the electronic coulomb repulsions that split the configuration into terms.

(c) Strong Field $V_c > \sum_i \frac{e^2}{r_{ij}} > \lambda \underline{L}.\underline{S}$

Here the crystal field is stronger than the coulomb repulsion term. There is considerable overlap between ligand orbitals and the electron distribution of the central ion and the situation can be envisaged as one in which there is a considerable amount of covalency in the bonding between ion and ligands.

The analysis which follows will be restricted to the medium field case but before proceeding it is possible to deduce quite a lot of information from the symmetry and form of V_c.

The crystal field approach assumes that in the region in which the electrons move the charge density arises only from the central ion itself and that the contribution from the ligands is zero. Moreover the central ion potential is included in the free ion hamiltonian with the result that the crystal field potential can be assumed to satisfy Laplace's equation,

$$\nabla^2 V_c = 0 \qquad (2.3)$$

in this region.

The solutions of (2.3) can be written as generalised Legendre polynomials of the form

$$V_c = \sum_n V_n^m = \sum_n \sum_{m=n}^{-n} \sum_k A_n^m r^n Y_n^m (\theta_k \phi_k) \qquad (2.4)$$

where the summation k is over the electrons of the central ion and the Y_n^m are the normalised harmonics

$$Y_n^m(\theta,\phi) = (-1)^m \left[\frac{1}{4\pi} \frac{(2n+1)(n-|m|)!}{(n+|m|!)} \right]^{\frac{1}{2}} P_n^m(\cos\theta) e^{im\phi} \qquad (2.5)$$

We will be interested in the matrix elements of V_c between the wavefunctions ψ_ℓ^k of the electrons in the free ion orbitals and it is useful to expand these wavefunctions as a sum of the same harmonics $Y_n^m(\theta,\phi)$. These expansions carry the restriction that $n \leq 2\ell$ where ℓ is the angular momentum quantum number of the orbital and consequently all elements $\langle\psi_\ell^k|V_n^m|\psi_\ell^k\rangle$ for which $n > 2\ell$ will be zero. In addition all the terms in (2.4) with odd n must be zero since the matrix elements for these will be integrals over all space of functions of odd parity. The term in $n = 0$ can also be ignored since it is a constant and as it shifts all levels of a configuration equally will not contribute in optical or magnetic transitions. These restrictions mean that for the iron group with $\ell = 2$ the only terms we need to consider are those with $n = 2$ and 4 and further since the potential must be real $A_n^m = -(A_n^{-m})^*$. The symmetry of V_c will also modify the form of its expression and a table of the expressions appropriate to V_c for various symmetries can be found in Low (1960).

Having achieved consistent expressions for the electron wavefunctions and the form of V_c, it is now necessary to evaluate the remaining non-zero matrix elements. This calculation is simplified by making use of the theorem of Operator Equivalents established by Stevens (1952). The theorem states that if two operators A and B have the same transformation properties, then in a manifold of constant J their matrix elements will be linearly related. Consequently it is possible, for example, to replace elements like x, y and z in the cartesian form for V_c by J_x, J_y and J_z and thus the evaluation is made considerably easier. Tables of the various operator equivalents are given by Low (1960) and Stevens (1952). Diagonalisation of this matrix of V_c between the wavefunctions of the free ion hamiltonian reveals how the free ion terms are split into 'levels' by the crystal field. Appendix II shows how the form, though not of course the magnitudes, of this splitting into levels can be deduced from group theory. The remaining terms in the hamiltonian, the spin orbit coupling and the Zeeman term, are usually dealt with by means of the spin hamiltonian, but before doing this it will be as well to clarify the development so far by means of an example.

2.1.3 Illustration of Crystal Field Theory : Cr^{3+}

Consider the case of a $(3d)^3$ ion such as Cr^{3+} in a cubic material such as MgO. The following analysis will hold for the isoelectronic ions Ti^{1+}, V^{2+} and Mn^{4+}, all of which have indeed been seen in MgO (Henderson and Wertz 1968). The electron configuration of Cr^{3+} is $(1s)^2$ $(2s)^2$ $(2p)^6$ $(3s)^2$ $(3p)^6$ $(3d)^3$. All but the $(3d)^3$ electrons go to make up the spherically symmetric closed shell configuration of argon and will be unaffected by the crystal field. The only effect of the closed shell core of electrons will be to partially 'screen' the $(3d)^3$ electrons from the nuclear potential and consequently change the radial dependence of their one electron orbitals. Having specified the configuration it is now necessary to consider how it is split into terms, each diagonal in L, S, M_L and M_S, by the coulomb repulsion between electrons. To facilitate this a table is constructed of all the possible M_L M_S states that can be formed by placing three electrons in the five available 3d orbitals, bearing in mind that each orbital can accommodate a maximum of two electrons provided their spins are paired. This enables us to pick out the terms and by means of the empirical Hund's rules to select the term of lowest energy. As this analysis is rather laborious for $(3d)^3$ electrons it is not presented in detail but the resulting term splittings are shown

CRYSTAL FIELD SPLITTING OF d^3 CONFIGURATION

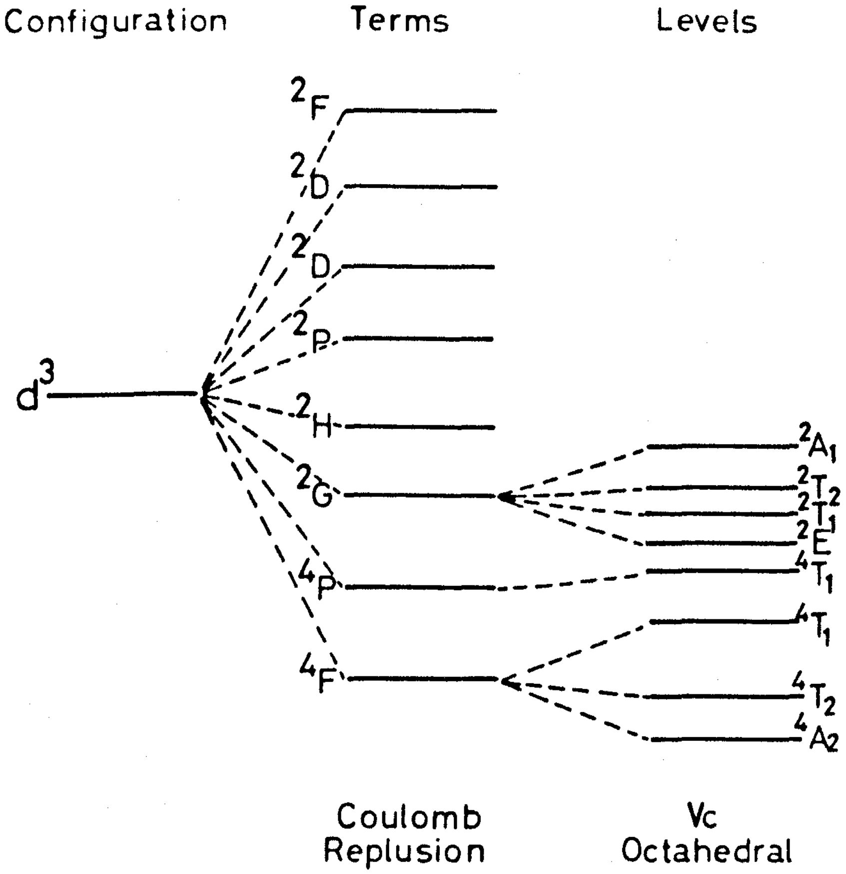

(after Tanabe and Sugano 1954)

FIGURE 2·1

in Figure 2.1. It may be noted here that whereas the Hund's rules are generally correct in specifying the ground term, they do not always give the correct ordering of the higher terms.

As can be seen from Figure 2.1, the ground state of Cr^{3+} is a ^4F term with $L = 3$ and $S = 3/2$. We now proceed to investigate how the octahedral crystal field of MgO will split this term. As indicated in Appendix II, we need to decide which irreducible representations of the octahedral group O are spanned by the D^3 representation of the full rotation group of the ^3F functions. From the character table of O (given in Cotton 1964) and the characters of the irreducible representations of O which can be constructed from a basis of third order spherical harmonics, we can find how many times each irreducible representation of the crystal point group O is contained in the $L = 3$ representation. (This problem is treated in detail in Appendix II). Thus:

$$D^3 = A_2 + T_1 + T_2 \tag{2.6}$$

and a field of octahedral symmetry will split the ^4F term into a singlet and two triplet levels. To deduce the ordering of these levels it is necessary to diagonalise the hamiltonian directly. Expressing the crystal field term in cartesian coordinates

$$V_c = \sum_i D_i(x_i^2 + y_i^2 + z_i^2 - 3/5\, r_i^2) \tag{2.7}$$

This satisfies Laplace's equation and transforms according to an irreducible representation D_4 of the rotation group. Making use of Stevens' operator equivalent method, we can replace x, y and z by

COMPARISON OF THE SYMMETRY OF f ORBITALS AND AN OCTAHEDRAL CRYSTAL FIELD

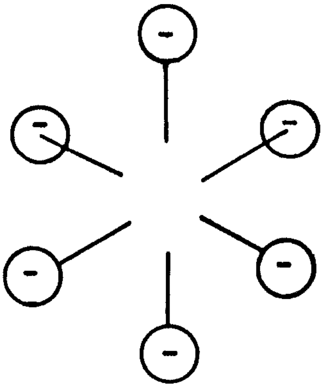

OCTAHEDRAL FIELD

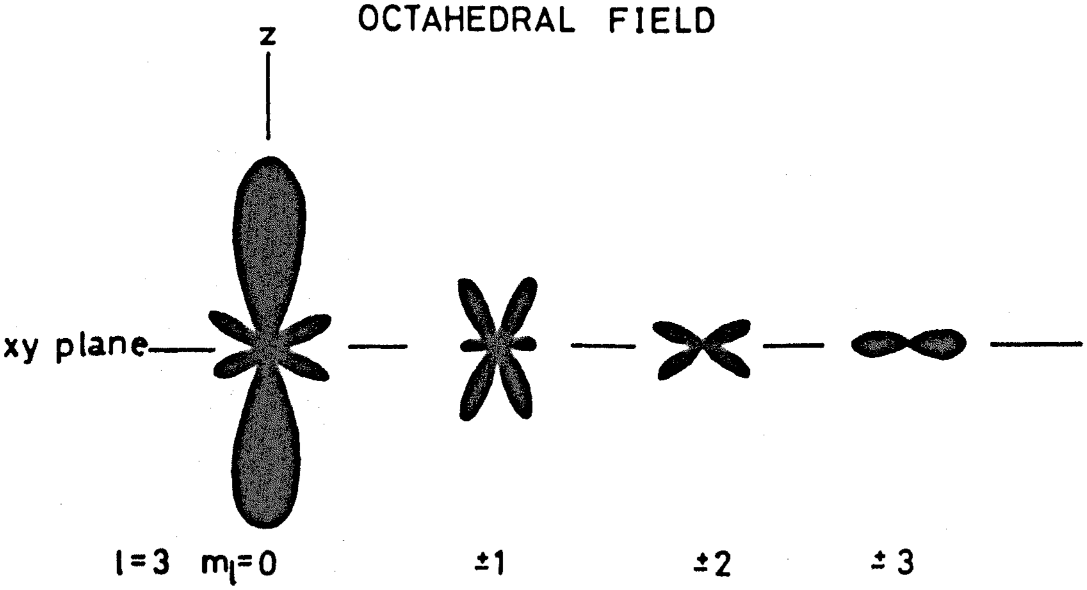

POLAR DIAGRAMS OF f ELECTRON ORBITALS
(after Pauling and Wilson 1935)

FIGURE 2·2

L_x, L_y and L_z and the required operator for V_c is

$$\frac{\beta r^{-4}}{20}\left[35L_z{}^4 - 30L(L+1)\,L_z{}^2 + 25L_z{}^2 - L(L+1) + 3L^2(L+1)^2\right] + \frac{\beta r^4}{8}(L_+{}^4 + L_-{}^4) \qquad (2.8)$$

Since V_c includes no spin operators, all that remains is to diagonalise its matrix between the orbital $|M_L>$ states of the ^4F term. This establishes the order of states (Figure 2.1) and gives splittings in terms of Dq where D depends on the crystal field strength and q($= \frac{2r^4}{105}$) on the radial part of the wavefunction.

The results of the above analysis can be more easily visualised by considering the physical effect of placing a ^4F term electron distribution in an octahedron of negative ions (Figure 2.2). The ^4F electron distribution can be thought of as a superposition of electrons occupying real forms of the f type orbitals which transform like the F term. Those orbitals with lobes pointing towards the negative ligands will suffer electrostatic repulsion and be raised in energy relative to those which avoid the ligands. Thus in an octahedral field the 7 f orbitals split into groups of 3, 3 and 1.

Figure 2.1 illustrates that an octahedral field will still leave some degeneracy in the higher energy levels. This degeneracy will be lifted by fields of lower symmetry and indeed a general theory due to Jahn and Teller states that in the event of the crystal field leaving the ground state degenerate this degeneracy will be removed by a local distortion of the atoms around the site, resulting in a lowering of the energy of the whole system. This removal of orbital degeneracy by the crystal field is sometimes referred to as orbital quenching.

It only remains now to introduce the spin of the electrons in the ground state of the Cr^{3+} ion in order to complete our description of its energylevels preparatory to a consideration of spin orbit coupling and magnetic effects. The ground state orbital singlet $^4A_2$ will have a four fold spin degeneracy and it might be expected that this degeneracy will be removed in the same way that the orbital degeneracy was. However a general theorem due to Kramer establishes that in the absence of a magnetic field all the energy levels of an ion with an odd number of electrons must be at least doubly degenerate. Thus we see that it is only possible for the crystal field to split the spin degeneracy of Cr^{3+} into two doublets which is in fact what happens.

2.2 The Spin Hamiltonian

The inclusion in the hamiltonian of the spin orbit coupling and Zeeman terms produces splittings in the ionic energy levels which are of the same order as the microwave quanta used in electron paramagnetic resonance. Consequently it is between these levels that transitions will be induced and resonance observed. Thus it is convenient to develop a formulation of the hamiltonian in which the experimental data can be speedily and economically summarised in terms of these interactions. Such a formulation is the effective spin hamiltonian of Pryce (1950) and Abragam and Pryce (1951), the development of which will be briefly presented here.

The two terms are considered together, a procedure justified by the fact that the stronger spin orbit coupling will vanish in first order for the orbital singlet ground state. Thus the perturbing hamiltonian is

$$\mathcal{H} = \lambda\underline{L}.\underline{S} + \beta\underline{H}(\underline{L} + 2\underline{S}) \qquad (2.9)$$

where the second term represents the Zeeman interaction between an applied field and the orbital and spin magnetic moments of the ion.

The shift in the energy of the ground state $|1>$ produced by admixtures from the higher levels $|n>$ is given by second order perturbation theory as:-

$$\Delta E = <1,M_{S_1}|\lambda\underline{L}.\underline{S} + \beta\underline{H}(\underline{L} + 2\underline{S})|1,M_{S_1}> + \sum_{n=2}^{N} \frac{|<1,M_{S_1}|\lambda\underline{L}.\underline{S} + \beta\underline{H}(\underline{L} + 2\underline{S})|n,M_{S_n}>|^2}{(E_1 - E_n)} \qquad (2.10)$$

As the orbital momentum is quenched to leave a singlet ground state

$$<1|\underline{L}|1> = 0$$

and only the spin terms contribute in first order.

The orbital eigenfunctions $|n>$ of the unperturbed hamiltonian are orthogonal so that

$$<n,M_{S_n}|\underline{S}|m.M_{S_m}> = 0 \quad \text{for } n \neq m$$

and consequently the spin terms vanish in second order reducing (2.10) to

$$\Delta E = \langle 1, M_{S_1} | 2\beta \underline{H}.\underline{S} | 1, M_{S_1} \rangle + \sum_{n=2}^{N} \frac{|\langle M_{S_n} | \lambda \underline{S} + \beta \underline{H} | M_{S_n} \rangle|^2 |\langle 1 | \underline{L} | n \rangle|^2}{(E_1 - E_n)}$$

At this point in the development of the spin Hamiltonian we 'remove' the spin states and retain the operator $\underline{S}$. This enables us to write the hamiltonian in a form convenient for a later evaluation between the actual spin states observed in resonance. Further, expressing L and $\underline{S}$ in terms of their components

$$\underline{S} = \sum_{i=x,y,z} \underline{S_i} \qquad \underline{L} = \sum_{i=x,y,z} \underline{\ell_i}$$

we have

$$\Delta E' = 2\beta \underline{H}.\underline{S} - \sum_{n=2}^{N} \sum_{ij} \frac{(\lambda \underline{S}_i + \beta \underline{H}_i)(\lambda \underline{S}_j + \beta \underline{H}_j) \langle 1 | \underline{\ell}_i | n \rangle \langle n | \ell_j | 1 \rangle}{(E_n - E_1)}$$

or

$$\Delta E' = 2\beta \underline{H}.\underline{S} - \sum_{i,j} \Omega_{ij} (\lambda^2 \underline{S}_i \underline{S}_j + \beta^2 \underline{H}_i \underline{H}_j + 2\beta\lambda \underline{H}_i \underline{S}_j) \tag{2.11}$$

where $\Omega_{ij} = \sum_{n=2}^{N} \dfrac{\langle 1 | \ell_i | n \rangle \langle n | \ell_j | 1 \rangle}{(E_n - E_1)}$

The term in $\beta^2 H_i H_j$ is a constant and represents a temperature independent paramagnetic moment induced on the ion. As it shifts all levels equally it can be ignored when considering transitions. Collecting the remaining terms of 2.11 together we get an expression for the spin hamiltonian

$$\mathcal{H}_s = \sum_{ij} \left[2(S_{ij} - \lambda \Omega_{ij}) \beta \underline{H}_i \underline{S}_j - \lambda^2 \Omega_{ij} \underline{S}_i \underline{S}_j \right]$$

which can be written in tensor notation as

$$\mathcal{H}_s = \beta\underline{H}.\underline{g}.\underline{S} + \underline{S}.\underline{D}.\underline{S}. \qquad (2.13)$$

where $\underline{g}$ and $\underline{D}$ are the second rank real symmetric tensors

$$g_{ij} = 2(S_{ij} - \lambda\Omega_{ij})$$
$$D_{ij} = -\lambda^2\Omega_{ij}$$

The formulation (2.13) includes only spin operators, the orbital angular momentum having been incorporated in the ansiotropic g tensor coupling the electron spin and applied magnetic field. This derivation illustrates how the spin orbit coupling may admix sufficient orbital angular momentum from higher levels into the ground state to lift its (2S+1) field degeneracy even in the absence of an applied field. This 'zero field splitting' is represented by the tensor D. The advantage of the spin hamiltonian is that it enables us to describe the behaviour of systems in which the zero field splitting is too great for all the transitions permitted by the $\Delta M_S = \pm 1$ selection rule to be observed. In these situations a suitable choice of a fictitious spin S' appropriate to the observed number of transitions will allow the spectrum to be described by (2.13).

By appropriate choice of axes x, y and z the g and D tensors can be diagonalised so that the general spin hamiltonian for any symmetry is

$$\mathcal{H}_s = \beta(g_{xx}H_xS_x + g_{yy}H_yS_y + g_{zz}H_zS_z) + D_xS_x{}^2 + D_yS_y{}^2 + D_zS_z{}^2 \qquad (2.14)$$

where it is assumed that the g and D tensor axes are coincident.

Alternatively the D tensor may be represented by

$$\underline{S}.\underline{D}.\underline{S} \;=\; D(S_z^2 - \tfrac{1}{3}S(S+1)) + E(S_x^2 - S_y^2) \qquad (2.15)$$

where $D = \tfrac{3}{2}D_z$ and $E = \tfrac{1}{2}(D_x - D_y)$.
By choosing $|D_x|<|D_y|<|D_z|$ the axes can always be chosen so that

$$0 \leq \frac{E}{D} \leq \tfrac{1}{3}$$

The term $\tfrac{1}{3}S(S+1)$ is included to fulfil the requirement that the tensor be traceless.

2.3 S State Ions

The ground state of an ion with a half filled shell (e.g. the $3d^5$ ions Mn^{2+} and Fe^{3+}) will be an orbital singlet or S term with a (2S + 1) fold spin degeneracy. As it is impossible for the crystal field, whatever its symmetry, to split the S term into levels, the only source from which the spin orbit coupling might admix orbital angular momentum into the ground state will be the higher energy terms.
As the term separations are considerable (25,000 cms^{-1} for d^5 in an octahedral field) such admixture should be very small and consequently there ought to be no zero field splitting of the spin states of an S state ion. This is contrary to observation and in order to summarise the spectrum, it is often necessary to resort to an extended hamiltonian including terms in S up to 2S + 1.

$$\mathcal{H} = \beta \underline{H}.\underline{g}.\underline{S} + D(S_z^2 - \tfrac{1}{3}S(S+1)) + E(S_x^2 - S_y^2)$$
$$+ \frac{F}{180}\left[35S_z^4 - 30S(S+1)S_z^2 + 25S_z^2 - 6S(S+1) + 3S^2(S+1)^2\right]$$
$$+ \frac{a}{6}\left[S_x^4 + S_y^4 + S_z^4 - \tfrac{1}{5}S(S+1)(3S^2 + 3S - 1)\right] \qquad (2.16)$$

where the terms in D and F, E and a represent the behaviour in tetragonal, rhombic and cubic fields respectively.

Several attempts have been made to explain this anomalous zero field splitting of S state ions notably by Van Vleck and Penny (1934) who considered the crystal field and spin orbit coupling as a combined perturbation on the free ion terms and went to a higher order of perturbation theory. This predicted splittings lower than those observed and Pryce (1950) suggested a first order spin spin interaction between different configurations ^6S ($3d^5$) and ^6D ($3d^4$ $4s^1$) combined with an axial field to account for D. These and other suggestions have been reviewed and evaluated by Sharma, Das and Orbach (1966).

2.4 Nuclear Interactions

So far we have considered only the magnetic moments of electrons and ignored the much smaller magnetic and electric quadrupole moments possessed by some nuclei. The electrons will interact with the nucleus of the paramagnetic ion and possibly, if their wavefunctions are sufficiently delocalised, with the nuclei of the surrounding ligands. A nucleus with a spin I will have (2I + 1) quantisation states in the magnetic field of the electrons and consequently each transition of the electronic 'fine structure' will be split into (2I + 1) 'hyperfine' components.

There are two contributions to this magnetic interaction between electrons and nuclei:-

(a) The Contact Interaction: This is an isotropic term introduced by Fermi to represent the energy of the nuclear moment in the magnetic field produced at the nucleus by electric currents associated with the spinning electron. It may be written

$$a\,\underline{I}.\underline{S} \tag{2.17}$$

where $a = \frac{8\pi}{3} g g_N \beta \beta_N |\psi(0)|^2$.

g_N and β_N are the nuclear g value and Bohr magneton and $\psi(0)$ is the electronic wavefunction at the nucleus. The wavefunctions of all but S orbitals have nodes at the nucleus and consequently the strength of this interaction provides a measure of the S character of the wavefunction.

(b) The Dipolar Interaction: This is an isotropic coupling analogous to the classical interaction between two dipoles and may be written quantum mechanically as

$$-\frac{g\beta g_n\beta_N}{\langle r^3\rangle}\left[\underline{I}.\underline{S} - 3(\underline{I}.\hat{\underline{r}}).(\underline{S}.\hat{\underline{r}})\right] \tag{2.18}$$

Besides the magnetic interaction there may be an electric quadrupole interaction between the electrons and the nucleus. This can be understood in terms of an electric field gradient caused by the anisotropy of the electronic charge distribution at the nucleus. In first order this gradient is independent of electronic spin and the interaction may be specified in the form

$$P_{ij}\, I_i\, I_j \tag{2.19}$$

where P_{ij} is tensor with components of order 10^{-3} cm^{-1}.

Collecting (2.17), (2.18) and (2.19) together and writing them in tensor notation, these interactions can be incorporated in the spin hamiltonian by adding

$$\left[A_zS_zI_z + A_xI_xS_x + A_yI_yS_y \right] + Q'\left[I_z^2 - \tfrac{1}{3}I(I+1)\right] - \gamma\beta_n.\underline{H}.\underline{I} \qquad (2.20)$$

to (2.14).

The first term represents the nuclear hyperfine interaction, the second the electric quadrupole coupling and the third the direct Zeeman interaction between the nuclear spin and the applied field which is usually small enough to ignore.

Normally in an electron spin resonance transition the electron quantum number changes by 1 while the nuclear quantum number m_I is unchanged. However at certain orientations of the centre to the applied field it is possible to observe transitions in which m_I also changes. The physical reason for the occurrence of such 'forbidden' transitions lies in the competition between the quadrupole moment trying to align the nucleus along the symmetry axis of the electronic crystal field and the magnetic field of the electrons which tries to align the nucleus off this axis. Several nuclear states become admixed and the resulting non-zero off diagonal matrix elements give a finite transition probability between different nuclear quantum states.

2.5 Molecular Orbital Theory

It was pointed out earlier that electrons with unpaired spins may be present in an insulator due to the presence of disrupted bands or other traps such as vacant lattice sites. The interpretation of resonance signals arising from such defect centres is rather more difficult than the case of transition metal centres since one cannot usually assume the existence of a centro-symmetric free ion hamiltonian as a starting point. Consequently the analysis is often more qualitative. The crucial starting point for the consideration of transition metal ion resonance centres was the assumption that the electron orbitals were essentially the one electron orbitals of the free ion. Analogously one begins the treatment of an electron trap by specifying the form of the electron orbitals. Here we make use of molecular orbital theory which attempts to find orbitals fulfilling the same function for molecules as the s, p, d etc. orbitals do for atoms. Once having achieved the molecular orbitals of a centre, we can specify its electronic structure by assigning electrons to these orbitals in accordance with the Pauli principle. In any particular case the determination of molecular orbitals usually proceeds by forming various linear combinations of the orbitals available on the atoms surrounding the centre (LCAO's). Symmetry considerations can often be used to eliminate various possible LCAO's and decide which are degenerate. In practice the experimentally observed spectrum can usually be summarised in terms of the spin hamiltonian of (2.14) and (2.20) suitably generalised to include the effects of transferred hyperfine interactions on the surrounding nuclei - often the most important clue as to the nature of the centre. The origins of the various terms in (2.14) and (2.20) are of course quite different in the case of electron traps, the g tensor anisotropy for example now being due to admixtures from higher molecular orbitals instead of from higher levels of the free ion ground term.

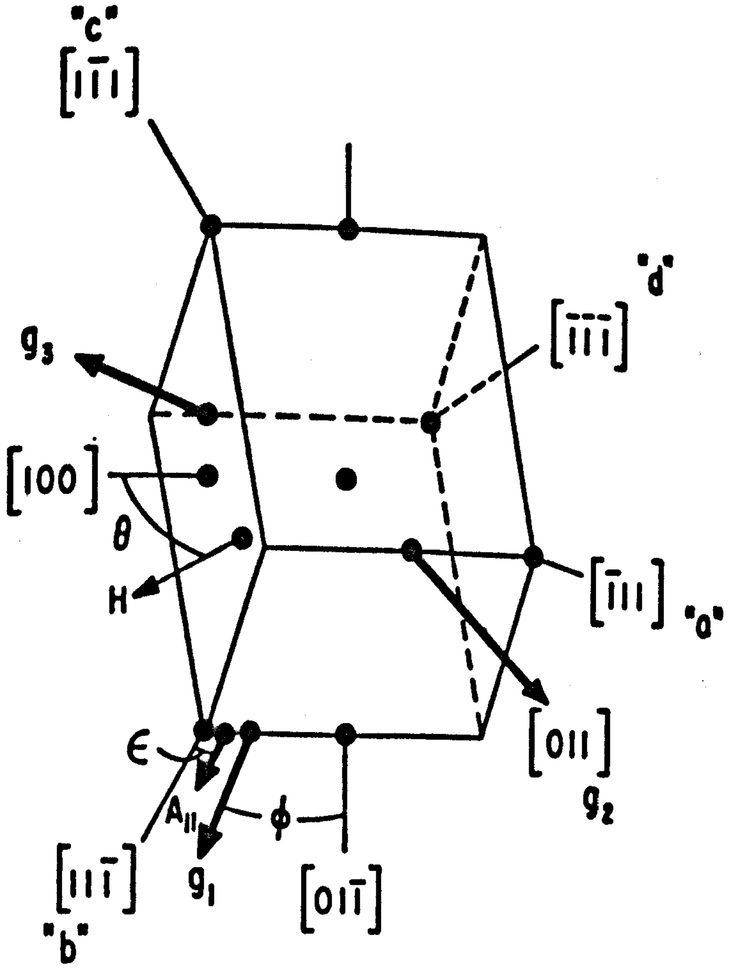

G6

$g_1 = 2.0004 \pm .0003$
$g_2 = 2.0020 \pm .0003$
$g_3 = 2.0041 \pm .0003$
$\phi = 27.6 \pm 0.5°$

$A_{\parallel} = 67.8 \pm 0.5\ (10^{-4})\ \mathrm{cm}^{-1}$
$A_{\perp} = 40.0 \pm 0.5\ (10^{-4})\ \mathrm{cm}^{-1}$
$\epsilon = +0.5 \pm 0.3°$

G7

$g_1 = 2.0012 \pm .0003$
$g_2 = 2.0135 \pm .0003$
$g_3 = 2.0150 \pm .0003$
$\phi = 29 \pm 1°$

$A_{\parallel} = 79 \pm 2\ (10^{-4})\ \mathrm{cm}^{-1}$
$A_{\perp} = 56 \pm 2\ (10^{-4})\ \mathrm{cm}^{-1}$
$\epsilon = -2 \pm 1°$

(after Watkins and Corbett 1965)

FIGURE 2.3

An excellent illustration of the molecular orbital approach to the analysis of resonance spectra arising from defect states is provided by the work of Watkins and Corbett on silicon. A brief account of one of the centres they identified, the divacancy, will be given here. A fuller treatment of this and related defects can be found in their papers (Watkins and Corbett 1965, Corbett 1966). A discussion of the success of their model# and its implications is given in a recent paper by Hagston (1970).

2.5.1 Illustration of Molecular Orbital Theory: The Silicon Divacancy

Electron irradiation of p-type and n-type silicon produces two e.p.r. spectra referred to as G6 and G7 respectively. Each spectrum consists of groups of lines from several inequivalent sites in the structure and each group, of a strong central line and weaker symmetrically disposed satellites, can be described by the spin hamiltonian

$$\mathcal{H} = \underline{H}\cdot\underline{g}\cdot\underline{S} + \sum_j \underline{I}_j\cdot\underline{A}_j\cdot\underline{S} \qquad (2.21)$$

The first term describes the anisotropy of the central line with respect to the orientation of the magnetic field to the crystal axis, while the second expresses an hyperfine interaction with the 4.7% abundant Si^{29} $(I = \frac{1}{2})$ nucleus at sites near to the defect. Comparison of the relative intensities of the main line and the satellites indicates that the Si^{29} must have a choice of two sites exactly equivalent about the defect centre. The principle values for the g and A tensors together with their directions for one of the inequivalent sites are shown in Figure 2.3.

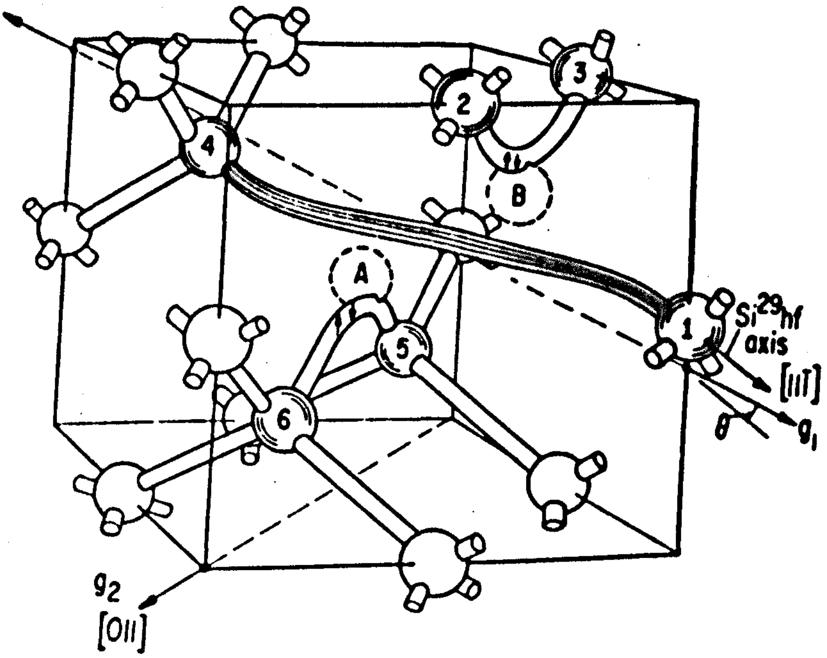

—The divacancy configuration proposed as giving rise to the Si—C and Si—J spectra. The vacancies are denoted by the A and B dashed circles. The electrons on silicon atoms 2 and 3, and on 5 and 6 form molecular bonds. E.p.r. arises from one (Si—J) electron or three (Si—C) electrons in an extended molecular orbital between silicon atoms 1 and 4. The principal axes of the *g*-tensor and Si^{29} *hf* interactions are shown.

(after Watkins and Corbett 1965)

FIGURE 2.4

The model proposed by Watkins and Corbett to explain these spectra is shown in Figure 2.4. It is the divacancy in which adjacent lattice sites A and B are vacant. The six broken bonds from the six atoms surrounding the divacancy are considered to form two 'bent' pair bonds between atoms 2-3 and 5-6 and one extended molecular orbital between atoms 1 and 4 as shown. In p-type silicon this extended molecular orbital holds one electron and gives rise to the G6 spectrum.
The higher Fermi level in n-type silicon populates the orbital with three electrons producing the G7 spectrum. This model explains the hyperfine splittings by interactions with Si^{29} at the equivalent sites 1 and 4, the <111> hyperfine axis corresponding to the directions of the broken bond at each site. The g tensor is tilted slightly away from this direction reflecting the overall character of the wavefunction.

A molecular orbital treatment of this defect based on LCAO's is shown in Figure 2.5. The atomic wavefunction at each atom ψ_i is considered to be a 3s3p hybrid and the one electron MO's are constructed by summing these over the surrounding atoms. The symmetry of the undistorted divacancy in silicon is D_{3d} and the molecular orbitals shown are those which transform according to the irreducible representations of this point group. The first two orbital singlets are filled by four electrons and the remaining electrons, one for the positive state and three for the negative, go into the e_u doublet. The degeneracy of this doublet is assumed to be lifted by a Jahn Teller distortion, lowering the symmetry to C_{2h}. The resulting energy level shifts are comparable to the energy level separations of the orbitals in D_{3d} symmetry and

ELECTRONIC STRUCTURE OF THE SILICON DIVACANCY

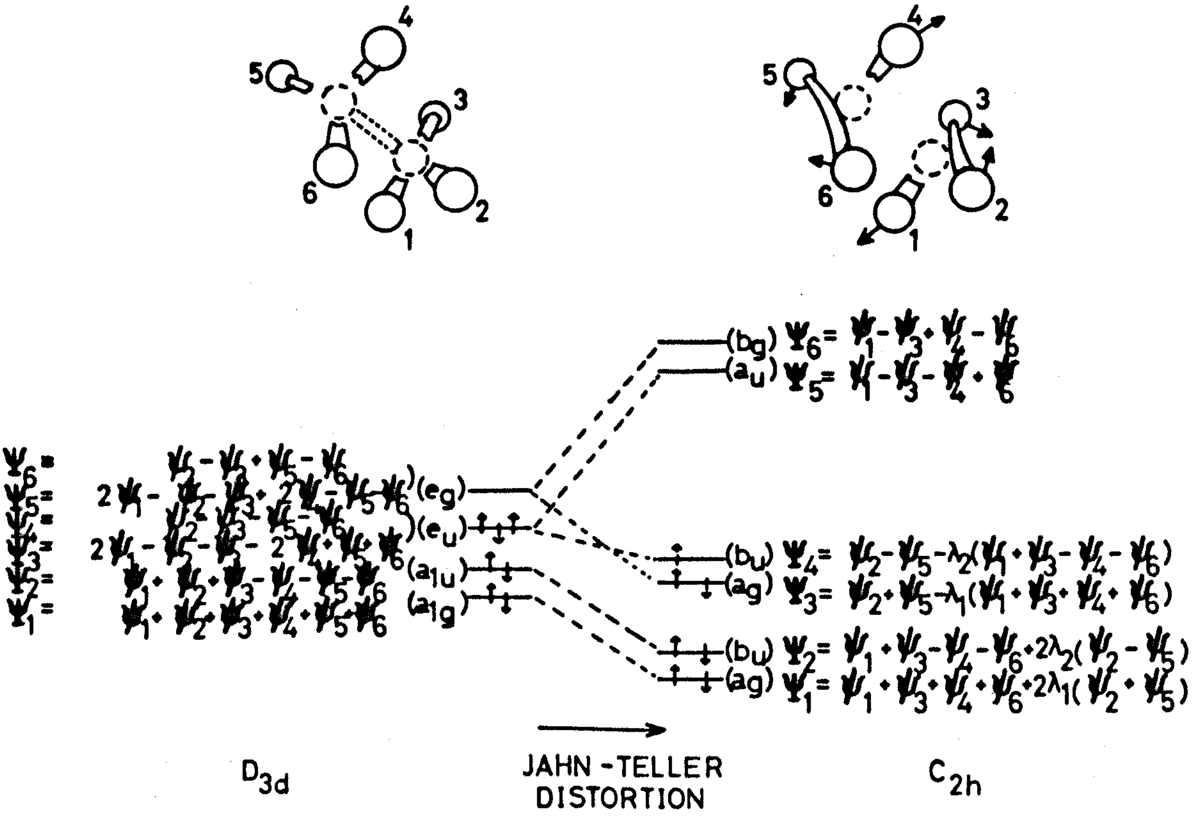

(after Watkins and Corbett 1965)

FIGURE 2·5

consequently this results in considerable mixing between e_g and a_{1g} and e_u and a_u. Consequently the wavefunctions in C_{2h} symmetry will reflect primarily the pair bonding between 2 and 3 (5 and 6) and only small admixtures of other orbitals remain.

Even though they ignored effects from next nearest neighbours, Watkins and Corbett were able to calculate approximately the observed hyperfine interaction. The magnitude of the g shifts expected from this structure is consistent with those observed and, more conclusively, the symmetry of the g tensor is compatible with the model. Stress splitting experiments and dynamic studies involving production rates and motional behaviour of related defects further support this assignment.

References

Abragam, A. and Pryce, M.H.L., Proc. Roy. Soc. (London) A205, 135 (1951).

Corbett, J.W., 'Solid State Physics Supplement 7' Ch. 3, 1966.

Cotton, F.A., 'Chemical Applications of Group Theory' (Wiley) 1964.

Eisberg, R.M., 'Fundamentals of Modern Physics' (Wiley) 1963.

Hagston, W.E., J. Phys. C. Inst. of Phys. & Phys. Soc. 3 No. 4, 791 (1970).

Henderson, B. and Wertz, J.E., 'Defects in Alkaline Earth Oxides' Adv. in Phys. 17 No. 70, 749 (1968).

Low, W., 'Solid State Physics Supplement 2' Ch. 2, 1960.

Murrell, J.M., Kettle, S.F.A. and Tedder, J.M., 'Valence Theory' Ch. 13 (Wiley) 1965.

Pryce, M.H.L., Phys. Rev. 80, 1107 (1950).

Pryce, M.H.L., Proc. Phys. Soc. A63, 25 (1950).

Sharma, R.R., Das. T.P. and Orbach, R., Phys. Rev. 149, 247 (1966).

Stevens, K.W.H., Proc. Phys. Soc. A65, 209 (1952).

Tanabe, Y. and Sugano, S., J. Phys. Soc. Japan 9, 753 (1954).

Tinkham, M., 'Group Theory and Quantum Mechanics' (McGraw-Hill) 1964.

Van Vleck, J.H. and Penny, W.G., Phil. Mag. 7, 961 (1934).

Watkins, G.D. and Corbett, J.W., Phys. Rev. 138, A543 (1965).

THE DECCA SPECTROMETER

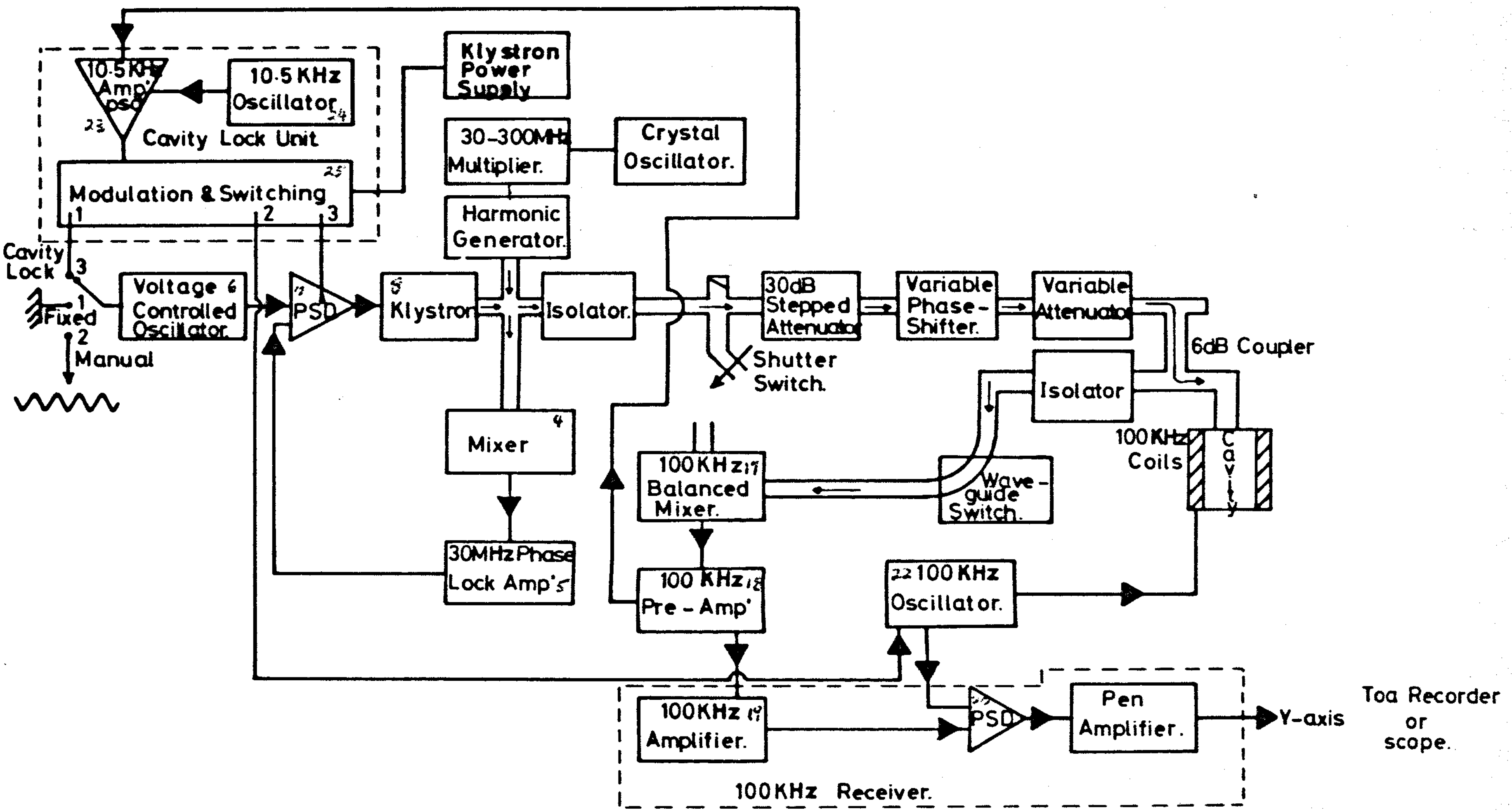

FIGURE 3.1

CHAPTER III

EXPERIMENTAL TECHNIQUES

The X band e.p.r. results reported in Chapters V and VI were obtained with Decca X2 and Varian 4500 spectrometers. The Q band work on Barium Oxide was performed using the Varian 4500 system with a V4561 Q band microwave bridge.

3.1 The Decca Spectrometer

A block diagram of those units of the Decca X2 spectrometer used in this work is shown in Figure 3.1. The X2 system includes superheterodyne detection facilities which were not used in this work and hence are not shown in the figure.

The spectrometer employs a fixed frequency klystron oscillator and a tunable resonant cavity. The klystron frequency is maintained by beating its output with an harmonic of a quartz crystal oscillator. The beat frequency is compared in a phase sensitive detector with the output of a voltage controlled oscillator and the difference signal produced controls the reflector potential and hence the klystron frequency. In addition the voltage controlled oscillator is tunable over a small range to allow the klystron to follow changes in the resonant frequency of the cavity as might be produced, for example, by temperature changes during the course of an experiment.

The klystron oscillator 8 has a nominal frequency of 9270 MHz. Precise control of the klystron frequency is achieved by phase locking to a harmonic of a stable 30 MHz quartz oscillator 1 housed in a constant temperature oven. The output from this oscillator is multiplied up to 300 MHz and applied to a crystal diode, mounted in the waveguide system, which acts as a harmonic generator. Three matching screws in the waveguide optimise the 31st harmonic at 9300 MHz and this is mixed with a sample of the klystron output in the crystal mixer 4. The 30 Mc/s beat frequency signal produced is amplified in a phase lock amplifier, 5, tuned to 30 Mc/s. The amplified signal is then compared with a reference signal from a voltage controlled oscillator 6 in a phase sensitive detector 7. The output from this phase sensitive detector, a d.c. voltage proportional to the phase difference between the two signals, controls the reflector potential and thus the frequency of the klystron. Any tendency of the klystron to change frequency appears first as a change of phase and generates sufficient voltage to maintain the original frequency.
The high spectral purity of the quartz oscillator ensures that fluctuations of the klystron frequency that are within the bandwidth of the phase lock loop are removed. The voltage controlled oscillator has little effect on the spectral purity of the output signal since its contribution is 310 times less important than that of the quartz oscillator. However the frequency of the klystron output does depend directly on the frequency of the voltage controlled oscillator, and thus by making this unit tunable the output signal can be tuned over a small range.

Thus:-

Klystron frequency = 310 × Crystal Oscillator frequency - Voltage Controlled Oscillator frequency

The voltage controlled oscillator then is the means by which the klystron frequency is varied. As shown in Figure 3.1 there are three ways of operating the voltage controlled oscillator (6).

1) Fixed at 30 MHz, klystron frequency 9270 MHz.
2) Manually controlled over 29 - 31 MHz, klystron tunable from 9269 - 9271 MHz.
3) Controlled by cavity lock system over 29 - 31 MHz, klystron automatically tuned over 9269 - 9271 MHz to follow changes in resonant frequency of cavity.

The phase locked klystron signal passes through an isolator, a cross guide coupler, a 30 dB switched attenuator, a variable phase shifter, a 50 dB precision rotatory vane attenuator and a 6 dB directional coupler to the sample cavity. The 6 dB coupler is designed so that the 6 dB loss can be in either the path of the power supplied to the cavity or the path of the reflected power.

The cavity used in this work was the Decca general purpose cavity. It operates in the TE_{102} mode and is of the rectangular waveguide type. A removable tuning rod controls the insertion length of four dielectric rods into the cavity so that it can be tuned to the frequency of the klystron. A second rod controls the size of the coupling hole between the waveguide and the cavity and there is a further control for fine tuning adjustments. Modulation coils in the cavity side walls provide a maximum field sweep within the cavity of 40 gauss when driven by the 100 kHz oscillator unit. The cavity has an unloaded Q of about 7000.

The reflected signal passes down the other arm of the directional coupler, through an isolator and a waveguide switch to the 100 kHz balanced mixer 17. The balanced mixer is biased by a sample of the klystron output signal applied by means of a crossguide coupler and shutter type waveguide switch. Since the magnetic field is modulated at 100 kHz the output of the mixer is thus an 100 MHz modulation of the beat frequency of the output and reflected microwave signals. This signal passes through the 100 kHz preamplifier 18 and then to the 100 kHz receiver which contains the main amplifier 19 and a phase sensitive detector 20. The 100 kHz oscillator 22 which drives the cavity modulation coils also provides the reference signal for 20 and thus the output from 20 is the first derivative of the E.S.R. spectrum which can be displayed on the Y axis of a TOA (Y-T) chart recorder or an oscilloscope.

In a system where the signal frequency remains constant it is necessary not only to tune the cavity to this frequency, but also to ensure that the cavity remains tuned while the spectrum is taken. This is the function of the cavity lock unit. A 10.5 kHz oscillator 24 is used to modulate the klystron reflector voltage. This frequency modulation of the klystron frequency results in a 10.5 kHz signal at the 100 kHz mixer 17, the phase of which varies with the cavity drift. This 10.5 kHz signal is extracted from the first stage of the 100 kHz preamplifier 18, amplified and applied to a phase sensitive detector 23 in the cavity lock unit. This phase sensitive detector compares the phase of the signal with the output of the 10.5 kHz oscillator and the resulting d.c. signal is used to control the reference oscillator 6.

The cavity corrected phase lock system described above is satisfactory if cavity detuning is limited to about ±1 MHz. However in some of the experiments performed in this work low temperatures were achieved by means of a continuous flow of cold Helium or Nitrogen gas through the specimen tube of the cavity. The resulting temperature fluctuations were such that the reference oscillator 6 could not compensate sufficiently and a direct cavity lock was achieved by connecting the output of the cavity lock unit phase sensitive detector 23 directly in series with the klystron power supply (point 3 on unit 25). This allows the klystron to change frequency by ±15 MHz to compensate for cavity detuning.

3.2 The Varian X and Q Band Spectrometers

Both Varian spectrometers, unlike the Decca, have tunable klystron oscillators and setting up is achieved by tuning the klystron until the central frequency of its mode coincides with the cavity dip. The difference in the power levels that can be generated at X and Q band frequencies leads to the adoption of quite different microwave bridges in the two spectrometers. In the X band spectrometer a balanced bridge is used, the klystron power being divided equally between the cavity and a balancing arm. The absence of such a large power reserve at Q band is met by employing a circulator to direct all but a fraction of the klystron power onto the cavity. The automatic frequency control, modulation, detection and display systems are common to both spectrometers.

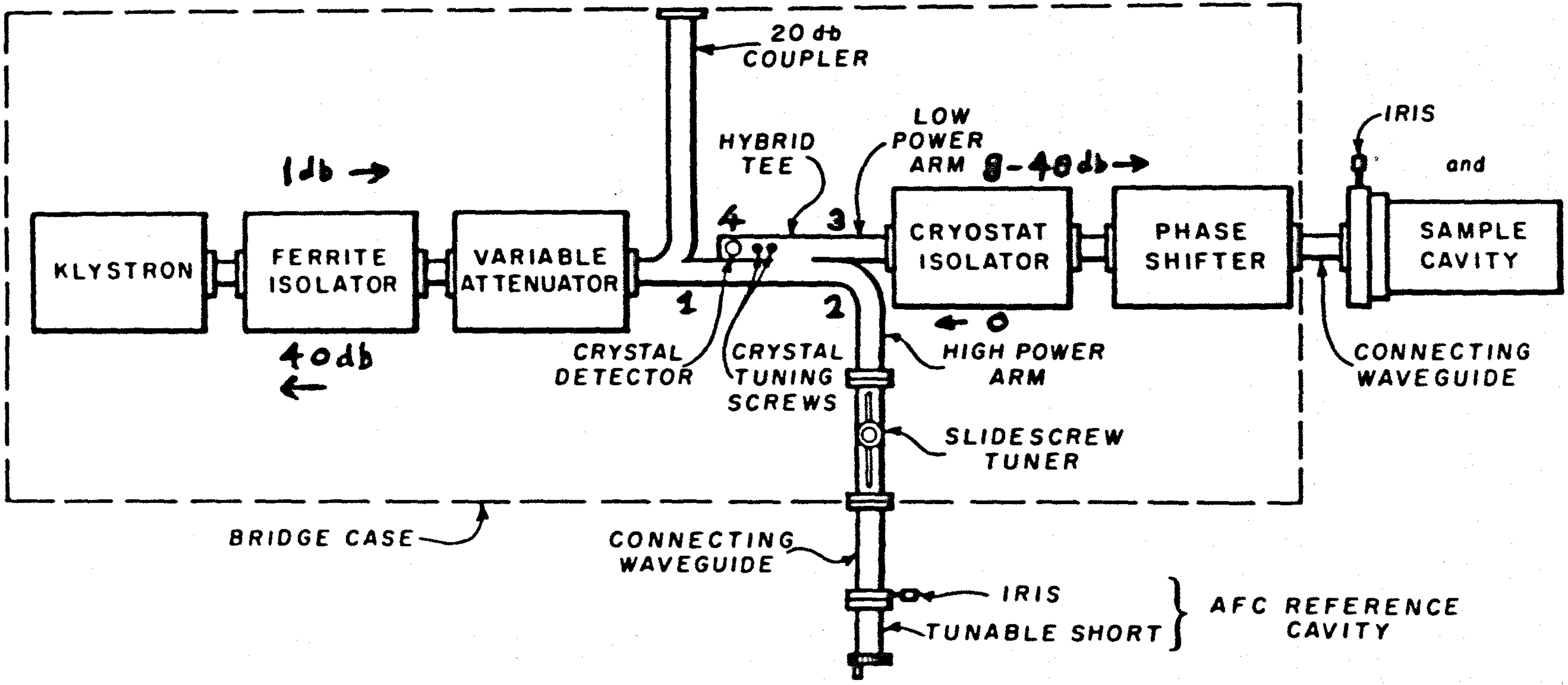

THE X BAND BRIDGE

FIGURE 3.2

3.2.1 The X band bridge

A diagram of the V-4500 X band microwave bridge is shown in Figure 3.2. The klystron is capable of generating in excess of 300 mW and this signal passes through a ferrite isolator and a variable attenuator to the first arm of the bridge. By attaching the cavity to arm 2 or arm 3, the system can be operated with high (20 - 25 dB below unattenuated klystron output) or low power levels incident on the cavity. The low power configuration illustrated in the figure allows the selection of absorption or dispersion mode operation. Klystron power from arm 1 is divided between arms 2 and 3 and the reflected signal from the cavity is detected by the crystal in arm 5. The detector crystal is biased by the slide screw tuner in arm 2 which can be varied to change both the mean power level and the phase of the microwave energy it reflects.
The amplitude of the microwaves reaching the cavity is set by the attenuator in arm 1 and the phase is determined by the phase shifter in arm 3. During resonance the sample absorbs microwave power and the resulting unbalanced condition of the bridge is detected by the crystal detector.

In a system with a tunable klystron it is necessary to measure the microwave frequency. For the work reported here this was done by attaching a waveguide to coaxial converter to the 20 dB coupler shown in the figure. This sample of the klystron output was mixed in a Hewlett Packard 540B transfer oscillator with a variable frequency of the order of 200 MHz. The variable frequency is tuned until zero beats are observed between the two signals. In this condition the klystron output must be

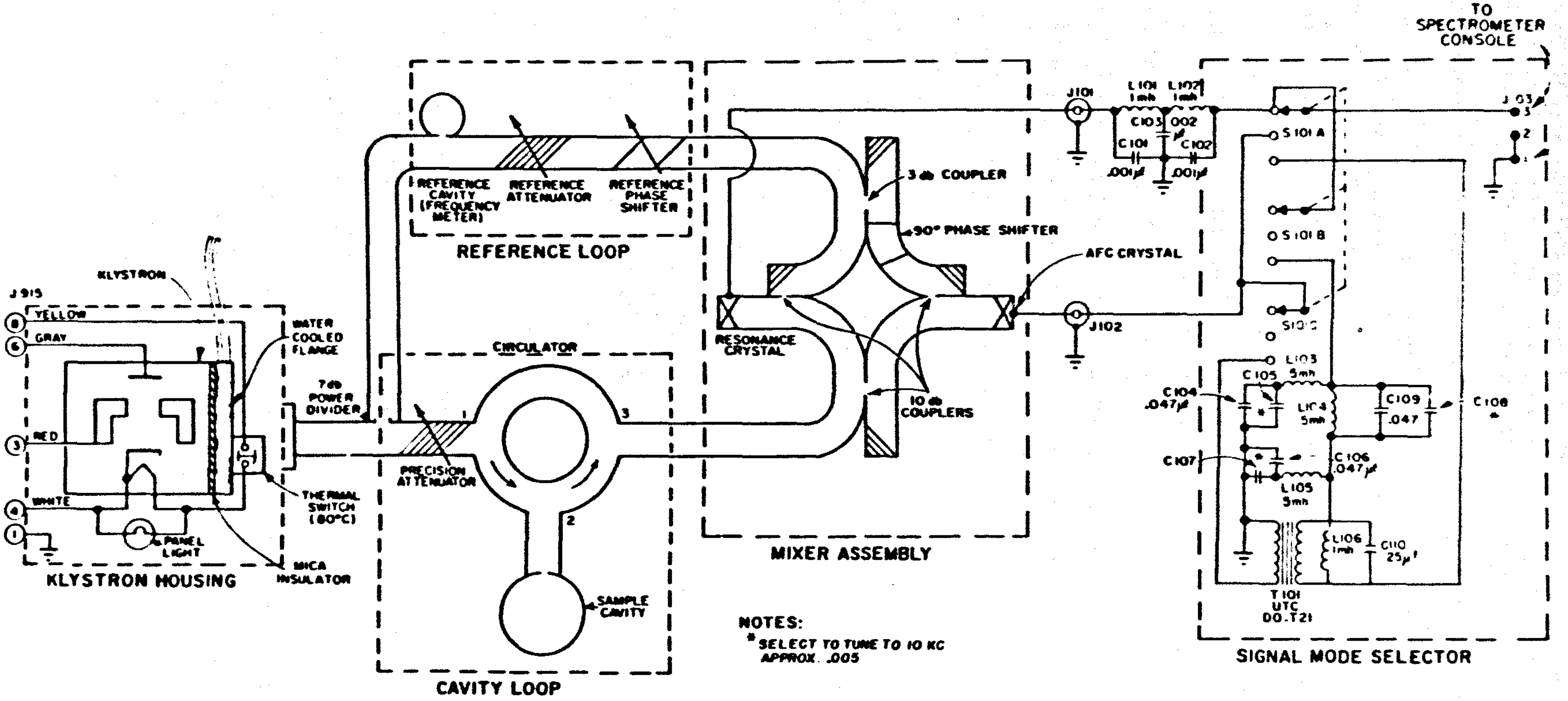

NOTES:
* SELECT TO TUNE TO 10 KC APPROX. .005

THE Q BAND BRIDGE

FIGURE 3.3

some harmonic of the frequency of the variable oscillator f_{v_1}.

$$f_{\text{klystron}} = n\, f_{v_1}$$

f_v was measured with a Hewlett Packard 544 D counter and a plug-in 525 C frequency counter unit to better than ±5 kHz. f_v was then varied until an adjacent zero beat condition occurred.

Then

$$f_{\text{klystron}} = (n + 1) f_{v_2}$$

Eliminating n

$$f_{\text{klystron}} = \frac{f_{v_2} f_{v_1}}{(f_{v_1} - f_{v_2})}$$

The klystron frequency was found to be stable with respect to the cavity to 1 part in 10^6 when the automatic frequency control was in operation.

3.2.2 The Q band bridge

Figure 3.3 shows the lay-out of the bridge which consists of a klystron oscillator, a reference loop, a cavity loop, a mixer assembly and a signal mode selector. The reflex klystron used has an output of about 50 mW at a frequency of 35 GHz. A 7 dB coupler diverts a small portion of the klystron output into the reference loop; the remainder passes through a variable precision attenuator to the cavity by means of a circulator. The circulator separates the reflected power from the incident power and passes it to the mixer where it meets the bucking power provided by the reference loop. A phase shifter in the reference loop allows the selection of dispersion mode operation and is used in conjunction with an attenuator to provide bias to the resonance crystal and microwave

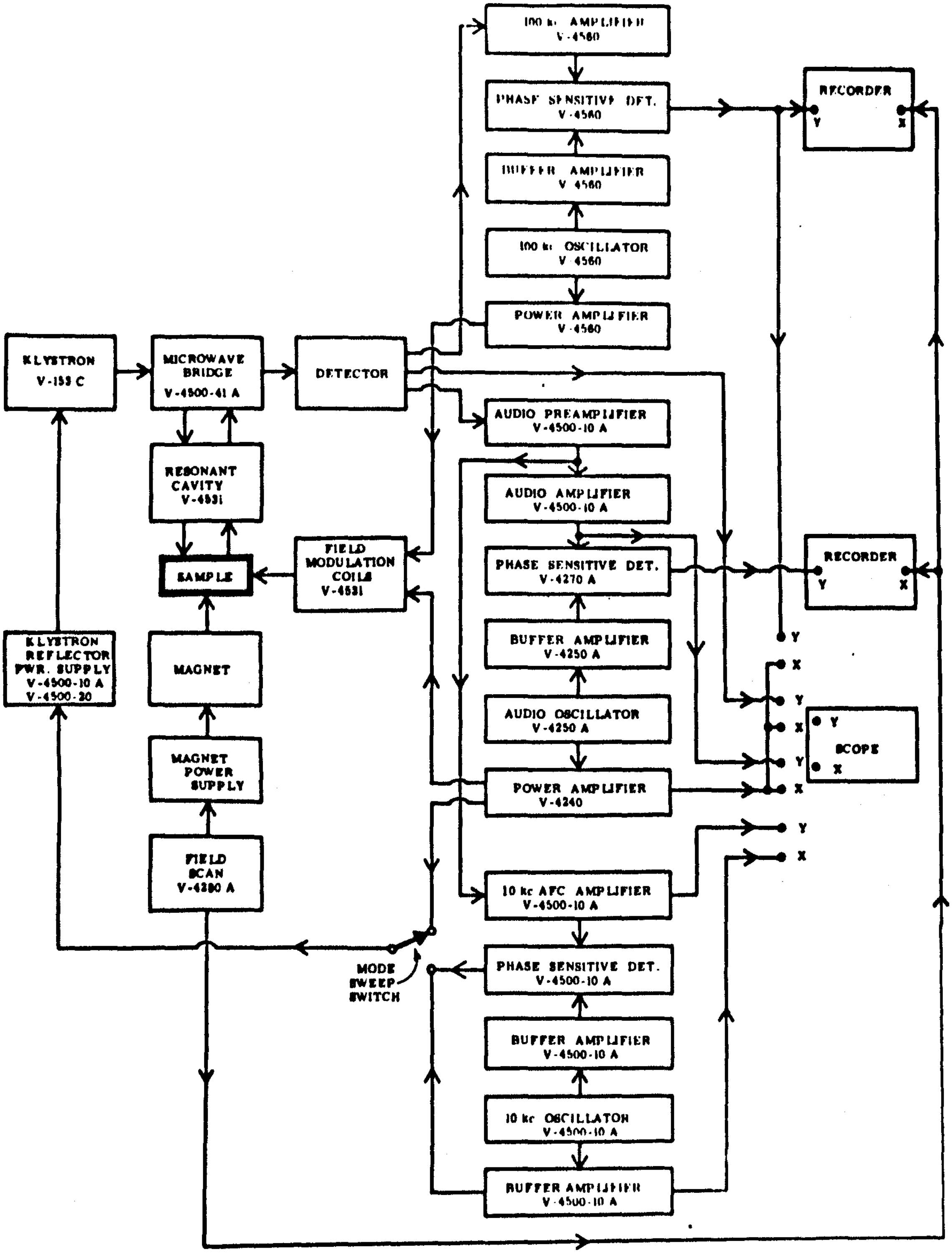

THE VARIAN SPECTROMETER

FIGURE 3.4

voltage to the A.F.C. crystal in dispersion operation. The reference loop also contains a precision cavity wavemeter graduated in units of 10 MHz which was used in this work to measure the operating frequency. Two detector crystals in the mixer enable the 10 kHz A.F.C. system to be employed when operating in either the absorption or dispersion mode. The phase angles of the microwaves differ by 90° at the two crystals. In the absorption mode the phase difference between the microwaves from the reference loop and those from the cavity is 0° and both the 100 kHz signal and the 10 kHz A.F.C. signal are taken from the resonance crystal. Dispersion mode operation results in a 90° phase difference between the two microwave paths at the resonance crystal and the 100 kHz signal is taken from here; the 10 kHz signal is now taken from the A.F.C. crystal where a 90° phase shifter in the mixer corrects for the phase difference between the microwave signals. The signal mode selector circuit permits the switching of the A.F.C. from one crystal to the other while detecting e.p.r., in either absorption or dispersion, at the resonance crystal.

3.2.3 Modulation, detection and A.F.C.

These units are common to both frequencies and are shown in Figure 3.4. The audio system is used both for signal display and initial setting up purposes. Its basic oscillator can be switched to produce a 20, 40, 80, 200 or 400 Hz signal which is then amplified. In setting up, this signal is applied to the klystron reflector via the mode sweep switch, allowing the klystron mode to be viewed on an oscilloscope.

The klystron is tuned by varying the reflector voltage until the cavity dip is superimposed on the central frequency of the mode. At Q band there is insufficient tuning range on the klystron to match the dip to the mode so the cavity is also tunable. The cavity dip is optimised in the centre of the klystron mode by means of a coupling screw between the cavity and the waveguide. Once the klystron is tuned the audio modulation is switched off by the mode sweep switch and the A.F.C. system switched on to keep the klystron on tune.

The A.F.C. system operates in a similar manner to the Decca system in that the klystron reflector voltage is modulated at 10 KHz thus producing a frequency modulation of the klystron output. If the klystron is operating at the frequency of the centre of the cavity dip, this 10 KHz signal will have zero amplitude upon reflection from the cavity. However, any drift of the klystron from this central frequency will produce a 10 KHz output proportional in amplitude to the slope of the cavity dip. After detection at the 'appropriate' detector in the bridge, this signal passes through the audio amplifier to a 10 KHz A.F.C. amplifier. It is then compared in a phase sensitive detector with a reference signal from the 10 KHz oscillator, the resulting d.c. voltage being applied as a correction to the klystron reflector power supply.

The Varian spectrometer can be operated with either audio or 100 Kc/s detection as both systems can be used to drive the cavity modulation coils. Phase sensitive detection is employed in both detectors and the resulting first derivative e.p.r. spectrum can be displayed on an oscilloscope or chart recorder. In the work reported here a TOA Y-T chart recorder was used.

3.2.4 The resonant cavities

The resonant cavities employed in this work were the V 4566 Q band cavity and the V 4533 X band rotating cavity.

Both cavities are of the right cylindrical type and operate in the TE_{011} mode. At both frequencies samples were inserted through an access hole in the centre of the cavity top plate adjacent to the waveguide. As mentioned previously it is necessary to tune the Q band cavity and this was achieved by varying the insertion of a tuning plunger which was threaded in the cavity from below. Both cavities had a matching screw which by governing the motion of a conducting rod through the iris gave a variable coupling facility. Modulation coils exterior to the cavities rotated with the magnet to ensure that the modulation field was always parallel to the d.c. magnetic field. These coils are part of the X band cavity construction, but at Q band are housed in an assembly supported by the magnet pole pieces. Relevant characteristics are given below:

	V 4566	V 4533
	Q Band	X Band
Frequency	35 GHz	9.5 GHz
Unloaded Q	7,000	20,000
100 Kc/s field modulation amplitude, peak to peak	15 gauss	10 gauss

3.3 Magnet Systems and Field Measurements

Both spectrometers were operated in conjunction with Varian V-3400 9" electromagnets and power supplies. The magnet in use with the Varian spectrometer was mounted on a trolley which could be rolled along a railway track between the X and Q band bridges. This magnet could also be rotated a full 360° about either cavity for angular variation studies. Shimmed pole pieces gave a maximum field of 15.25 kilogauss with air gap of 1¾" for Q band operation. Work at X band necessitated the removal of these pole pieces to accommodate the X band cavity and the increased gap of 2½" lowered the maximum field to 10 kilogauss. Magnetic field control was provided by a Varian Mk I Fieldial.

The magnet used with the Decca spectrometer had a rather larger air gap of 3¼" which reduced the maximum field attainable to 8.5 kilogauss. The rectangular shape and the protruding tuning rods of the Decca cavity restricted rotation of the magnet to ±15° of the forward position, a restriction that was overcome by mounting specimens on a goniometer and rotating inside the cavity. A Mk II Fieldial was used to control the field of this magnet. Both Fieldials employ a Hall effect probe, mounted on one of the magnet pole pieces, to keep the field in the gap at the value selected on the dial. A difference between the actual and selected field generates an error signal which is applied to the power supply regulator circuits in much the same way as an A.F.C. system. The Fieldial was found to be a great aid in finding and taking preliminary measurements of e.p.r. spectra but for accurate measurements reliance was placed on proton resonance units. Two such units were built in accordance with Robinson's

PROTON RESONANCE UNITS

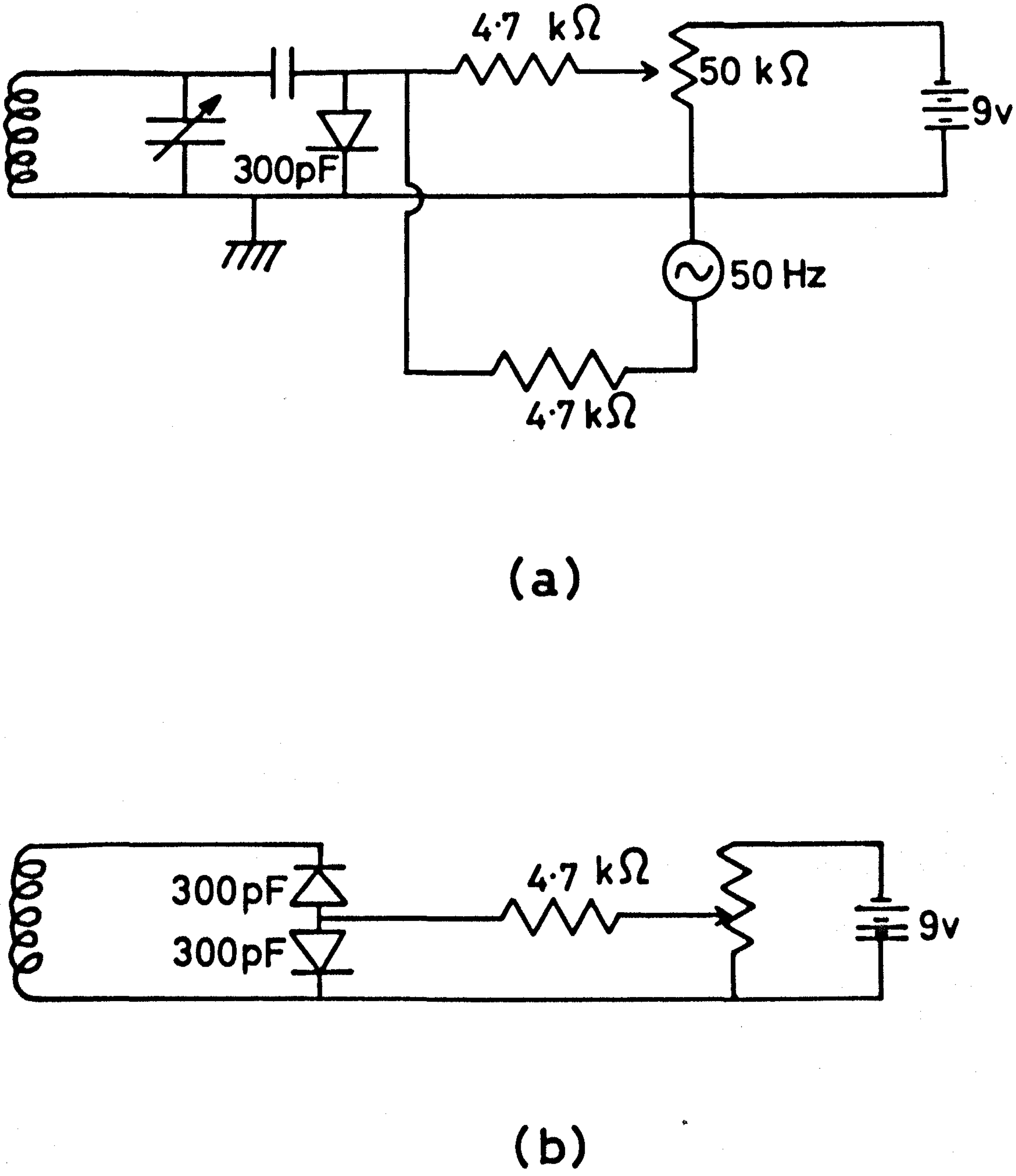

FIGURE 3·5

design (1965), one for X band use and the other for use at Q band. The X band proton resonance unit was used mainly to measure line positions in $CaWO_4$ and, as some of these lines were quite narrow (600 mg), the 50 Hz field modulation required to observe the proton resonance signal made simultaneous observation of the e.p.r. lines to be measured impossible. Consequently it was decided to abandon the 50 Hz modulation of the field and frequency modulate the proton resonance oscillator instead. This was done by applying a 50 Hz signal to a vericap included in the tuned circuit as shown in Figure 3.5a. The central proton resonance frequency was measured by locating a condition of minimum beats with a harmonic of a quartz oscillator in a heterodyne frequency meter unit. The high frequency proton resonance unit was also modified as shown in Figure 3.5b. The mechanical tuning capacitor was replaced by two vericaps as shown, and the resulting control of the oscillating frequency by means of the rheostat made operation much simpler. The frequency of this oscillator was measured with a Hewlett Packard frequency counter. Spectra were recorded on a TOA Y-T chart recorder while the field was swept by means of a motor driven potentiometer in the Fieldial control unit. Over the ranges used the field sweep was found to be linear to within the stability of the proton resonance units (1 in 10^{10}).

3.4 Low Temperature Equipment

Low temperature experiments were performed with the Decca spectrometer. Initially a 'cold finger' technique was employed, the specimen being cemented to a copper rod which extended into the nitrogen reservoir

BACK REFLECTION LAUE TECHNIQUE

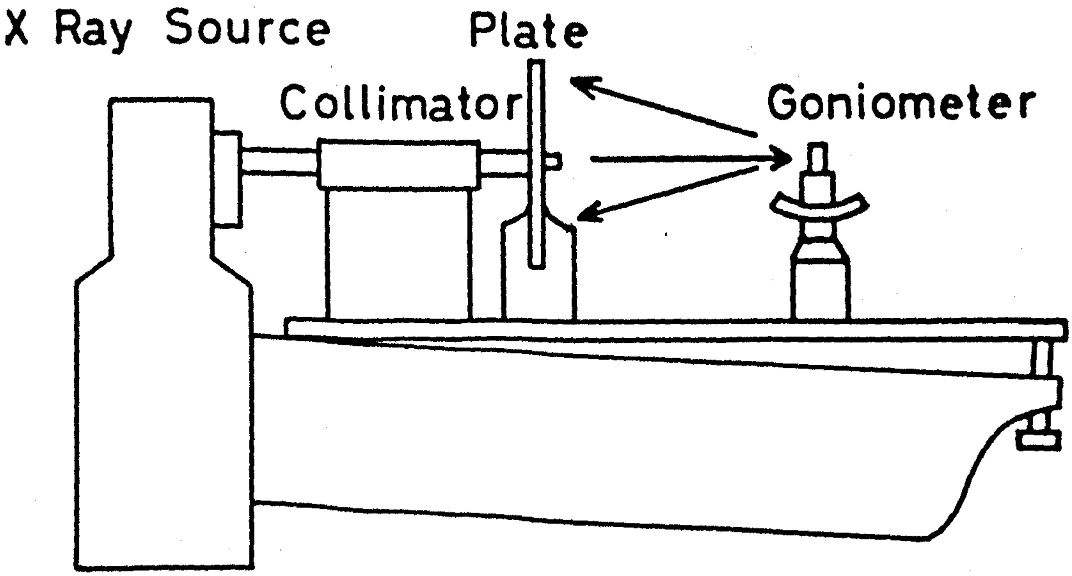

FIGURE 3·6

of the dewar. Nitrogen was excluded from the cold finger itself as the bubbling disturbed the cavity Q. This technique was rejected, however, as it made it particularly difficult to align specimens accurately.

A gas flow system was adopted which allowed crystals to be mounted on a goniometer and hence aligned to the same accuracy as at room temperature. The technique involved the insertion of an evacuated quartz tube into the cavity. The specimen was lowered into the tube from the top and the cold gas flow connected to the bottom of the tube. For liquid nitrogen temperatures nitrogen gas from a high pressure cylinder was passed through a metal refrigerating coil immersed in a liquid nitrogen bath.

The temperature could be varied by adjusting the flow rate. Lower temperatures were achieved by transferring helium gas to the bottom of the tube directly from a helium dewar by means of an evacuated stainless steel transfer tube. No absolute measurements of temperature were performed though the operation of identical systems on other spectrometers yields temperatures down to 100°K for nitrogen (Assabghy 1970) and 10°K for helium (Dowsing 1969).

3.5 Orientation and Mounting of Crystals

To interpret an e.p.r. spectrum it is necessary to know the directions of the crystal axes in the specimen to be observed. It was by no means clear where the principal axis directions of the $CaWO_4$ crystals lay and to decide this recourse was made to X-ray diffraction. A Phillips PW 1030 X-ray system was used to take back reflection Laue photographs as shown in Figure 3.6. The 40 kV, 15 mA, electron beam, incident on a tungsten target,produced a 'white' X-ray spectrum which was directed at the crystal. The crystal mount was a two circle goniometer which enabled corrections to be made to its orientation between exposures. Exposure times of four hours yielded reasonable diffraction photographs.

To simplify and determine the symmetry of the e.p.r. spectrum it was necessary to perform angular variation studies in particular crystal planes. This was accomplished by mounting the crystals on teflon wedges machined to the required angles; a technique that was particularly useful with $CaWO_4$ where the planes required were rather obscure. It was necessary to use quite small wedges, typical dimensions being 3 mm diameter and 8 mm long, as the sample axis hole at Q band was only 2 mm diameter and for low temperature work at X band the crystal plus wedge had to rotate within the 5 mm diameter bore of the flow tube. On the Varian systems anisotropy studies could be performed by rotating the magnet, but on the Decca it was necessary to mount the crystal on a goniometer. As the $CaWO_4$ spectra were very sensitive to misorientation a two circle goniometer was designed. A small internal wheel, to which the crystal was cemented, could be rotated by means of a flexible cotton loop passing over an external wheel thus providing three dimensional control of crystal orientation in situ. To ensure that alignment in the desired plane had been achieved, it was checked that directions which should be equivalent produced identical spectra.

3.6 Microscopes

The optical microscopy work reported in Chapter IV was performed on a Vickers projection microscope and a Russian MNM-7 vertical metallographical microscope. Electron microscopy was performed with the department's Hatachi HS-75 transmission electron microscope.

References

Assabghy, F.Y.I., Private communication (1970).

Dowsing, R.D., Private communication (1969).

Robinson, F.N.H., J. Sci. Inst. 42, 653 (1965).

TABLE 4.1

	Ionic Radii in Å	Lattice Constant a/2 for Oxide	Ratio of Ionic Radii in Oxide	Maximum Interstitial Radius
O^{2-}	1.40	-	-	-
Mg^{2+}	0.65	2.1	0.46	0.75
Ca^{2+}	0.99	2.4	0.71	0.88
Sr^{2+}	1.13	2.54	0.81	0.93
Ba^{2+}	1.35	2.75	0.96	1.0

(Ionic Radii after Pauling 1948)

CHAPTER IV

PRELIMINARY SURVEY OF BaO AND $CaWO_4$

4.1 Barium Oxide

4.1.1 Crystal structure and nature of BaO

Barium Oxide crystallizes in the NaCl type face centered cubic structure. The bonding is predominantly ionic, the diamagnetic ions of Ba^{2+} and O^{2-} having the complete electron shells appropriate to the inert gases of Xenon and Neon respectively, and the material is an insulator with a band gap of 5 eV (Apker et al. 1951). Barium Oxide decomposes rapidly in ordinary air into Barium Hydroxide. The reaction rate for this process is so rapid even at very low vapour concentrations that the material is the best of the known chemical drying agents for gases (Sproull et al. 1951).

The crystal structure consists of two interpenetrating face centered cubic arrays of anions and cations laterally displaced by one half of the lattice constant a of the unit cell. It is usefully described by considering the unit cell in which Ba^{2+} and O^{2-} ions are situated as follows:-

Ba^{2+}	(0,0,0)	($^a/2$,0,$^a/2$)	($^a/2$,$^a/2$,0)	(0,$^a/2$,$^a/2$)
O^{2-}	(0,0,$^a/2$)	($^a/2$,0,0)	(0,$^a/2$,0)	($^a/2$,$^a/2$,$^a/2$)

The lattice constant for BaO is 5.5A (Pauling 1948). This is the distance between like ions, the separation between nearest neighbours, unlike ions, will be half this, 2.75A. Table 4.1 shows the ionic sizes and lattice constants of other alkaline earth oxides with this structure. It may be noted that as the size of the metal ion increases down the series, Ba^{2+} being almost equal in size to O^{2-}, the size of the space in the centre of the primitive cell will also increase. This is an important consideration in the evaluation of possible sites for impurities. The last column of the table lists the radius of the largest sphere, assuming close packing, that can be inserted into this space in the lattice without disturbing the structure. The majority of impurity ions have radii exceeding this maximum value for MgO and CaO and so one expects them to enter the lattice substitutionally. In the last two oxides however, there is a distinct possibility of interstitial sites provided charge compensation requirements can be satisfied. This point will be taken up in the next chapter in connection with the siting of an Mn^{2+} impurity observed in BaO.

Of course the majority of crystals contain macroscopic defects in the form of dislocations, inclusions, subgrain boundaries and the like and impurities may well associate with such features. However paramagnetic resonance detection of point defects produces a signal which is the coherent sum over all similar sites in the crystal and the effect of macroscopic defects is usually limited to broadening the resonance line. As noted earlier an important contribution to line broadening is the presence of nuclei with non zero spin. In BaO intrinsic nuclear spins are present in the form of the isotopes Ba^{135} (6.6% abundance), Ba^{137} (11.3% abundance) both with $I = 3/2$ and of O^{17} (0.04% abundance) with $I = 5/2$.

4.1.2 Crystal growth

Several techniques have been developed for growing single crystals of BaO. Sproull et al. (1951) produced crystals as large as 1 × 10 × 10 mm by vapour deposition onto MgO seed crystals inside a cavity of compressed BaO powder at a temperature of 1400°C. Crystallization from a melt of Barium Hydroxide held at 550°C for a 30 to 40 day period (Lynch and Lander 1959) has produced good but fairly small crystals. Gambino (1965) has successfully used a modified Verneuil method in which the material is melted onto the tip of a refractory rod in a hot flame. In order to reach the high melting point of BaO, Gambino used an induction coupled plasma torch as a heat source.

The crystals used in this work were grown from the melt by workers at the Physics Department, University of Missouri, using a modification of the Arc Fusion method developed for other alkaline earth oxides. A thoroughly mixed powder of BaO plus any impurities it is desired to incorporate in the lattice is compressed around four carbon electrodes. When an arc is struck between the electrodes a region of molten oxide is formed which is prevented from rapid cooling by the outer solid layers. For good crystal growth the melting temperature of 1923°C must be held closely since the material evaporates readily above this temperature. Crystals of varying size up to 8 × 3 × 2 mm were obtained in this manner. Doping concentration will, of course, vary with position in the melt and as no zone refining type process is possible with such a high melt temperature, it is necessary to use starting materials of high purity.

The crystals obtained from these melts showed three distinct regions of colouration: blue, green and transparent. The presence of an unusual manganese spectrum and the knowledge that a high concentration of manganese had been included in the melt lead to the suspicion that the blue crystals were $BaMnO_4$. Attempts to determine the crystal structure using the back reflection Laue X-ray technique were unsuccessful due to the high X-ray absorption coefficient of Ba and the formation of Barium Hydroxide on the surface. However, the demonstration that the spectrum had four fold and six fold axes and the cleavage of crystals along faces consistent with a <100> designation was taken as sufficient evidence for cubic BaO crystals.

4.1.3 Summary of previous work on BaO

The original stimulus for work on BaO arose out of attempts to understand phenomena associated with thermionic emission from oxide coated cathodes. Early studies were performed on Polycrystalline and powdered BaO and were concerned with the nature of electron traps and conduction processes. A review of this early work complete with an extensive bibliography may be found in a paper by Blewett (1946). The complex nature of these processes combined with improvements in crystal growing techniques (Sproull et al. 1951, Lynch and Lander 1959, Gambino 1965) caused the centre of interest to shift to single crystal work. It was soon noted that crystals grown by these methods were often blue or red in colour instead of being transparent. The work of Dash (1953) and Kane (1951) demonstrated that whenever red crystals formed there was always evidence of contact with molten Barium. Consequently the centres giving rise to red colouration are thought to be either colloidal Barium or aggregates of Oxygen vacancies, though the question is by no means resolved.

In contrast the cause of blue colouration is now fairly well understood mainly as a result of three related pieces of work (Reddington 1952, Dash 1953, Sproull et al. 1953). Dash showed that blue colouration could be induced in transparent crystals by heating in the vapour of Ba, Mg, Ca or Al which indicated that the colour was associated with an excess of metal ions. Since the optical absorption curve was independent of the type of metal ion, this ruled out the mechanism of direct migration of vapour ions to interstitial sites in the crystal though there remained the possibility that substitution of metal ions for Ba^{2+} might in all cases lead to the formation of Ba interstitials. Alternative mechanisms postulated were some kind of aggregate centre or the trapping of electrons at vacant oxygen sites produced by the diffusion of oxygen ions to the surface and consequent extension of the crystal at the expense of its stoichiometry. From comparisons of optical and chemical methods of measuring the excess metal content, Sproull et al. (1953) deduced that the Ba excess was probably dispersed atomically rather than colloidally. These workers also measured the diffusion rate of the blue colouration mechanism and, by comparison with Reddington's (1952) radioactive tracer determination of the self diffusion rate of Ba in BaO, established that the blue colour could not be associated with Barium transport. From these studies it is reasonable to deduce that blue colour is associated with the presence of Oxygen vacancies due to an excess of Barium.

The particular usefulness of e.p.r. as a tool for studying point defects has been applied to BaO in attempts to deduce the nature of defects

TABLE 4.2

E.P.R. PARAMETERS OF DEFECTS IN BaO

Defect	Temperature	g value	Fine Structure ($\times 10^{-4}$cms^{-1})	Hyperfine Structure ($\times 10^{-4}$cms^{-1})
F^+		1.936		
Eu^{2+}	4.2°K	1.9915	$b_4 = +19.0$	A^{151} 29.6
				A^{153} 13.1
Gd^{3+}	77°K	1.9918	$b_4^0 = -1.91$	A^{155} 4.8
			$b_6^0 = 0.73$	A^{157} 3.65

present and if possible to correlate their electronic structure with optical absorption (Bessent et al. 1968, Zollweg 1955), photo-electric emission (Apker et al. 1951), photo-conductivity (Dash 1953) and Hall effect (Pell 1952) measurements. A difficulty in using e.p.r. arises from the high dielectric constant of BaO ($\varepsilon = 34$ at microwave frequencies) and consequent non-resonant microwave loss (Bever and Sproull 1951). Carson et al. (1959) reported that such microwave losses were higher in coloured than in transparent crystals and attributed this to the presence of conduction electrons though they were unable to decide whether this was due to colloidal Barium or bulk conductivity from thermally excited electrons in BaO itself. In the work reported here, microwave loss was high, but not noticeably larger in coloured crystals though a broad e.p.r. signal, possibly due to conduction electrons, was observed in blue specimens.

The e.p.r. spectrum arising from one electron trapped at an oxygen vacancy (the F^+ centre in the notation of Henderson and Wertz 1968) has been reported (Carson et al. 1959, Mann et al. 1969), conclusive identification being provided by the hyperfine interaction with the nuclei of Ba^{135} and Ba^{137} at the six equivalent sites surrounding the vacancy. At present there is some dispute as to the correlation of this centre with the 2eV optical absorption band (Carson et al. 1959, Bessent et al. 1968, Henderson and Wertz 1968, Turner 1969).

In contrast with the other alkaline earth oxides there have been very few reports of transition metal ions in BaO. The rare earths Eu^{2+} (Overmeyer and Gambino 1964) and Gd^{3+} (Mann and Holroyd 1968) have been observed. No iron transition group elements have been reported

<100> →

x 270

PLATE 4.1

except for a temperature dependent study of the hyperfine coupling of Mn^{2+} in BaO powder by Zdansky (1968) which will be discussed in detail in the next chapter. These results are summarised in Table 4.2.

4.1.4 Microscopy studies

The observation that the manganese spectrum (described in Chapter V) occurred only in blue crystals lead to an investigation of the nature of the crystals by optical and transmission electron microscopy. This investigation revealed several features having implications for the e.p.r. spectrum and of interest in themselves.

Otpical studies were made in transmission and to limit the formation of an opaque layer of $Ba(OH)_2$ the crystals were immersed in carbon tetrachloride. The most significant features observed were the macroscopic square shaped, dark, colloidal defects shown in Plate 4.1. These defects varied in size up to 10 × 10μ and were distributed through the crystal so that by focusing up and down different particles could be brought in and out of focus. It was always possible to resolve the sharp edges and right angled corners of a particular colloid. Plate 4.1 also shows that the square edges of the defects are remarkably aligned and, from comparison with the external shape of the crystals, parallel to <100> crystal directions. When viewed under high power some of these defects, whilst retaining a dark square boundary, were not completely opaque but had a 'partially filled' appearance. Some of the colloids shown in Plate 4.1 may be seen by closer inspection to demonstrate this effect. These defects were observed in all crystals but were smaller and less numerous in the green and blue regions.

Green

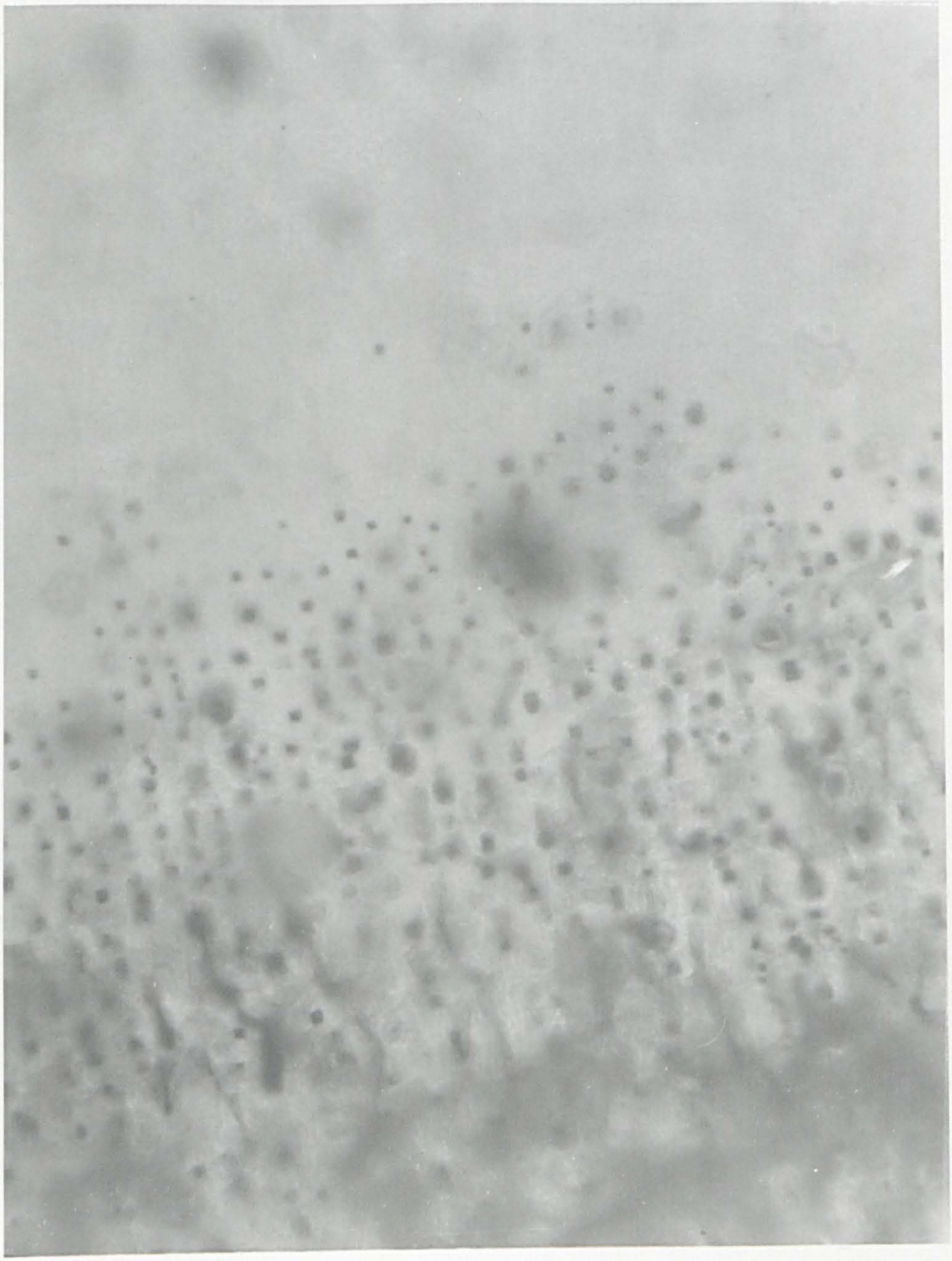

Trans-
parent

x 154

PLATE 4.2

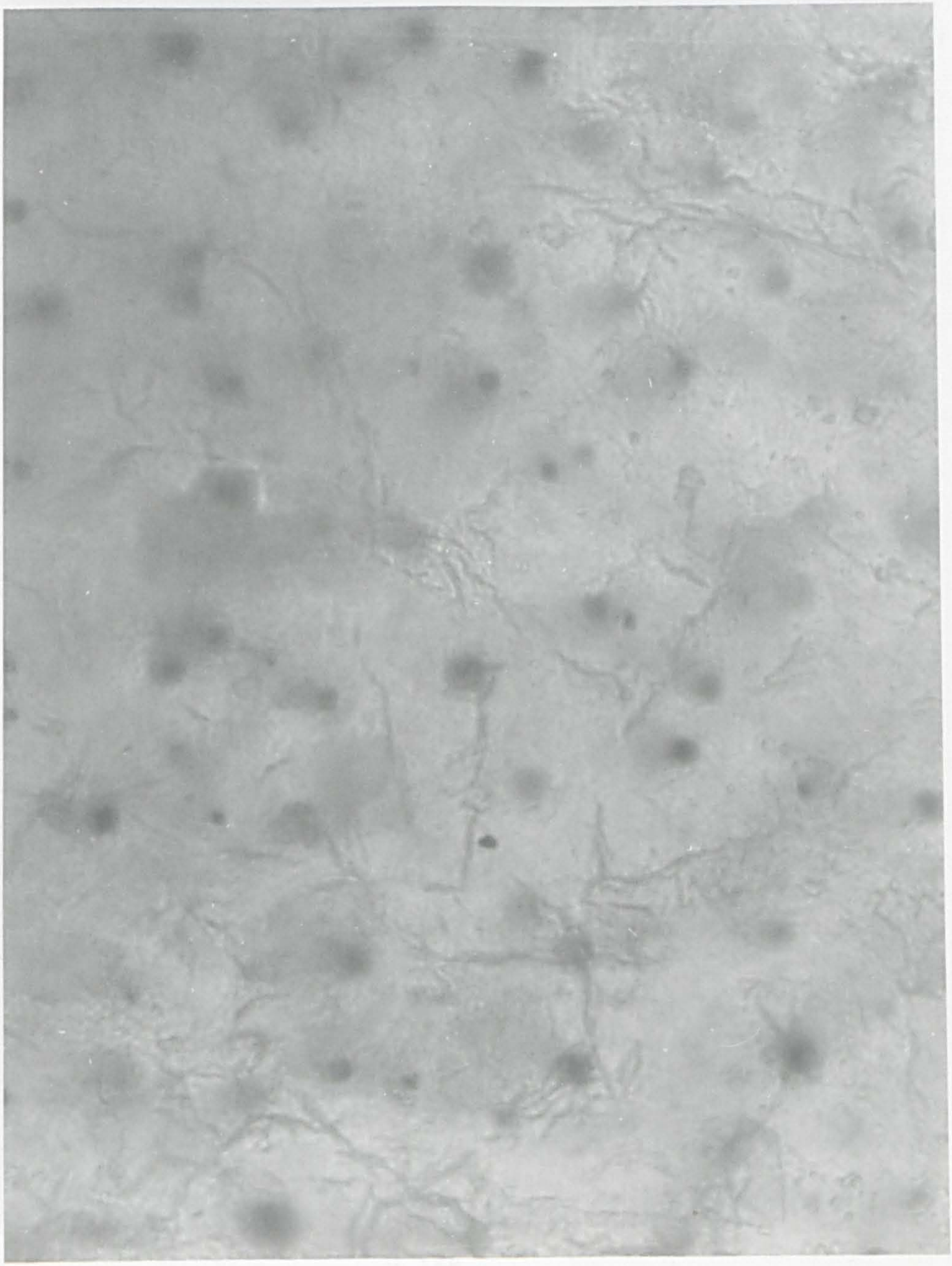

x 340

PLATE 4.3

Plate 4.2 illustrates a quite definite falling off of concentration which coincided with the boundary between a transparent and a green region of one crystal. The large vague dark spots on this and other plates are contamination effects on the glass-crystal interface which are, of course, out of focus.

Hypotheses as to the nature of these colloids must be very speculative though one which suggests itself immediately is that they are composed of excess Barium metal. It may be noted that Barium crystallizes in a cubic phase. However the identification of precipitates is always difficult and, as a cautionary example, one might remark on the pyramidal colloids observed in MgO by Bowen (1963) and which Venables (1963) was subsequently able to show were precipitates of ZrO_2. These precipitates appear in MgO when the Zr impurity concentration is as low as 1 ppm, far less than the concentration of other impurities which are not observed to form colloids.

Plate 4.3 shows a network of dark surface cracks appearing on all crystals and possibly associated with the formation of $Ba(OH)_2$. A photograph (Plate 4.4) of blue BaO at lower magnification illustrates a background network extending through the depth of the material. The cubic colloids may be seen as a faint spread of black dots.

Electron microscopy studies were made of different coloured crystals using a variety of techniques of specimen preparation in an effort to find a way of minimising the formation of the hydroxide. In an attempt to discover the nature of the colloidal defects, one crystal was dissolved in water. If the colloids were metal then they should be left

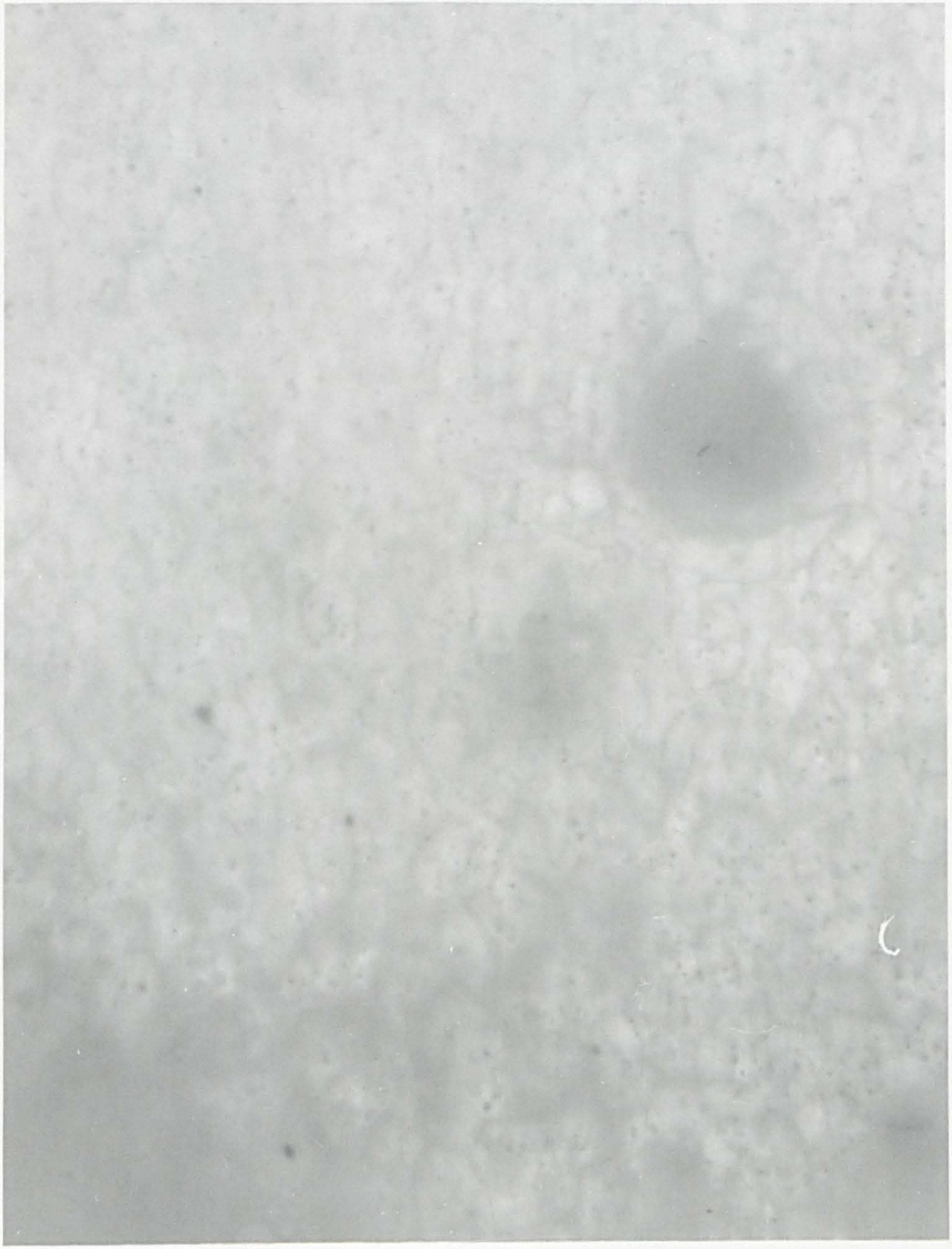

x 65

PLATE 4.4

x 6000

PLATE 4.5

PLATE 4.6

in suspension and a specimen mount swept through the solution might be expected to collect some of them. Unfortunately nothing was found which extended the optical work though features attributable to $Ba(OH)_2$ were observed. The right hand side of Plate 4.5 shows how the long sharp whiskers of $Ba(OH)_2$ aggregate to form the dark mass on the left. Plate 4.6 is an electron diffraction pattern observed, on two separate instances, from these specimens which is identifiable as arising from a twinned crystal of quartz. It cannot be concluded that the BaO crystals contained quartz however, as this might easily have resulted from contamination of the mount during specimen preparation.

This work and particularly the observation of the large ordered colloids illustrates how important it is to study the macroscopic structure of crystals upon which e.p.r. experiments are conducted. The colloids, for example, are sufficiently large and aligned that point defect centre e.p.r. signals might be observed arising from them as well as from the BaO lattice. Although viewing through crossed polaroids revealed no macroscopic strain gradients in the crystals, the existence of these several macroscopic defects will undoubtedly set up local strains in the lattice and, by 'modulating' the environment of point defects over the whole specimen, act as an inhomogeneous broadening mechanism on the e.p.r. line shapes. It may be noted that at some orientations the manganese spectrum reported in Chapter V had line widths of 10 to 20 gauss, quite broad for manganese.

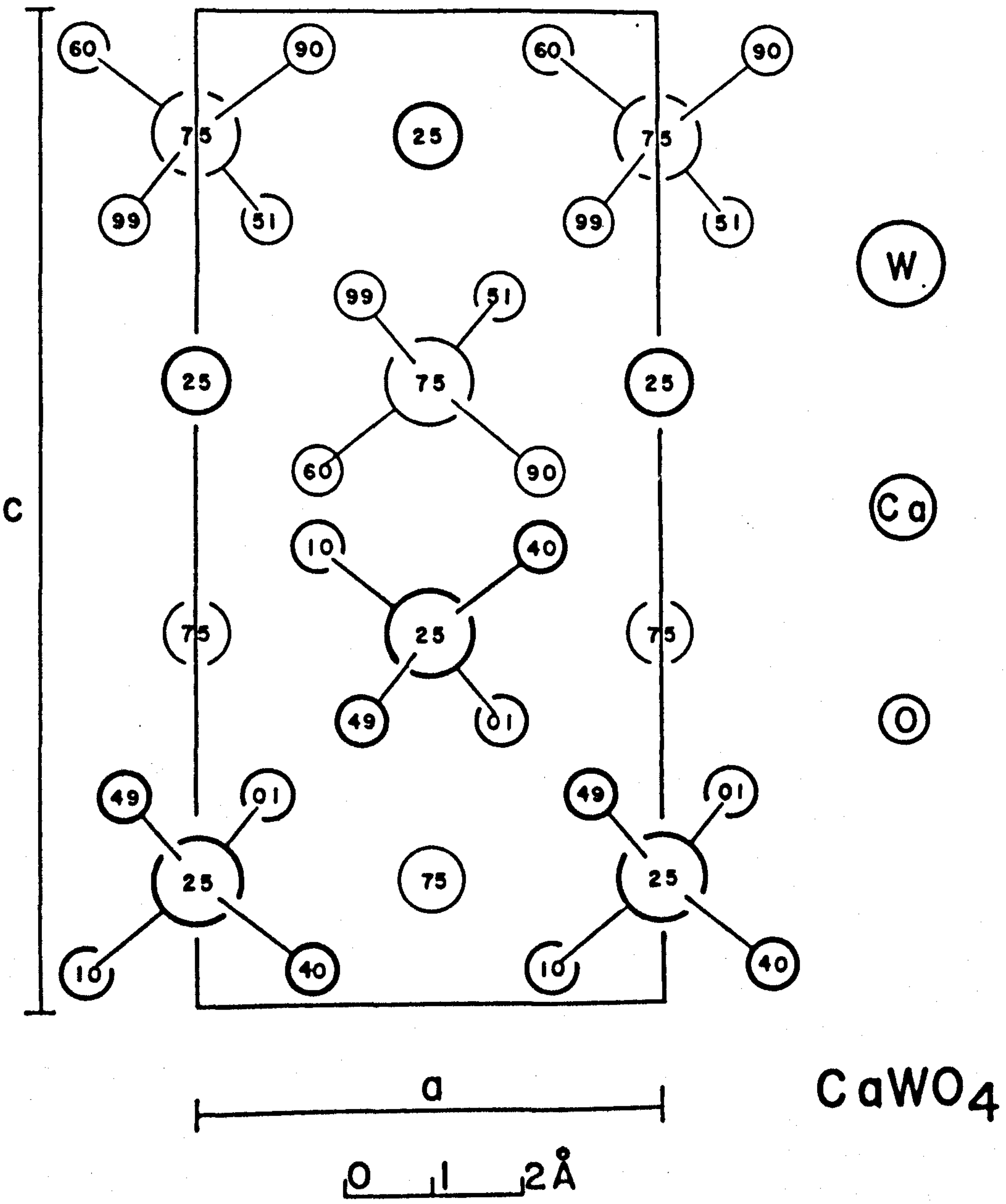

(after Zalkin and Templeton 1964).

FIGURE 4.1

4.2 Calcium Tungstate

4.2.1 Crystal structure and nature of $CaWO_4$

Calcium tungstate crystallizes in the Scheelite structure with four molecules in the unit cell. It is a tetragonal structure made up of linked metal-oxygen tetrahedra, the Ca and W ions occupying the sites of two interpenetrating diamond lattices. The space group is C_{4h}^{6} ($I4_1/a$) and the unit cell has parameters

$$a = b = 5.24 \text{ A}$$

$$c = 11.38 \text{ A}$$

Choosing an origin of coordinates on a W ion, the positions of the ions in the unit cell may be expressed in Wycoff's notation (1960) as:-

$$\begin{array}{lll} W : & (4a) & 0\ 0\ 0;\ \ 0\ \tfrac{1}{2}\ \tfrac{1}{4};\ \ B.C. \\ Ca : & (4b) & 0\ 0\ \tfrac{1}{2};\ \ \tfrac{1}{2}\ 0\ \tfrac{1}{4};\ \ B.C. \\ O : & (16f) & \pm(x,y)z;\ \ \pm(x,\tfrac{1}{2}+y),\ \tfrac{1}{4}-z; \\ & & \pm(\overline{y},x)\overline{z};\ \ \pm(\overline{y},\tfrac{1}{2}+x),\ \tfrac{1}{4}+z; \end{array}$$

Figure 4.1 shows a projection of the structure onto the a c plane of the unit cell.

The exact positions of the oxygen ions were for some time in doubt. Sillen and Nylander (1943) from considerations of ionic radii, hard sphere packing and comparison with other Scheelites deduced them to be:

$$x = 0.25 \pm .02$$

$$y = 0.15 \pm .02$$

$$z = 0.075 \pm .015$$

These values have been confirmed and their accuracy refined by X-ray diffraction (Zalkin and Templeton 1964) and neutron diffraction (Kay et al. 1964) studies. These studies show the WO_4 unit to be a slightly distorted tetrahedron with a W-O bond distance of 1.79Å. The WO_4^{2-} system may be considered to be ionically bonded to the Ca^{2+} ions, the Ca and O's having separations of 2.44Å and 2.48Å. The point symmetry at both the Ca and the W site is S_4 and the oxygens lie on 4_1 type screw axes. The presence of these screw axes means that there is no mirror plane perpendicular to the c axis with the result that the two <001> planes at the ends of a crystal are not equivalent.

In recent years crystals of the Scheelite family and particularly $CaWO_4$ have been increasingly studied as potential host lattices for various rare-earth laser systems. Laser action has been observed from several trivalent rare earths in $CaWO_4$, the most successful being Nd^{3+} from which continuous operation has been achieved at room temperature (Johnson 1963). The development of this field may be seen from the papers of Nassau, Broyer, Johnson, Mimms, McGee, Van Uitert and Soden who also refer to related work.

There are several reasons why $CaWO_4$ provides such a suitable host lattice for laser systems. Most important perhaps is that recent developments in the techniques of crystal growth have made it possible to grow large single crystals of good optical quality. The chemical stability of the material compared to other, water soluble, salts is also an advantage as is its hardness. $CaWO_4$ has a hardness comparable to that of Iron and the ability to grow crystals which are relatively free from strain means that the line widths of impurity spectra are quite narrow. This is an important consideration for efficient laser operation and, in softer materials, strain has been found to be a major contribution to the line widths of both optical and e.p.r. transitions. In addition the line broadening from the nuclear spins of the host ions is much reduced in $CaWO_4$, the only isotopes with non-zero nuclear spin being Ca^{43} (0.13%), O^{17} (0.04%) and W^{183} (14.3%) and the magnetic moments of these nuclei are relatively small. The incorporation of a trivalent impurity into a divalent lattice necessarily introduces charge compensation problems and, as there are several mechanisms of restoring the balance, this results in an undesirable proliferation of absorption and emission bands. An important advance, however, has been made by incorporating monovalent alkali atoms in the lattice to act as a charge compensation mechanism (Nassau 1963). The addition of Na^+ to the Nd^{3+}:$CaWO_4$ system, for example, increases the number of absorption bands thus facilitating pumping, and by concentrating and reducing the number of emission bands lowers the threshold for laser operation by a factor of three.

When, as is usually the case for transition metal ions, the impurity is paramagnetic, e.p.r. provides a useful complementary tool to the optical study of such systems. E.P.R. yields information about the ground state of the ion and also about the crystal field, both of which are important determinants of its optical properties. In addition e.p.r. may be used to determine the lattice site occupied by the impurity and possibly also the positions of other impurities such as might be included for charge compensation purposes. It has also been suggested that the spin states of ions with large zero field splittings in $CaWO_4$, such as Gd^{3+} (Hempstead and Bowers 1960, Van Uitert and Soden 1960) might themselves be used for three level maser operation. This latter suggestion presumably also offers the possibility of easy tuning of the maser output by varying the applied magnetic field and hence the energy separation of the spin states. These considerations have given rise to a considerable amount of e.p.r. work on transition metals in $CaWO_4$. Spectra have been reported from nearly all the rare earth and iron group elements sometimes located at both the Ca^{2+} and W^{6+} sites and often in association with other defects. As a comprehensive review of all this work is beyond the scope of this thesis, particular studies will be referred to where relevant, and as a representative sample one might mention the work of Mimms et al. (1961) on Ce^{3+} and Er^{3+}, Forrester and Hempstead (1962) on Tb^{3+}, Kedzie et al. (1964) on Cr^{5+} and Mahootian et al. (1968) on V^{4+}.

The presence of defects other than doped substitutional impurities was noted very early in the development of this field. Cronemeyer and Beabien (1964) reported that flash tube irradiation of the Nd^{3+}:$CaWO_4$ system darkened the crystal and raised the threshold for laser action. The colour could be removed completely by annealing at 300°C for several hours. Agarbayejari and Merlo (1965) demonstrated that vacuum reduction of doped crystals produced changes ranging from a faint smokey colour to a deep purple, whereas similar treatment of pure $CaWO_4$ left it unchanged. It would seem likely that the incorporation of trivalent impurities in the lattice 'loosens up' the structure, possibly for example by the generation of charge compensating vacancies, and that this promotes ionic migration

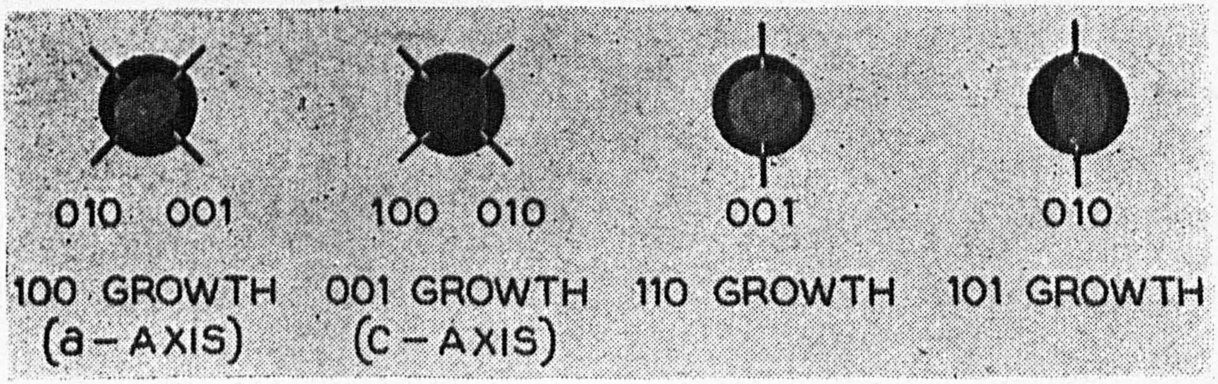

Cross sections of pulled $CaWO_4$ crystals.

(after Nassau and Broyer 1962)

FIGURE 4.2

and the formation of electron traps. The various colouration mechanisms then would seem to be defects in the structure of the lattice possibly in association with impurities. Several e.p.r. studies have been made of such 'damage' centres in $CaWO_4$ and these will be discussed in a later section. However, it may be noted that, as in other complex systems, the situation is rather confused and the nature of e.p.r. centres is less well understood than in the simpler cubic materials such as the alkali-halides and alkaline-earth oxides. In the work reported here, studies were made of defect centres present in $CaWO_4$ crystals which had been subjected to light and heavy doses of neutron irradiation. The defects created by radiation damage are often the same as those produced by other mechanisms and irradiation is a convenient way of generating a high concentration of defects. It may be noted, however, that neutron irradiation tends to produce larger concentrations of aggregate defects than other mechanisms.

4.2.2 Crystals used in this work

The crystals of $CaWO_4$ used in this work were grown by workers at the Royal Radar Establishment (Malvern) using the recently perfected Czochralski growth technique (Nassau and Broyer 1962). In this method the melt is established at just about the 1,600°C melting point by means of a platinum/rhodium thermocouple which controls the current supplied to r.f. heater coils. Growth initiates readily on the end of a platinum wire and good single crystal boules of $CaWO_4$ may be drawn from the melt without the use of seed crystals. After pulling the crystals were annealed in air at 1520°C for 20 hours to reduce strain and facilitate cutting.

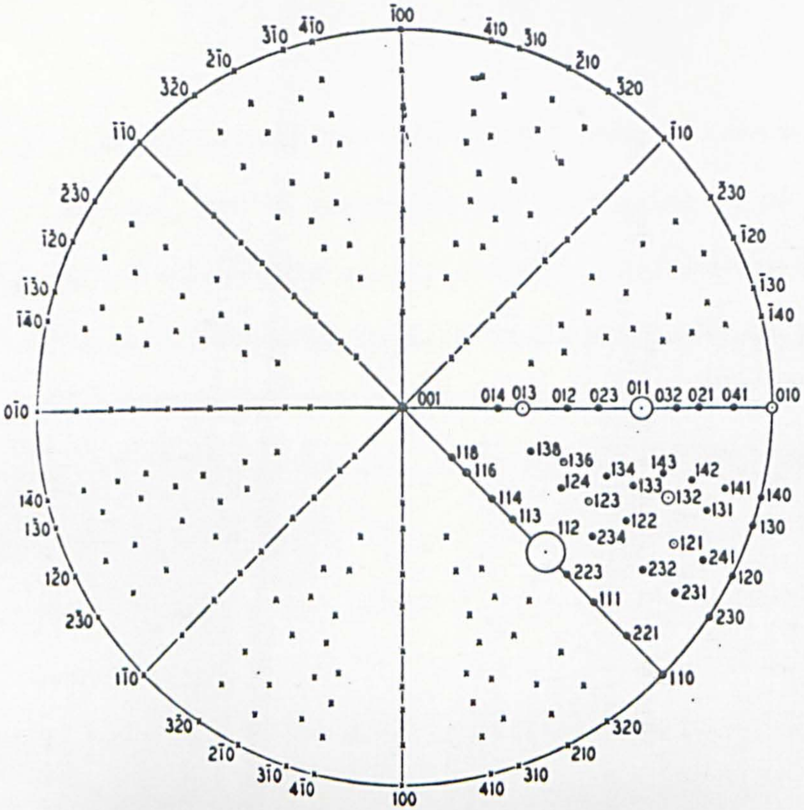

Stereographic projection

(after Nassau 1960)

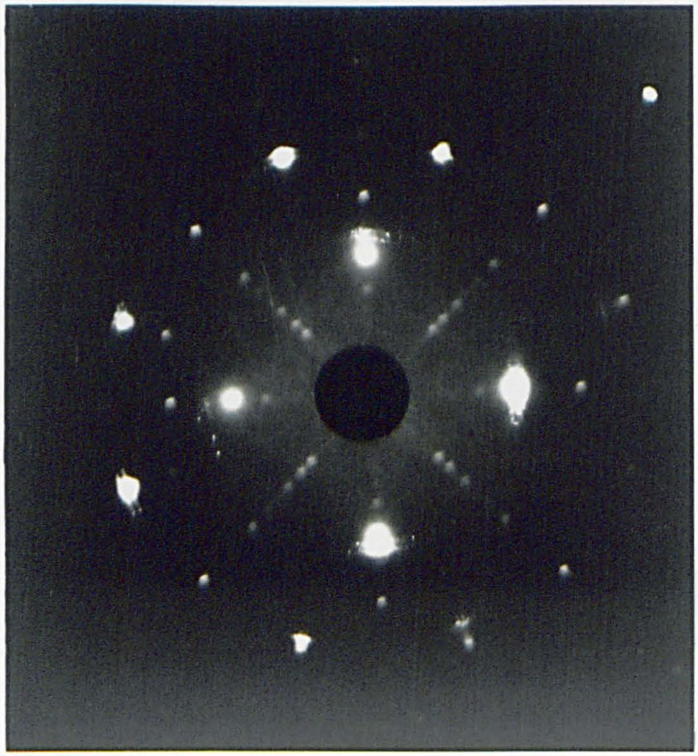

X ray diffraction pattern along c axis of $CaWO_4$

FIGURE 4.3

The as-received boules had the characteristic cross sections noted by Nassau and Broyer (Figure 4.2) for crystals pulled along <100> and <001> directions. However in order to interpret the hamiltonians summarising the behaviour of defect spectra it is necessary to be quite sure of the positions of the crystal axes with respect to external forms. Consequently an X-ray diffraction study was made to determine axis directions of several crystals. The back reflection Laue technique was employed using the apparatus described in section 3.5 and it was found that exposure times of four hours produced reasonable photographs. Figure 4.3 shows a comparison of the diffraction pattern observed with the beam incident on a c axis, and the stereographic projection of Nassau (1960). It can be seen that it is possible to unambiguously assign the various crystal directions using this technique. The assignment was consistent with the cross-sectional shape of the boules, and also with the positions found for the principal axis directions of an Mn^{2+} spectrum, present in several crystals, and previously reported by Hempstead and Bowers (1960).

Crystals were cut from the boules using a low speed variable pressure diamond cutter developed for this purpose by workers at R.R.E. (Malvern) (Fynn and Powell 1966). Irradiations were performed in the BEPO and DIDO reactors of A.E.R.E. (Harwell). Two dosages were used; a light one of $5 - 50 \times 10^6$ nvt at 30°C in BEPO which produced a light brown/yellow colouration and a heavy one of 5×10^{18} nvt at 45°C in DIDO which turned the crystals opaque and a deep purple in colour.

4.2.3 Damage centres in $CaWO_4$

Several studies have been made of defect centres created in $CaWO_4$ by irradiation. The e.p.r. centres produced are correlated with the complex thermoluminescence, thermo-conductivity, and photo-conductivity processes in the material but the exact relationships between these processes and the e.p.r. centres is still unclear. All these electronic properties of $CaWO_4$ are sensitive to the irradiation mechanism employed, the temperature of irradiation, subsequent thermal history and the presence of impurities. Several e.p.r. spectra have been reported and in order to present a unified picture this work will be summarised according to the models that have been proposed for the various spectra. Often of course several centres are reported as occurring together and, as expected, there is evidence of dynamic relationships between some defects. However it is not yet possible to give a detailed and unambiguous description of these relationships.

V_k Centre

This is probably the most established damage centre in $CaWO_4$ (Zeldes and Livingston 1961, Born et al. 1968, Koehler et al. 1969, Born et al. 1970). It consists of a hole localised between two tungsten tetrahedra and is termed a V_k centre by analogy with a similar centre formed in alkali-chloride crystals (Castner and Kanzig 1957, Slichter 1963). It is produced by γ- and X-ray irradiation at $77^{\circ}K$ and may be recognised by its hyperfine interaction with W^{183}. The ratio of the intensities of the hyperfine lines to the central line suggests the presence of two

TABLE 4.3a

V_k CENTRE

	g value	Direction Cosines		
		a	b	c
g_1	2.0010	0.101	0.540	-0.836
g_2	2.0065	0.699	-0.636	-0.326
g_3	2.0354	0.708	0.551	0.442

TABLE 4.3b

WO_4^{3-} CENTRE

	g value	Direction Cosines		
		a	b	c
g_1	1.5716	0.547	-0.837	0.008
g_2	1.6334	0.832	0.543	-0.111
g_3	1.8482	0.089	0.068	0.994

(after Zeldes and Livingston 1961)

equivalent W sites (Born et al. 1970) and the spectrum can be described by a hamiltonian of the form

$$\mathcal{H} = \beta \underline{S}.\underline{g}.\underline{H} + a\,\underline{S}(\underline{I}_1 + \underline{I}_2)$$

with $S = \frac{1}{2}$ and $I_1 = I_2 = \frac{1}{2}$.

The principal directions and values of the g tensor are shown in Table 4.3a. The centre anneals out with rising temperature and is not stable at room temperature. Zalkin and Templeton showed that the centre could be bleached out with u-v light which suggests that u-v radiation releases electrons from other traps in the lattice, and also correlated the growth and decay of this spectrum with the growth and decay of a higher field species which they attributed to WO_4^{3-}. Born et al. (1968) supported this dynamic relationship between the two defects and by assuming that the back reaction between them was radiative were able to correlate the disappearance of their e.p.r. spectra with thermo-luminescence behaviour. However in crystals doped with Pb Born et al. (1970) were able to create the V_k centre without the corresponding WO_4^{3-} centre and further the luminescence accompanying the decay of the V_k centre was followed by an increase in the intensity of an e.p.r. signal identified as Pb^{3+} at a Ca^{2+} site. This would seem to suggest that the impurity centre is a more favoured electron trap than the tungsten tetrahedron. These authors also suggested that the angles of an oxygen molecular ion 'bridge' between the two tungsten tetrahedra of the defect were consistent with the directions of g_2 taking into account the polarisation of the surroundings which would be produced by a stable self-trapped hole.

WO_4 Complexes

In their work on the V_k centre Zeldes and Livingston also observed a spectrum, present after γ-irradiation at $77^{\circ}K$ which could be fitted to

$$\mathcal{H} = \beta \underline{S}.\underline{g}.\underline{H}$$

with $S = \frac{1}{2}$ and with the principal values and directions of the g tensor axes as indicated in Table 4.3b. There was also an anisotropic hyperfine interaction with a single W^{183} nucleus but the parameters of this interaction could not be determined. The spectrum annealed out with the V_k centre with rising temperature as previously described and the defect was assigned to WO_4^{3-}. Born et al. (1968) observed a similar spectrum with the same order of g value and similar temperature dependence but did not investigate it in detail. In order to explain the g value directions of this centre Zeldes and Livingston postulate that it is stabilised but electronically undisturbed by the presence of some other lattice defect. This assignment is supported by Chu and Kikuchi (1968) who also suggest that a similar spectrum of Azarbayejani (1965) is also a stabilised but undisturbed WO_4^{3-} centre. These conclusions are based on the analysis of a spectrum with similar parameters to these two which was present after neutron irradiation (Chu and Kikuchi 1966) and which could be assigned to a WO_4^{3-} defect in association with a Ca vacancy.

A recent spectrum reported by Sayer and Lynch (1970) present after low temperature ultra-violet irradiation is attributed to WO_4^{-}. Lynch and Sayer also associate this defect with the luminescence previously

TABLE 4.4

WO_3^- CENTRE

	g_z	g_x	g_y
	1.914	1.675	1.646
θ	57°	33°	90°
ϕ	32°	212°	122°

θ = angle from c axis

ϕ = angle from a axis in ab plane

(after Chu and Kikuchi 1966)

ascribed to the V_k centre. The assignment of the spectra to WO_4^- must however be treated with caution since the reported hamiltonian and g values do not correspond to the angular variation shown for the spectrum.

WO_3 Complexes

In their neutron irradiation studies Chu and Kikuchi (1966 and 1968) also observed a spectrum which although it could only be observed at low temperature did not appreciably anneal out after long periods at room temperature. This spectrum consisted of four lines, attributed to inequivalent sites in the structure, each accompanied by two widely spaced satellites (280 gauss along c axis) which arose from an anisotropic hyperfine interaction with one W^{183} nucleus. The g values and principal directions of the g tensor are given in Table 4.4. Unfortunately the exact form of the hamiltonian is not quoted, although angular variation studies and uniaxial stress measurements identify the spectra with a WO_3^- complex, i.e. a tungsten tetrahedra which has lost on oxygen.

This spectrum is also noted by Mason et al. (1968) in connection with thermo-luminescence though there is some confusion as to whether it is best regarded as WO_3^- or W^{5+} in association with an O vacancy. The same workers (Koehler et al. 1969) also report a spectrum which they attribute to WO_3^- in association with a Ca vacancy and suggest that this is the high field spectrum referred to by Born et al. (1968). However as neither group of authors give the spin hamiltonian and only cursorily mention the g values it is difficult to draw any conclusions about the defect.

Impurity associated defects

Besides the many spectra attributed to transition metal ions at normal lattice sites, there have also been several e.p.r. centres reported which arise from impurities in association with other defects. From their work on vacuum reduced crystals containing Mo, Azarbayejani and Merlo (1965) deduced that the impurity is located at the W site as diamagnetic Mo^{6+} but that during reduction oxygen vacancies are preferentially trapped at the impurity site permitting the formation of paramagnetic Mo^{5+}. Similarly Mahootian et al. (1966) tentatively attribute one of the Vanadium spectra they observe to V in a Ca site in association with an oxygen vacancy. Koehler et al. (1969) discuss the possibility that one of their spectra arises from paramagnetic W-coupled to one or more Nb^{4+}'s. Sayer and Lynch (1970) indicate that Cu^{2+} impurities may act as 'catalysts' in the production of damage centres by low temperature irradiation with ultra-violet light and Born et al. (1970) report a super-hyperfine interaction between Pb^{3+} at a Ca^{2+} site and four surrounding W^{183} nuclei. This latter study throws some doubt on the hitherto assumed pure ionicity of the Ca^{2+} - $WO_4{}^{2-}$ bonds.

Interstitials

$CaWO_4$ has a closed packed structure and no positive identification of spectra with interstitial atoms has been made in the literature. Chu and Kikuchi (1966) in their paper on neutron irradiated $CaWO_4$ mention a group of lines stable at room temperature with g values slightly greater than 2. As other centres in their study are attributed to Ca and O vacancies, they suggest these lines may arise from Ca or O interstitials but were unable to correlate their angular variation with the crystal structure.

References

BaO

Apker, L., Taft, E. and Dickey, J. Phys. Rev. 84, 508 (1951).

Bessent, R.G., Cavenett, B.C. and Hunter, I.C. J. Phys. Chem. Sol. 29, 1523 (1968).

Bever, R.S. and Sproull, R.L. Phys. Rev. 83, 801 (1951).

Blewett, J.P. J. Appl. Phys. 17, 643 (1946).

Bowen, D.H. Trans. Brit. Cer. Soc. 62, 771 (1963).

Carson, J.N., Holcombe, D.F. and Ruchardt, H. J. Phys. Chem. Sol. 12, 66 (1959).

Dash, W.C. Phys. Rev. 92, 68 (1953).

Gambino, R.J. J. Appl. Phys. 36, 656 (1965).

Henderson, B. and Wertz, J.E. Adv. in Phys. 17, 749 (1968).

Kane, E.O. J. Appl. Phys. 22, 1214 (1951).

Lynch, R.T. and Lander, J.J. J. Appl. Phys. 30, 1614 (1959).

Mann, K.E. and Holroyd, L.V. Phys. Stat. Sol. 28, K27 (1968).

Mann, K.E., Holroyd, L.V. and Cowan, D.L. Private communication (1969).

Overmeyer, J. and Gambino R.J. Phys. Lett. 9, 108 (1964).

Pauling, L. 'The Nature of the Chemical Band' p.363 (Cornell) 1948.

Pell, E.M. Phys. Rev. 87, 457 (1952).

Reddington, R.W. Phys. Rev. 87, 1066 (1952).

Sproull, R.L., Dash, W.C., Tyler, W.W. and Moore, A.R. Rev. Sci. Inst. 22, 410 (1951).

Sproull, R.L., Bever, R.S. and Libowitz, G. Phys. Rev. 92, 77 (1953).

Turner, J.J. Solid State Comm. 7, 635 (1969).

Venables, J.D. J. Appl. Phys. 34, 293 (1963).

Zdansky, K. Phys. Stat. Sol. 28, 181 (1968).

Zollweg, R.J. Phys. Rev. 97, 288 (1955).

$CaWO_4$

Azarbayejani, G.H. Bull. Am. Phys. Soc. 10, 1131 (1965).

Azarbayejani, G.H. and Merlo, A.L. Phys. Rev. A 137, 489 (1965).

Born, G.K., Grasser, R.J. and Scharmann, A.O. Phys. Stat. Sol. 28, 583 (1968).

Born, G.K., Hofstaetter, A. and Scharmann, A.O. Phys. Stat. Sol. 37, 255 (1970).

Castner, T.G. and Kanzig, W. J. Phys. Chem. Solids. 3, 178 (1957).

Chu, K.C. and Kikuchi, C. IEEE Trans. Nucl. Sci. 13, 41 (1966).

Chu, K.C. and Kikuchi, C. Phys. Rev. 169, 752 (1968).

Cronemeyer, D.C. and Beabien, M.W. J. Appl, Phys. 35, 1779 (1964).

Forrester, P.A. and Hempstead, C.F. Phys. Rev. 126, 923 (1962).

Fyn, G.W. and Powell, W.J.A. Industrial Diamond Review 26 No. 308, 284 (1966).

Hempstead, C.F. and Bowers, K.D. Phys. Rev. 118, 131 (1960).

Johnson, L.F. J. Appl. Phys. 34, 897 (1963).

Johnson, L.F.. Boyd, G.D., Nassau, K. and Soden, R.R. Phys. Rev. 126 14066 (1962).

Kay, M.I., Frazer, C.C. and Almodovar, I. J. Chem. Phys. 40, 504 (1964).

Kedzie, R.W., Shane, J.R. and Kestigan, M. Phys. Lett. 11 No.4, 286 (1964).

Koehler, H.A., Kikuchi, C. and Mason, D.R. Phys. Stat. Sol. 31, K1 (1969).

Mahootian, N., Kikuchi, C. and Viehann, W. J. Chem. Phys. 48, 1097 (1968).

Mason, D.R., Koehler, H.A. and Kikuchi, C. Phys. Rev. Lett. 20, No.9, 451 (1968).

Mimms, W.B., Nassau, K. and McGee, J.D. Phys. Rev. 123, 2059 (1961).

Mimms, W.B. and Gillen, R. Phys. Rev. 148, 148 (1966).

Nassau K. Trans. Met. Soc. AIME 218 October (1960).

Nassau, K. and Broyer, A.M. J. Appl. Phys. 33, 3064 (1962).

Nassau, K. and Loiacono. G.M. J. Phys. Chem. Sol. 24, 1503 (1963).

Nassau, K. J. Phys. Chem. Sol. 24, 1511 (1963).

Sayer, M. and Lynch, G.F. Phys. Stat. Sol. 37, 673 (1970).

Sillen, L.G. and Nylander, A.L. Arkiv Kemi Geol. No. 4 1 (1943).

Slichter, 'Magnetic Resonance' Chap. 7, (Harper and Row) 1963.

Van Uitert, L.G. and Soden, R.R. J. Appl. Phys. 31, 328 (1960).

Wyckoff, R.W.G. 'Crystal Structures' Vol. 3 20 (wiley) 1965.

Zalkin, A. and Templeton, D.H. J. Chem. Phys. 40, 501 (1964).

Zeldes, H. and Livingston, R. J. Chem. Phys. 34, 247 (1961).

CHAPTER V

E.P.R. INVESTIGATIONS OF BARIUM OXIDE

As mentioned in Chapter IV several crystals of BaO varying markedly in colour and size were available for investigation. The extreme reactivity of the material was a major problem which could not be fully overcome but it was possible to slow down the rate of crystal decomposition considerably by covering them with grease and storing in an evacuated desiccator. Before each e.p.r. experiment the layer of Barium Hydroxide that had formed during storage was scraped away and a fresh layer of 'signal free' silicon grease applied. The problem was particularly acute during low temperature work since the grease had a tendency to crack and flake away leaving the crystal unprotected and allowing water to condense on it during warming up. The high dielectric constant of the material caused considerable microwave loss and consequent lowering of cavity Q in e.p.r. experiments.

Preliminary surveys, both at liquid nitrogen and room temperatures, were made at X band on transparent and coloured crystals in an attempt to observe the F^+ spectrum reported by several workers (Carson et al. 1959, Mann et al. 1969). In the course of these studies an unusual and previously unreported Mn spectrum was observed in a large 2 × 3 × 5mm blue-green crystal. The spectrum appeared when the applied magnetic field was parallel to <110> crystal directions and disappeared, breaking up into components and losing intensity very rapidly when the field was rotated from this crystal direction. A rotation of two degrees caused a reduction of over a third in the peak height of some e.p.r. lines and by ten degrees no trace of the spectrum could be discerned above the noise level. Closer examination of the crystal revealed the presence of a well defined <100> plane boundary between its blue and green regions and it was cleaved exactly along this boundary. The spectrum was not present in the green region and extensive searches on other crystals made it possible to conclude that the spectrum only appeared in blue regions.

5.1 X Band Studies of the Mn^{2+} Spectrum

The spectrum was studied at room and liquid nitrogen temperatures using the Decca spectrometer. Low temperature work was originally performed using the 'cold finger' technique in which the specimen is mounted on the end of a copper rod and inserted into the microwave cavity inside a double walled evacuated finger dewar. The copper rod extends upwards through a plug which freezes in the neck of the finger, into a Nitrogen bath outside the cavity and the specimen is thus cooled by conduction. However the sensitivity of the spectrum to orientation coupled with the need to extract the specimen as quickly as possible to prevent condensation during warming up, led to the early rejection of this technique in favour of the continuous flow method described in Chapter III. The advantage of the latter technique is that it allows the specimen to be mounted on a goniometer and removed from the apparatus quickly when the experiment is over. Liquid nitrogen temperatures made little difference to the actual spectrum being studied but by considerably reducing a large background signal made observations much easier.

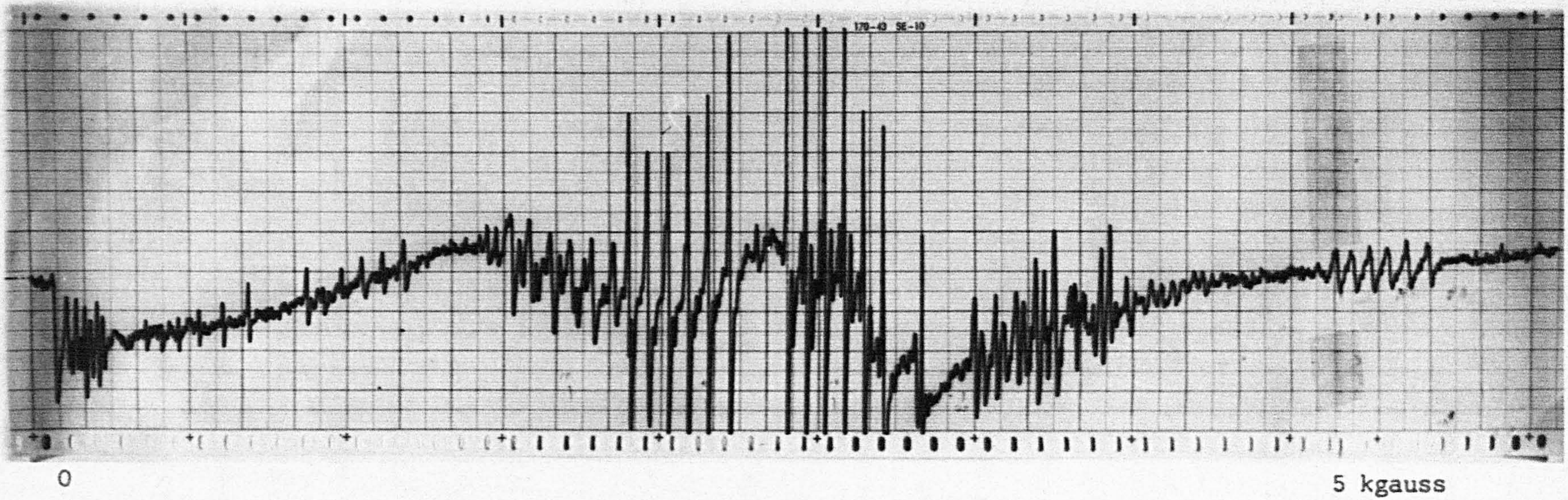

<110>

FIGURE 5.1

The spectrum was simplest along <110> and <111> crystal directions and was made up of several distinct groups of six equally intense lines, characteristic of the hyperfine pattern expected from Manganese, scattered over a range of six kilogauss. The various groups collapsed and dispersed at other orientations with the exception of a very low field group of lines, which, although anisotropic, retained their intensity. This group occurred at fields of less than 500 gauss, as measured on the fieldial, and since there was a residual field present in the yoke even when no current was flowing in the magnet coils it was not possible to record the 'beginning' of the spectrum. Reversing the field direction and thus opposing the residual field lowered the net field and hence allowed more of the group to be observed but the initial surge of current in the coils always meant that this group was 'jumped' into.

Identification of the spectrum as arising from some charged state of Mn was made on the basis of the characteristic six line hyperfine splitting of this ion. The separation between hyperfine components showed large second order effects, more pronounced in low field groups as expected. However the fine structure of the spectrum could not be correlated at X band with that expected from Mn. The spectrum observed with $\underline{H}$ along <110> directions is shown in Figure 5.1 and consists of two intense groups of lines, of the type normally associated with $M_S = +\frac{1}{2}$ to $M_S = -\frac{1}{2}$ fine structure transitions, situated around 2,395 gauss (g = 2.76) and 2,985 gauss (g = 2.21). Two groups of less intense and broader lines of the type that might be expected from $M_S = +{}^3\!/_2$ to $M_S = +\frac{1}{2}$ fine structure transitions in a 'normal' Mn spectrum could be observed at 1,950 gauss

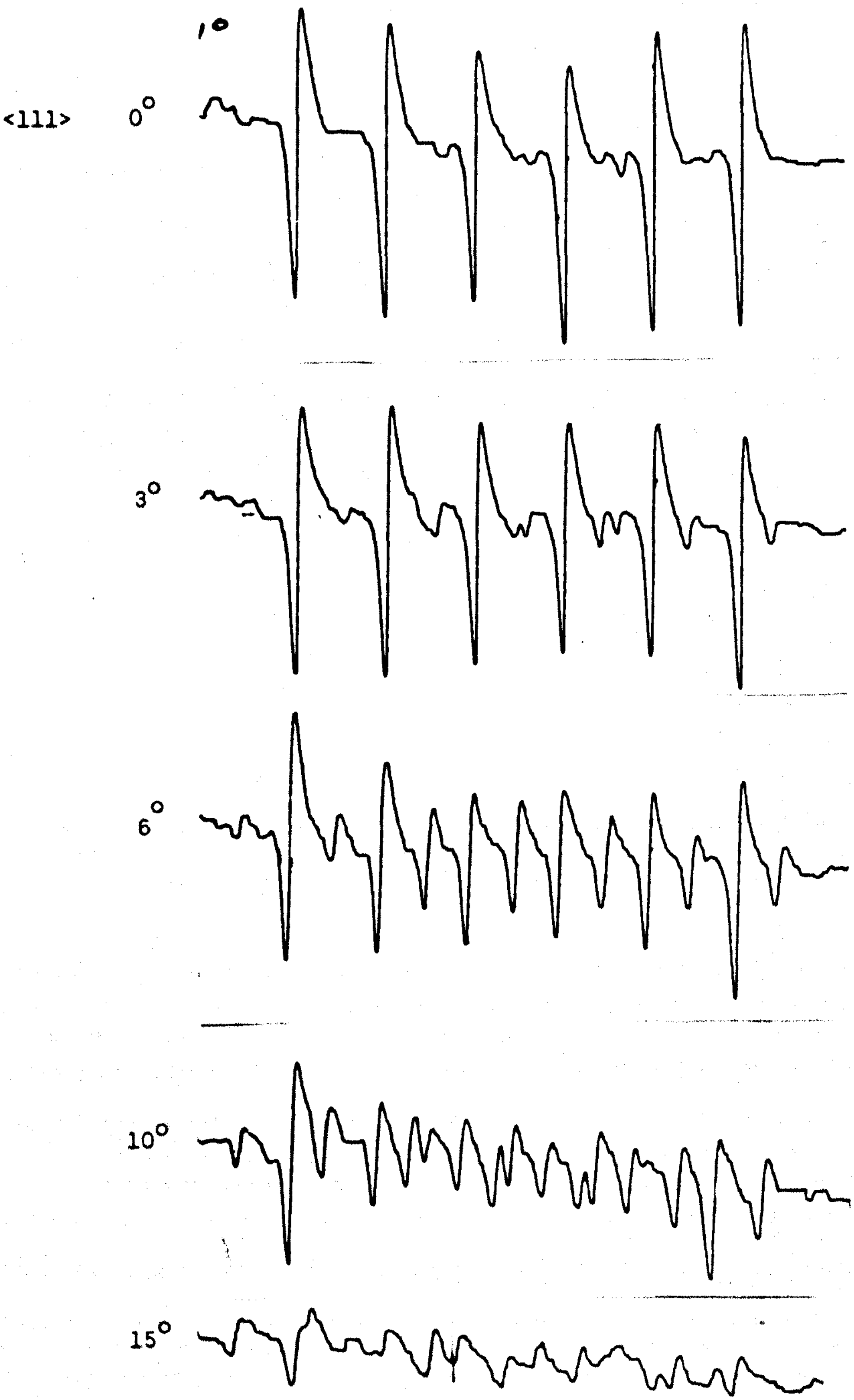

FIGURE 5.2

(g = 3.39) and 5,081 gauss (g = 1.3) and in addition two overlapping sets of lines of 'intermediate' width and intensity to the other types occurred at 3,710 gauss (g = 1.78) and 3,992 gauss (g = 1.65) respectively. In addition to these main groups there were several weak groups to low field. Along <111> directions the spectrum again simplified and formed groups of intense lines. In this direction three groups of '$+\frac{1}{2} \rightarrow -\frac{1}{2}$' lines were formed centred at 1,605 gauss (g = 4.12), 3,310 gauss (g = 2.00) and 5,007 gauss (g = 1.32) with two groups of the broader '$+\frac{3}{2} \rightarrow +\frac{1}{2}$' type lines at 2,100 gauss (g = 3.15) and 6,627 gauss (g = 0.99). Angular variation studies in <100>, <110> and <111> planes failed to reveal any information concerning the angular dependence of these various groups of lines owing to rapid loss of intensity with angle. The break up of the 5,007 gauss group along the <111> direction under rotation is shown in Figure 5.2.

The results of the X band studies described above made it possible to make some deductions about the nature of this Mn centre. Firstly the odd angular dependence of the spectrum, quite unlike Mn in other alkaline earth oxides, and especially the break up of the groups of lines observed in <110> and <111> directions suggested that several equivalent sites in the structure were involved. The existence of the very low field lines, if they were in fact associated with the same centre as the rest of the spectrum, suggested that the zero field splittings of the fine structure levels of the Mn ion were of the same order as the X band quantum, i.e. ~0.3 cms^{-1}. This would also explain why the observed fine structure pattern bore no resemblance to the five component spectrum predicted by a perturbation theory treatment of the Mn Hamiltonian (2.16) since the assumption D >> $\hbar\nu$ made it that this treatment would not hold for this centre. The zero field splittings between the various fine structure energy levels of Mn^{2+} are 2D, 4D and 6D. Consequently D might roughly be expected to be either 0.15 cms^{-1}, 0.075 cms^{-1} or 0.05 cms^{-1} depending upon which transition the low field lines are associated with. In order to simplify the problem investigations were continued at Q band frequencies on the Varian spectrometer.

5.2 Q Band Studies of the Mn^{2+} Spectrum

Q band studies were necessarily made on smaller crystals, 2 × 1 × 1 mm, which were cleaved from the crystals investigated at X band. To achieve angular variation studies in <110> and <111> planes, crystals were mounted on appropriately angled wedges which were then lowered through the sample hole into the cavity. To check that a given plane, the <111> for example, was parallel to the plane of rotation of the field, the spectrum was compared along equivalent directions, in this case the three <110> directions 60° apart, and the specimen mount adjusted by crudely pushing it to one side or the other of the sample hole until the equivalent directions gave identical spectra.

The e.p.r. spectrum was much easier to interpret at Q band since although the peak intensity of lines was still very angular dependent it was possible to see the majority of the spectrum at all orientations. Furthermore at Q band the microwave quantum is four times larger than at X band and consequently, as expected, the predictions

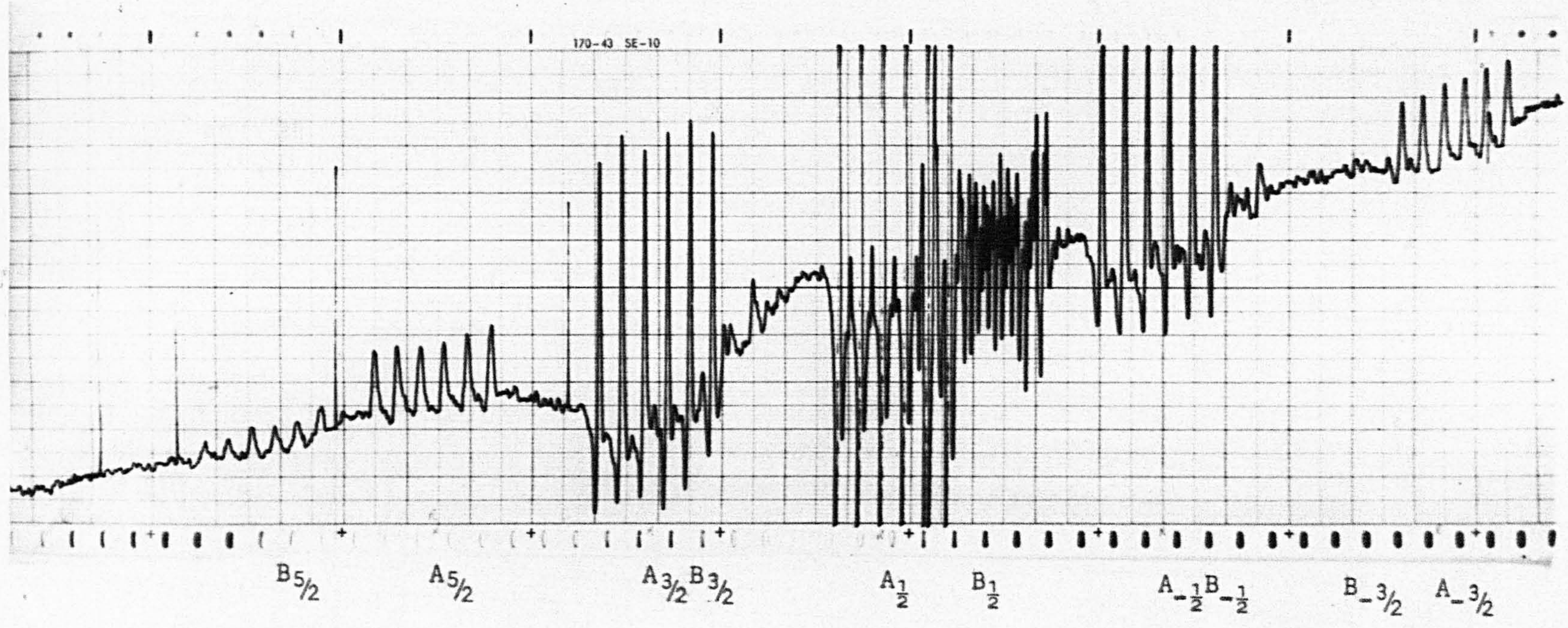

<110>

FIGURE 5.3

of perturbation theory were more closely followed. Rotations in the <100> and <110> planes, failed to reveal the symmetry of the spectrum although it was obvious that with well over a hundred lines observed there must be at least four inequivalent sites involved. Further it was apparent that some of these sites become equivalent along <111> and <110> and thus caused the great increases in intensity along these directions observed at X band. The recognition that the spectra along <111> and <211> directions were similar led to an angular variation study in the <111> plane and this finally resolved the symmetry of the spectrum. In the <111> plane one set of five fine structure components remained almost invariant and this suggested that the spectrum could be fitted to a Hamiltonian of the form:

$$\mathcal{H} = \beta\underline{H}.\underline{g}.\underline{S} + D(S_z^{\,2} - \tfrac{1}{2}S(S+1)) + E(S_x^{\,2} - S_y^{\,2}) + A_zI_z + B(I_xS_x + I_yS_y) \qquad (5.1)$$

with the D term predominant and the z axis along a <111> crystal direction. As there are four different <111> type directions in a cubic structure one would expect to interpret the whole spectrum as arising from centres with this hamiltonian but with z axes distributed over these four directions.

Thus in the <111> plane the invariant components arise from those centres with their principal axis at right angles to the plane of rotation and the remaining anisotropic lines are due to similar sites along the three other <111> type directions. In the <110> direction the sites are equivalent in pairs and along the <111> split into a single site with its zero field splitting axis parallel to the applied magnetic field and a group of three equivalent sites. The Q band spectra observed

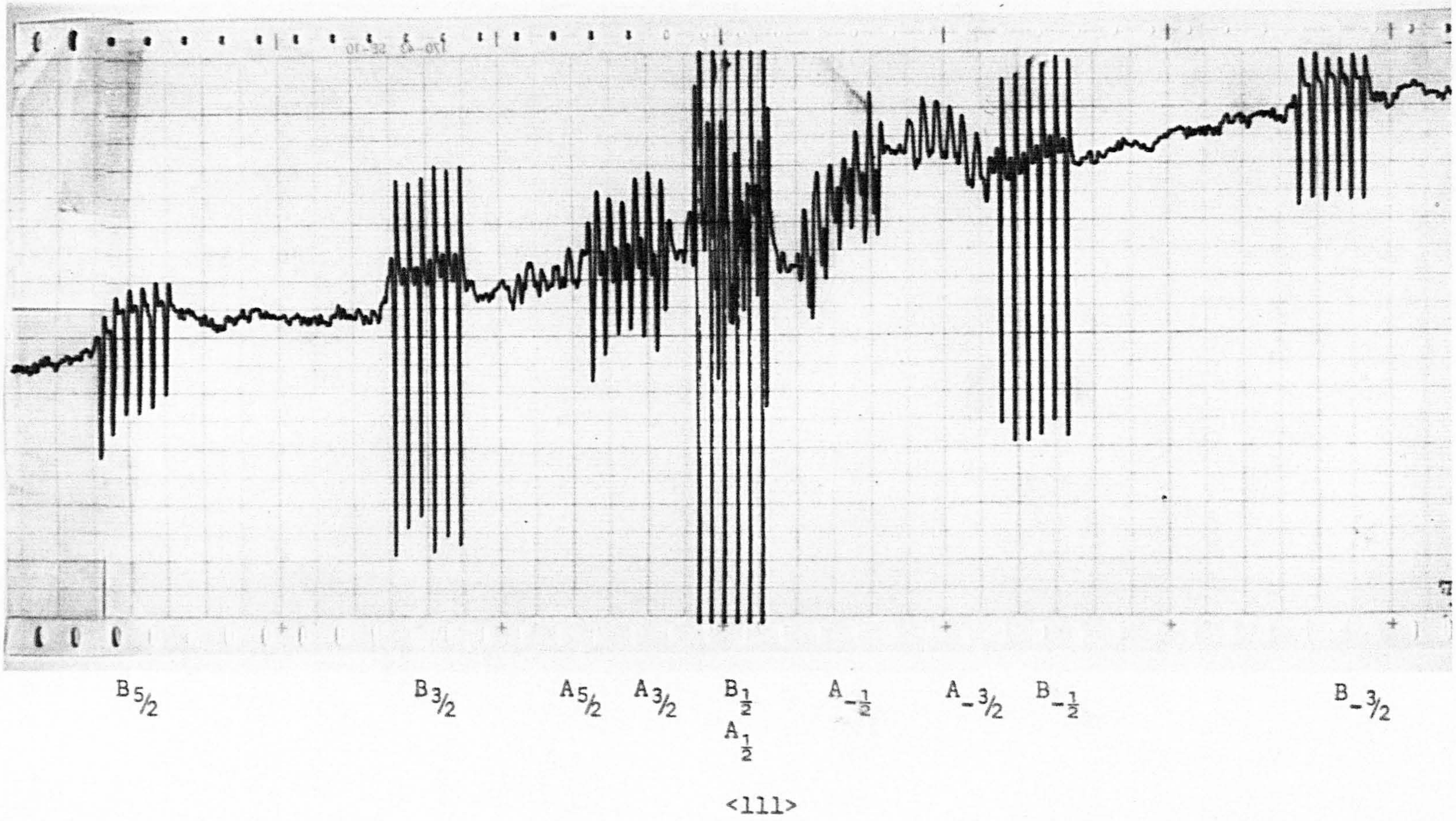

FIGURE 5.4

along these two directions are shown in Figures 5.3 and 5.4, together with a key specifying the origin of each group of lines. The letters A, B, C and D refer to the four <111> type directions in the structure while the subscripts $+5/2$, $+3/2$ etc. specify the M_S value of the fine structure level from which the transition occurs. To avoid confusion only the fields of the fine structure transitions from which each group of six hyperfine lines derive have been marked. The spectra observed along <100> directions are much less informative than the <110> and <111> spectra since although all four sites are equivalent along this direction the polar angle of $\theta = 54.74^{\circ}$ is such as to lead to the near collapse of all their fine structure components, which produces a very confused pattern of lines. For a general orientation when all four sites will be inequivalent we expect to see $2S = 5$ fine structure transitions each split into $(2I + I) = 6$ hyperfine components, associated with each site, making a total of 120 lines in all. Not all these lines can be seen for a given orientation, however, as the line width and intensity of components varies considerably with angle and the outer fine structure groups particularly are often too broad to be discerned above the noise level. However evidence has been found for the existence and predicted angular dependence of all lines required by this assignment of the spectrum. There remain however quite a number of extra lines, especially in the spectrum found along <110> directions, the origin of which is a little uncertain. These will be discussed in a later section (section 5.7).

It may be noted from the spectrum observed along the <111> direction (Figure 5.4) that the spectral lines arising from the 'A' site

ANGULAR VARIATION OF PEAK TO PEAK HEIGHT

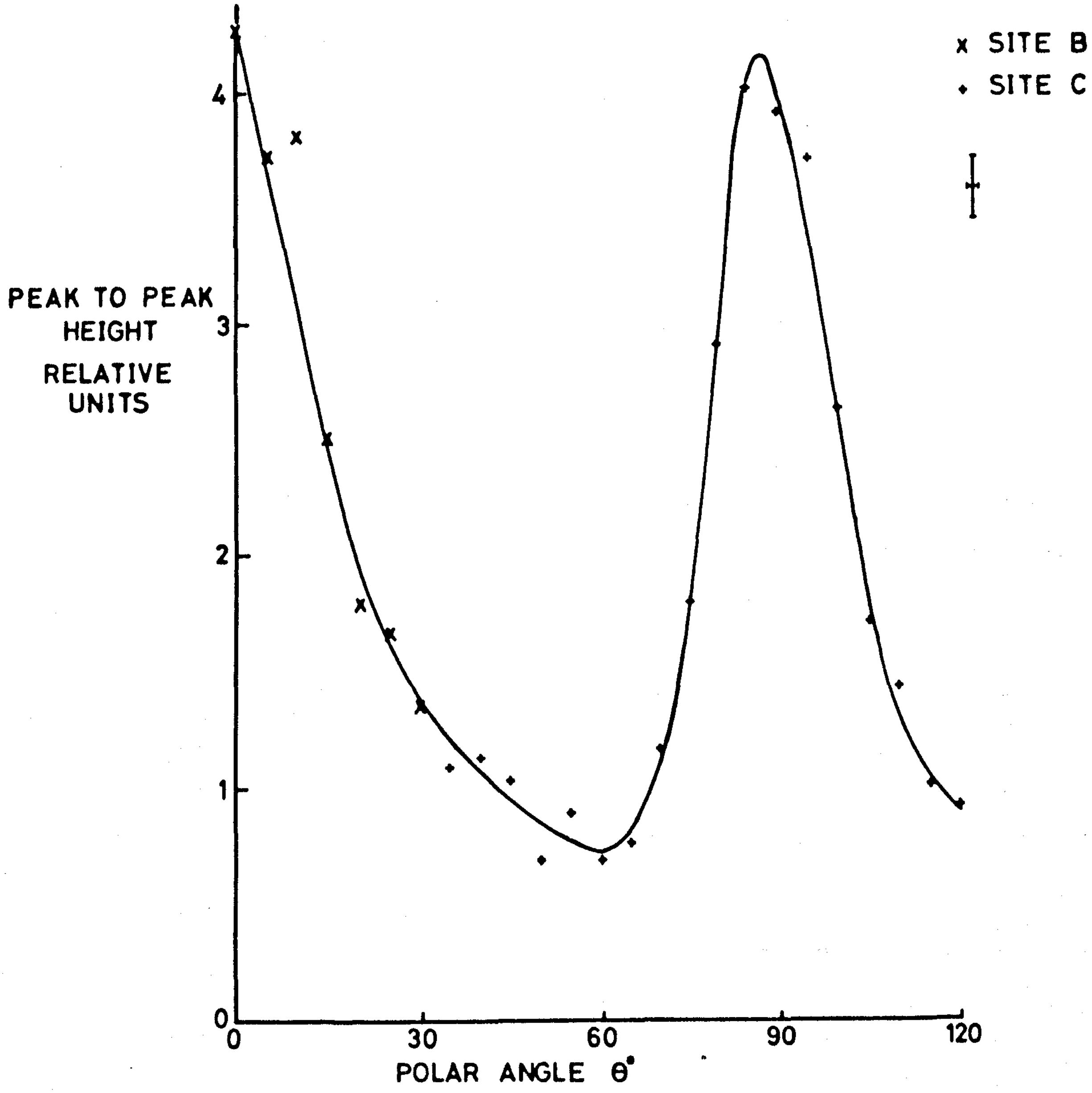

FIGURE 5·5

with polar angle $\theta = 0^\circ$, are much more intense than those observed from the three other sites with $\theta = 70.5^\circ$. This is an illustration of the general dependence of the intensity of these lines on the polar angle. Advantage was taken of the presence of more than one site to construct Figure 5.5, showing the dependence of the peak-to-peak height of the first derivative of lines on θ, from spectra taken in a <110> plane of the crystal. As illustrated by the figure the intensity is greatest when $\theta = 0^\circ$ corresponding to the applied field being along the zero field splitting axis and has a subsidiary maximum when $\theta = 90^\circ$. A similar study in the <111> plane on components for which $\theta = 90^\circ$ revealed no dependence on the polar angle ϕ, the peak-to-peak height being constant to within experimental accuracy. Line widths as estimated from measurements of the peak-to-peak width of first derivative traces were much less sensitive to orientation and no variation comparable to that of the peak-to-peak heights could be discerned. However it must be pointed out here that owing to overlapping of lines, line width measurements could only be made to an accuracy of ±20%. The widths of $M_S = +\frac{1}{2} \rightarrow -\frac{1}{2}$ transitions were found to be 5 gauss ± 1 gauss.

This description of the symmetry and form of the spectrum is essentially correct. The spectra observed along <110> and <111> directions at Q band and at X band have been shown to be consistent with a predominantly axial centre with principal axis along a <111> direction. The hamiltonian parameters determined for the centre predict the observed spectrum at both frequencies and the calculated angular variations of the spectrum in the <100>, <110> and <111> planes at Q band are consistent with the observed variations.

g TENSOR AXIS SYSTEM

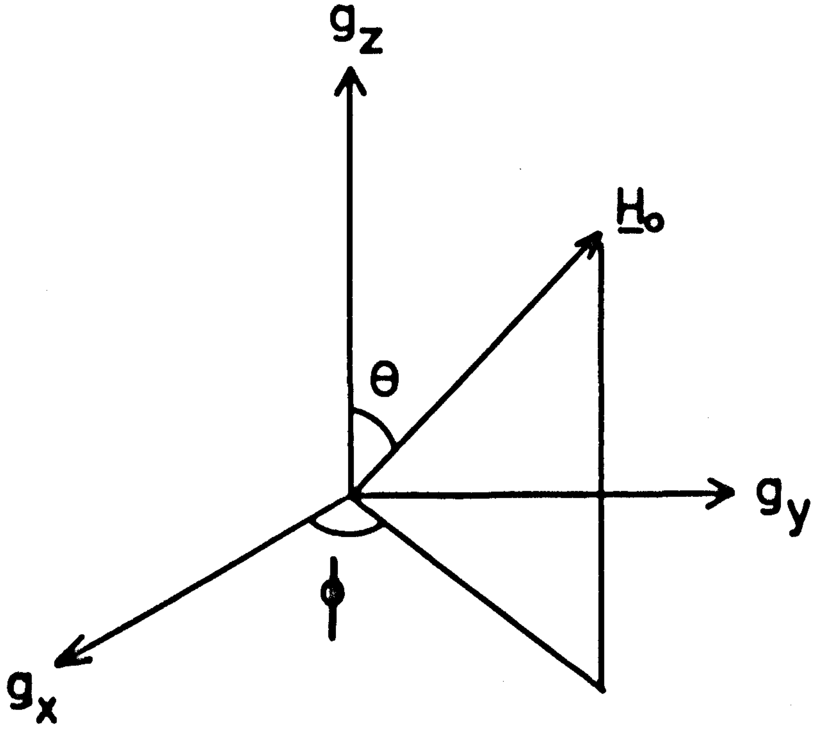

FIGURE 5·6

5.3 Determination of Hamiltonian Parameters

Having deduced the overall form and symmetry of the spectrum it is now possible to carry out a detailed analysis of spectral line positions and determine the various parameters of the spin hamiltonian. Firstly however it is necessary to adopt some system of relating the direction of the applied magnetic field in the laboratory frame of reference to the magnetic axes of the defect centre. The latter will of course, also be related to the crystalline axes. There are in common use two alternative but equivalent ways of making this specification. The first is to work in a system based upon the magnetic field (Dowsing and Ingram 1969); the z axis is taken to be the direction of $\underline{H}$ and the spin, fine structure and hyperfine terms in the hamiltonian are transformed through the polar angles θ and ϕ thus relating the hamiltonian to a centre with $\underline{g}$ tensor axes at these angles to $\underline{H}$. This produces a somewhat unwieldy expression for a general orientation and consequently it is convenient to transform the hamiltonian into the g tensor system. Choosing the x, y and z directions to be coincident with the principal axis directions of the $\underline{g}$ tensor and specifying θ and ϕ as in Figure 5.6, then the components of the magnetic field in this system are:-

$$H_x = H_o \sin\theta \cos\phi$$
$$H_y = H_o \sin\theta \sin\phi$$
$$H_z = H_o \cos\theta$$

Assuming that the $\underline{D}$ tensor and hyperfine tensor $\underline{A}$ have the same axis system as the $\underline{g}$ tensor, then the spin hamiltonian (5.1) becomes

$$\mathcal{H} = g_z\beta H_o\cos\theta\, S_z + g_x\beta H_o\sin\theta\cos\phi\, S_x + g_y\beta H_o\sin\theta\sin\phi\, S_y$$
$$+ D\left[S_z^{\,2} - \tfrac{1}{3}S(S+1)\right] + E(S_x^{\,2} - S_y^{\,2}) + A_zS_zI_z + B(S_xI_x + S_yI_y) \quad (5.2)$$

In determining the form of the spectrum expected from this hamiltonian it is often possible to assume that the microwave quantum $h\nu \gg$ D, E, A and B and then apply the results of perturbation theory to yield an approximate solution (Bleaney 1951, Low 1960). This leads to analytical expressions for the energy levels of the system which may then be used in conjunction with the selection rules $\Delta M_S = \pm 1, \Delta m_I = 0$ to predict the spectrum. However when, as is the case here, the zero field splitting parameter D is of the same order as $h\nu$ the perturbation theory result will be invalid for a general orientation of $\underline{H}$ to the magnetic axes. It is then necessary to consider all the terms in the hamiltonian simultaneously which involves setting up the energy matrix between the $|M_Sm_I\rangle$ states of the ion and performing a direct diagonalisation to arrive at the energy levels. This procedure is rather lengthy especially for an $S = \frac{5}{2}$ state and in this work resort was made to a digital computer.

Before treating the general angular dependence of the spectrum, however, it is possible to determine the main hamiltonian parameters by considering the special cases of $\underline{H}$ being parallel to the principal magnetic axes. When $\theta = 0^\circ$, corresponding to $\underline{H}$ being along the z axis, the terms in g_x and g_y vanish making it possible to factorise the energy matrix directly. Applying the selection rules $\Delta M_S = \pm 1$, $\Delta m_I = 0$ to the expressions for the energy levels (Low 1960) then the allowed transitions will occur when

$$h\nu = g_z\beta H + (M_S-\tfrac{1}{2})2D + \frac{E^2}{2g_z\beta H_o}\{\frac{29}{2} - 6M_S(M_S-1)\}$$
$$+ Am_I + \frac{B^2}{2g_z\beta H_o}\{\frac{35}{4} - m_I{}^2\} + \frac{B^2}{2g_z\beta H_o}(2M_S-1)m_I \qquad (5.3)$$

The observed resonance fields will be given by

$$H_{M_S m_I} = H_o - (M_S-\tfrac{1}{2})\frac{2D}{g_z\beta} - \frac{E^2}{g_z{}^2\beta^2 H_o}\{\frac{29}{4} - 3M_S(M_S-1)$$
$$- \frac{Am_I}{g_z\beta} - \frac{B^2}{g_z{}^2\beta^2 H_o}\{\frac{35}{4} - m_I{}^2\} - \frac{B^2}{2g_z{}^2\beta^2 H_o}(2M_S-1)m_I \qquad (5.4)$$

where $H_o = \frac{h\nu}{g_z\beta}$.

H_o was found from the centre of the hyperfine group associated with the $M_S = +\frac{1}{2}$ to $-\frac{1}{2}$ transition after having first found the hyperfine parameters and checked that the small second order shifts are negligible for the fields employed at Q band. Since the frequency was known this made it possible to determine g_z. It will be shown later that the second order contribution to the fine structure splitting from E can be safely ignored as being well within the limits of experimental accuracy.
A value for 4D could then be found from the separation of the centres of the hyperfine groups associated with the $M_S = +\frac{3}{2} \rightarrow +\frac{1}{2}$ and the $M_S = -\frac{1}{2} \rightarrow -\frac{3}{2}$ fine structure transitions. This gave $D = 0.0778\ \mathrm{cm}^{-1}$. Since the absolute sign of D could not be determined in these experiments it will be taken as positive; the only difference in the analysis introduced by a negative D would of course be to require a redesignation of the fine structure quantum numbers M_S.

When we come to the problem of determining E, g_x and g_y it is first of all necessary to make some choice of x and y axes in the $\theta = 90^\circ$ plane. Normally the choice is made such that the y axis is the direction in the $\theta = 90^\circ$ plane in which the fine structure separations are greatest and some estimate of the size of E can be made from the anisotropy in these separations in this plane. Examination of the spectra taken in the <111> plane, which would correspond to the xy plane of the g tensor for one site, revealed that any anisotropy in the separation of the $M_S = +3/2 \rightarrow +\frac{1}{2}$ to $M_S = -\frac{1}{2} \rightarrow -3/2$ transitions for this site was less than six gauss out of the ~1,600 gauss produced by D, a figure that was within the accuracy of the experiments. This places an upper limit on the value of E of 0.0005 cm^{-1} and the centre can effectively be considered axial, the ratio of E/D being less than .003. Furthermore the positions of the hyperfine group associated with the $M_S = +\frac{1}{2} \rightarrow -\frac{1}{2}$ transition were also invariant in this plane to within experimental error, inferring that $g_x = g_y$ as expected for an axial centre. The result of factorising the energy matrix for the $\theta = 90^\circ$ plane of an axial centre does however produce an expression involving second order terms in D which, with such a large D value, will not be negligible in this case. Consequently it was decided to determine $g_\perp$ by cycling the computer diagonalisation procedure for various values of $g_\perp$ until a reasonable fit to the spectrum was obtained.

5.4 Direct Diagonalisation of the Energy Matrix

The program used in these calculations was developed by Dowsing from a procedure outlined by Swalen and Gladney (1964). It was written in FORTRAN 4 and the computations were performed on the University Eliot 41/30 digital computer. As the 32,000 word store of this machine was insufficient to handle the 36 by 36 energy matrix of the full hamiltonian 5-2 evaluated between all the spin states of Mn^{2+}, it was necessary to exclude the hyperfine terms and consider only the 6 by 6 matrix of the fine structure and Zeeman terms set up between the states of the electron spin.

The programme required input values for the microwave frequency, the electron spin, the polar angles θ and ϕ and the hamiltonian parameters g_x, g_y, g_z, D and E. In addition it was necessary to divide the field range over which it was desired to search for transitions into a number of steps of specified field interval. A brief description of the programme will be given here, a fuller specification of a more versatile programme may be obtained from Dr. R.D. Dowsing.

A subroutine is used to set up the matrix, making use of the matrix form of the various operators as illustrated in Appendix I. A small problem arises with the introduction of imaginary matrix elements by the S_y operator. This is overcome by doubling the size of the matrix such that (A + iB) is specified as $\begin{pmatrix} A & -B \\ B & A \end{pmatrix}$ and use is made of the mathematical result that if the eigenvectors of the former j × j matrix are $u_j + iv_j$ the eigen vectors of the 2j × 2j real form will be u_j, v_j. The doubled matrix is diagonalised by another subroutine making use of the Jacobi

TABLE 5.1

HAMILTONIAN PARAMETERS FOR Mn^{2+} BaO

$g_z = 2.0017 \pm .0001$

$g_\perp = 2.0013 \pm .0005$

$D = 0.0778 \pm .001\ \text{cms}^{-1}$

$E < 0.0005\ \text{cms}^{-1}$

$A = 67.5 \pm 0.5 \times 10^{-4}\ \text{cms}^{-1}$

$B = 68.5 \pm 0.5 \times 10^{-4}\ \text{cms}^{-1}$

method in which the operations performed on A to reduce it to diagonal form and display its eigenvalues are simultaneously applied to a unit matrix I of the same dimension, thus transforming the columns of I into the eigenvectors of A.

The eigenvalues for the first value of the field are stored and the process is repeated for the first step increase in field. The separations between all pairs of energy levels at the two field values are then compared with the size of the quantum. If a transition could occur within this step length it would be registered by a change in the sign of the difference between the energy separation of the two levels concerned and the quantum. Thus by monitoring the sign of $(E_i - E_j - h\nu)$ as the field is stepwise increased it is possible to deduce when and between which levels a transition will be observed. For each transition registered an interation procedure is started which progressively reduces the field intervals within the given step until the field at which the transition occurs is determined to an accuracy specified by the programmer. The eigenvectors of the levels involved in the transition are then determined and a further subroutine uses them to calculate the transition probability. When the total field range has been covered in this manner, details of the transitions are printed out.

The programme was first used to check the values of D and g_z determined for the $\theta = 0^{\circ}$ direction. Good agreement was found to within the experimental error for both the X band and Q band data. Various values of $g_{\perp}$ were then cycled to produce a best fit for the position of the central fine structure line in the $\theta = 90^{\circ}$ plane. Agreement with experiment

FIELD DEPENDENCE OF ENERGY LEVEL SPLITTING

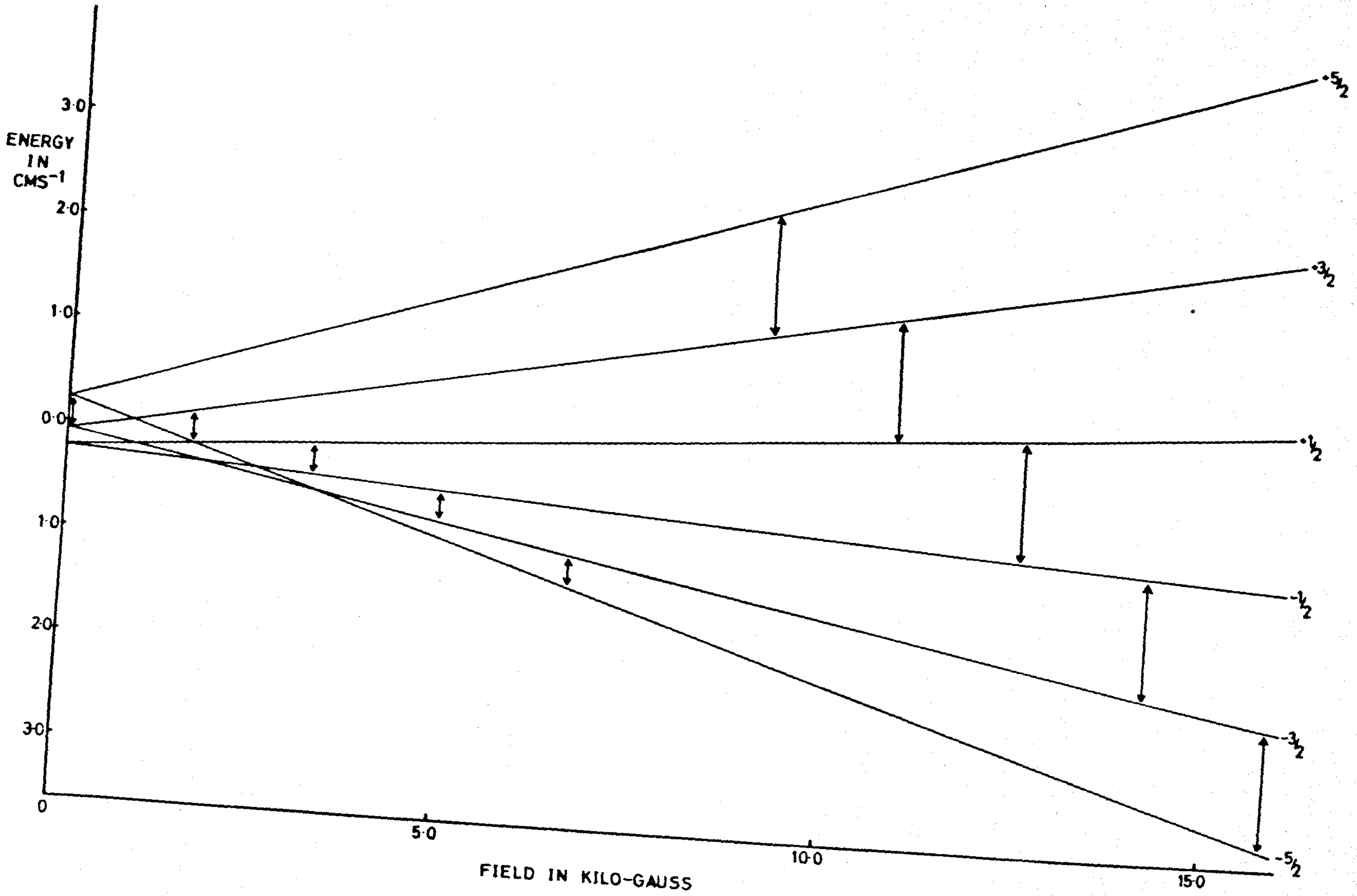

FIGURE 5·7

was not so satisfactory in this plane however where discrepancies of up to 15 gauss occurred in the experimental and calculated positions of the outer fine structure components at Q band. The fit could be improved by varying D but only at the expense of the results achieved in the $\theta = 0^{\circ}$ direction. Consequently it was decided to adopt the value of D giving the best results along the $\theta = 0^{\circ}$ direction and thus 'concentrate the error' into the $\theta = 90^{\circ}$ plane. A study was made of the effect of including non-zero E values in the matrix but in order to have any noticeable effect E was required to be at least ten times larger than the upper limit placed on it by the results of the anisotropy study performed in the <111> plane. The set up routine was modified to include the a and F terms of hamiltonian (2.16) but a similar conclusion was reached, that any value of these parameters large enough to affect the results introduced an unacceptable degree of anisotropy into the spectrum. However this discussion is perhaps to over-emphasise what is in fact a small discrepancy, and when we consider that the chosen hamiltonian parameters predict the spectrum observed both at Q band and at X band along <111> directions, in which inequivalent sites with $\theta = 0^{\circ}$ and $\theta = 70.5^{\circ}$ are involved, and for <110> directions, where the sites form pairs with $\theta = 90^{\circ}$ and $\theta = 35.26^{\circ}$, the overall agreement between theory and experiment is quite good. The final values for the hamiltonian parameters are listed in Table 5.1.

Figure 5.7 shows the splitting of the energy levels of this centre as a function of the applied field. The diagram corresponds to the applied field being parallel to the axis of the zero field splitting

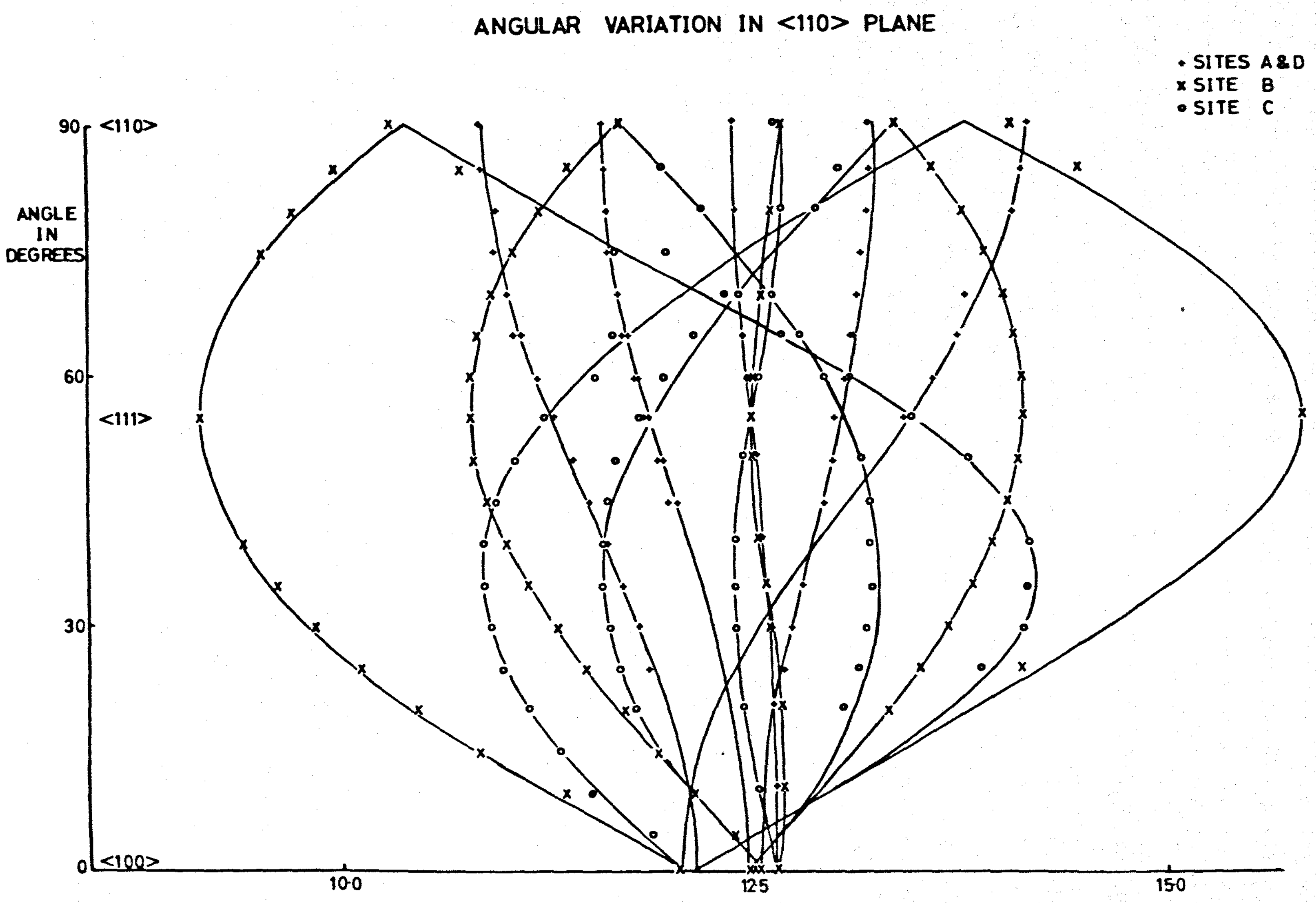
ANGULAR VARIATION IN <110> PLANE
+ SITES A&D
x SITE B
o SITE C
ANGLE IN DEGREES
90
<110>
60
<111>
30
0
<100>
10·0
12·5
15·0
FIELD IN KILO-GAUSS

FIGURE 5·8

tensor and the transitions observed at X band and Q band are marked. It may be noted that the very low field resonances observed at X band correspond to transitions between the ±$^3/_2$ and ±$^5/_2$ states before these have appreciably diverged. The many weak groups of lines observed at low field at X band undoubtedly arise from transitions which would normally be forbidden but are allowed by the mixing of states in this region. This will be particularly the case for sites where H is not along the principal axis of the D tensor.

5.5 Angular Variation of the Spectrum

As a further check on the correctness of the specified form of the hamiltonian and the directions of the g tensor axes of the centre it was decided to compare the predicted angular variation of the whole spectrum with that observed in the <110> and <111> crystal planes at Q band. As there are four sites involved, assuming E = 0, and as the prediction of the spectrum observed from each site at a given orientation of the field to the crystal axes depended upon feeding the appropriate polar angles for that site into the diagonalisation programme, a substantial amount of coordinate geometry calculation was first necessary. To facilitate this a computer programme was written which, from specified direction cosines of the g tensor axes with respect to the crystal axes and a description of the crystal plane in which H was to be rotated, calculated the polar angles of the site at five degree intervals in the rotation of H. As in practice it is virtually impossible to align a crystal exactly in an e.p.r. cavity, a facility was included in the

ANGULAR VARIATION IN <111> PLANE

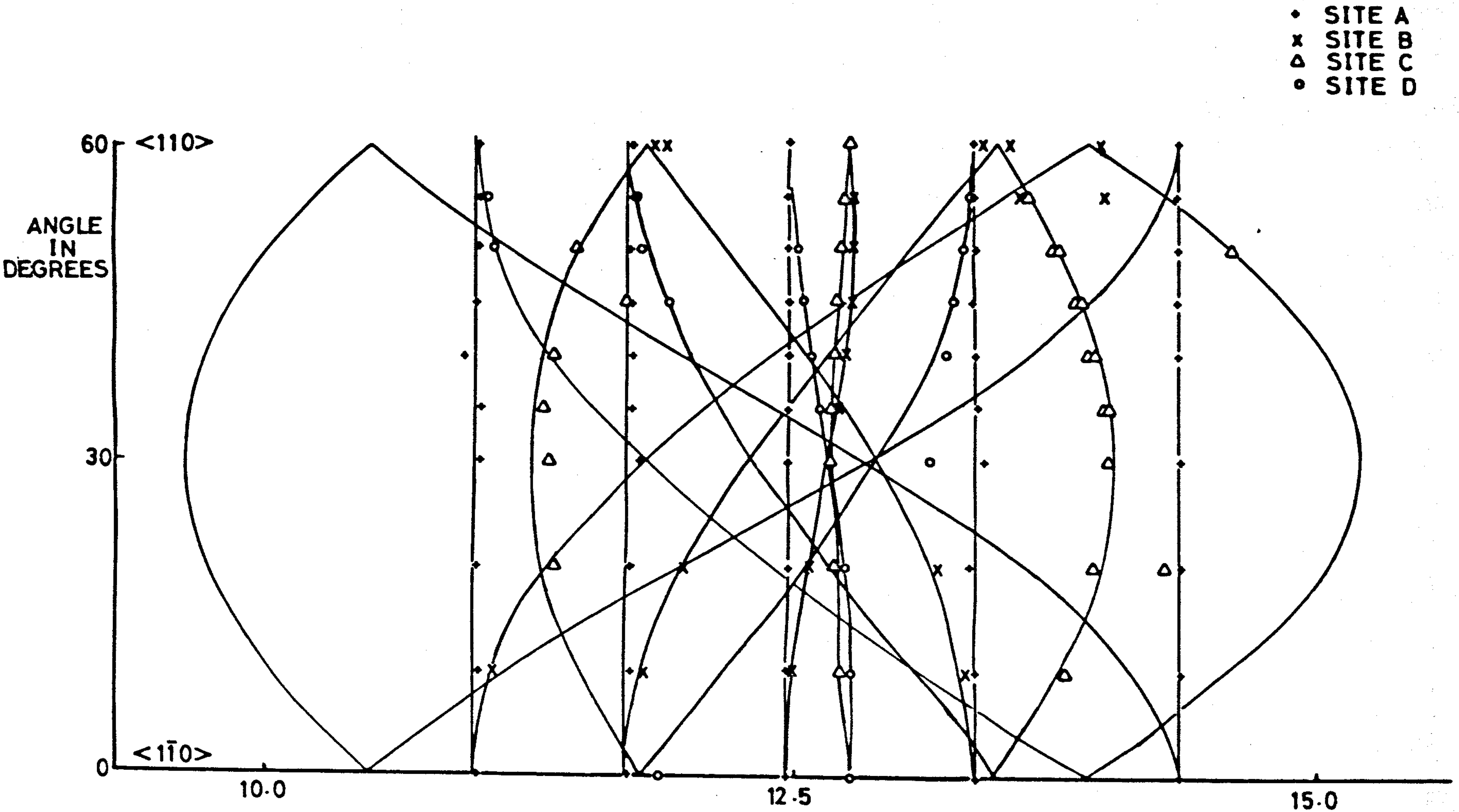

FIGURE 5.9

programme to consider the effects of a given misalignment of the crystal, expressed in Eulerian angle form (Rutherford 1960), on the polar angles of all the sites as H was rotated.

Figures 5.8 and 5.9 show the results of these angular variation studies. To reduce the confusion that would result from plotting all a hundred and twenty lines, each hyperfine group is represented by a point midway between its two central components. Owing to the angular dependence of line intensity mentioned earlier, it was impossible to observe all lines at all angles, a difficulty that was particularly acute in the <111> plane measurements. However, as the figures show, there is very good agreement between the lines observed and their predicted angular variation in these two planes and this combined with similar agreement between theory and earlier data taken in <100> planes leaves no doubt that this is the correct assignment of the spectrum.

5.6 Hyperfine Structure

As mentioned earlier the most prominent indication that this spectrum arose from a Manganese centre was provided by the six line hyperfine splitting of all fine structure components. This is attributed to interaction of the electron wave function with the nuclear spin $I = 5/2$ of the 100% abundant Mn^{55} nucleus. Along the $\theta = 0^o$ direction the hyperfine terms in the hamiltonian produce a splitting of the fine structure transitions which is represented by the terms in the second line of equation (5.4). It can be seen from this expression that the parameter A may be determined directly by measuring the separation of the middle two

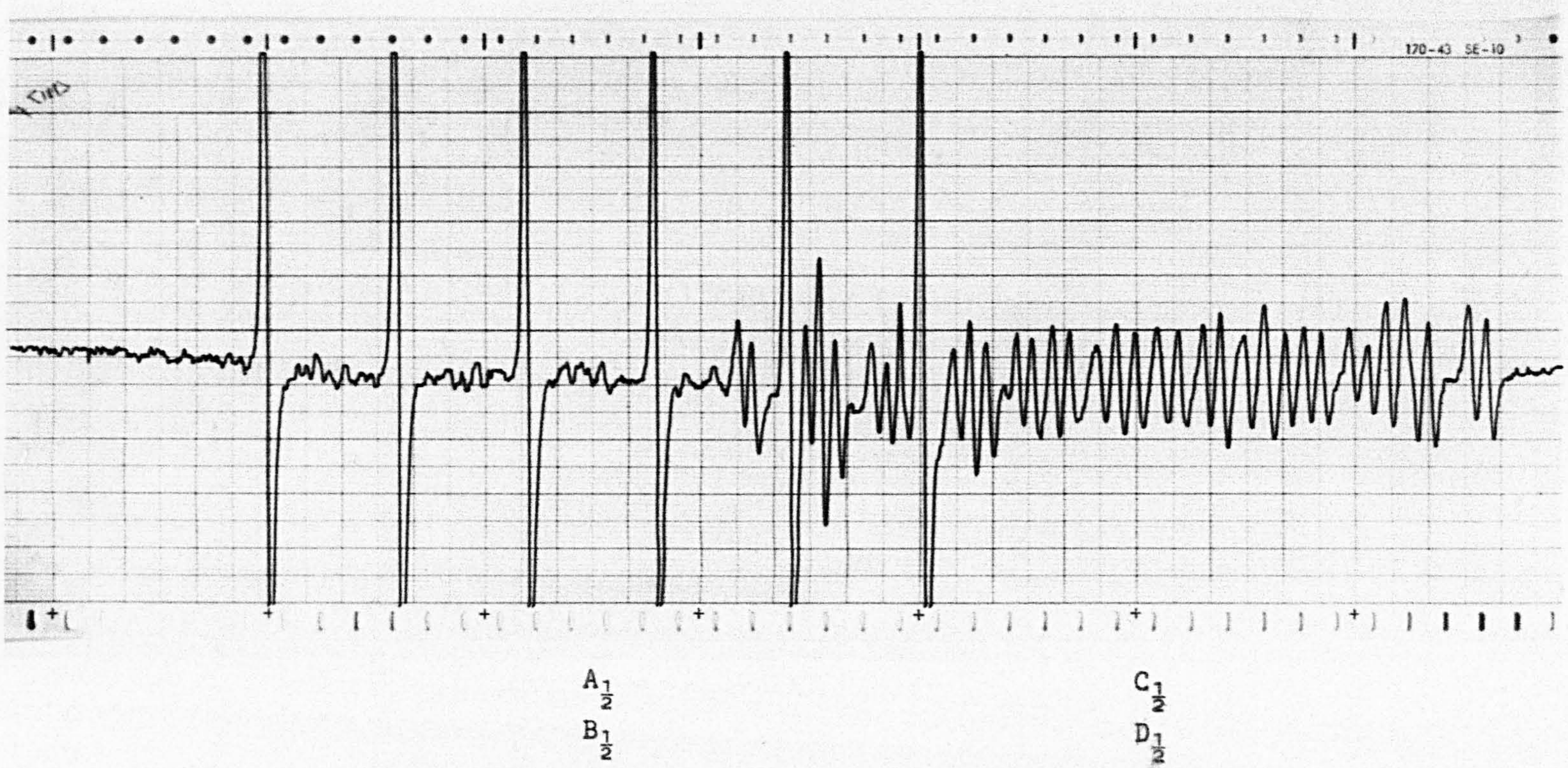

<110>

FIGURE 5.10

hyperfine components of the $M_S = +\frac{1}{2} \rightarrow -\frac{1}{2}$ transition since for these lines the various second order contributions either cancel or shift each line equally.

Performing a similar factorisation of the energy matrix in the $\theta = 90^\circ$ plane and assuming axial symmetry we achieve:

$$H_{M_S m_I} = \text{Fine structure transition } M_S - \frac{Bm_I}{g_\perp\beta} - \frac{(A^2 + B^2)}{g_\perp{}^2\beta^2 H_o}\,\frac{1}{4}\left\{\frac{35}{4} - m_I{}^2\right\} - \frac{AB}{2g_\perp{}^2\beta^2 H_o}(2M_S - 1)m_I \qquad (5.5)$$

and again by concentrating on the separation of the middle two components of the $M_S = +\frac{1}{2}$ transition it is possible to ignore second order effects and determine B. A check on the spectra taken in the <111> plane for the site with $\theta = 90^\circ$ established that B was constant to within experimental accuracy in this plane and hence the hyperfine structure was axial. The hyperfine parameters determined in this way are shown in Table 5.1.

5.7 Anomalous Spectral Lines

Figure 5.10 is a trace of the first derivative spectrum recorded in the region of $g = 2.0$ when the applied field was parallel to a <110> crystal direction. Underneath is a plan of the spectrum expected from the $M_S = +\frac{1}{2} \rightarrow -\frac{1}{2}$ fine structure transitions of the two pairs of equivalent sites and it is immediately apparent that while the six doubly intense lines expected from these sites with $\theta = 90^\circ$ are present, there are many more lines to high field than the other group of six expected from the sites with $\theta = 35^\circ$. The origin of these lines has not been conclusively established although two possible theories have been explored. There are between 35 and 40 equally intense lines. A detailed analysis of their angular dependence has proved impossible owing to the overlap of components and changes in intensity but the general movement of the group is consistent with that expected from inequivalent <111> sites in accordance with the previous analysis.

The first hypothesis considered was that they arose from a small rhombic component which introduced a dependence on ϕ into the spectrum and implied that each <111> direction, being a three-fold axis, has associated with it three inequivalent sites making twelve sites in all. This, when combined with a small misalignment of the crystal, would predict $2 \times 3 \times 6 = 36$ equally intense lines arising from the two <111>'s making 35° with the <110>. This hypothesis was tested, making use of the facility for considering the effects of crystal misalignment on the polar angles for the various sites, which had been incorporated into the solid geometry programme described in section 5.5. It was discovered that the polar angles for the two sites making angles of 35° to this direction were over twice as sensitive to misalignment than those of sites at 90°. A misalignment of 3° of the crystal produced a difference of up to 10° in the polar angles θ for the two '35°' sites which when combined with the sensitivity of the hamiltonian to θ in this region caused a forty gauss difference between the $+\frac{1}{2} \rightarrow -\frac{1}{2}$ fine structure transitions from the two sites. This is of the order of magnitude required to explain this splitting in the <110> data. The hypothesis of an E term splitting these two transitions into six components had to be rejected however, since the differences of twenty or so gauss required would have been accompanied by much larger sub-splittings of the other fine structure components, none of which were observed.

The most likely explanation of these lines however is that they result from a slight misalignment, which makes the two sites inequivalent, and further that the spectra from each site exhibits the various forbidden lines first discussed by Bleaney and Rubins (1961) and observed very frequently in manganese spectra. These lines arise because for off axis orientations of H to the tensor axes the term $B(S_xI_x + S_yI_y)$ in the hamiltonian (5.2) incorporates into the energy matrix off-diagonal contributions connecting states with different nuclear quantum numbers m_I. This produces a finite but orientation dependent probability of observing transitions in which the nuclear quantum number changes by one unit. The relative intensity of these 'forbidden' lines to the allowed lines derived by Bleaney and Rubins using perturbation theory is

$$\left(\frac{3D \sin 2\theta}{4g\beta H}\right)^2 \left\{1 + \frac{S(S+1)}{3M_S(M_S-1)}\right\}^2 \{I(I+1) - m_I^2 + m_I\} \tag{5.6}$$

which is a maximum when $\theta = 45^\circ$. Even though a perturbation theory treatment is not applicable to this case it is reasonable to suppose that the relative intensities of these lines will show a similar angular dependence. Bleaney and Rubins also point out that for a sufficiently large value of $\frac{D}{g\beta H}$, i.e. comparable to the value achieved by the large D value of this centre, the forbidden transitions may rival the allowed transitions in intensity. These transitions are specified by the selection rules $\Delta M_S = \pm 1$ $\Delta m_I = \pm 1$ and give rise to five doublets situated between the allowed hyperfine lines. In addition transitions appropriate to a $\Delta m_I = \pm 2$ selection rule are also frequently observed. The actual positions of these forbidden lines as well as their intensities are strongly dependent on θ.

For several reasons it has not been possible to assign the anomalous lines in this spectrum directly to the forbidden transitions discussed above. Firstly the spectrum is confused by the presence of two sites which, owing to misalignment, will have different values of θ. Secondly there is the consideration that the angular dependence of the spectrum depicted by perturbation theory might not necessarily apply in this case and complicating matters still further is the orientation dependence of the line widths described in section 5.2 and illustrated in Figure 5.5.

However, performing a line count on this hypothesis, we have two sites each with six allowed lines, ten $\Delta m_I = \pm 1$ and eight $\Delta m_I = \pm 2$ forbidden lines, making a total of forty-eight lines in all. Taking into account the possibilities of overlap and low intensity for some lines this figure is in reasonable agreement with the thirty-five to forty lines actually observed. Moreover, the fact that some lines certainly disappear as θ approaches 0° or 90° is in accordance with the behaviour expected on this model. In conclusion it is reasonable to assign these lines to a combination of misalignment and the presence of forbidden lines of comparable intensity to the allowed lines.

<u>TABLE 5.2</u>

HAMILTONIAN PARAMETERS OF Mn^{2+} IN ALKALINE EARTH OXIDES

Material	Temp.	g	$a\times10^{-4}cms^{-1}$	$D\times10^{-4}cms^{-1}$	$A\times10^{-4}cms^{-1}$	Symmetry
MgO	290°	2.0010	19.01	-	-81.11	Cubic
CaO	290°	2.0011			80.7	
	77°				81.6	Cubic
	20°		6.0	-	-81.7	
SrO	290°	2.0012	4.3	-	-78.7	Cubic
	77°	2.0014			80.2	
BaO	290°	$g_{\parallel}=2.0017$	-	778.0	A 67.5	Axial
		$g_{\perp}=2.0013$			B 68.5	

(Data on other Oxides from Henderson and Wertz 1968)

5.8 Discussion of the Mn^{2+} Centre

Before discussing possible models for this defect it is interesting to compare its symmetry and spin hamiltonian parameters with those found for Mn^{2+} in other cubic alkaline earth oxides. These results are summarised in Table 5.2 and it is immediately apparent that there are striking fundamental differences between the situation prevailing in MgO, CaO and SrO and the results reported here for BaO. The most notable differences are in the symmetry of the site (axial in BaO and cubic in the others) and, probably as a result of this, in the magnitude of the zero field splitting which is very much larger in BaO. There is also a less striking but quite definite reduction in the magnitude of the hyperfine coupling parameter in BaO compared to the other oxides. The value of A found for this centre is some twenty per cent less than that found by Zdansky (1968) from a study of the temperature dependence of A in BaO powders; this study will be discussed in more detail later. I hope to show that these differences may be accounted for in terms of a model for the defect based on the conclusions of theoretical studies of monovalent impurities in the alkali-halides.

Perhaps the most obvious model for this defect is one which acknowledges the relative sizes of the ions involved (Table 4.1) and places the Mn^{2+} ion in the body centred interstitial site of the unit cell. There is easily enough room, on ionic size considerations, for the ion to be located at this site and further, remembering that the blue colouration of the crystal is associated with oxygen vacancies, we might suppose that the association of the Mn^{2+} with such a vacancy produces the

MODELS FOR Mn^{2+}:BaO

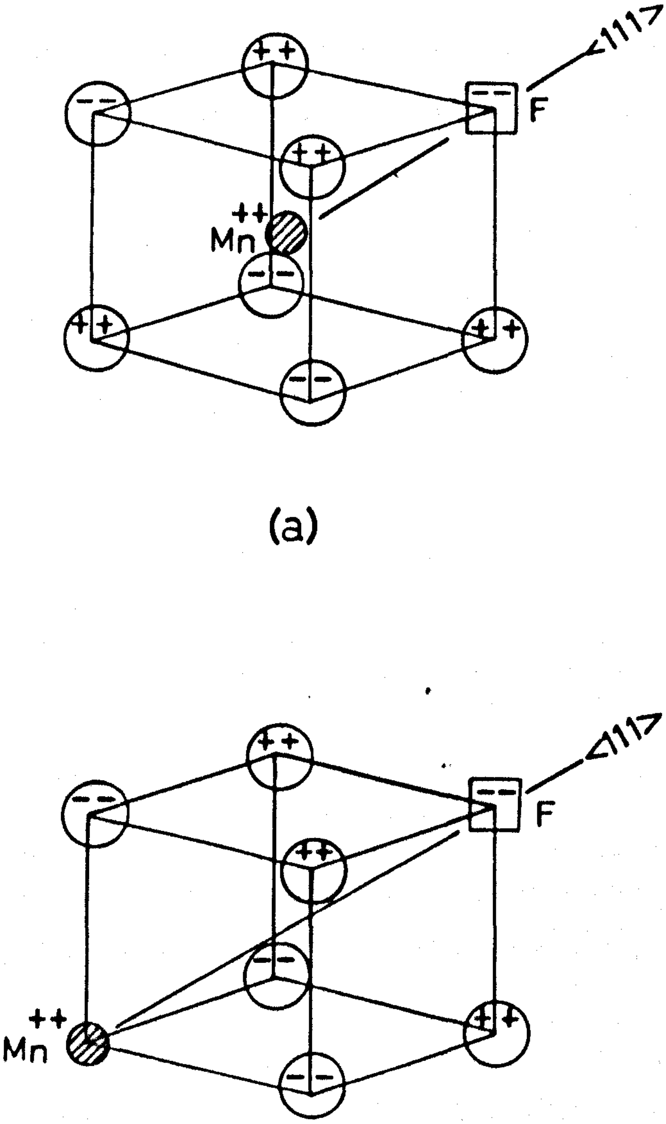

(a)

(b)

FIGURE 5·11

observed distortion along a <111> direction. The difficulty with this model is of course the problem of charge compensation and although it is well established that the charge compensation mechanisms associated with substitutional monovalent and trivalent ions in these materials need not be local (Henderson and Wertz 1968) it is unlikely that a complex such as this, with a net imbalance of four charges, would be stable. Some local charge compensation might be expected to occur by the vacancy trapping one or two electrons to form the well established F^+ or F centres. In the latter case this would also explain the absence of the expected F^+ spectrum from these crystals since the F centre is diamagnetic (section 5.11). Alternatively the spectrum might result from a defect in which the Mn^{2+} ion, occupying a Ba^{2+} site, is associated with an F centre at the next nearest neighbour O^{2-} site, again producing an axial defect with a <111> axis. These two models are sketched in Figure 5.11 and have the advantage that the Mn^{2+} spectrum is associated with the blue colour of the crystals in which it is observed. In an attempt to verify this possible association with an F centre, the Mn^{2+} spectrum was observed at X band at room and liquid nitrogen temperatures whilst the crystal was irradiated with ultra-violet light from a high pressure mercury lamp. That no discernable change in the spectrum occurred is of course quite inconclusive since it is possible that if there is an F centre associated with the Mn^{2+}, its electrons might be too tightly bound to the defect to be removed by this mechanism or alternatively that the experimental arrangements were not efficient enough to produce a detectable concentration of excited defects. Both these models do, however, suffer from the serious deficiency that not all the Mn^{2+} ions in the crystal would be expected to be associated with an F centre or similar defect. One ought, then, to see a spectrum from these other sites and, in the case of the second model, from those defects with F centres at the nearest neighbour sites along <100> directions. It is possible that the large background signal, also unique to blue crystals (section 5.11) is due to Mn^{2+} ions at other sites which are broadened out by thermal processes. This is the case for one Mn^{2+} spectrum in NaCl (Watkins 1959) and in this context it may be noted that Zdansky also reported a large background signal in his Mn doped BaO powders. However the disappearance of the NaCl spectrum upon cooling was accompanied by the increase in intensity of other Mn^{2+} spectra unlike the situation here where cooling merely removed the broad line without either noticeably increasing the axial spectrum or producing other spectra.

A more likely model for the defect, however, though one which is unfortunately not correlated with the blue colouration, is that it is a substitutional Mn^{2+} ion which is displaced from the lattice site in a <111> direction and occupies an 'off centre' position. Such off centre sites are well known for small radius monovalent substitutional impurities in the alkali halides (Smoluchowski 1968) and arise when a movement of the impurity ion off the lattice site combined with relaxations of the surrounding ions lowers the energy of the system. These systems are usually diamagnetic and the defects have been recognised by means of the accompanying dielectric (Sack and Moriarity 1965), thermal (Lombardo and P~~h~~ohl 1965, Bogardus and Sack 1966) and mechanical (Byer and Sack 1966) effects. However the consequence of the fall in symmetry accompanying such a distortion on a paramagnetic ion such as Mn^{2+} will be to lift the degeneracy of its spin levels. This then is a possible mechanism for producing the observed Mn^{2+} spectrum.

At first sight it might seem likely that displacement of the impurity will occur whenever it is smaller than the ion it is replacing. Detailed calculations however reveal that the actual position of the impurity depends upon a delicate balance of several competing contributions to the energy of the system, the most important being the repulsive forces generated by overlapping of the 'electron clouds' of ions, these tending to maintain the structure, and the polarisation properties of both impurity and host ions which favour distortions. Thus in order to decide whether this model is a reasonable projection of the behaviour of the divalent system pertaining here, it is necessary to look at the theory of these centres rather closely.

Several authors have approached the problem theoretically (Mathew 1965, Dienes et al. 1966, Wilson et al. 1967, Quigley and Das 1967) and agreement between theory and experiment has been achieved for the eleven systems in the alkali-halides for which data is available. The general technique is to adopt a polarisable point ion model and to express, in terms of the coordinates of the impurity and lattice ions, the various contributions to the energy of the system which will change upon distortion. The effects of distortions are then investigated by varying the ionic coordinates in a cyclical manner and evaluating the change in energyof the system. In this way it is possible to construct

TABLE 5.3

COMPARISON OF Li^+:KCl WITH Mn^{2+}:BaO

(a) : Ionic Radii

	Å		Å
Li^+	0.82	Mn^{2+}	0.80
K^+	1.46	Ba^{2+}	1.35
Cl^-	1.59	O^{2-}	1.40

Ratio

$K^+/Cl^- = 0.92$ $Ba^{2+}/O^{2-} = 0.96$

(Li:KCl data after Dienes et al. 1966)
(Mn:BaO data after Pauling 1948)

(b) : Polarizabilities

	$\alpha \times 10^{-24}$ cms^3		$\alpha \times 10^{-24}$ cms^3
Li^+	0.03	Mn^{2+} (cp Ca^{2+}	No data 1.1
K^+	1.33	Ba^{2+}	2.5
Cl^-	2.96	O^{2-}	0.5 ↔ 3.2

(after Tessmann et al. 1953)

an energy contour diagram of the system with respect to ion movements and hence determine the minimum energy configuration. Furthermore by investigating the sign of the determinant formed from second derivatives of the energy terms with respect to small ion motions, it can be decided whether the various minima are stable and whether or not they will be attained. A detailed treatment, of course, requires the use of a digital computer especially as the relaxations of ions several unit cells away from the impurity are often found to be important. However it is possible to draw some tentative conclusions about the behaviour of Mn^{2+} in BaO from these studies.

The first point that emerges is that the result clearly depends upon the relative sizes of the ions involved. It is also encouraging that amongst those alkali-halide systems that do relax the predominant movement of the impurity is along a <111> direction. Quigley and Das, for example, showed that for Li^+ in KCl and KBr and Na^+ in CsF, systems which have similar ionic radii ratios to Mn^{2+} in BaO, (Table 5.3a) there is a distinct minimum energy associated with a <111> displacement of the impurity and they further concluded that similar off centre minima might be expected for small divalent impurities in the alkaline-earth oxides. They do, however, anticipate extra difficulties in performing calculations for these systems owing to the diffuse nature of O^{2-} and the probable inadequacy of the pure Born-Mayer type potentials they used. However it is at least possible to examine the expressions used for the most important energy terms in the calculation and see whether doubling the charges produces any radical imbalance. The expression for the energy of the system may be written

$$E = E_{Static} + E_{Polarisation} + E_{Dipole\text{-}Dipole} + E_{Repulsion}$$

where the terms represent: the coulomb electrostatic energy, the energy of polarisation of the ions arising from the interaction of the dipoles formed at the relaxed sites with the electric field at those sites, the interaction energy of the various dipoles and the mutual repulsion of ions caused by overlap of their electron clouds. Examination of the forms adopted for the first three terms (Wilson et al. 1967) reveals that doubling the charge leads to a four-fold increase in the energy of these terms

$$E_{stat} = \tfrac{1}{2} \sum_{\substack{ij \\ i\neq j}} \frac{e_i e_j}{|\underline{r}_{ij}'|} - \tfrac{1}{2} \sum_{\substack{ij \\ i\neq j}} \frac{e_{ij}}{|r_{ij}|}$$

$$E_{pol} = -\tfrac{1}{2} \sum_{i} \alpha_i \underline{E}_i^{\,2}$$

$$E_{dip.dip} = \tfrac{1}{2} \sum_{\substack{ij \\ i\neq j}} \alpha_i \alpha_j \frac{E_i . E_j}{|r_{ij}'|^3} - \frac{3(\underline{r}_{ij}' . E_i)(\underline{r}_{ij}' . E_{ij})}{|r_{ij}'|^5}$$

where $\underline{r}_{ij} = \underline{r}_i - \underline{r}_j$ is the vector distance between ions i and j in their lattice positions and $\underline{r}_{ij}' = \underline{r}_i' - \underline{r}_j'$ is the corresponding distance for the relaxed positions. $\underline{E}_i$ is the electric field at the i^{th} ion in its relaxed position and may be expressed as

$$\underline{E}_i = \sum_j \frac{e_j \, \underline{r}_{ij}'}{|\underline{r}_{ij}'|^3}$$

It is easily seen that each expression is simply multiplied by four upon changing e_i to $2e_i$. The Polarisation and Dipole-Dipole terms do involve the polarisability of the ions too, of course, though here again, as Table 5.3b shows, the ratios of these quantities are roughly the same in the two systems.

The Repulsion term however is more difficult to assess and has been dealt with in the alkali-halides in terms of various phenomenological potentials, the parameters of which have been fitted to such measured quantities as lattice constant and compressibility. A fuller discussion of this may be found in the references (especially Dienes et al. 1966 and Wilson et al. 1967) but on a naive level it might be expected that as the charge clouds of the ions are denser and as the alkaline earth oxides are known to be harder than the alkali halides, then the repulsive term might be expected to increase considerably too.

In conclusion it may be said that this model for the defect, an off centre substitutional Mn^{2+} ion, is a reasonable one and one which is compatible with theoretical studies of such defects in alkali halides. The effect on these latter calculations of considering a doubly charged system is to increase the various energy terms in roughly the same ratio and hence preserve their 'balance', though here it must be noted that the important repulsive term is difficult to evaluate. One deficiency of the model is that it does not expressly relate the defect to the blue colouration of the crystals to which the spectrum is unique, though models which do attempt this suffer from other equally serious objections.

5.9 Comparison with Zdansky's Experiments

It is interesting to compare the results reported here with the work of Zdansky (1968) on the temperature dependence of the hyperfine coupling of Mn^{2+} in powdered BaO. He worked at X band and observed two sextets, one centred in the region of g = 2.0 and the other, with a smaller hyperfine splitting, at higher fields. He attributed these spectra to Mn^{2+} and Mn^{4+} respectively but as he does not give the g values of the groups it is difficult to decide if they arise from the centre reported here. This difficulty is enhanced by the large anisotropy observed in the intensity of this spectrum at X band which makes it hard to forecast the results expected from the averaging of orientations achieved in a powder. However there is good reason to believe that the sextet Zdansky attributed to Mn^{4+} does in fact arise from the Mn^{2+} defect observed here. The suggested association is that Zdansky's higher field group arise from a summing over all orientations of the group observed here at 3710 gauss ($g = 1.78$) when H was parallel to a <110> direction (section 5.1). These lines arise from the $+\frac{1}{2}$ to $-\frac{1}{2}$ transitions of those sites which have the principal <111> axis of their zero field splitting at right angles to $\underline{H}$ when $\underline{H}$ is along <110>. As the spin hamiltonian for this centre has axial symmetry, the position of these lines will be invariant in the appropriate $\theta = 90^{\circ}$ <111> plane. Furthermore the intensity of these lines falls off more slowly with rotation in a <111> plane than does that of other lines. Combining this fact with the relative insensitivity of the hamiltonian to θ with θ near 90° (section 5.7) it is reasonable to expect this group to gain rapidly over the others when performing a summation of intensity over all orientations of the crystallites in a powder.

If this association is correct then the problem arises as to the identity of the g = 2.0 sextet that Zdansky performed his temperature dependent studies on. The larger hyperfine splitting of this sextet makes it unlikely that it is associated with the spectrum reported here, even though there is a group in this region, originating from the $+\frac{1}{2}$ to $-\frac{1}{2}$ transition when $\theta = 0^{\circ}$, which might also be expected to 'sum' rapidly. It is unlikely that it is Mn^{4+} since the higher charged state is usually accompanied by a fall in the value of A (Henderson and Wertz 1968). The most probable explanation is that it is Mn^{2+} at some other site in the structure.

Zdansky's work was concerned with the contribution of local modes of vibration of the ion to its hyperfine coupling. As the defect reported here seems to be an off centre ion, it would undoubtedly have local modes of vibration associated with it, possibly even amounting to a 'resonance' between several equivalent off centre positions (Smoluchowski 1968) and hence a temperature dependent study of its hyperfine coupling would thus provide a check on the 'resonance mode' theory of vibration developed by Zdansky. This system is particularly useful since as there are several equivalent sites involved it is possible to study more than one orientation of the defect to the applied field at once. Orbach and Simanek (1966) suggested that the admixture of excited configurations into the ground configuration, of an ion, by a dynamic phonon-induced non cubic field should produce a temperature dependent contribution to the hyperfine coupling. By assuming a Debye spectrum for the lattice phonons they were able to successfully explain the observed dependence for Mn^{2+} in MgO

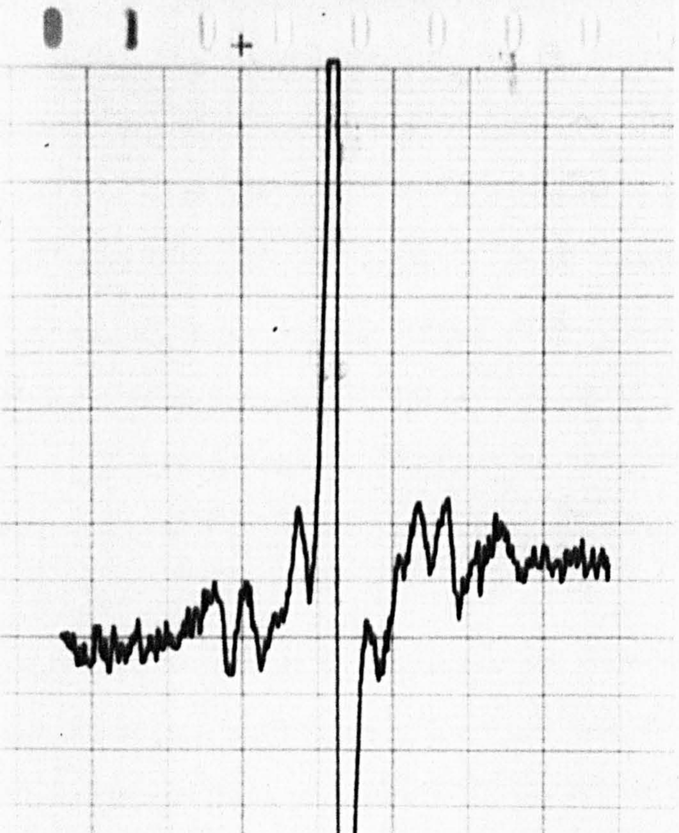

FIGURE 5.12

(Simanek and Huang 1966) and CaO (Rosenthal et al. 1967). The theory breaks down however for Mn^{2+} in SrO (Rosenthal et al. 1967) and in BaO (Zdansky) and Zdansky postulates that the discrepancy in ionic size between impurity and host ion leads to a reduction of the coupling between the impurity and the lattice and the dominance of local modes of vibration over the Debye spectrum of lattice phonons. Unfortunately the implications of an off centre site for the Mn^{2+} ion were realised at a rather late stage in this work and have not yet been investigated.

5.10 Gd^{3+} Spectrum

The spectrum of Gd^{3+} was observed in all the crystals of BaO, both coloured and transparent, that were investigated at X band. This spectrum has been reported previously by Mann and Holroyd (1968) who studied it at 77°, 4° and 2°K and were able to observe both the hyperfine structure and the seven component fine structure. The work reported here was conducted at room and liquid nitrogen temperatures and only the central $+\frac{1}{2}$ to $-\frac{1}{2}$ fine structure line was observed. However it was possible to conclusively identify the spectrum on the basis of the agreement of its g value with that reported by Mann and Holroyd and from the hyperfine splittings. Figure 5.12 shows the spectrum recorded at 77°K. The central line arises from the four even isotopes of Gd which have zero nuclear spin and a total relative abundance of 70%. The two odd isotopes however, Gd^{155} and Gd^{157} with relative abundances of 14.7% and 15.6% respectively, both have a nuclear spin of $^3/_2$ and, since they have slightly different magnetic moments, give rise to two sets of four lines symmetrically

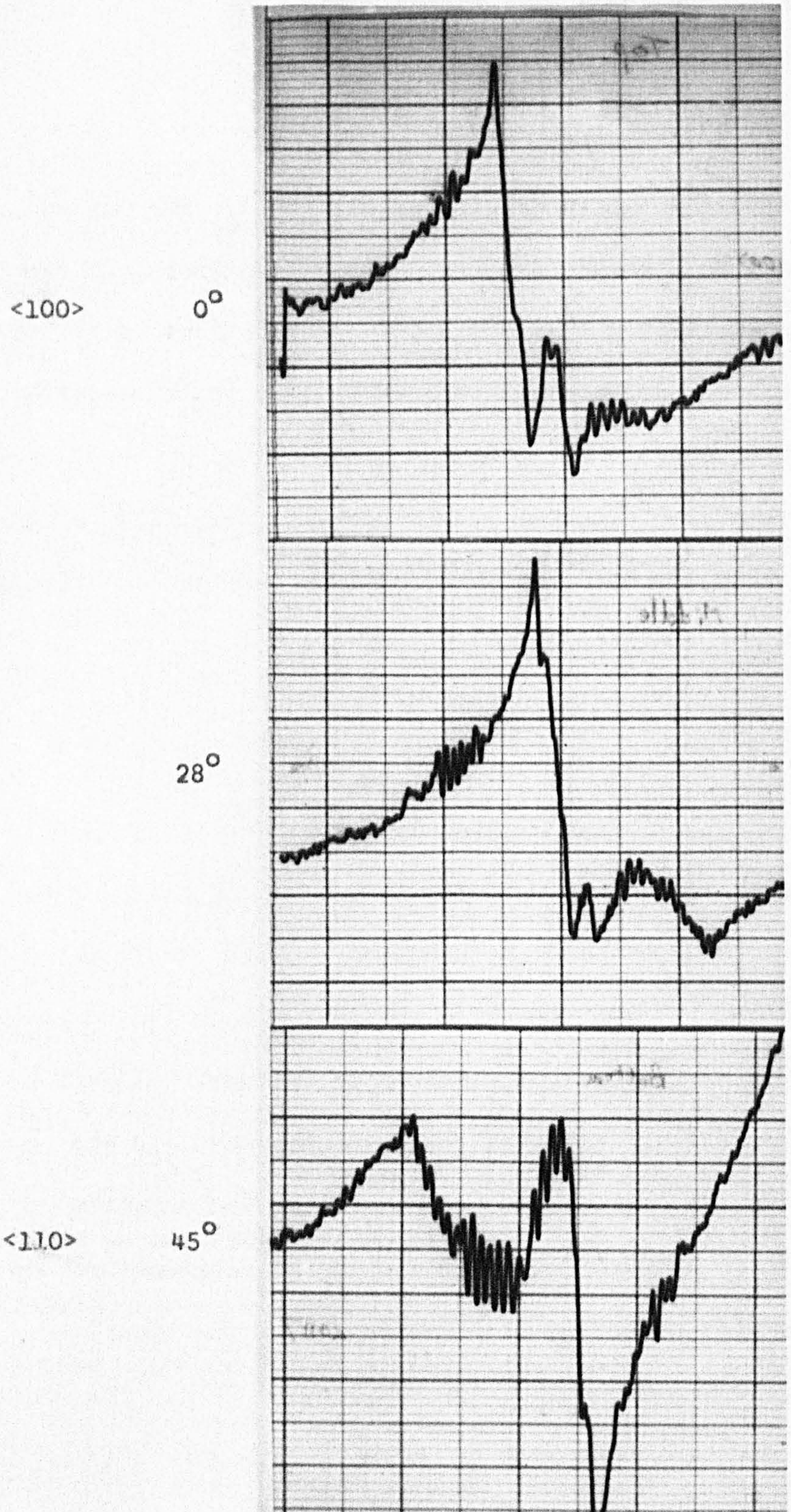

FIGURE 5.13

disposed about the central line as shown in the figure. It was not possible to resolve the inner pair of peaks but the hyperfine parameters for the two nuclei could be accurately determined from the separations of the outer components. The hamiltonian parameters determined for this spectrum are given below and compared with those of Mann and Holroyd:

This work	Mann and Holroyd
$g = 1.99165 \pm 0.00005$	1.9918 ± 0.0002
$A_{155} = 4.65 \pm 0.3 \times 10^{-4}\text{cms}^{-1}$	$4.80 \pm 0.2 \times 10^{-4}\text{cms}^{-1}$
$A_{157} = 3.51 \pm 0.3 \times 10^{-4}\text{cms}^{-1}$	$3.65 \pm 0.2 \times 10^{-4}\text{cms}^{-1}$

5.11 Unidentified Spectra in BaO

An interesting feature observed at X band was a very broad spectrum which was found to be unique to blue crystals. The spectrum is shown in Figure 5.13 for three orientations in the <100> plane and it consists of two components with a peak-to-peak width of some six hundred gauss centred at $g = 2.0$ and accompanied by a much broader line to low field. This spectrum was anisotropic, the two central lines being coincident when H is along <110> and having a maximum separation along <100> directions. These lines disappeared at X band at liquid nitrogen temperatures and were hardly noticeable at Q band at room temperature. That the spectrum is unique to blue crystals is intriguing and it is tempting to associate it with the Ba^{2+} excess that blue colouration implies. However a more thorough study is required before any conclusions can be made. The previously described Mn^{2+} spectrum may be seen in the figure, superimposed on this line and it is immediately apparent how the broad line interfered with the observation of the Mn^{2+} spectrum.

Besides the spectra so far described a single isotropic line was observed at X band in several crystals. The line was some forty gauss wide and had a g value of 2.0054 ± .00005. As the line had no satellites or associated fine structure, it was impossible to identify it. No spectrum with a similar g value has been reported in BaO (Henderson and Wertz 1968).

It was expected that the method adopted in growing these crystals (section 4.12) would result in the formation of F^+ centres, single electrons trapped at oxygen vacancies. The F^+ spectrum was absent from all crystals observed however and this led to suggestions that the predominant vacancy centre was the diamagnetic F centre with two trapped electrons. Accordingly, attempts were made to observe the excited state resonance of these defects by irradiating with ultra-violet light and populating the excited triplet state (Henderson and Wertz 1968). No excited resonances were observed however, probably due to a combination of a small concentration of F centres, too short relaxation times for the excited state and insufficient illumination.

References

Beyer, R.S. and Sproull, R.L., Phys. Rev. 83, 801 (1951).

Bleaney, B., Phil. Mag. 42, 441 (1951).

Bleaney, B. and Rubins, R.S., Proc. Phys. Soc. 77, 103 (1961).

Bogardus, H. and Sack, H.S., Bull. Am. Phys. Soc. 11, 229 (1966).

Byer, N.S. and Sack, H.S., Phys. Rev. Lett. 17, 72 (1966).

Carson, J.N., Holcombe, D.F. and Ruchardt, H., J. Phys. Chem. Solids 12, 66 (1959).

Dienes, G.J., Hatcher, R.D., Smoluchowski, R. and Wilson, W., Phys. Rev. Lett. 16, 25 (1966).

Dowsing, R.D., Department of Computer Science, University of Swansea, Private Communication.

Dowsing, R.D. and Ingram, D.J.E., J. Mag. Res. 1, 517 (1969).

Henderson, B. and Wertz, J.E., Adv. in Phys. 17 No. 70, 749 (1968).

Lombardo, G. and Pohl, R.O., Phys. Rev. Lett. 15, 291 (1965).

Low, W., Solid State Physics Supplement 2, (Academic Press) 1960.

Mann, K.E., Holroyd, L.V. and Cowan, D.L., 'F Centres in BaO' Private Communication (1969).

Mann, K.E. and Holroyd, L.V., Phys. Stat. Sol. 28, K27 (1968).

Mathew, J.A.D., S.S. Comm. 3, 365 (1965).

Orbach, R. and Simanek, E., Phys. Rev. 145, 191 (1966).

Quigley, R.J. and Das, T.P., Phys. Rev. 164, 1185 (1967).

Rosenthal, J., Yarmus, L. and Bartram, R.H., Phys. Rev. 153, 407 (1967).

Rutherford, D.E., "Classical Mechanics" p.150 (Oliver and Boyd) 1960.

Sack, H.S. add Moriarity, M.C., S.S. Comm. 3, 93 (1965).

Simanek, E. and Huang, N.L., Phys. Rev. Lett. 17, 699 (1960).

Smoluchowski, R., Proc. XVth Colloque Ampere, Grenoble (1968); (North-Holland Publishing Company, Amsterdam-London) 1969.

Swalen, J.D. and Gladney, H.M., I.B.M. Journal of Research and Development, p. 515 (November 1964).

Tessman, J.R., Kahn, A.H. and Shockley, W., Phys. Rev. 92, 890 (1953).

Watkins, G.D., Phys. Rev. 113, 79 (1959).

Wilson, W.D., Hatcher, R.D., Dienes, G.J. and Smoluchowski, R., Phys. Rev. 161, 888 (1967).

Zdansky, K., Phys. Stat. Sol. 28, 181 (1968).

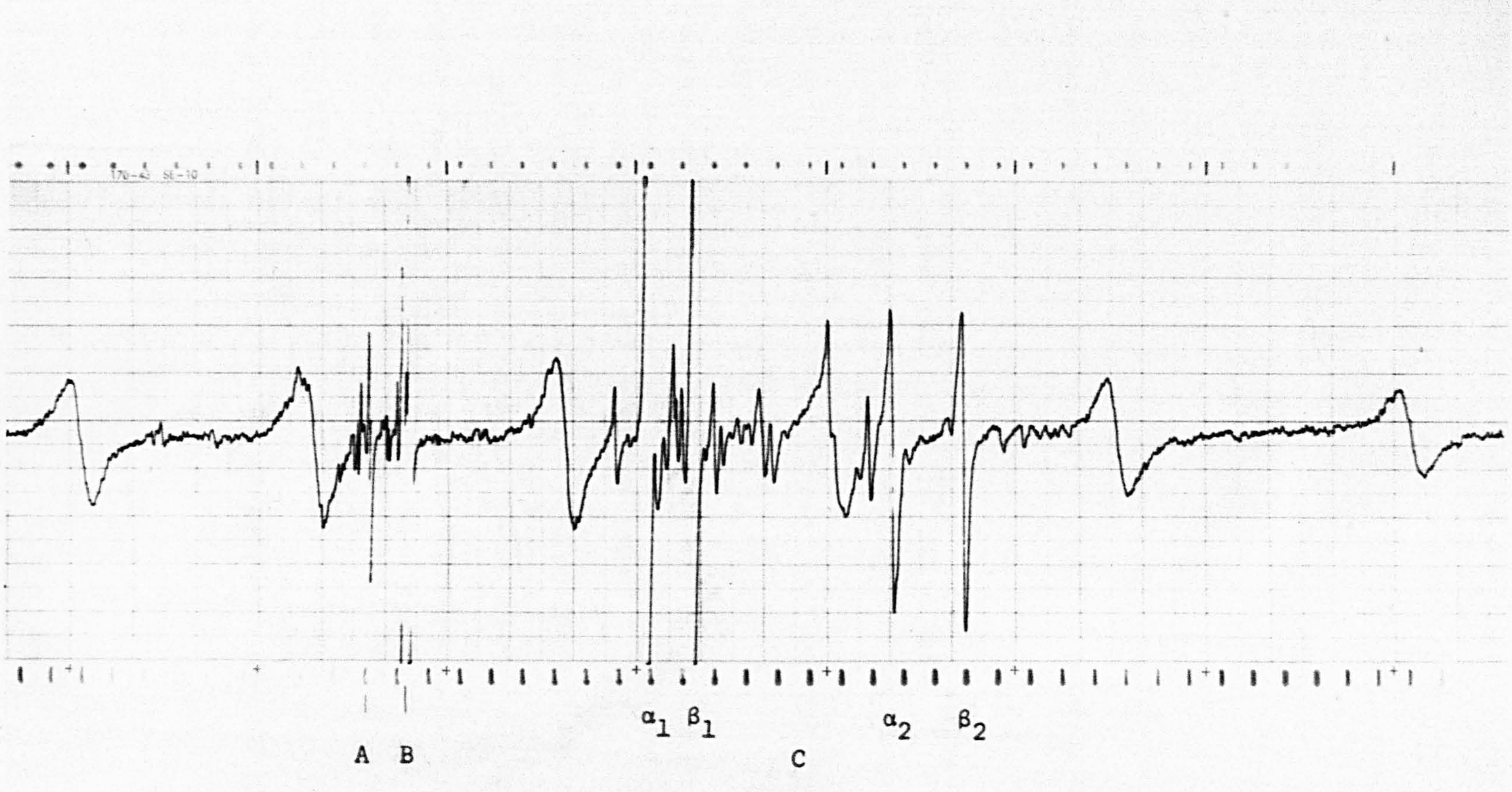

<100>

FIGURE 6.1

CHAPTER VI

E.P.R. INVESTIGATIONS OF CALCIUM TUNGSTATE

Preliminary surveys revealed extensive e.p.r. absorption spectra in both lightly and heavily irradiated crystals of Calcium Tungstate. In addition to other spectra the lightly irradiated crystals exhibited the thirty line Mn^{2+} spectrum reported by Hempstead and Bowers (1960) and a brief study was made of this spectrum in order to verify the assignment of crystalline axes from X-ray diffraction evidence (section 4.2.2). As the overall spectra from both kinds of crystal were very complex, it was decided to select several of the more prominent groups of lines for detailed analysis. The absence of the Mn^{2+} spectrum and the greatly increased intensity of signals in the heavily irradiated crystals made them the most profitable candidates for detailed study and consequently all the damage centre spectra reported here were observed in these crystals. Attempts have been made to locate similar spectra in the lightly damaged crystals but with no success.

6.1 Preliminary Survey

E.P.R. studies of $CaWO_4$ were performed at room, liquid nitrogen and liquid helium temperatures on the Decca and Varian X band spectrometers. Figure 6.1 shows the spectrum observed over a range of two and a half kilo-gauss from heavily irradiated crystals. The spectrum was taken at liquid nitrogen temperature with the magnetic field applied parallel to a

<100> crystal axis. The broad manganese spectrum extending over this region has an effective g value of ~1.76 and is too broad to be observed at room temperature. This spectrum is quite unlike the Mn^{2+} spectrum usually seen in $CaWO_4$ and which was observed in the lightly irradiated crystals and in the boules from which the heavily irradiated crystals were cut before irradiation. Besides the manganese spectrum the absorption consists essentially of a group of lines in the region of 3300 gauss ($g \sim 2.0$) and a more extensive group to higher fields (3800 gauss, $g \sim 1.74$).

Closer examination of the low field group revealed it to be made up of extremely narrow lines and much broader lines. At room temperature the narrow lines were predominant and changed very little upon cooling to liquid nitrogen though they could be more easily saturated at the lower temperature. (1 m.watt as opposed to 20 m.watt at room temperature). The broader lines, however, narrowed considerably and dominated this region at low temperatures. From angular variation studies the narrow lines could be classified as belonging to two quite different sets termed the A spectrum and the B spectrum, the B lines being approximately twice as intense as the A lines.

The high field lines, designated the C spectrum, consist of two broad lines (15 to 20 gauss) and accompanying satellites at room temperature. Cooling to liquid nitrogen and liquid helium temperatures however reveals each broad line to be an envelope of two intense narrow lines with several weaker satellites and many seemingly unrelated lines.

Before describing the detailed investigations of these spectra it will be useful to first consider the implications of the crystal structure of $CaWO_4$ for an e.p.r. investigation.

6.2 Crystal Structure and E.P.R. Spectrum of $CaWO_4$

The four Ca sites in the unit cell, like the four W sites, are equivalent in pairs. The environment of oxygens around one pair of sites is related to the environment around the other pair by a reflection in the <001> plane with the result that the e.p.r. spectra from the two sites will be identical. A naive assumption that the bonding is ionic between units of Ca^{2+} and WO_4^{2-} predicts that the axes of the crystal field in the <001> plane will lie along the <100> type crystalline axes. As the oxygens do not lie along <100> directions, then they will cause the crystal field axes to deviate from these directions by an amount commensurate with the extent to which the negative charge cloud of WO_4^{2-} is localised upon them. An example of this may be seen in the spectra of Gd^{3+} and Mn^{2+}, substituted at Ca^{2+} sites, where the magnetic axes of both impurities in this plane lie at 9° to the <100> directions (Hempstead and Bowers 1960).

For a paramagnetic species without any special symmetry, such as an interstitial ion, there will be four sites in the structure related by four fold rotations around the c axis and four more obtained from these by a reflection in the <001> plane. In an e.p.r. experiment these sites will be equivalent in pairs and each species will thus contribute four sets of absorption lines. In the ab plane these sets of lines will be merged in pairs and along the c axis the spectrum will collapse to a single set of lines.

The presence of the screw axis assigns a direction to the crystalline c axis and unless this direction is known for the crystal under investigation then there will be ambiguity in relating the g tensor

E.P.R. AND THE SYMMETRY OF $CaWO_4$

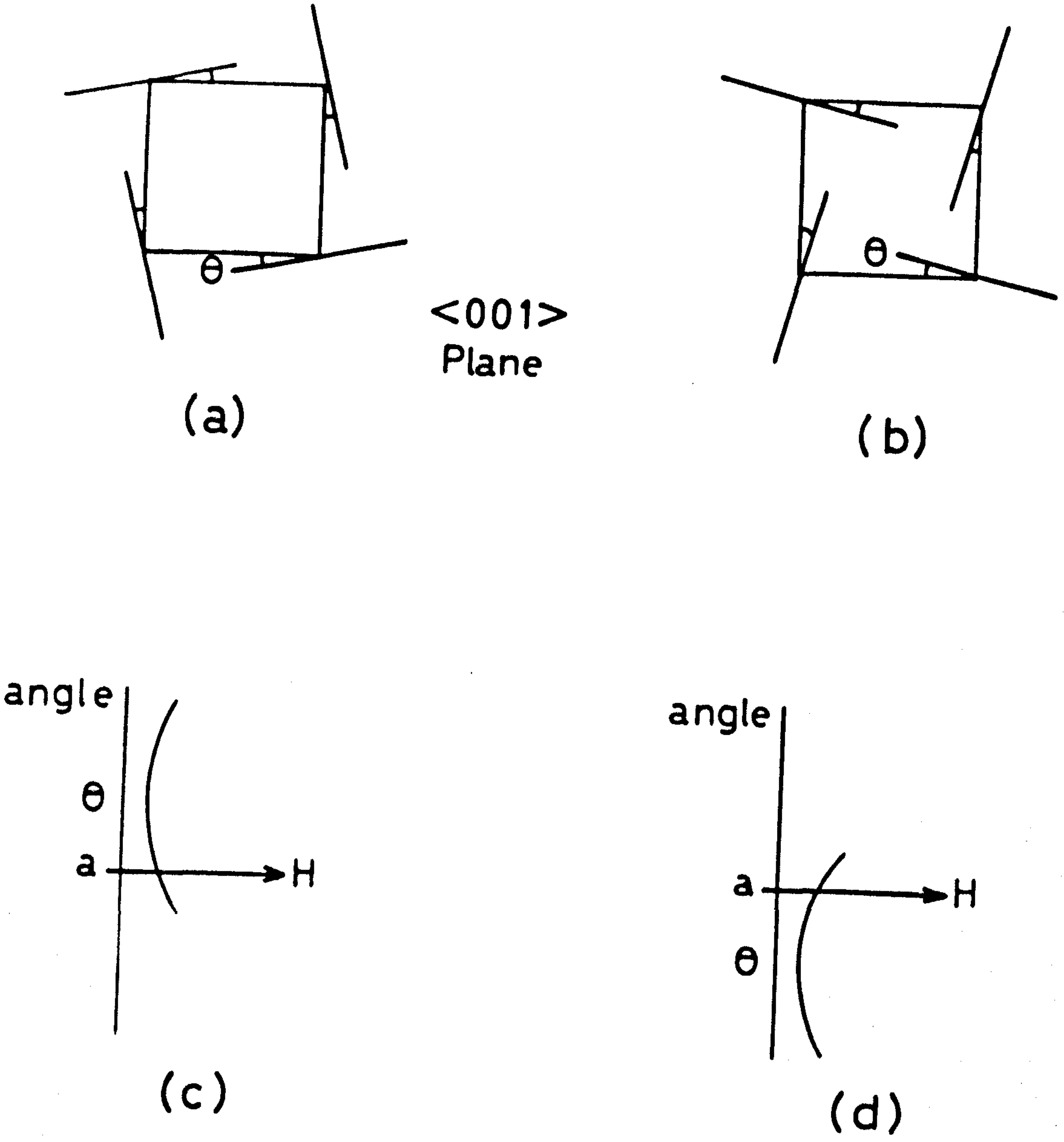

FIGURE 6·2

axes to the actual positions of atoms in the structure. How this ambiguity arises may be seen from the following example. Suppose experimentally it is found that a particular spectrum has a g tensor axis, say g_x, at an angle θ to a <100> crystal axis in the <001> plane. There are two possible ways of relating this g tensor to the crystal structure as illustrated in Figure 6.2a and b where the centre of the g tensor is assumed to be located at a W site and the diagrams depict the <001> plane of the unit cell. The angular variations of the spectra expected from these two assignments are shown in Figure 6.2c and d and of course differ only in phase. However unless the direction of the c axis of the crystal is known, it is impossible from determining the phase of the e.p.r. spectrum to unambiguously deduce the relationship between g_x and the atomic positions. This may be seen by putting $\theta = 31^\circ$ where, if the c axis is positive out of the paper in the diagrams, g_x in 6.2a will coincide with the projection of the W-O bonds onto the <001> plane and 6.2b will place g_x at 62° to these projections.

6.3 Mn^{2+} Spectrum

This spectrum has been reported previously by Hempstead and Bowers (1960) and was briefly studied in this work in order to check the assignment of crystal axes. The spectrum may be described by the spin hamiltonian of (2.16) with D, a and F fine structure terms and A and B hyperfine terms. No E term is required and the spectrum has two g values $g_{||}$ and $g_{\perp}$ determined by Hempstead and Bowers to lie along the c axis and at 9° to an a axis in the (001) plane, respectively. These authors write the spin hamiltonian as

$$\mathcal{H} = B_2^{\,0}\, O_2^{\,0} + B_4^{\,0}\, O_4^{\,0} + B_4^{\,4}\, O_4^{\,4} \qquad (6.1)$$

where the $O_n^{\,m}$ are the operators of Baker et al. (1958) and express their results in terms of $b_2^{\,0}$, $b_4^{\,0}$ and $b_4^{\,4}$. The relationship between the various systems of parameters is as follows:-

$$b_2^{\,0} = D = 3\,B_2^{\,0}$$
$$b_4^{\,0} = \frac{a}{2} + \frac{F}{3} = 60\,B_4^{\,0}$$
$$b_4^{\,4} = \frac{5a}{2} = 60\,B_4^{\,4}$$

For consistency the results presented here will be expressed in the $b_2^{\,0}$, $b_4^{\,0}$, $b_4^{\,4}$ system. As the parameters of the hamiltonian had been accurately determined by Hempstead and Bowers it was thought unnecessary to use the proton resonance units and field measurements were made with the Varian Mark I Fieldial. This procedure is justifiable since it was only desired to determine the axes of the spectrum and although the Fieldial was found to be imprecise as a determinant of absolute field positions, it was quite adequate as a measure of the separations between components.

The axes of a large well cut crystal were determined by X ray diffraction as described and the crystal was mounted in what, on the basis of this assignment, was considered to be an ac plane. E.P.R. spectra were then taken with the applied field parallel to the a and c axes. Following Hempstead and Bowers the fields at which transitions occur along these two directions are given by:-

c axis

$\theta = 0^\circ$

$$M_S = \pm 5/2 \leftrightarrow \pm 3/2 \qquad g_{\parallel}\beta H = h\nu \mp \left[4b_2{}^0 + 4b_4{}^0\right] - \left[Am + B^2(35 - 4m^2 \pm 16m)/8h\nu\right]$$

$$M_S = \pm 3/2 \leftrightarrow \pm \tfrac{1}{2} \qquad g_{\parallel}\beta H = h\nu \mp \left[2b_2{}^0 - 5b_4{}^0\right] - \left[Am + B^2(35 - 4m^2 \pm 8m)/8h\nu\right] \tag{6.2}$$

$$M_S = +\tfrac{1}{2} \leftrightarrow -\tfrac{1}{2} \qquad g_{\parallel}\beta H = h\nu - \left[Am + B^2(35 - 4m^2)/8h\nu\right]$$

a axis

$\theta = \pi/2^\circ \quad \phi = \pm 9^\circ$

$$M_S = \pm {}^5{}_2 \leftrightarrow +3/2 \qquad g_{\perp}\beta H = h\nu \mp \tfrac{1}{2}\left[-4b_2{}^0 + 3b_4{}^0 + b_4{}^4 \cos 4\phi\right] + \frac{(b_2{}^0)^2}{h\nu} - \left[Bm + (A^2 + B^2)(35 - 4m^2)/16h\nu \pm 2AB_m/h\nu\right]$$

$$M_S = \pm 3/2 \leftrightarrow \pm \tfrac{1}{2} \qquad g_{\perp}\beta H = h\nu \mp \frac{1}{8}\left[-8b_2{}^0 - 15b_4{}^0 - 5b_4{}^4 \cos 4\phi\right] - \frac{5}{4}\,\frac{(b_2{}^0)^2}{h\nu} - \left[Bm + (A^2 + B^2)(35 - 4m^2)/16h\nu \pm AB_m/h\nu\right] \tag{6.3}$$

$$M_S = +\tfrac{1}{2} \leftrightarrow -\tfrac{1}{2} \qquad g_{\perp}\beta H = h\nu - \frac{2(b_2{}^0)^2}{h\nu} - \left[Bm + (A^2 + B^2)(35 - 4m^2)/16h\nu\right]$$

TABLE 6.1

M_n^{2+}:CaWO$_4$

HAMILTONIAN PARAMETERS

	This Work	Hempstead and Bowers (1960)
	Room Temperature	77°K
$g_{\|\|}$	2.0016 ± 0.005	1.99987 ± 0.0001
$g_{\|}$	2.0177 ± 0.005	1.99980 ± 0.0002
b_2^0	$-129.0 \pm 5.0 \times 10^{-4}\text{cms}^{-1}$	$-137.6 \pm 0.3 \times 10^{-4}\text{cms}^{-1}$
b_4^0	$-3.3 \pm 5.0 \times 10^{-4}\text{cms}^{-1}$	$-1.2 \pm 0.3 \times 10^{-4}\text{cms}^{-1}$
b_4^4	$-11.5 \pm 5.0 \times 10^{-4}\text{cms}^{-1}$	$-11.5 \pm 0.3 \times 10^{-4}\text{cms}^{-1}$
A	$-85.8 \pm 2.0 \times 10^{-4}\text{cms}^{-1}$	$-88.9 \pm 0.1 \times 10^{-4}\text{cms}^{-1}$
B	$-85.0 \pm 2.0 \times 10^{-4}\text{cms}^{-1}$	$-89.5 \pm 0.1 \times 10^{-4}\text{cms}^{-1}$

It was possible to fit the spectrum to these relationships and the parameters found for the hamiltonian are shown in Table 6.1. The discrepancy in g values between this work and that of Hempstead and Bowers is explicable in terms of the imprecision of the Fieldial. There is a slight but acceptable difference in the values found for the hyperfine parameters and reasonably good agreement in the determinations of the fine structure terms. More importantly there is complete agreement in the relative signs of b_2^0, b_4^0 and b_4^4; these have all been shown negative in order to be consistent with the low temperature determination of the absolute sign of b_2^0 by Hempstead and Bowers. The relative sign of b_4^4 is in fact indeterminate as the spectrum exhibits extremes at 9° and 54° from an a axis in the <001> plane. However by assigning $\phi = 0^\circ$ to the extreme at 9° from the a axis Hempstead and Bowers determined b_4^4 to have the same sign as b_2^0 and b_4^0. In the work reported here 4ϕ was assumed to be 36° as would be appropriate in this assignment for spectra recorded along an a axis. Since the actual determination of b_4^4 depends of course on the accuracy of b_2^0 and b_4^0 and on sizeable second order effects, the exact agreement between the value found here and that of Hempstead and Bowers is perhaps best regarded as rather fortuitous.

It can be safely concluded that to well within the margin of error the signs of the fine structure parameters found for this spectrum are consistent with the assignment of crystal axes. Once the validity of the X ray technique was firmly established, it was used to determine the axes directions of crystals not exhibiting the Mn^{2+} spectrum.

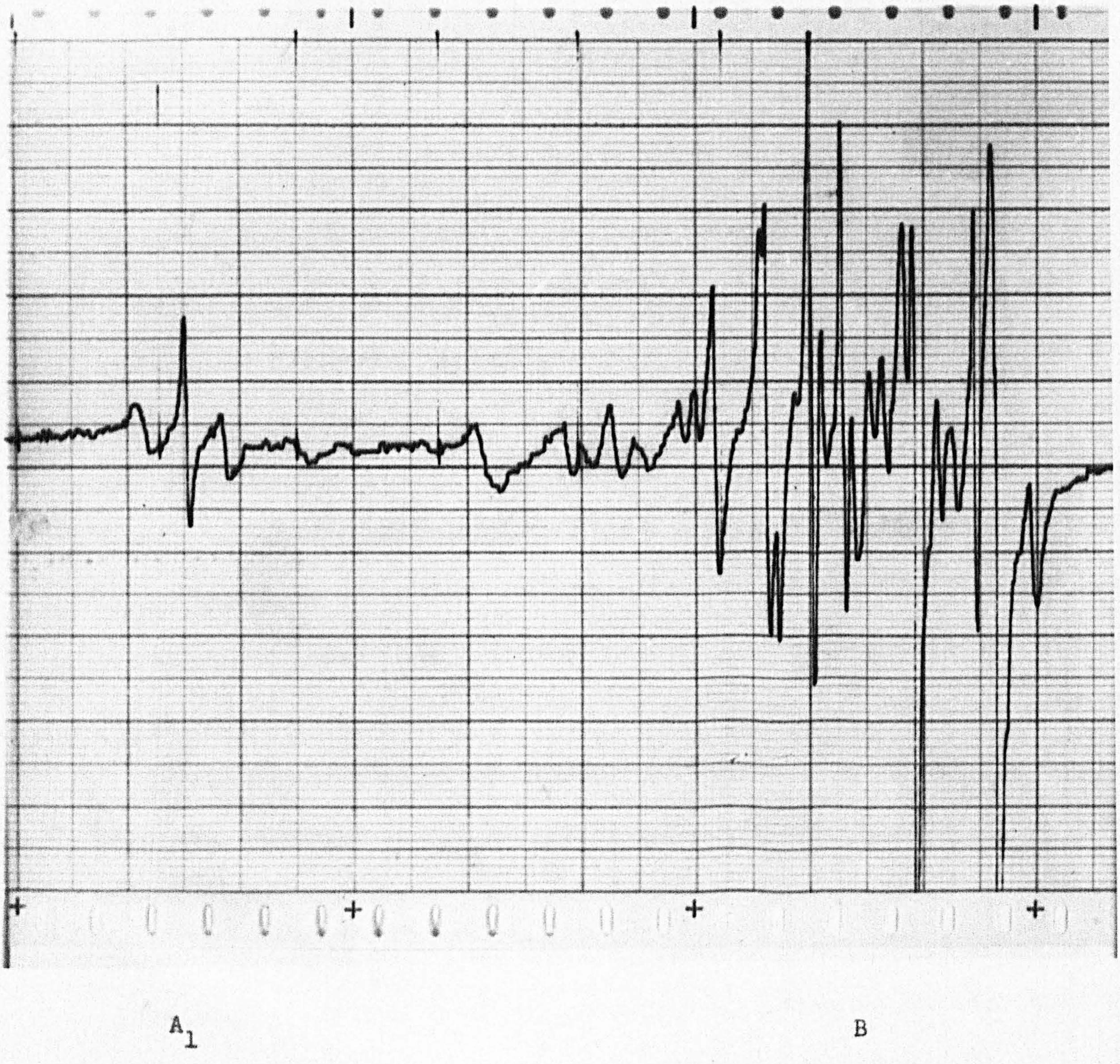

FIGURE 6.3

6.4 The A Spectrum

The A spectrum consists of four very narrow lines (600 mgauss) designated A_1 A_2 A_3 and A_4, each of which is accompanied by two broader and smaller satellites. The lines have g values slightly greater than 2.0 and show an anisotropy of some seventy to a hundred gauss. Figure 6.3 shows a typical spectrum observed at room temperature, only one of the groups of three can be clearly seen - the other three being obscured by the lines to high field. These latter have been loosely termed the B spectrum and will be discussed in a later section. The satellite lines are considered to be fine structure and the four component spectrum is attributed to an $S = {}^3\!/_2$ centre which can be located at four inequivalent sites in the structure as previously described. The broader line widths of the outer components of each group is consistent with this assignment when one considers that the width of resonance lines in $CaWO_4$ is usually attributed to statistical fluctuations in the local crystal field, produced by strain gradients, and that transitions associated with larger quantum numbers are more dependent on the crystal field. A similar effect was observed in the fine structure components of the Mn^{2+} spectrum.

The A spectrum showed two unusual features. Firstly though the anisotropy of the centre of each group of lines, the g tensor anisotropy, was small it was still substantially greater than the fine structure splitting. This is in marked contrast with the discussion of the spectra expected from transition metal ions (section 2.2) where it was suggested that Δg is derived from and will be less than D, the splitting of the spin states by the crystal field. Secondly, the fine structure splittings showed no relation to the axes of the g tensor and it is now known that the two tensors are not in fact coincident.

Several practical difficulties were experienced in the detailed investigation of this spectrum, the major one being the multitude of broader lines in this region which became confused with and obscured the outer fine structure components. This problem was so pronounced that it was some time before these lines were even noticed. The presence of the more intense and complex B spectrum also presented problems since for many orientations it obscured the A groups. Cooling to liquid nitrogen temperatures made the situation worse, since the background signals increased considerably in intensity relative to the A spectrum. Consequently all measurements reported here on this spectrum are taken from data obtained at room temperature. It was found that a modulation amplitude of 0.4 gauss whilst broadening the central lines provided the optimum ratio of the fine structure lines to the background signals.

The first priority was to determine the axes and principal values of the g tensor and to do this, advantage was taken of the result from the perturbation theory treatment (Bleaney 1951, Low 1960) that to first order the positions of the lines from an $S = 3/2$ centre will be given by:-

$$H_{M_S} = H_o - \frac{(M_S - \frac{1}{2})}{g\beta}\left[D\left(\frac{3g_{\parallel}^2\cos^2\theta}{g^2} - 1\right) - 3E\left(\frac{g_{\parallel}^2\cos^2\theta}{g^2} - 1\right)\cos 2\phi\right] \quad (6.4)$$

Thus the position of the central line corresponding to $M_S = +\frac{1}{2}$ will be independent of D to this order of magnitude and may be expressed

(a) <110>

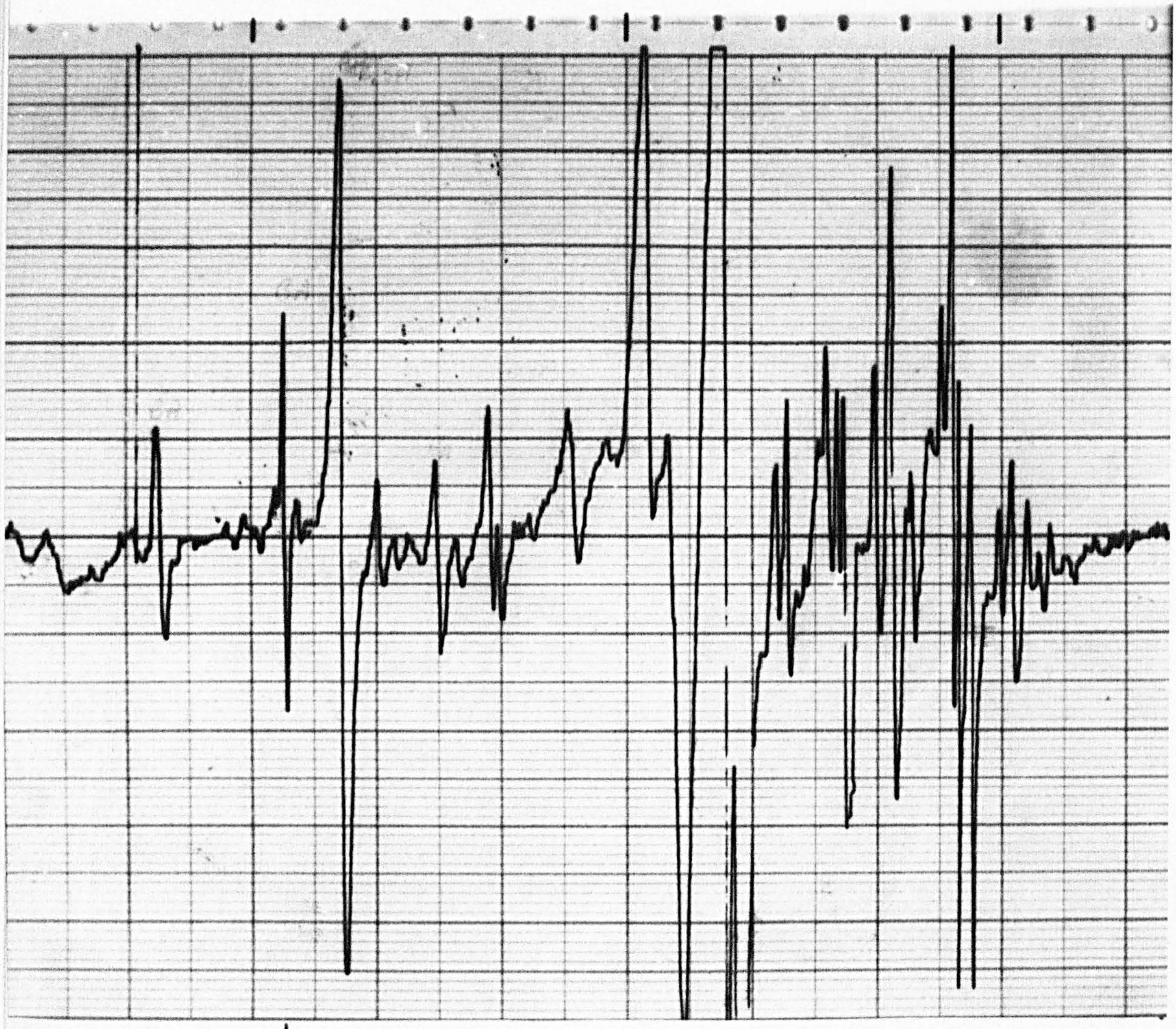

(b) 1° from <110>

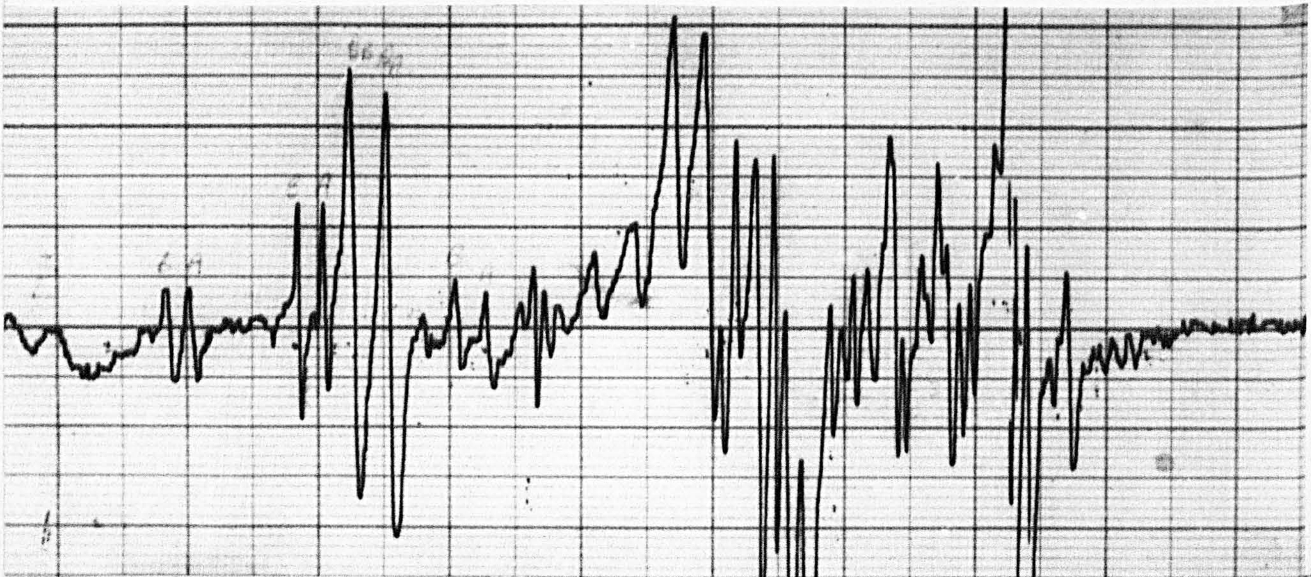

FIGURE 6.4

$$H_{+\frac{1}{2}} = \frac{h\nu}{g\beta}$$

the g tensor being given by

$$g^2 = g_z^2\cos^2\theta + g_y^2\sin^2\theta\sin^2\phi + g_x^2\sin^2\theta\cos^2\phi$$

6.4.1 Determination of the g tensor

Since the central lines of this spectrum are so narrow they provide a very accurate measure of how well the crystal is aligned in the spectrometer. To perform angular variation studies of this spectrum the two circle goniometer described in section 3.5 was constructed and with its use it was possible to demonstrate that the central lines from the four sites collapsed to a single line along the c axis and to a pair of lines for directions in the ab plane as required by the symmetry of the structure. It was much more difficult however to align a crystal such that the rotation of the magnetic field was confined to a particular crystal plane. Figure 6.4a shows a spectrum taken at liquid nitrogen temperature with the applied field parallel to a <110> direction. The lines from two sites, A_1 and A_2, are coincident in this direction as shown. However a rotation of 1° from this direction out of the ab plane splits these lines by two gauss (4 linewidths) as shown in Figure 6.4b. It may be noted that the other lines in this region show a similar sensitivity to orientation.

In an early attempt to resolve the nature of this spectrum the magnetic field was rotated in a plane at right angles to the direction of a W-O bond. This orientation was achieved by mounting the crystal on a teflon wedge machined to an angle of 33° and aligned at 31° to an a axis in the <001> plane. Provided that the direction of the c axis has been correctly assigned this arrangement results in the W-O bond direction being parallel to the axis of the wedge which can then be mounted vertically in the cavity. If the centre had been associated with a W-O bond then one component would have been invariant in this plane (provided of course the spectrum is axial) and the other three related by phase differences of 120°. The results of this experiment though inconclusive were very useful in eliminating ambiguities in subsequent interpretations of the spectrum.

To determine the g tensor the method used by Zeldes and Livingston (1961), in which the anisotropy is first expressed relative to the crystal axes, was employed. Several attempts were made to establish the ab and ac planes accurately but misorientations of a few degrees were unavoidable. Consequently measurements were made on all four lines in these planes and errors due to misorientation reduced by averaging their g tensor components. For each line we express the hamiltonian as:-

$$\mathcal{H} = \beta \underline{S}.\underline{g}.\underline{H} \tag{6.5}$$

where $\underline{g}$ is a symmetric tensor of the second rank. The effective g values of the four lines, determined from $g\beta H = h\nu$, were recorded as a function of angle in the ab and ac planes. The effective g value is related to the tensor of (6.5) by

$$g = (\underline{h}.\underline{g}.\underline{g}.\underline{h})^{\frac{1}{2}} \tag{6.6}$$

where $\underline{h}$ is a unit vector parallel to the applied field. Expressing $\underline{h}$ in the direction cosines of $\underline{H}$ with respect to the a,b,c crystal axes we have

ANGULAR VARIATION OF THE A SPECTRUM IN THE ab PLANE

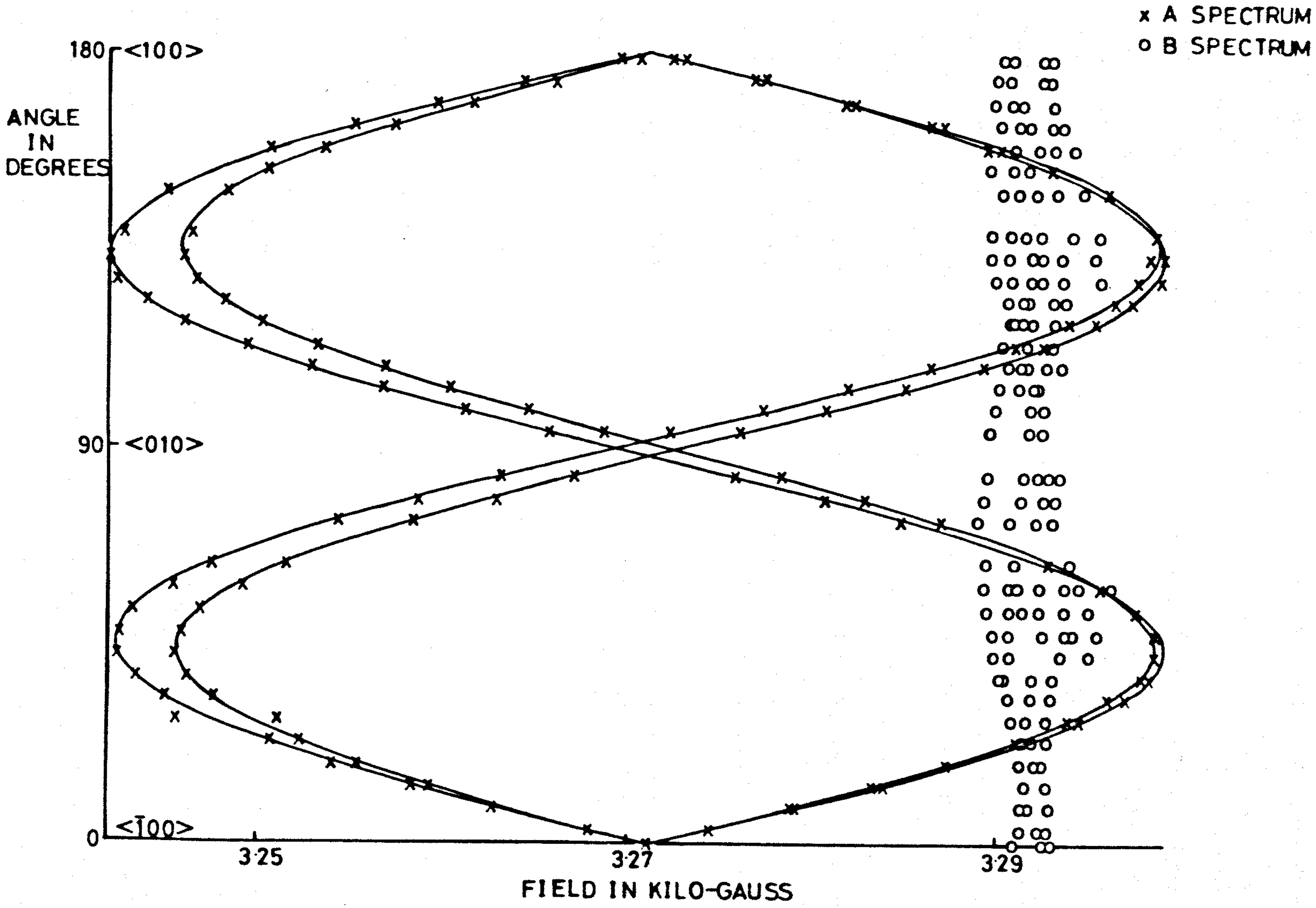

FIGURE 6·5

$$g^2 = G_{aa}h_a^2 + G_{bb}h_b^2 + G_{cc}h_c^2 + 2G_{ab}h_a h_b + 2G_{ac}h_a h_c + 2G_{bc}h_b h_c \quad (6.7)$$

and the nine G_{ij} will be the components of the symmetric tensor

$$\underline{G} = \underline{g}\cdot\underline{g} \quad (6.8)$$

If one line is expressed as in (6.7) the expressions for the other three lines may be generated from (6.7) by fourfold rotations of the tensor about the c axis.

In the ac plane (6.7) reduces to

$$g^2 = G_{aa}\cos^2\alpha + G_{cc}\sin^2\alpha + G_{ac}\sin 2\alpha$$

where α is the angle between $\underline{H}$ and the a axis. The expression in the ab plane is similar with the c components replaced by the b's. A least squares fit procedure was used to determine the values of G_{ij} giving the best fit between the effective g values of the lines and orientation in these two planes. Figure 6.5 shows the fit achieved in the ab plane. The values of G_{aa} determined from the two planes were in agreement to better than 0.03%. Misorientation produced the following differences in the absolute values found for the G_{ij} of the four lines:

G_{aa} ± 0.25%	G_{ab} ± 6%
G_{bb} ± 0.25%	G_{ac} ± 20%
G_{cc} ± 0.25%	G_{bc} ± 20%

Though the G_{ac} and G_{bc} cross terms were fifty times smaller than the diagonal terms, they are of course important in that they govern the extent to which the principal axes of the tensor deviate from the c axis.

TABLE 6.2

HAMILTONIAN PARAMETERS FOR THE A CENTRE

(a) G Tensor Parameters

GAA	4.1
GBB	4.1
GCC	4.05
GAB	+0.07
GAC	+0.05
GBC	+0.05

(b) g Tensor

Principal values	Direction cosines a	b	c
$g_z = 2.048 \pm .005$	0.6417	0.6417	0.4201
$g_y = 2.007 \pm .005$	-0.7071	0.7071	0.0000
$g_x = 2.004 \pm .005$	-0.2971	-0.2971	0.9075

MOUNTING OF CaWO FOR GENERAL ORIENTATION

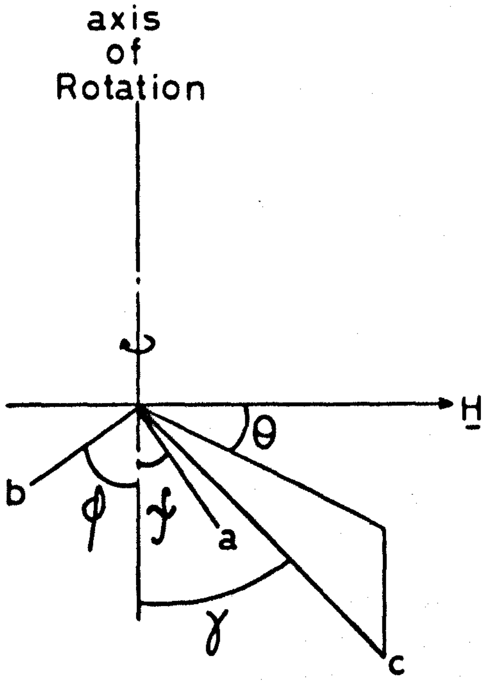

FIGURE 6·6

Owing to the difficulty of correlating lines in the two planes it was not possible to establish the sign of the G_{ab} cross term relative to the signs of G_{ac} and G_{bc} for the four lines. To resolve these problems the average of the absolute values of the G_{ac} and G_{bc} was taken and it was decided to check this procedure and explore the sign correlations of the cross terms by using the data taken in the plane at right angles to a W-O bond direction.

If the crystal is mounted as shown in Figure 6.6, such that the a, b and c axes make angles of ψ, ϕ and γ to the axis of rotation then the angular variation of the spectrum will be given by

$$\begin{aligned} g^2 = {} & G_{aa}\sin^2\psi\cos^2(\theta-\theta_A) + G_{bb}\sin^2\phi\cos^2(\theta+\theta_B) + G_{cc}\sin^2\gamma\cos^2\theta \\ & + 2G_{ab}\sin\psi\sin\phi\cos(\theta-\theta_A)\cos(\theta+\theta_B) + 2G_{ac}\sin\psi\sin\gamma\cos\theta\cos(\theta-\theta_A) \\ & + 2G_{bc}\sin\phi\sin\gamma\cos\theta\cos(\theta+\theta_B) \qquad (6.9) \end{aligned}$$

where $\theta_A = \cos^{-1}(-\frac{1}{\tan\gamma\tan\psi})$, $\theta_B = \cos^{-1}(-\frac{1}{\tan\gamma\tan\phi})$ and θ is the angle that the applied field makes with the projection of c onto this plane of rotation. A small computer programme was written to calculate and plot out the angular variation of all four lines in a plane specified by ϕ, ψ and γ and for values assigned to the G_{ij}. It was then easy to specify $\phi = 44^\circ$, $\psi = 64^\circ$ and $\gamma = 57^\circ$ corresponding to the W-O bond data and deduce, from the eight possible combinations of relative signs, which was the correct one for each particular line. The actual specification was fortunately quite unambiguous and the final parameters for the G_{ij} for one line are listed in Table 6.2a. These gave good agreement with the data from the plane perpendicular to a W-O bond as shown in Figure 6.7.

ANGULAR VARIATION OF THE A SPECTRUM IN A PLANE PERPENDICULAR TO A WO BOND

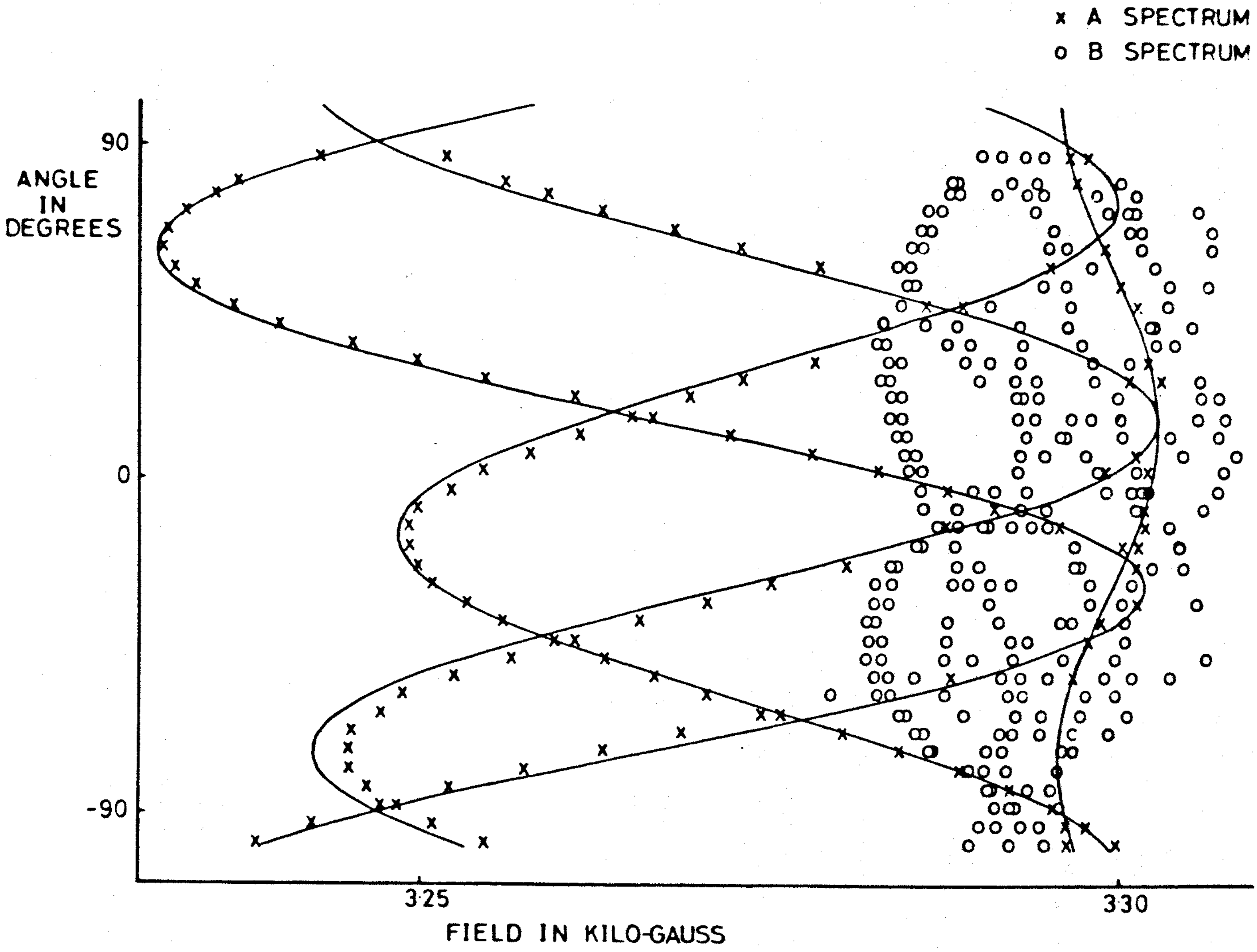

FIGURE 6·7

It was now possible to diagonalise the G_{ij} tensor, the eigenvalues of which are the principal values of the g tensor. The corresponding eigenvectors are the direction cosines of the g tensor axes with respect to the crystal axes. These are shown in Table 6.2b and it can be seen that one of the principal axes is deduced to lie along a <110> direction while the other two are in the <110> plane at 65° and 25° from the c axis respectively. It follows from this assignment that for this spectrum the four sites should also be equivalent in pairs in the ac plane and that the four lines should collapse to a single line along the a axis. This latter prediction was verified with the two circle goniometer; the spectrum is shown in Figure 6.8.

As a final check on the g tensor and to prepare for a study of the fine structure lines, a crystal was mounted on a 45° wedge and an angular variation study performed in a <110> plane. Fine adjustments to the plane of rotation were made by raising the base of the magnet slightly with a jack. Though this sounds a crude procedure it did give fine control of the orientation and besides avoiding backlash effects experienced with with the goniometer, made it possible to use larger crystals and hence achieve greater signal intensity. The <110> plane corresponds to the g_z g_x plane for the A_1 and A_2 sites and from the data taken in this plane (Figure 6.9) it was possible to refine the values for these g values slightly and also to note that the turning points of g_z occurred at 66° to the c axis rather than 65°. Having established the g tensor accurately attention was now turned to the fine structure line.

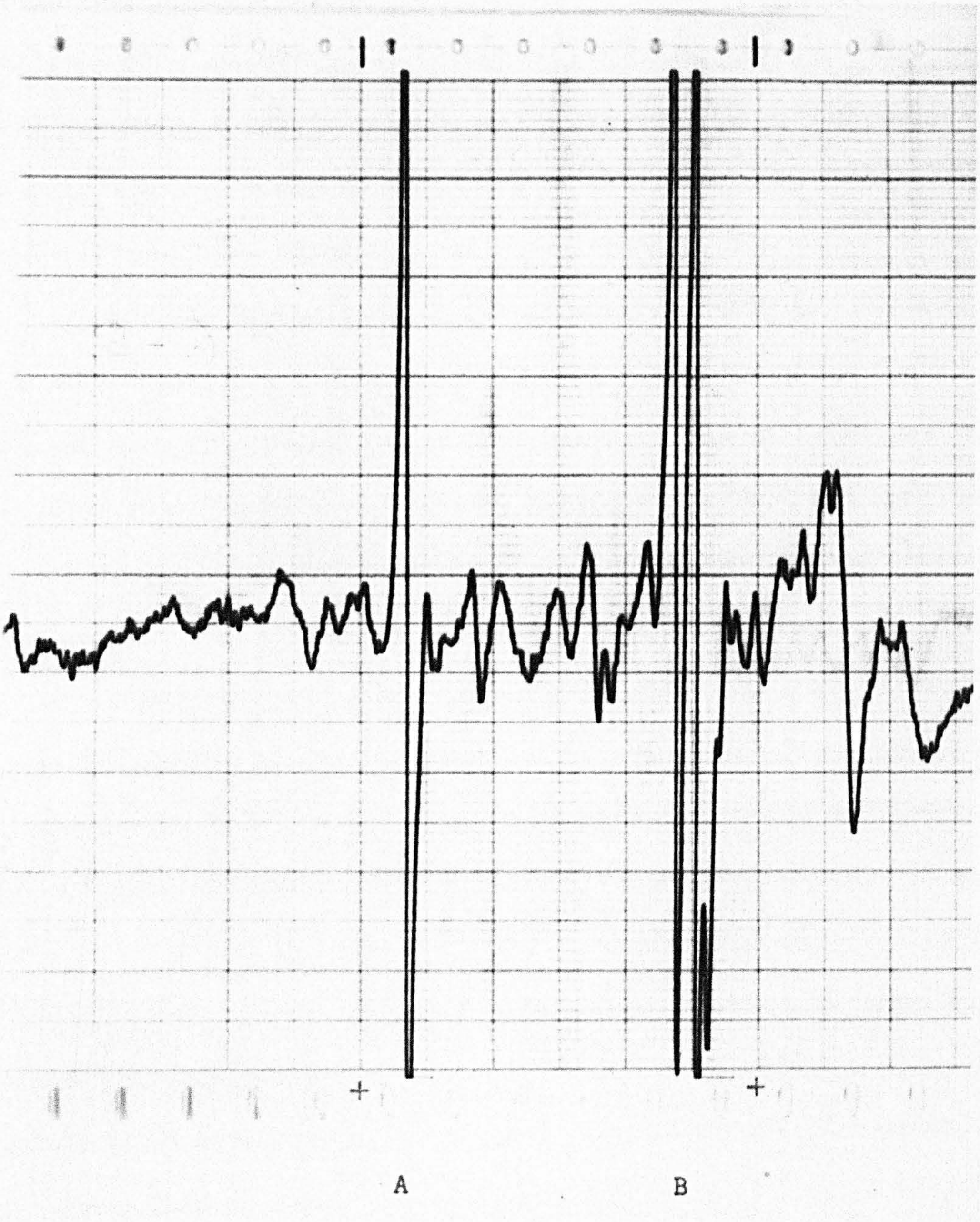

<100>

FIGURE 6.8

ANGULAR VARIATION OF THE A SPECTRUM IN THE <110> PLANE

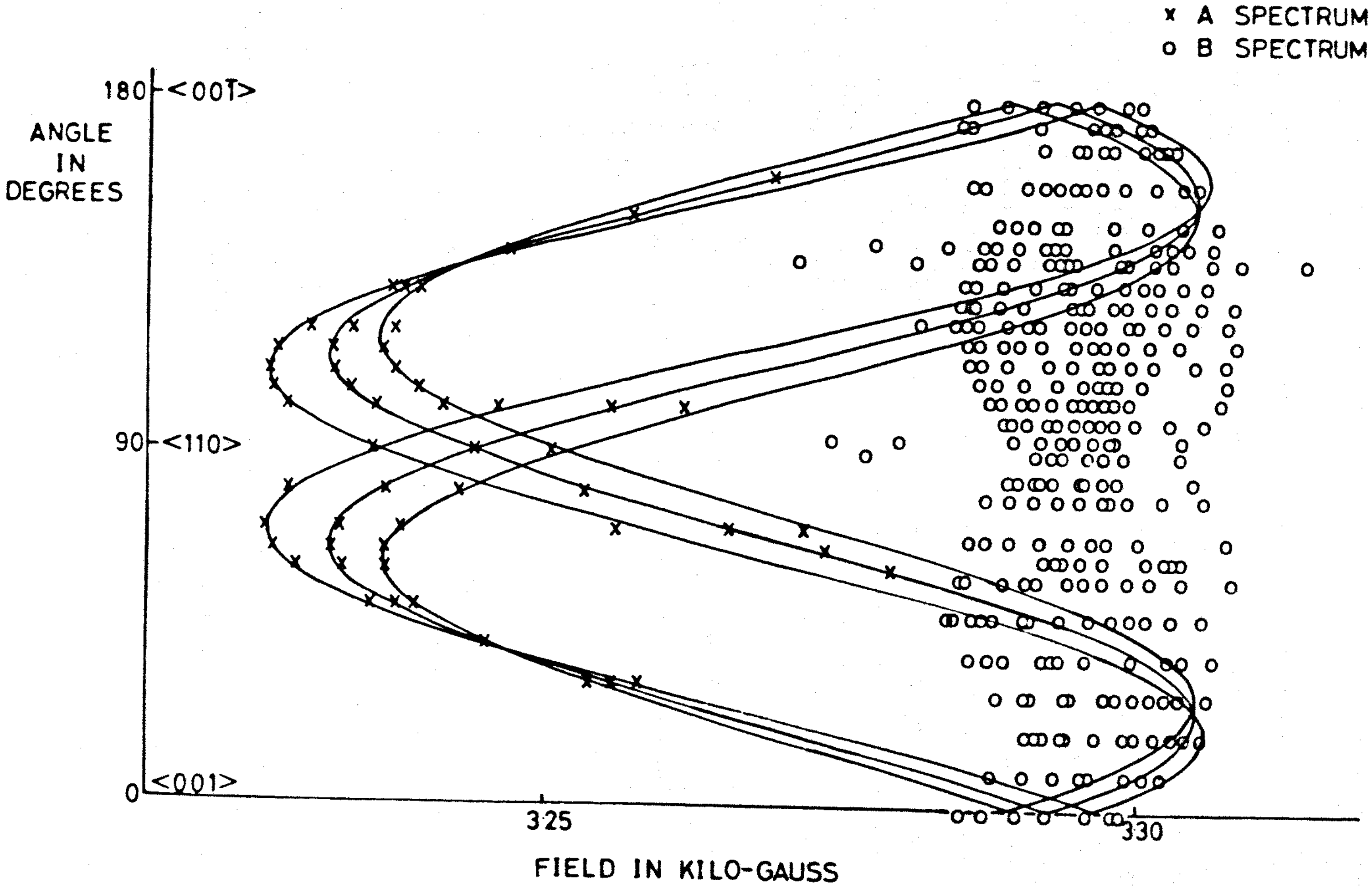

FIGURE 6·9

6.4.2 Determination of the D tensor

The angular variation of two sets of satellite lines can be clearly seen in Figure 6.9. Their origin is not immediately obvious however, since the extrema of their separation bears no resemblance to the turning points of the g tensor. The possibility that they arise from hyperfine interaction with a W^{183} nucleus is remote since, besides being broader than the central line at room temperature, they are not always symmetrically disposed about it. It was thought at first that they might arise from a D tensor which is coincident with g but that for some reason the outer fine structure components are more sensitive to misorientation. Thus slight misorientations might explain the anomaly in separation and also the slightly different turning points observed for each fine structure line in Figure 6.9. Consequently a study was made of the possible changes in angular variation which could be produced by specified misalignments incorporated into the plotting programme by means of the Euler angle formulae. This revealed that for all six ways of relating the D tensor colinearly to the g tensor, the misalignment required to produce the fine structure anomalies observed must be at least 5° and, further, that this misalignment would be indicated by the behaviour of the central lines from different sites. In view of this it was decided to investigate the possibility of the D and g tensor axis systems being non-coincident.

As this problem has not to my knowledge been treated in the literature, a first order perturbation theory derivation of the angular variation expected in this situation is included in Appendix III.

Since the g tensor axes had been well established relative to the crystal axes it was decided to express both the angular variation of $\underline{H}$ in a given crystal plane and the undetermined D tensor in this axis system. $\underline{g}$ will thus be diagonal and $\underline{S}.\underline{D}.\underline{S}.$ may be written as a nine component tensor, the cross terms expressing the rotations of the axes of $\underline{D}$ from the axes of $\underline{g}$. From Appendix III we have for a general orientation of $\underline{H}$ to $\underline{g}$:-

$$\begin{aligned} H_{M_S} = H_o - \frac{(M_S-\frac{1}{2})}{g\beta}\Bigg(& D_{xx}.\frac{3g_x{}^2\sin^2\theta\cos^2\phi}{g^2} + D_{yy}.\frac{3g_y{}^2\sin^2\theta\sin^2\phi}{g^2} \\ & + D_{zz}.\frac{3g_z{}^2\cos^2\theta}{g^2} + D_{xy}.\frac{3g_xg_y\sin2\phi\sin^2\theta}{g^2} \\ & + D_{xz}.\frac{3g_xg_z\sin\phi\sin2\theta}{g^2} + D_{yz}.\frac{3g_yg_z\sin\phi\sin2\theta}{g^2}\Bigg) \qquad (6.10) \end{aligned}$$

where as usual $g^2 = g_z{}^2\cos^2\theta + g_y{}^2\sin^2\theta\sin^2\phi + g_x{}^2\sin^2\theta\cos^2\phi$ and the condition that $\underline{D}$ has zero trace

$$D_{xx} + D_{yy} + D_{zz} = 0 \qquad (6.11)$$

has been included. The first three terms of (6.10) are of course equivalent to the expression for a coincident system (6.4).

In evaluating the elements of $\underline{D}$ it was necessary to work in crystal planes in which the position of the lines for some groups were separate from the B spectrum for a significant arc of rotation, a strong restriction when it is considered that the g_x and g_y turning points both lie within the B spectrum. The <110> data shown in Figure 6.9 gave an adequate determination of D_{zz} D_{xx} and D_{xz} and the curves through the fine structure lines in this figure are least squares fits to these three parameters. The cross term D_{xz} proved to be larger than the D_{xx}

ANGULAR VARIATION OF THE A SPECTRUM IN THE ac PLANE

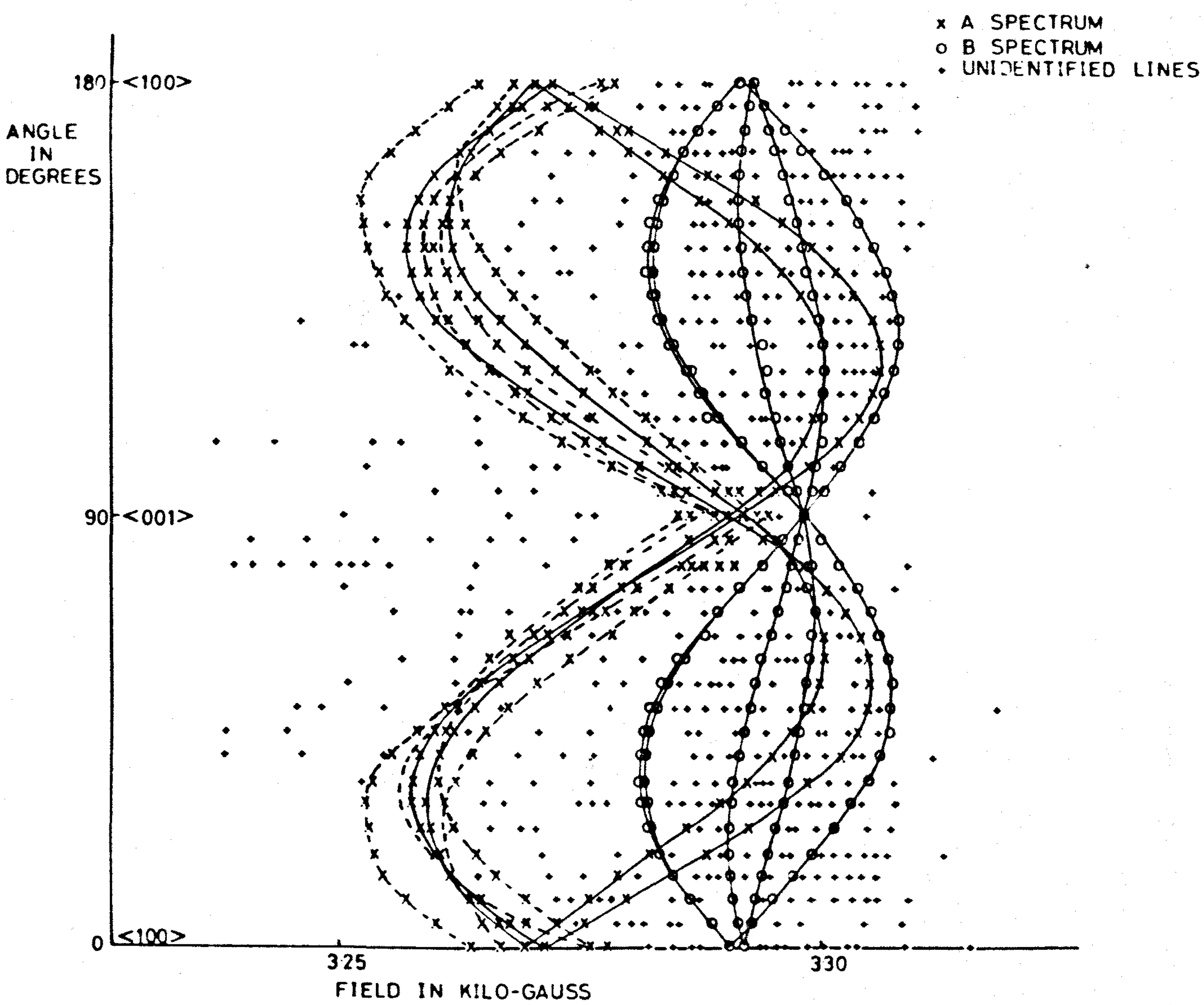

FIGURE 6·10

TABLE 6.3

D TENSOR PARAMETERS FOR THE A CENTRE

D Tensor Components in $\underline{g}$ tensor axis system

$D_{xx} = 1.21 \times 10^{-4}\mathrm{cms}^{-1}$

$D_{yy} = -4.11 \times 10^{-4}\mathrm{cms}^{-1}$

$D_{zz} = 2.90 \times 10^{-4}\mathrm{cms}^{-1}$

$D_{xz} = 1.72 \times 10^{-4}\mathrm{cms}^{-1}$

$D_{xy} = -1.69 \times 10^{-4}\mathrm{cms}^{-1}$

$D_{yz} = -0.93 \times 10^{-4}\mathrm{cms}^{-1}$

(a)

D Tensor			
Principal Values	Direction Cosines with respect to g tensor axes		
	g_x	g_y	g_z
$4.32 \times 10^{-4}\mathrm{cms}^{-1}$	0.5558	-0.2005	0.8068
$0.31 \times 10^{-4}\mathrm{cms}^{-1}$	0.7891	-0.1780	-0.5879
$-4.63 \times 10^{-4}\mathrm{cms}^{-1}$	0.2615	0.9634	0.0593

(b)

term which removed any suspicion that the tensors might be coincident. D_{yy} could be determined from these parameters and the zero trace condition, but the determination of D_{xy} and D_{yz} proved more difficult. After unsuccessful attempts to establish the $g_z g_y$ plane for one site, an angular variation was performed in the ac plane in which g_z has a dominating effect on each pair of equivalent sites for alternate quadrants of the plane. It was not possible to establish the ac plane exactly with the result that each pair of sites was slightly inequivalent for most orientations of H. This data is shown in Figure 6.10 where the curves through the field positions are empirical sketches of the angular dependence of the various lines. D_{xy} and D_{yz} were determined from the differences of the fine structure splittings for two near equivalent sites in this plane. A least squares fit to this data gave the magnitude and relative signs of these terms. However since the pairs of equivalent sites in this plane are related by having opposite directions for g_y, and hence opposite signs for the cross terms of D which include y, it was impossible without knowing which site produced which lines to deduce the actual signs of D_{xy} and D_{yz} or indeed their signs relative to the other terms. Fortunately, however, it is sufficient to know the relative signs of the other terms and the signs of these terms relative to each other in order to unambiguously determine the D tensor. Table 6.3a lists the components of D and Table 6.3b lists its principal values and the direction cosines of its axes relative to the g tensor. It can be seen that the D tensor is almost completely rhombic and further that its axes are rotated considerably from the g tensor axes. The implications of these results will be discussed in a later section.

TABLE 6.4

G TENSOR PARAMETERS OF 4 LINES OF THE B SPECTRUM IN THE AC PLANE

GAA	GCC	GAC
4.046	4.031	0.009
4.051	4.031	-0.030
4.046	4.031	-0.008
4.050	4.032	0.031

6.5 The B Spectrum

As Figures 6.3 and 6.8 show, the B spectrum was a complex group of lines with similar g values to those of the A spectrum. At liquid nitrogen temperatures the spectrum was dominated by broader and more intense lines, as shown in Figure 6.4. The main lines of the spectrum had similar linewidths and showed the same saturation dependence as the A lines, but were roughly twice as intense. The overall anisotropy of the spectrum was less than for the A spectrum and this combined with its complexity prevented an accurate determination of its g tensor. It was possible to follow the angular variation of the four most intense lines in the ac plane as indicated in Figure 6.10 and the G_{aa}, G_{cc} and G_{ac} components of these angular variations are listed in Table 6.4.

No hyperfine or fine structure relationships could be established between these main lines and the many smaller and intermediate lines of the spectrum, but it is quite possible that such relationships do exist.

It seems certain that like the A lines, the four intense lines of the B spectrum arise from the same paramagnetic species at different sites in the structure. They collapse to a single line with a g value of 2.007 ± 0.001 along the c axis and to two lines along an a axis. It can be seen from the spectrum taken along an a axis (Figure 6.8) where, owing to the special symmetry of their g tensor, the A lines collapse to a singlet, that the B lines do remain a doublet along this direction. From this it can be deduced that the B lines have different g tensor axes to those of the A lines and further that none of these axes lie along a <110> direction. Unfortunately it was not possible to trace the angular variation a axis

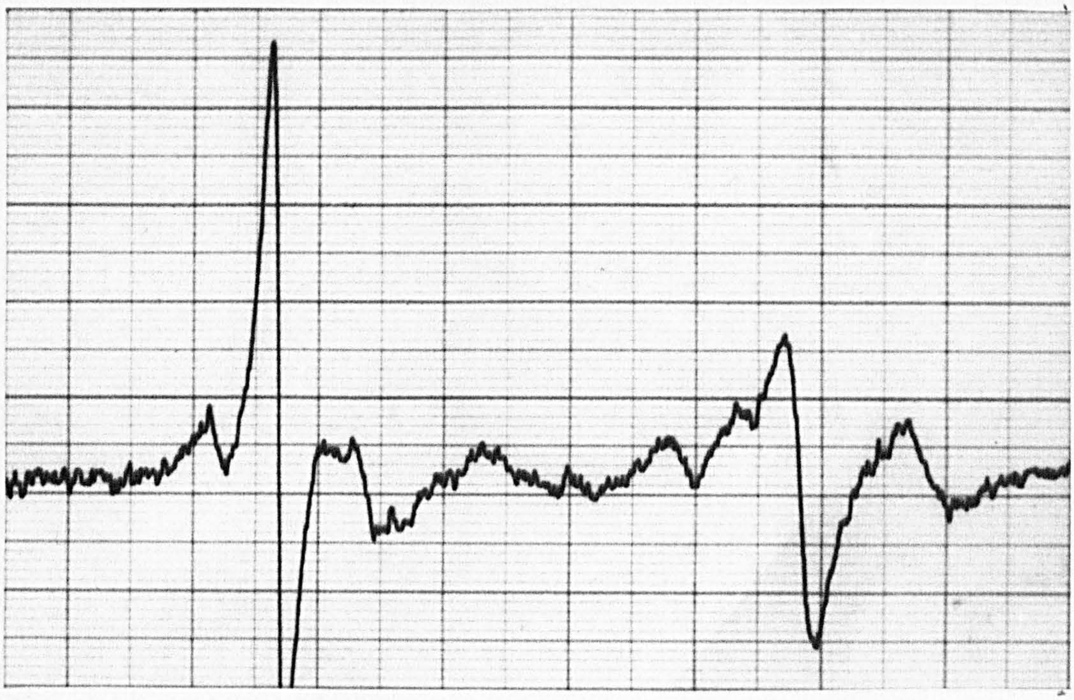

(a) Room Temperature

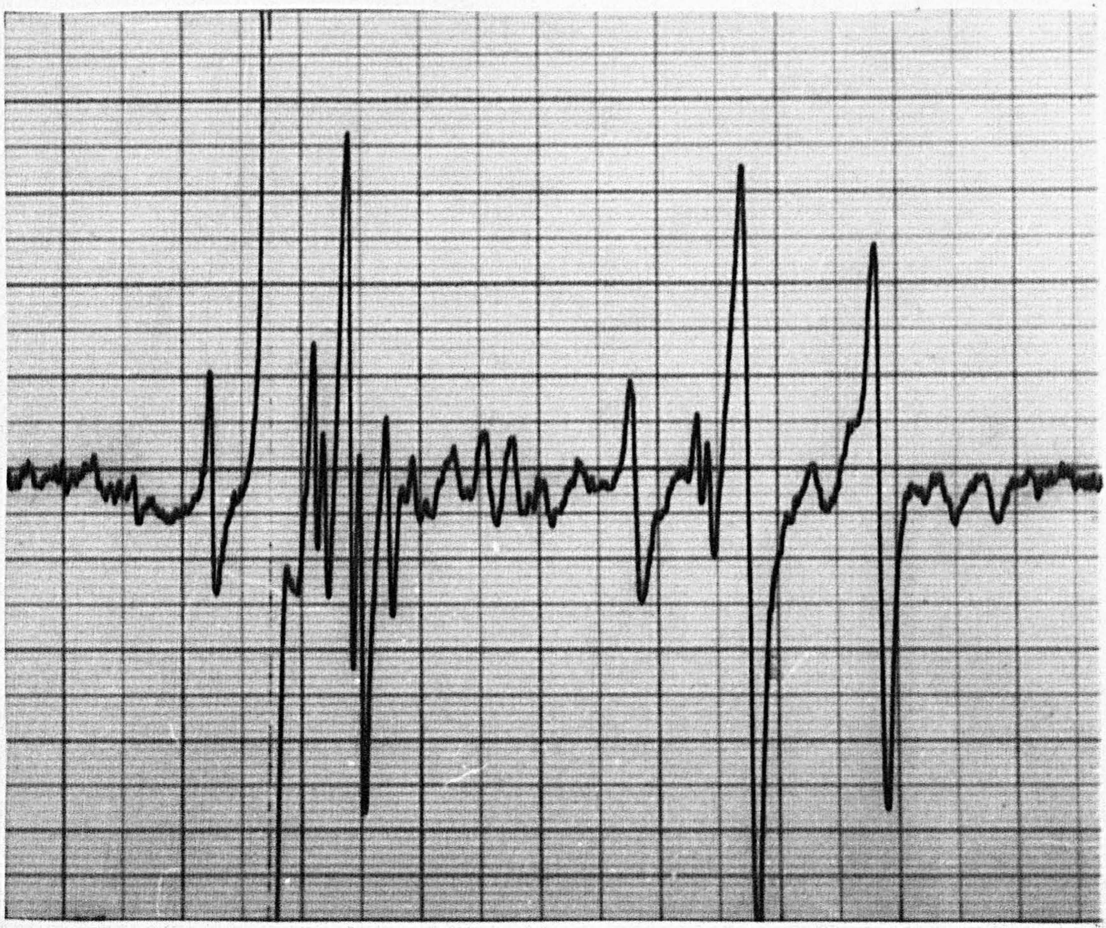

(b) 77°K

FIGURE 6.11

of this spectrum with any certainty in either the <110> plane (Figure 6.9) the ab plane (Figure 6.5) or the plane at right angles to a W-O bond (Figure 6.7), and consequently an exact specification of the nature of the centre giving rise to this spectrum cannot be made.

6.6 C Spectrum

The C spectrum was observed in the region of 3,800 to 4,000 gauss and at room temperature it consisted of two prominent broad lines, termed α_1 and α_2, each with two smaller lines, considered to be hyperfine structure, symmetrically disposed to either side. In addition each of the main lines was accompanied by an even broader line to higher field. These lines will be referred to as β_1 and β_2. From the angular variation of the line widths and field positions of α_1 and α_2 in the ac and ab planes the two lines could be seen to be related simply by differences in phase from which it was deduced that they arise from the same centre at different sites in the structure. Figure 6.11a shows the spectrum observed with H parallel to an a axis where the linewidth for α_1 is ~15 gauss and for α_2 ~20 gauss. The two lines collapse along a c axis (Figure 6.12a) α_1 being almost invariant in the ac plane.

Cooling to liquid nitrogen (Figures 6.11b and 6.12b) radically increased the definition of the spectrum and revealed the presence of many more lines which were either too broad to be observed at room temperature or had been swamped by the main lines. The linewidths of the α lines decreased by a factor of three and those of the β lines by slightly more though they remained broader than the α lines.

c axis

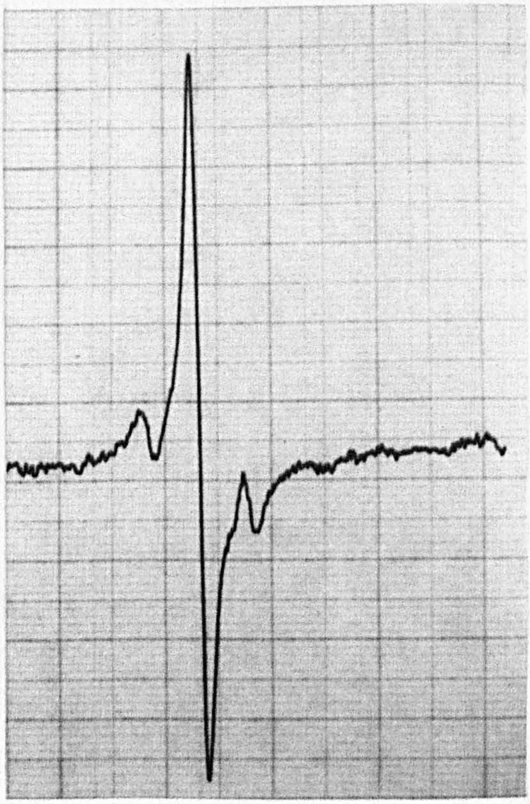

(a)
Room Temperature

(b)
77°K

FIGURE 6.12

Hyperfine structure could be observed on both the α and β lines and the presence of weaker lines outside the main components revealed that it arose from an interaction with two equivalent W^{183} nuclei. The hyperfine splitting was also observed to be anisotropic, its magnitude being related to the anisotropy in field position of the α and β lines.
Among the new lines discerned at liquid nitrogen were four sharp lines, termed the γ lines, which had similar widths to the hyperfine structure of the α lines but a quite different angular dependence. The γ lines were not investigated fully owing to their confusion with other components at most orientations, but from their angular behaviour in the ab plane it seems unlikely that they are related to the other lines discussed here.

Angular variation studies of the spectrum were performed at room and liquid nitrogen temperatures in the ab, ac and <110> planes. The spectrum was also investigated at liquid helium temperature along the a and c axes and at a few other orientations in the ac plane.

6.6.1 Determination of the Hamiltonian

Interpretation of this spectrum posed some initial difficulty since it was not known whether or not the α and β lines were related. The single line appearing at room temperature along the c axis was revealed as a doublet at liquid nitrogen temperatures, though from the data taken in the ac plane it was not possible to establish the composition of this doublet in terms of the α and β lines. This problem was resolved by using the A spectrum (section 6.4.1) to align the crystal accurately in a <110> plane and then performing an angular variation study with a modulation amplitude of 0.2 gauss which emphasised the difference in width between the α and β lines. Besides establishing that the low field component of the c axis doublet was formed from the α lines and the higher one from the β lines this experiment also revealed that each of α_1, α_2, β_1 and β_2 was composed of two lines which were slightly inequivalent in this plane. In the ab plane α_1 and β_1 and α_2 and β_2 moved as two doublets, π/2 out of phase with each other and with turning points ~15° from an a axis. Experiments at liquid helium temperature sharpened both the α and the β lines but revealed nothing new about their possible relationship, variations in power level having the same effect on each type of line. In summary the spectrum had the following significant features:-

(a) Quite large g shifts

c axis	$g_\alpha \sim 1.79$	$g_\beta \sim 1.77$
12° from a axis in ab plane	g_{α_1} 1.80	$g_{\beta_1} \sim 1.77$
	g_{α_2} 1.50	$g_{\beta_2} \sim 1.44$

(b) Similar angular dependence of the α and β lines in ab, ac and <110> planes

(c) At all orientations the β lines were broader and to higher field of the corresponding α lines.

(d) The linewidth of each line was considerably anisotropic.

(e) Anisotropic interaction with two equivalent ^{183}W nuclei ($I = \frac{1}{2}$)

c axis $a_\alpha = a_\beta$

a axis $a_{\alpha_1} \sim 2 \times a_{\alpha_2}$

$a_{\beta_1} \sim 2 \times a_{\beta_2}$

(f) Temperature dependent line widths.

The temperature dependence of the linewidths and their broadness at room temperature is strongly suggestive of an $S = 1$ centre. However, of the three ways of grouping these lines in pairs to form an $S = 1$ system, two, $(\alpha_1\alpha_2)$ $(\beta_1\beta_2)$ and $(\alpha_1\beta_2)$ $(\alpha_2\beta_1)$, can be ruled out since it is unlikely that a D term could explain either the angular dependence of the line widths of these lines or the different hyperfine splittings observed on different M_S components (e). This leaves the possibility of $(\alpha_1\beta_1)$ $(\alpha_2\beta_2)$ and the spectra in the ab and ac planes can be fitted to the hamiltonian of (6.10) with $D_{xx} = -11.8 \times 10^{-4}\text{cms}^{-1}$, $D_{yy} = 41.4 \times 10^{-4}\text{cms}^{-1}$, $D_{zz} = 54.1 \times 10^{-4}\text{cms}^{-1}$ and zero cross terms. This fitting must, however, be regarded as fortuitous since though the magnitudes of the components are consistent, their relative signs are incompatible with the requirement of a zero trace for the D tensor. For example, reversing the sign of D_{yy} would satisfy (6.11) but to be consistent would require α_1 and β_1 to cross in the ab plane, which they do not do (c).

The elimination of the $S = 1$ possibilities means that we must postulate the spectrum as arising from two different centres, each with $S = \frac{1}{2}$, one giving rise to the α lines and the other to the β lines. The identical angular dependence of the two sets of lines would then seem to be coincidental or alternatively might arise from a more fundamental relationship between the centres such as their being different charge states of the same defect (cp the Silicon Divacancy, section 2.5.1).

6.6.2 Determination of the g tensor

If the hypothesis that the α and β lines arise from two $S = \frac{1}{2}$ centres is correct, then the spectra can be summarised in terms of the general hamiltonian (6.5). Initial attempts to fit the spectra by assuming that one principal direction of the g tensor was along the c axis produced a reasonable fit to data taken in the ac and ab planes but a better fit could be achieved by including the cross terms of (6.7). The G_{ac} and G_{bc} cross terms required were quite small and since α_1 and α_2 could not be unambiguously resolved as doublets in the ac plane, it seemed possible that the need for them arose from misorientation of the crystal. These cross terms of course govern the angles between the principal axes of the g tensor and the crystalline c axis and if they are zero for a given species then the four possible sites in the structure will be equivalent in pairs at all orientations. This difficulty could be resolved from data taken in a <110> plane where the doublet nature of α_1 α_2 β_1 and β_2 was revealed and it could be concluded that G_{ac} and G_{bc} were not in fact zero for either centre. A slight inconsistency was exhibited between angular variations performed in the ab, ac and <110> planes, the angle between <110> and <100> directions specified on the basis of the ac and <110> plane data being 40° to 43° instead of 45°, for the data taken in what was supposedly the ab plane. Of the three sets of data, that taken in the ab plane was less reliable as it had been recorded with a faster field sweep, thus increasing the magnitude of measurement errors. The <110> plane data, however, was known to be very accurate since the crystal had first been aligned by means of the A spectrum (section 6.4.1). Consequently the

TABLE 6.5

HAMILTONIAN PARAMETERS OF THE α CENTRE

G Tensor

$G_{aa} = 2.336$

$G_{bb} = 3.187$

$G_{cc} = 3.185$

$G_{ab} = 0.295$

$G_{ac} = 0.035$

$G_{bc} = 0.012$

g tensor

	Principal values	Direction cosines		
		a	b	c
g_1	1.811 ± .005	0.2982	0.9545	0.0094
g_2	1.785 ± .005	-0.0400	0.0026	0.9992
g_3	1.497 ± .005	0.9537	-0.2983	0.0389

TABLE 6.6

HAMILTONIAN PARAMETERS OF THE β CENTRE

G Tensor

$G_{aa} = 2.121$

$G_{bb} = 3.034$

$G_{cc} = 3.142$

$G_{ab} = 0.287$

$G_{ac} = -0.068$

$G_{bc} = 0.016$

g tensor

	Principal values	Direction cosines		
		a	b	c
g_1	1.774 ± .005	-0.0971	-0.1110	0.9891
g_2	1.766 ± .005	0.2686	0.9540	0.1334
g_3	1.429 ± .005	0.9584	-0.2786	0.0628

ANGULAR VARIATION OF THE C SPECTRUM IN THE <110> PLANE

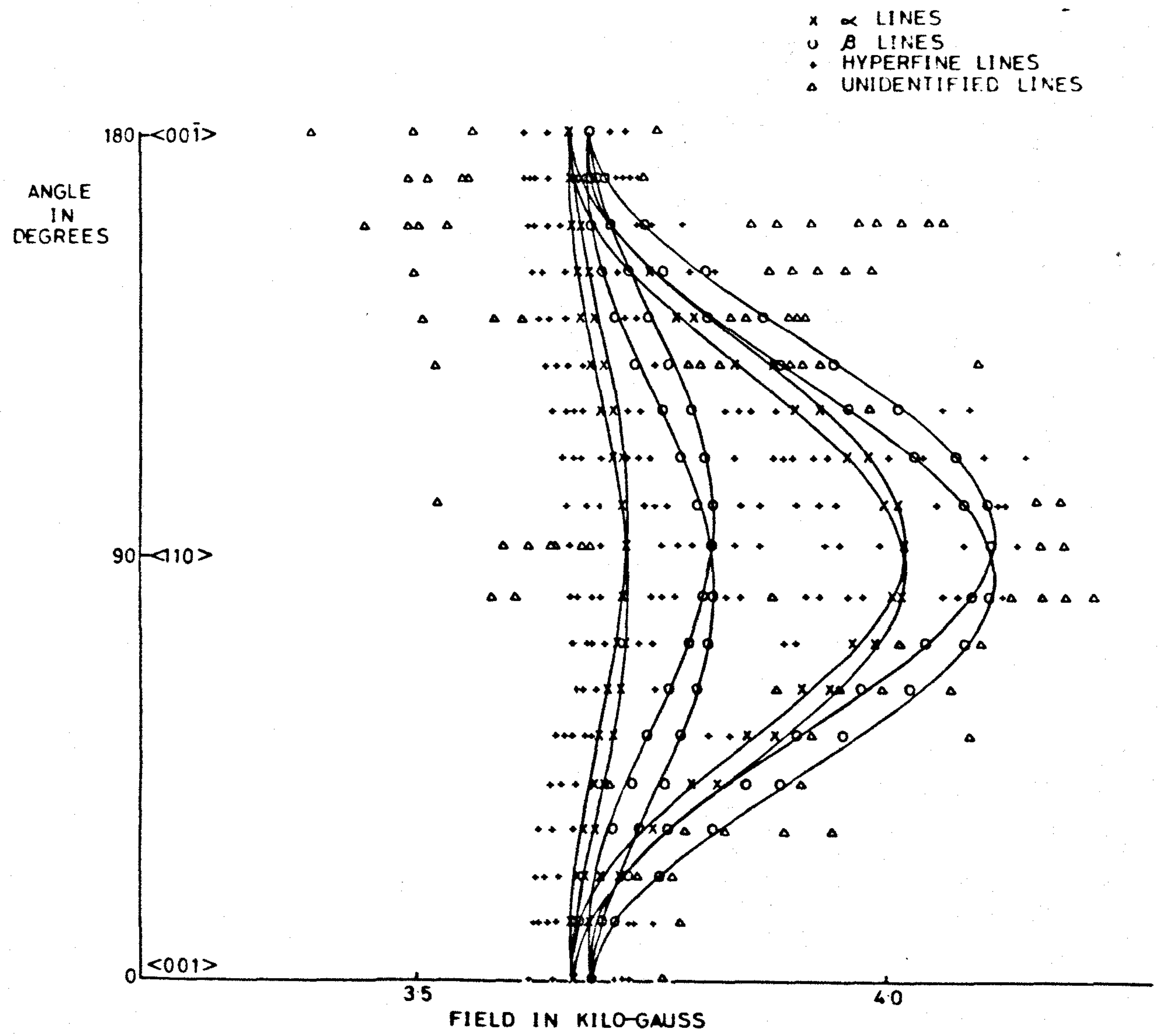

FIGURE 6·13

elements of G_{ij} for both the α and β lines were determined from the ac and <110> plane data. G_{cc}, G_{aa} and G_{bb} could be found by a least squares fit to the ac data, taking advantage of the $\pi/2$ phase differences between α_1 and α_2 and β_1 and β_2. The spectra taken along a <110> direction then enabled G_{ab} to be determined. G_{ac} and G_{bc} are responsible for the slight splitting of each of α_1, α_2, β_1 and β_2 in the <110> plane, the separations being:-

Low field G_{ab} +ve $\quad \Delta H_\theta \propto |G_{ac} + G_{bc}| \dfrac{\sin 2\theta}{\sqrt{2}}$

High field G_{ab} +ve $\quad \Delta H_\theta \propto |G_{ac} - G_{bc}| \dfrac{\sin 2\theta}{\sqrt{2}}$

Since the separation of the high field doublet was always larger than that of the low field doublet for both α and β lines, G_{ac} and G_{bc} must be of opposite sign. The magnitude of these terms was found by a graphical method which involved a comparison of the moduli of their sums and differences with the appropriate separations observed when H was applied at an angle of 60° to c in the <110> plane. The components determined for $\underline{G}$ and the corresponding $\underline{g}$ tensor are shown in Tables 6.5 and 6.6 for the α and β lines respectively. Figure 6.13 shows the agreement between these hamiltonians and the experimental data taken in the <110> plane, the doublet nature of the lines can be clearly seen. A comparison with the ac plane data is shown in Figure 6.14, where it may be noted that the doublet splittings predicted are often within the linewidth of the observed lines. Figure 6.15 shows the slight disagreement of the hamiltonians determined in this way with the data taken in the ab plane. A rough estimate shows that a misorientation of some 6° spread over the

ANGULAR VARIATION OF THE C SPECTRUM IN THE ac PLANE

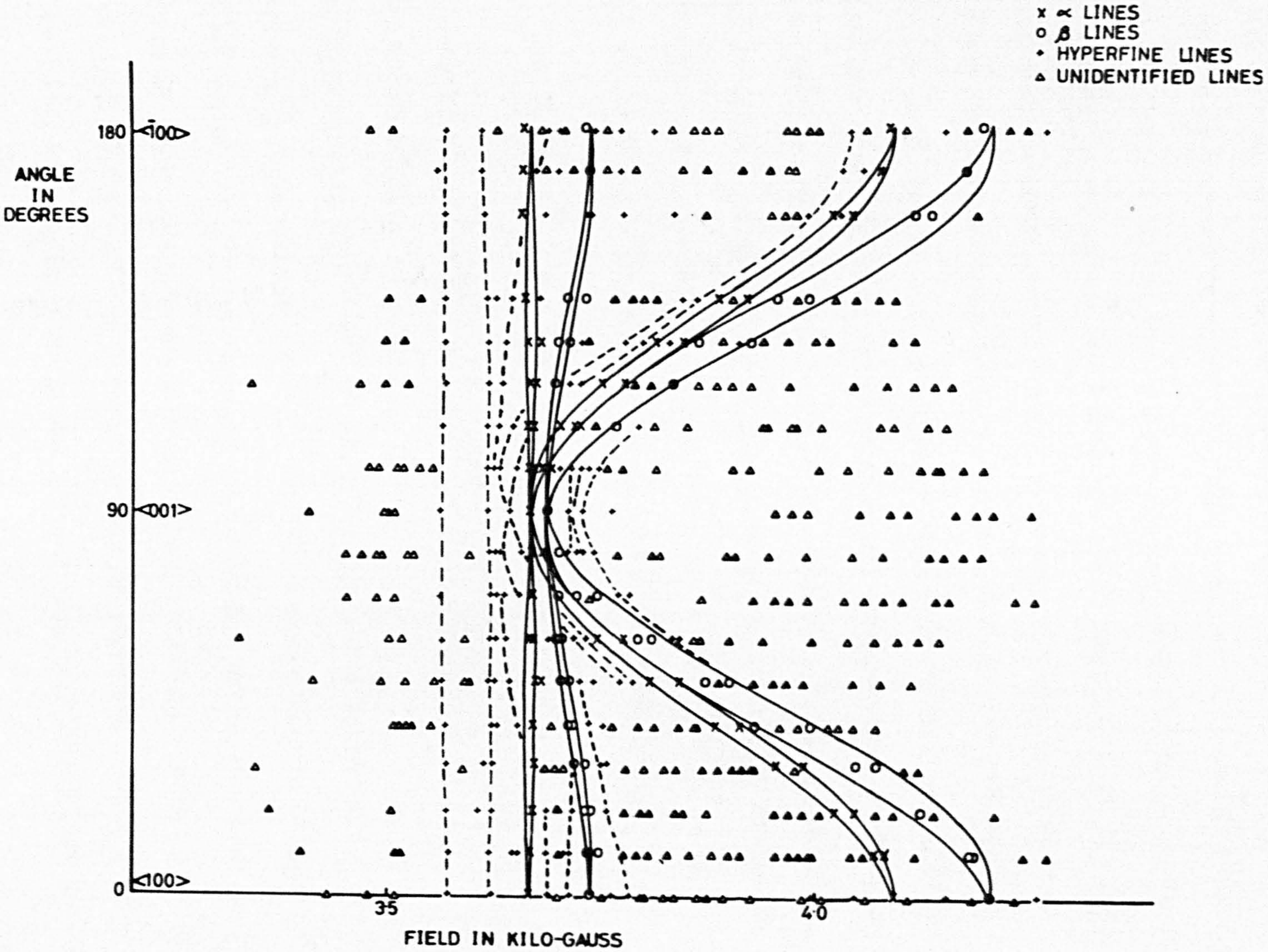

FIGURE 6·14

ANGULAR VARIATION OF THE C SPECTRUM IN THE ab PLANE

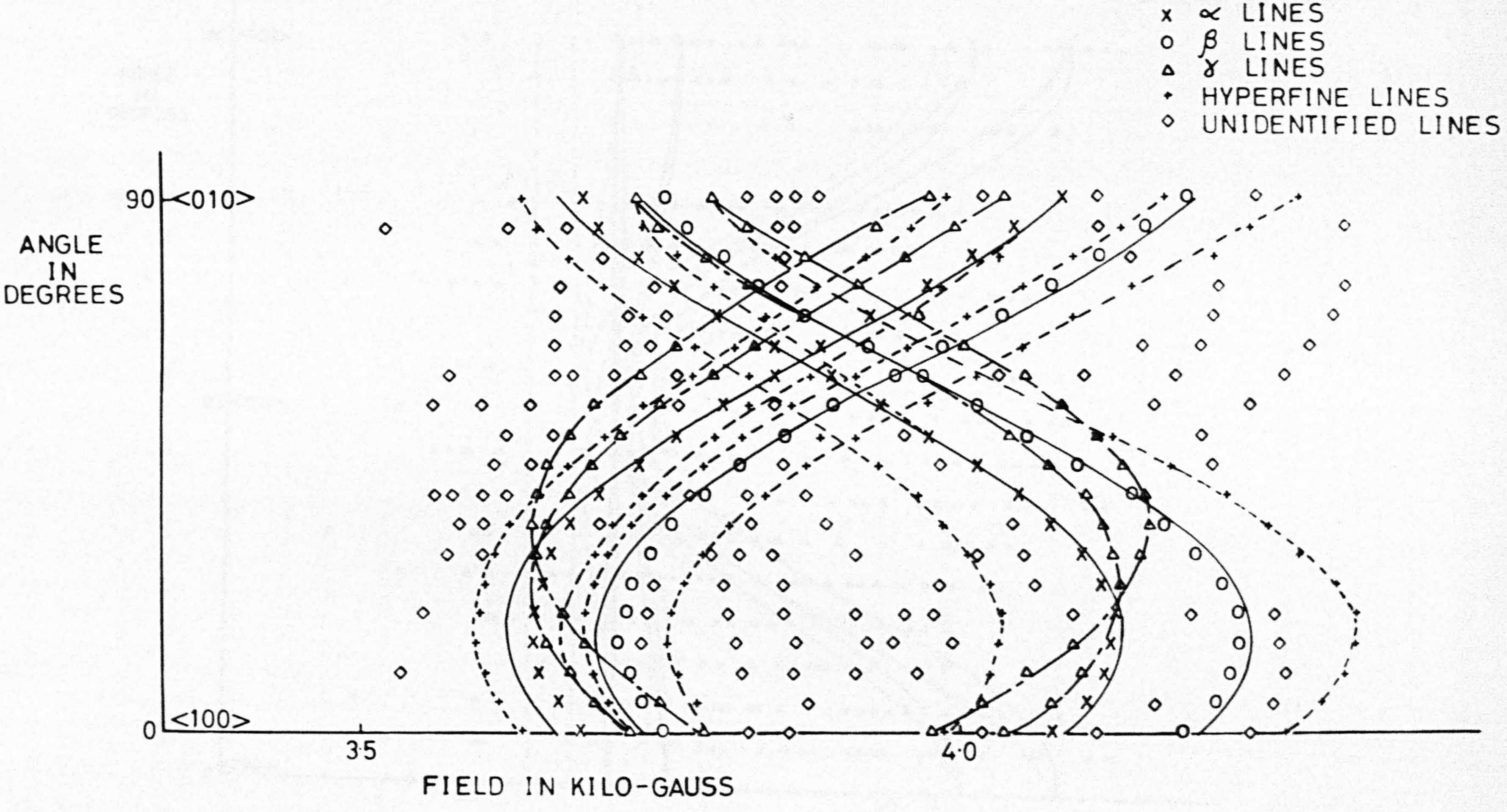

FIGURE 6·15

three Euler angles α, β and γ could produce this mismatch. The angular variation of the γ lines has also been sketched in on the ab plane data.

6.6.3 Hyperfine interactions

As mentioned previously both the α and the β lines were accompanied by hyperfine structure. Apart from impurities the only isotope with non zero nuclear spin which is present in the material in significant quantities is the 14% abundant W^{183} with $I = \frac{1}{2}$. The relative intensity of the hyperfine lines to the main lines is consistent with this being the origin of the interaction and further the presence of two very much weaker lines, the same distance away from the outer components of this splitting, indicates that two W^{183} nuclei at equivalent sites are involved. These outer components would then arise from those defects which had both sites occupied by W^{183} and a total nuclear spin of 1. The ratio of the intensities of the various lines on this model are:

$$\begin{array}{ccccc} 0.007 & & 0.16 & & 1.0 \\ & : & & : & \\ I = \pm 1 & & I = \pm\frac{1}{2} & & I = 0 \end{array}$$

and though no accurate intensity measurements were made this corresponds roughly to the relative intensities observed.

The hyperfine interaction may be represented by adding the following term to (6.5):

$$A\,S_z(I_{1z} + I_{2z}) + B(S_x(I_{1x} + I_{2x}) + (I_{1y} + I_{2y})S_y) \qquad (6.11)$$

where $I_1 = \pm\frac{1}{2}$ or 0 and $I_2 = \pm\frac{1}{2}$ or 0.

The angular dependence of the hyperfine interaction, as illustrated in Figures 6.13, 6.14 and 6.15, is isotropic in the ac plane and reaches a maximum (which is hard to discern since one component on the α line is hidden by the β line and vice versa) in the region of the low g value. This maximum is, however, insensitive to orientation and the hyperfine separation is the same to within experimental error when the spectrum is observed along the nearby a axis. This point will be returned to in a later section.

The angular dependence of the hyperfine splitting has not been fitted in detail to (6.11) but from measurements made along the axes the hamiltonian parameters are

$$A = 167.4 \pm 5.0 \times 10^{-4}\text{cms}^{-1}$$

$$B = 87.4 \pm 2.0 \times 10^{-4}\text{cms}^{-1}$$

6.7 Discussion

The assignment of defect models to the spin hamiltonians describing $CaWO_4$ spectra is rather more difficult than for the cases of cubic materials or other simple oxides. Besides the lower symmetry of the system there is the more fundamental difficulty provided by the strongly covalent nature of the WO_4^{2-} complex which invalidates many comparisons with the better understood and more extensively studied ionic systems. This covalency means for example that defects in the WO_4^{2-} complex itself are best treated in terms of molecular orbital theory since the point charge assumptions of crystal field theory will not be valid within this system. Crystal field theory might be thought to have more applicability to regions outside of the WO_4^{2-} complex though of course its predictions will be considerably influenced by the charge distribution assumed for the complex. For these and other reasons very little is known of the structure of defects in $CaWO_4$ (section 4.2.3). There seems to be a strong tendency for intrinsic lattice defects to associate with impurities and this is probably the reason why the spectrum observed from the lightly irradiated crystals was more complex than that observed from the heavily irradiated ones. Higher dosage might be expected to saturate impurity associated defects and lead to reduced spectral intensity by the formation of several forms of aggregate defect and the line broadening resulting from increased strain in the lattice. This is a reasonable explanation of the absence of the normal Mn^{2+} spectrum after heavy irradiation and the reappearance of the Mn in the unusual and strongly temperature dependent spectrum shown in Figure 6.1. The spectra from intrinsic defects on the other hand will be expected to increase in intensity with dose rate, though there is the possibility that at very high dosages the predominant defects might well be aggregates of simpler defects. Bearing these considerations in mind it is felt that the spectra studied in detail in this work are unlikely to be associated with impurities and are probably simple intrinsic defects in the lattice.

6.7.1 The A spectrum

The most striking feature of the A spectrum is the need to invoke non-coincident g and D tensors in order to explain its angular variation and this obviously prompts speculation as to whether or not the lines attributed to fine structure really are fine structure.

Alternative hypotheses however seem to lead to equally, if not more unlikely anomalies in the spectrum, but before discussing these it will be as well to draw attention to an inadequacy in the present treatment. It was noted that the central line did not always lie in the centre of the outer components and that this orientation dependent shift was sometimes of the order of one to two gauss in a splitting of some ten gauss. The accuracy with which separations of lines can be measured is, of course, considerably greater than determinations of absolute line positions and consequently it is in order to discuss such changes. This sort of shift is of the kind that is usually expected from second order effects, however with such a small value of D shifts of the order of 10% are very unlikely. A determination of the analytical expression for the angular dependence of second order terms involving all the components of equation (14) in Appendix III would, of course, be quite formidable and consequently the second order contribution was evaluated for a single direction along which the effect was most pronounced, namely a <110> direction. Even allowing for the increase due to the off diagonal elements this contribution was over an order of magnitude too small to explain the discrepancy. This would seem to mitigate against this interpretation though it is possible that by using the more fundamental hamiltonian of Koster and Statz (1959), which is derived solely from symmetry considerations and in low symmetry would allow the inclusion of terms in S^3, this discrepancy might be explained. With such a small value of D and with the accuracy to which these splittings are known any extra terms permitted in the hamiltonian are of course significant.

As mentioned briefly in section 6.4.2, there are a number of reasons why hyperfine interaction with W^{183} can be ruled out as a possible origin of these lines. Firstly, taking into account the line widths, the overall intensity ratios observed for the three lines is more in keeping with the 3:4:3 expected for fine structure than with the .07:.86:.07 predicted from the isotopic abundances. The slight shift of the central line would of course be even more difficult to explain on this hypothesis although Tomlinson and Henderson (1969) did observe a slight isotopic g shift (.13 gauss) in the hyperfine structure from $^{47}Ti^{+}$ and $^{49}Ti^{+}$. However as this effect is presumably due to differences in nuclear mass, it is unlikely that differences of the order of 1 or 2 in ~180 could produce the larger effects observed here.

The possibility that the three lines are unrelated and arise from centres with almost identical g tensors is very unlikely and the only remaining possibility seems to be that they are due to some kind of aggregate centre such as exchange coupled pairs. The 'D' splitting would then be attributed to dipolar interaction between electron spins.

$$\mathcal{H} = g^2\beta^2 \sum_{j>i} \left(\frac{\underline{S}_i\cdot\underline{S}_j}{r_{ij}^{\ 3}} - \frac{3(\underline{S}_i\cdot\underline{r}_{ij}).(\underline{S}_j\cdot\underline{r}_{ij})}{r_{ij}^{\ 5}} \right)$$

which predicts an interaction energy of $\sim \frac{8 \times 10^{-1}}{r^3}$ cms^{-1} between two spins r Å apart. In order to produce a D term of about ten gauss the two spins would need to be at least 10 Å apart which, since it is greater than a unit cell distance, would suggest that several possible interactions ought to be observed. This difficulty is exacerbated by the

TENSOR AXES FOR THE A CENTRE

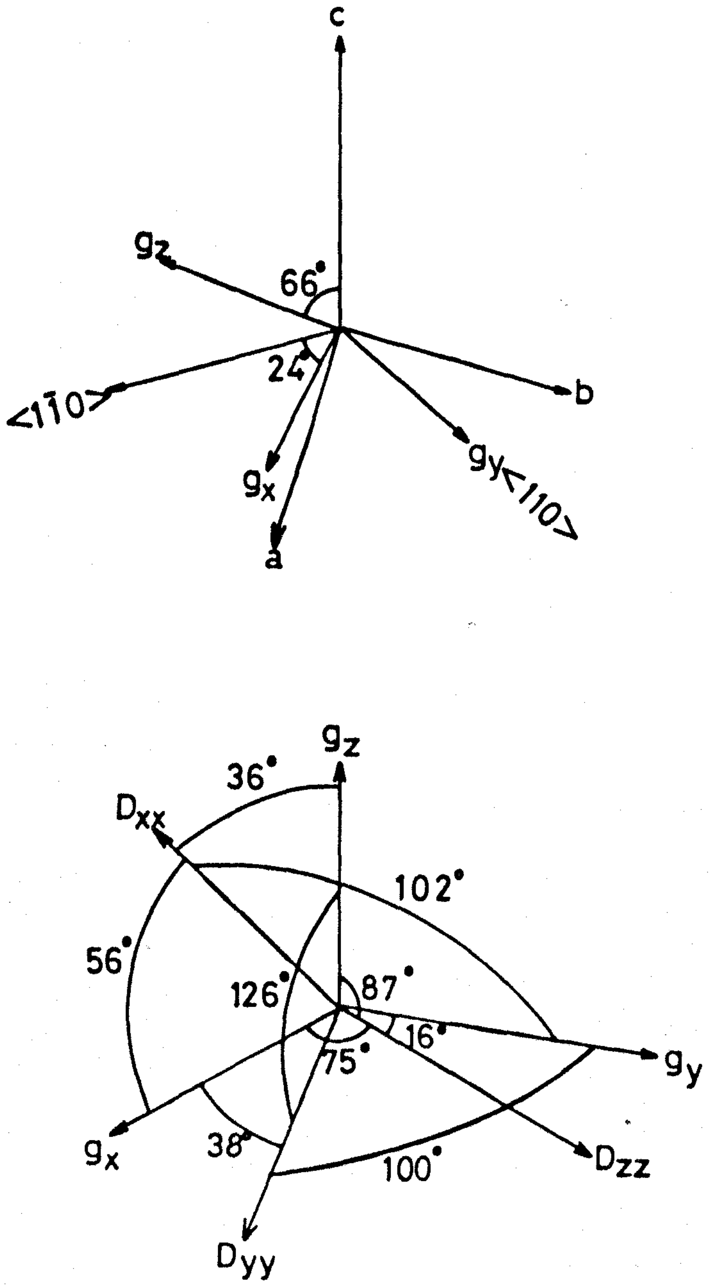

FIGURE 6·16

symmetry properties of the material. If for example we suppose the simultaneous existence of $S = \frac{1}{2}$ centres giving rise to the central line and $S = 1$ pairs produced by interaction of these centres then, since the single centres will occupy A_1 A_2 A_3 and A_4 sites in the structure, there should be interaction between A_i and A_j sites where $i \neq j$ besides the combinations with $i = j$. These various possibilities predict more interactions than are observed since the environment between the various pairs will be different, though it is possible in this context that some of the lines in the B spectrum might arise in this way.

In conclusion it is felt that the most likely explanation of the A spectrum is in terms of the non-colinear g and D tensors assumed in section 6.4 and on this basis a speculative model for the defect is discussed.

6.7.2 O^+ model

Figure 6.16 shows the directions of the g tensor axes of the A spectrum relative to the crystal axes and of the directions of the D tensor axes relative to those of the g tensor. It was expected at first that the axes of the D tensor might transform back to the crystal axes but even allowing for the few degrees of indeterminancy in both systems, neither tensor seems to bear any obvious relation to the axes of the crystal. There is also no doubt that the two systems do not even share a common direction and following Nye (Physical Properties of Crystals, 1967, p.23) this immediately makes it possible to deduce the point symmetry of this site. The presence of any symmetry elements about a defect centre places very strong restrictions on the relationships between

PROPOSED MODEL FOR THE A CENTRE IN $CaWO_4$

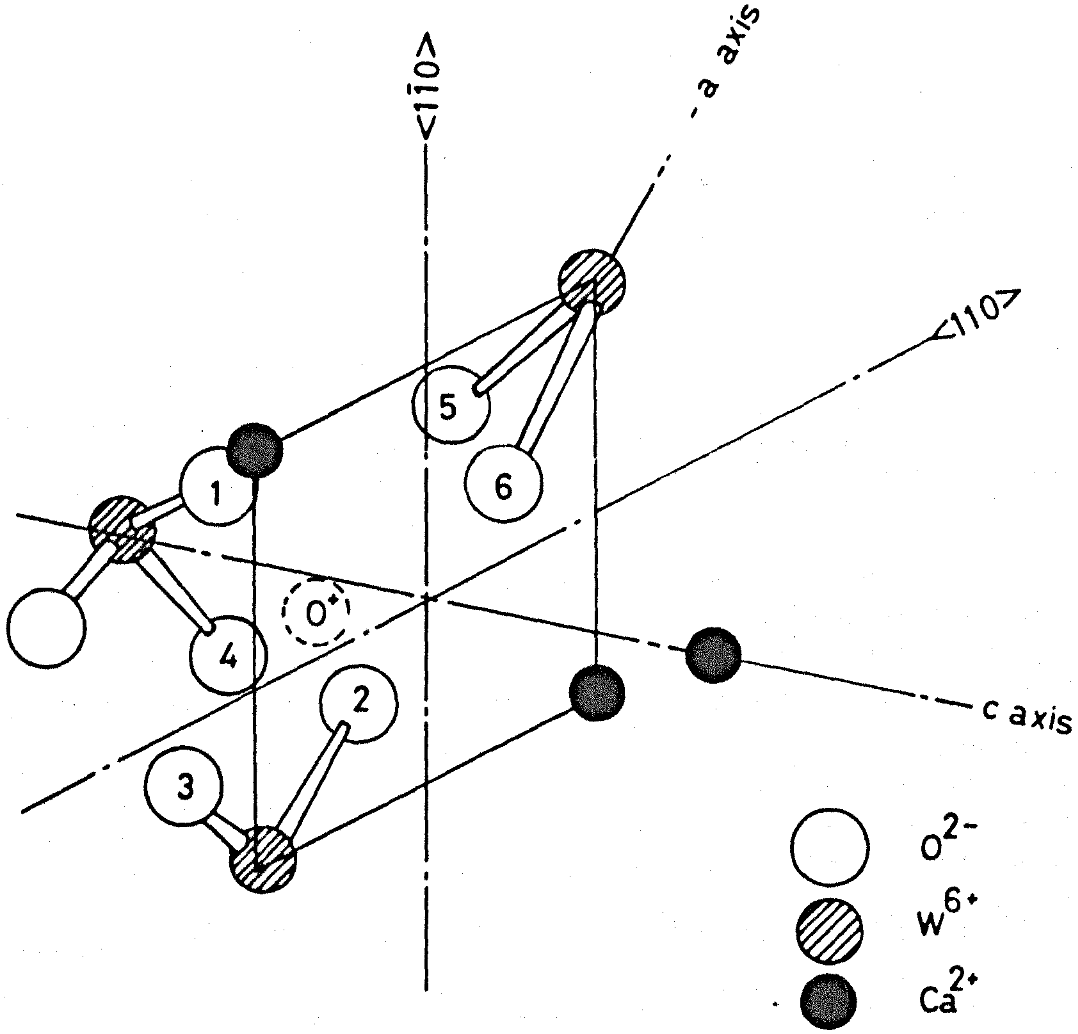

FIGURE 6·17

tensors describing various physical properties. For example monoclinic symmetry, in which there is only a C_2 element, requires that two tensors will have at least one axis colinear and in order to allow the situation here, where the relationship between the two systems can be described in terms of six independent variables, it is necessary to go to triclinic symmetry in which there is no symmetry or at most an inversion. This restricts the point group to either C_1 or C_i and this extreme requirement is probably the reason why non-colinear g and D tensors are not usually observed.

In choosing a model for the species the narrow line widths and relative ease of saturation of the lines at liquid nitrogen temperature are strongly suggestive of the long relaxation times of S state ions. The centre has spin $3/2$'s and its spectrum is predominant after heavy irradiation indicating some intrinsic defect. One model fulfilling these requirements is O^+, the low symmetry seeming to indicate an interstitial site. It is reasonable to suppose that the neutrons displace oxygens and that their charge state is subsequently altered by the γ irradiation always present in reactor irradiations. To achieve a similar electronic state with Ca it is necessary to postulate the formation of Ca^{5+} which seems unlikely.

The site suggested is illustrated in Figure 6.17 where the O^+ occupies a small space between six oxygens. The ionic radius of O^{2-} is 1.46 Å and the radius of oxygen when in tetrahedral covalent bonds, as here, is 0.66 Å (Kittel, Introduction to Solid State Physics, 1967 p.105). As the separation between oxygens across this site is some 4 Å this

ENERGY LEVELS OF FREE ION O^+

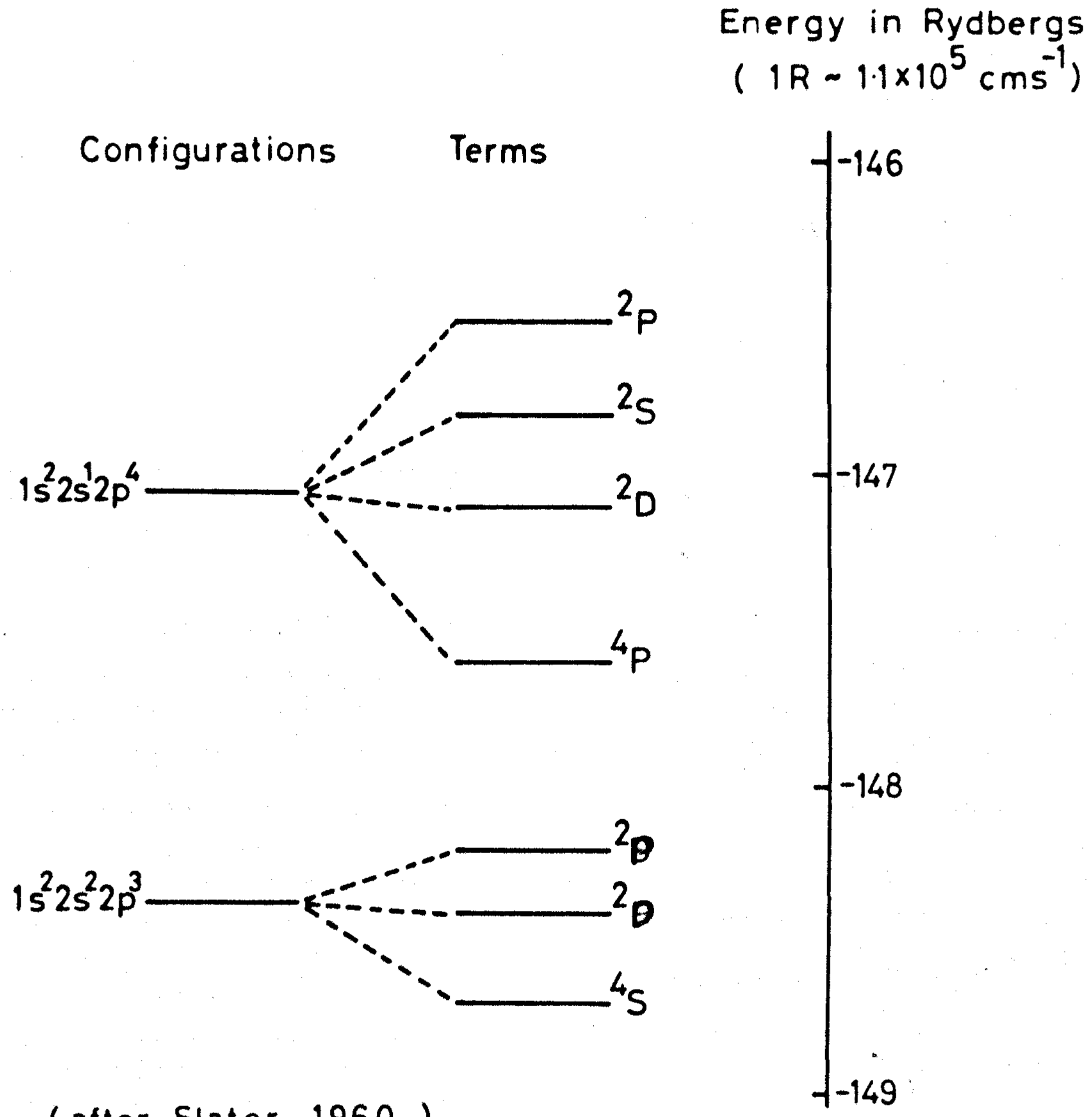

(after Slater 1960)

FIGURE 6·18

leaves between 1.2 and 2.7 Å for the O^+, which is a reasonable figure. The crystal field in this region will be small as can be seen by considering the WO_4^{2-} to be a point charge at the W site and it is reasonable to suppose that O^+ will be quite stable in this potential well. This site is attractive since if the ion is off the exact centre of the complex the g_z and g_x axes point to the oxygens marked 2 and 4 in the figure and further the point symmetry will then be C_1, fulfilling the requirement for non-colinear g and D tensors.

The calculation of the magnitude of these quantities is difficult for an S state ion, though following Bartram et al. (1965) who considered the case of O^+ in Al_2O_3, a calculation has been performed (Dugdale 1970) for the defect located at the centre of this complex where there is a C_2 axis. The ground term of O^+, as shown in Figure 6.18, is ^4S and, of course, in first order there will be no mixing in of orbital momentum from higher terms by either the crystal field or the spin-orbit coupling. In higher orders, however, there are some contributions and using elements for the crystal field allowed by the symmetry of this site and the matrix elements between these states tabulated by Bartram et al. (1965), the D splitting is calculated as $\sim 270.0 \times 10^{-4} \text{cms}^{-1}$. This calculation assumed that the WO_4^{2-} were point charges at W sites and allowing for a more realistic charge distribution of zero on the W and $-\frac{1}{4}$ on each O the value for D is reduced to $\sim 120.0 \times 10^{-4} \text{cms}^{-1}$. Both figures are, of course, two orders of magnitude too large and further, the calculated anisotropy of the g tensor is less than that observed. It is possible, however, to conceive of a mechanism by which these difficulties might be reduced and

which also might explain the non-colinearity of the two tensors.
The symmetry of this site permits odd terms in the expression for the crystal field which might well introduce some admixture into the ground term from the terms of the next lowest configuration. This configuration is of opposite parity to the ground configuration and has a ^4P term lowest in energy. The crystal field terms connecting states within the ground configuration will be of the form $x^2 - y^2$ while those connecting the two configurations may be represented as xyz. The rotations of co-ordinates required to diagonalise these two systems need not be identical which would result in different axes for the two interactions.
This mechanism provides contributions to both the g and D tensor and one possible explanation of the observed smallness of D is that it results from a near cancellation of quite large contributions. It is not possible to prove this, of course, since the actual value calculated is quite sensitive to the exact location of the ion and the charge distribution of the WO_4^{--} and consequently, this must remain as a tentative speculation.
One possibility that might be checked is to apply electric fields to the specimen, since if the g tensor is determined by such mechanisms it ought to be quite sensitive to changes in the local electric field at the site.

6.7.3 The C Spectrum

The possibility of ascribing models to the C spectra has not been investigated in any great detail, though there are several significant conclusions which may be drawn from the data. Firstly the close resemblance of the behaviour of the α and β lines and especially their identical hyperfine interactions suggests that the centres from which they arise are closely related. They might be expected to arise from different charge states of the same defect, or alternatively from a defect such as an O_2^- ion which might have two similar environments in the structure. Secondly the large g shifts observed indicate the presence of orbital angular momentum and this is probably the explanation of the sensitivity of this spectrum to temperature changes. The splitting of both α and β lines into doublets in the <110> plane demonstrates that neither centre has a principal g tensor axis parallel to a c axis though the precise angle of divergence cannot be specified to an accuracy of more than a few degrees.

The hyperfine interaction is probably the strongest clue as to the origin of these spectra. It may be remembered that there are two equivalent W sites involved and, from the structure, W sites have nearest neighbour W's along <012> and <100> directions. It would seem, from the symmetry of the spectrum, that it is the latter pair of sites that is involved and, furthermore, an assumption that the principal axis of the hyperfine interaction lies along a <100> direction rather than along the nearby g tensor axis is quite consistent with the spectrum (section 6.6.3). One prediction of this designation of the hyperfine axis, namely that the hyperfine splitting on all of the main lines should be identical along a <110> direction, is fulfilled, though, owing to the complexity of components, it is difficult to follow the complete angular dependence of the hyperfine splitting in this plane.

In conclusion it would seem that like the V_k centre (section 4.2.3), both the α and β spectra arise from defects associated with two WO_4^{2-} complexes spaced along <100> directions. Unlike the V_k centre, however, these spectra are stable at room temperature and have large negative g shifts. Bearing in mind the possible explanation of the A spectrum in terms of O^+ interstitials, it is tempting to consider these spectra as oxygen vacancies or divacancies in these complexes. Further speculation, however, requires a molecular orbital treatment of these models of the sort performed by Watkins for the silicon divacancy.

6.8 Conclusion

In conclusion it can be seen that a considerable amount of further work is required before the nature of these and other defects in $CaWO_4$ is properly understood. From the studies reported here, it seems possible that the A spectrum arises from interstitial O^+ and, more speculatively, the C spectrum from oxygen deficiency in complexes of two WO_4^{2-} units. Little can be concluded about the B spectrum, except that like the other two centres it is most probably an intrinsic defect rather than an impurity associated one. None of the three centres have been reported previously, though it is possible that the 'α' lines mentioned briefly by Chu and Kikuchi (1966) might be the A or B spectra reported here. Together these three sets of spectra account for the major portion of the microwave absorption of heavily damaged $CaWO_4$ at room temperature.

Having established the hamiltonian parameters of some of these centres it might now be possible to deduce more about their nature from studies of their dynamic relationships under thermal and optical excitation. In this context, however, it must be remembered that several other sets of spectra, which have not yet been investigated, were also observed in these crystals especially at low temperatures. These spectra indicate the presence of other defects which might well participate in the overall dynamic behaviour of the material.

References

Baker, J.M., Bleaney, B. and Hayes, W., Proc. Roy. Soc. (London) A247, 141 (1958).

Bartram, R.H., Swenberg, C.E. and Fournier, J.T., Phys. Rev. 139, 941 (1965).

Bleaney, B. Phil. Mag. 42, 441 (1951).

Chu, K.C. and Kikuchi, C., IEEE Trans. Nucl. Sci. 13, 41 (1966).

Dugdale, D.E., Private communication (1970).

Hempstead, C.F. and Bowers, K.D., Phys. Rev. 118, 131 (1960).

Kittel, C., "Introduction to Solid State Physics" (Wiley) 1967.

Koster, G.F. and Statz, H., Phys. Rev. 113, 445 (1959).

Low, W., Solid State Physics Suppl. 2 (1960).

Nye, J.F., "Physical Properties of Crystals" (Oxford) 1967.

Slater, J.C., "Quantum Theory of Atomic Structure" (McGraw Hill) 1960.

Tomlinson, A.C. and Henderson, B., J. Phys. Chem. Solids 30, 1793 (1969).

Zeldes, H. and Livingston, R., J. Chem. Phys. 34, 247 (1961).

APPENDIX I

THE RULES OF QUANTUM MECHANICAL OPERATORS

In quantum mechanics every physical observable is associated with the operations of an operator on a domain of operands. The quantised energy levels of a system are equated with the eigenvalues of the matrix of the appropriate hamiltonian operator evaluated between the permitted operands.

Of the operators associated with angular momentum, the orbital ones have classical counterparts, for example:

$$\underline{L}_z = \frac{\hbar}{i}\left(z\frac{\partial}{\partial x} - x\frac{\partial}{\partial z}\right)$$

whereas the spin operators, acting only on the spin states, do not. The domain of operands for these operators are the wavefunctions of electrons specified by their orbital and spin quantum numbers. The rules for evaluating matrix elements of the basic angular momentum operators $\underline{L}$ and $\underline{S}$ are set out below.

$$S_z|M_LM_S> = M_S|M_LM_S> \qquad L_z|M_LM_S> = M_L|M_LM_S>$$

$$S_x = \tfrac{1}{2}(S_+ + S_-) \qquad L_x = \tfrac{1}{2}(L_+ + L_-)$$

$$S_y = \frac{1}{2i}(S_+ - S_-) \qquad L_y = \frac{1}{2i}(L_+ - L_-)$$

where

$$S_+|M_LM_S> = (S(S+1)-M_S(M_S+1))^{\frac{1}{2}}|M_L.M_S+1> \qquad L_+|M_LM_S> = (L(L+1)-M_L(M_L+1))^{\frac{1}{2}}|M_L+1,M_S>$$

$$S_-|M_LM_S> = (S(S+1)-M_S(M_S-1))^{\frac{1}{2}}|M_L.M_S-1> \qquad L_-|M_LM_S> = (L(L+1)-M_L(M_L-1))^{\frac{1}{2}}|M_L-1,M_S>$$

$$\underline{S}^2 = \underline{S}_x{}^2 + \underline{S}_y{}^2 + S_z{}^2 \qquad \underline{L}^2 = \underline{L}_x{}^2 + \underline{L}_y{}^2 + \underline{L}_z{}^2$$

A particular hamiltonian is often expressed as a combination of these and other operators and it is useful in evaluating matrix elements to bear in mind the orthogonality of the operands and the independence of spin and orbital operators which eliminate many contributions, for example:

$$\langle M_S M_L | S_z L_z | M_S M_{L-1} \rangle = M_S M_{L-1} \langle M_S M_L | M_S M_{L-1} \rangle = 0$$

In the case of the spin hamiltonian, where all the operators and operands are concerned solely with spin, matrix evaluation can be simplified by use of the Pauli spin matrices. These are the matrices of the various spin operators between the spin states of a system and as an example the ones used in the analysis of the Mn^{2+}:BaO spectrum reported in Chapter V are listed below:

$\underline{S = 5/2}$

$$S^2 = \frac{35}{4} \begin{pmatrix} 1 & 0 & 0 & 0 & 0 & 0 \\ 0 & 1 & 0 & 0 & 0 & 0 \\ 0 & 0 & 1 & 0 & 0 & 0 \\ 0 & 0 & 0 & 1 & 0 & 0 \\ 0 & 0 & 0 & 0 & 1 & 0 \\ 0 & 0 & 0 & 0 & 0 & 1 \end{pmatrix} \qquad S_z = \begin{pmatrix} 5/2 & 0 & 0 & 0 & 0 & 0 \\ 0 & 3/2 & 0 & 0 & 0 & 0 \\ 0 & 0 & \frac{1}{2} & 0 & 0 & 0 \\ 0 & 0 & 0 & -\frac{1}{2} & 0 & 0 \\ 0 & 0 & 0 & 0 & -3/2 & 0 \\ 0 & 0 & 0 & 0 & 0 & -5/2 \end{pmatrix}$$

$$S_x = \begin{pmatrix} 0 & \sqrt{5}/2 & 0 & 0 & 0 & 0 \\ \sqrt{5}/2 & 0 & \sqrt{2} & 0 & 0 & 0 \\ 0 & \sqrt{2} & 0 & 3/2 & 0 & 0 \\ 0 & 0 & 3/2 & 0 & \sqrt{2} & 0 \\ 0 & 0 & 0 & \sqrt{2} & 0 & \sqrt{5}/2 \\ 0 & 0 & 0 & 0 & \sqrt{5}/2 & 0 \end{pmatrix} \qquad S_y = i \begin{pmatrix} 0 & -\sqrt{5}/2 & 0 & 0 & 0 & 0 \\ \sqrt{5}/2 & 0 & -\sqrt{2} & 0 & 0 & 0 \\ 0 & \sqrt{2} & 0 & -3/2 & 0 & 0 \\ 0 & 0 & 3/2 & 0 & -\sqrt{2} & 0 \\ 0 & 0 & 0 & \sqrt{2} & 0 & \sqrt{5}/2 \\ 0 & 0 & 0 & 0 & \sqrt{5}/2 & 0 \end{pmatrix}$$

THE C_{2v} GROUP

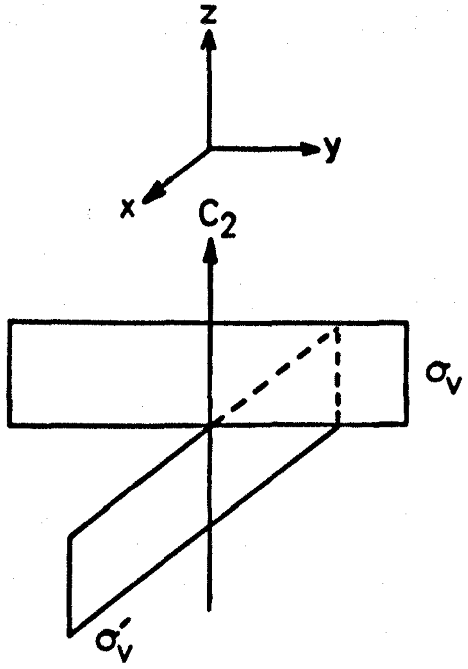

I - Identity Transformation

C_2 - Rotation about Principal axis by π

σ_v - Reflection in a Plane containing Principal axis

σ_v' - Reflection in a Plane containing Principal axis

(a) SYMMETRY OPERATIONS

	I	C_2	σ_v	σ_v'
I	I	C_2	σ_v	σ_v'
C_2	C_2	I	σ_v'	σ_v
σ_v	σ_v	σ_v'	I	C_2
σ_v'	σ_v'	σ_v	C_2	I

(b) MULTIPLICATION TABLE

FIGURE 7·1

APPENDIX II

GROUP THEORETICAL TREATMENT OF CRYSTAL FIELD SPLITTINGS

Point Groups and Representations

The regular structure of crystals guarantees the existence of transformations such as reflections, rotations and inversions which when applied about a point in a crystal carry the structure into itself. These transformations are termed symmetry operations and the collection of all the symmetry operations about a particular point satisfies the mathematical requirements of a group. Consequently the successive application of any two symmetry elements in the group must always be equivalent to the application of one other element. The group multiplication table summarises this interdependence of elements for a particular group. Figures 7.1a and 7.1b show the symmetry elements and multiplication table of the C_{2v} group.

To make it easier to deal with symmetry groups it is usual to seek a collection of matrices, one representing each symmetry element, which, under the rules of matrix multiplication, satisfy the group multiplication table. Such a collection of matrices is termed a representation and it expresses mathematically the operations of the group on a set of functions. A set of functions which transform according to a representation is said to form a basis for the representation. Figure 7.2 illustrates that the functions x and y of Figure 7.1a form a basis for a matrix representation of the C_{2v} group. There is no limit to the number of sets of functions that can be found to form bases for group

A BASIS FOR A REPRESENTATION OF THE C_{2v} GROUP

$$I \begin{pmatrix} x \\ y \end{pmatrix} = \begin{pmatrix} 1 & 0 \\ 0 & 1 \end{pmatrix} \begin{pmatrix} x \\ y \end{pmatrix} = \begin{pmatrix} x \\ y \end{pmatrix}$$

$$C_2 \begin{pmatrix} x \\ y \end{pmatrix} = \begin{pmatrix} -1 & 0 \\ 0 & -1 \end{pmatrix} \begin{pmatrix} x \\ y \end{pmatrix} = \begin{pmatrix} -x \\ -y \end{pmatrix}$$

$$\sigma_v \begin{pmatrix} x \\ y \end{pmatrix} = \begin{pmatrix} 1 & 0 \\ 0 & -1 \end{pmatrix} \begin{pmatrix} x \\ y \end{pmatrix} = \begin{pmatrix} x \\ -y \end{pmatrix}$$

$$\sigma_v' \begin{pmatrix} x \\ y \end{pmatrix} = \begin{pmatrix} -1 & 0 \\ 0 & 1 \end{pmatrix} \begin{pmatrix} x \\ y \end{pmatrix} = \begin{pmatrix} -x \\ y \end{pmatrix}$$

FIGURE 7.2

representations and it is always possible to combine the matrices of several representations A_i into a larger matrix B and thus produce a new and larger dimensioned representation. However no matter how the rows and columns of such an enlarged representation are permutated by rotation of the basis functions, it is always possible to find a matrix X in the group which, when applied as a similarity transformation on B, 'reduces' it to 'block diagonal' form, allowing its component representations A_i to be elucidated. Thus

$$X\,B\,X^{-1} = \begin{pmatrix} A_1 & 0 & 0 \\ 0 & A_2 & 0 \\ 0 & 0 & A_3 \end{pmatrix}$$

A representation which cannot be reduced further is termed an irreducible representation and a given group has a finite number of such irreducible representations, which will also be mutually orthogonal. It is always possible to choose the basis functions of a representation in such a way as to reveal its component irreducible representations.

The Hamiltonian and the Symmetry of a centre

The hamiltonian of a defect centre must be invariant under a symmetry operation R of the point group to which the centre belongs since, by definition, the environments before and after the symmetry operation are indistinguishable. Thus $\mathcal{H}$ and R commute and hence if

$$\mathcal{H}\psi_f = E_f\psi_f$$

then

$$\mathcal{H}(R\psi_f) = E_f(R\psi_f)$$

Thus $R\psi_f$ and ψ_f are degenerate eigenfunctions of $\mathcal{H}$ and consequently $R\psi_f$ must be expressible as a linear combination of the degenerate set of ψ_f's. Since this is true for any operation R in the point group, the ψ_f's must form a basis for a representation of the point group. Furthermore a suitable choice of basis functions formed from combinations of the ψ_f ought to reveal the irreducible representations of the group and hence demonstrate how the initially degenerate eigenfunctions of $\mathcal{H}$ will be split in a crystal field of a given symmetry. The reasoning behind this important deduction is that the degeneracy of functions providing a basis for an irreducible representation of the point group cannot be lifted by symmetry operations of that point group.

Fortunately to find the irreducible representations in a given case it is necessary to consider only the characters of the group elements in the representation and not the full matrix form. This is a consequnnce of the fact that no rotation can change the character of a matrix representation and hence this character $\chi(B)$ must be a linear combination of the characters of its irreducible representations $\chi(A_i)$:-

$$\chi(B) = \sum_i n_i \chi(A_i) \qquad (1)$$

where n_i is a non-negative integer.

Thus by finding the character table of the representation of the point group formed by the degenerate eigenfunctions of the hamiltonian and comparing this with the characters of the irreducible representations of the point group, the form of the crystal field splitting may be deduced.

As an illustration of the technique consider the case of Cr^{3+} in MgO referred to in Chapter II. The ground term is ^4F and consequently there will be seven degenerate eigenfunctions of $\mathcal{H}$ described by the spherical harmonics with $\ell = 3$. They form a basis for a seven dimensional representation of the cubic group O since any symmetry operation of O transforms them into linear combinations of themselves. We need to know the irreducible representations spanned by this representation. The character table of the representation is formed from the traces of the various matrices which represent each symmetry operation. To determine its elements we choose wavefunctions for the component F states which simplify the calculation. Thus taking the axis of the rotation concerned as the z direction for the wavefunctions and writing them in complex form, we see that any rotation α about this axis merely changes the polar angle from ϕ to $\phi + \alpha$. The seven components depend on ϕ as follows:

$$e^{3i\phi},\ e^{2i\phi},\ e^{i\phi},\ e^{0},\ e^{-i\phi},\ e^{-2i\phi},\ e^{-3i\phi}$$

Thus a rotation R_α may be expressed

$$R_\alpha \begin{pmatrix} e^{3i\phi} \\ e^{2i\phi} \\ e^{i\phi} \\ e^{0} \\ e^{-i\phi} \\ e^{-2i\phi} \\ e^{-3i\phi} \end{pmatrix} = \begin{pmatrix} e^{3i\alpha} & 0 & 0 & 0 & 0 & 0 & 0 \\ 0 & e^{2i\alpha} & 0 & 0 & 0 & 0 & 0 \\ 0 & 0 & e^{i\alpha} & 0 & 0 & 0 & 0 \\ 0 & 0 & 0 & e^{0} & 0 & 0 & 0 \\ 0 & 0 & 0 & 0 & e^{-i\alpha} & 0 & 0 \\ 0 & 0 & 0 & 0 & 0 & e^{-2i\alpha} & 0 \\ 0 & 0 & 0 & 0 & 0 & 0 & e^{-3i\alpha} \end{pmatrix} \begin{pmatrix} e^{3i\phi} \\ e^{2i\phi} \\ e^{i\phi} \\ e^{0} \\ e^{-i\phi} \\ e^{-2i\phi} \\ e^{-3i\phi} \end{pmatrix}$$

TABLE 7.1

CHARACTER TABLE OF O GROUP

O	E	$8C_3$	$3C_2$	$6C_2$	$6C_4$
A_1	1	1	1	1	1
A_2	1	1	1	-1	-1
E	2	-1	2	0	0
T_1	3	0	-1	-1	1
T_2	3	0	-1	1	1

D_3 REPRESENTATION

O	E	$8C_3$	$3C_2$	$6C_2$	$6C_4$
D_3	7	1	-1	-1	-1

and hence the character of the matrix representing this operation is

$$\chi(R_\alpha) = e^{3i\alpha} + e^{2i\alpha} + e^{i\alpha} + e^{0} + e^{-i\alpha} + e^{-2i\alpha} + e^{-3i\alpha} = \frac{\sin \frac{7\alpha}{2}}{\sin \frac{\alpha}{2}}$$

Generally for a ground term with a quantum number L this becomes

$$(R_\alpha) = \frac{\sin(2L + 1)\frac{\alpha}{2}}{\sin \frac{\alpha}{2}}$$

As an example the character of the C_4 element of O corresponding to a rotation by $\frac{\pi}{2}$ is given by:-

$$(C_4) = \frac{\sin \frac{7\pi}{4}}{\sin \frac{\pi}{4}} = -1$$

The character tables for this representation D^3 of O and for the irreducible representations of O are shown in Table 7.1. The linear combination required to satisfy 1 is

$$D^3 = A_{2g} + T_{1g} + T_{2g}$$

and thus the ^4F term splits into a singlet and two triplets. The subscript g indicates that the wavefunctions of ^4F are centro-symmetric, i.e. they are symmetrical in planes containing the C_4 axis.

APPENDIX III

PERTURBATION THEORY TREATMENT OF THE CASE OF NON-COINCIDENT g AND D TENSORS

It is required to find an expression for the angular variation of the spectrum described by the spin hamiltonian:-

$$\mathcal{H} = \beta\underline{S}.\underline{g}.\underline{H} + \underline{S}.\underline{D}.\underline{S} \tag{1}$$

in which the principal axes of $\underline{g}$ and $\underline{D}$ are non-coincident.

The Zeeman term of (1) may be written

$$\mathcal{H} = \beta(g_x S_x H_x + g_y S_y H_y + g_z S_z H_z) \tag{2}$$

and in the g tensor axis system (Figure 5.6), the components of $\underline{H}$ are

$$\begin{aligned} H_z &= H\cos\theta \\ H_x &= H\sin\theta\cos\phi \\ H_y &= H\sin\theta\sin\phi \end{aligned} \tag{3}$$

As is usual in such treatments (Bleaney 1951), we first perform a rotation from this axis system (x,y,z) to the magnetic axis system (x',y',z') in which the Zeeman term is diagonal. Expressing the relationship between the two systems in terms of the Euler angles α, β and γ (Rutherford p.152):

$$\begin{pmatrix} x \\ y \\ z \end{pmatrix} = \begin{pmatrix} (\cos\gamma\cos\alpha\cos\beta - \sin\gamma\sin\beta) & (-\sin\gamma\cos\alpha\cos\beta - \cos\gamma\sin\beta) & \sin\alpha\cos\beta \\ (\cos\gamma\cos\alpha\sin\beta + \sin\gamma\cos\beta) & (-\sin\gamma\cos\alpha\sin\beta + \cos\gamma\cos\beta) & \sin\alpha\sin\beta \\ -\cos\gamma\sin\alpha & \sin\gamma\sin\alpha & \cos\alpha \end{pmatrix} \begin{pmatrix} x' \\ y' \\ z' \end{pmatrix} \tag{4}$$

and the spin operators become:

$$S_x = (\cos\gamma\cos\alpha\cos\beta-\sin\gamma\sin\beta)S_x' + (-\sin\gamma\cos\alpha\cos\beta-\cos\gamma\sin\beta)S_y' + \sin\alpha\cos\beta S_z'$$

$$S_y = (\cos\gamma\cos\alpha\sin\beta+\sin\gamma\cos\beta)S_x' + (-\sin\gamma\cos\alpha\sin\beta+\cos\gamma\cos\beta)S_y' + \sin\alpha\sin\beta Sz'$$

$$S_z = -\cos\gamma\sin\alpha\, S_x' + \sin\gamma\sin\alpha\, S_y' + \cos\alpha\, S_z' \tag{5}$$

Substituting these expressions into (2) and collecting the terms in S_z'

$$\mathcal{H} = \beta(g_xH_x\sin\alpha\cos\beta + g_yH_y\sin\alpha\sin\beta + g_zH_z\cos\alpha)S_z' \tag{6}$$

where we require the terms in S_x' and S_y' to vanish, i.e.

$$g_xH_x(\cos\gamma\cos\alpha\cos\beta-\sin\gamma\sin\beta) + g_yH_y(\cos\gamma\cos\alpha\sin\beta+\sin\gamma\cos\beta) + g_zH_z(-\cos\gamma\sin\alpha) = 0$$

simultaneously with (7)

$$g_xH_x(-\sin\gamma\cos\alpha\cos\beta-\cos\gamma\sin\beta) + g_yH_y(-\sin\gamma\cos\alpha\sin\beta+\cos\gamma\cos\beta) + g_zH_z(\sin\gamma\sin\alpha) = 0$$

without loss of generality this can be achieved by setting

$$\gamma = 0^\circ$$
$$\beta = \mathrm{Tan}^{-1}\left(\frac{g_y}{g_x}\frac{H_y}{H_x}\right) \tag{8}$$
and
$$\alpha = \mathrm{Tan}^{-1}\left(\frac{g_xH_x\cos\beta + g_yH_y\sin\beta}{g_zH_z}\right)$$

By making use of (3) we have

$$\sin\beta = \frac{g_y\sin\phi}{g_\perp} \qquad \cos\beta = \frac{g_x\cos\phi}{g_\perp}$$
$$\tag{9}$$
and
$$\sin\alpha = \frac{g_\perp\sin\theta}{g} \qquad \cos\alpha = \frac{g_z\cos\theta}{g}$$

where $g_\perp^2 = g_x^2\cos^2\phi + g_y^2\sin^2\phi$

and $g^2 = g_z^2\cos^2\theta + g_y^2\sin^2\theta\sin^2\phi + g_x^2\sin^2\theta\cos^2\phi$

The equations (9) represent the rotation into the magnetic axis system under which (6) reduces to

$$\mathcal{H} = g\beta H\underline{S}_z' \qquad (10)$$

We are now in a position to consider the $\underline{D}$ tensor which we may write in the g tensor axis system (x.y.z) as

$$\underline{S}.\underline{D}.\underline{S} = (S_xS_yS_z)\begin{pmatrix} D_{xx} & D_{xy} & D_{xz} \\ D_{yx} & D_{yy} & D_{yz} \\ D_{zx} & D_{zy} & D_{zz} \end{pmatrix}\begin{pmatrix} S_x \\ S_y \\ S_z \end{pmatrix} \qquad (11)$$

or

$$\underline{S}.\underline{D}.\underline{S} = D_{xx}S_x^2 + D_{yy}S_y^2 + D_{zz}S_z^2 + D_{xy}(S_xS_y + S_yS_z) + D_{xz}(S_xS_z + S_zS_x) + D_{yz}(S_yS_z + S_zS_y) \qquad (12)$$

since it is symmetric.

If the D tensor were coincident with the g tensor then of course the cross terms would be zero. In this case, however, it is necessary to retain them.

In order to make (11) consistent with (10), it is required to perform the same rotation into the magnetic axis system. From (5) and the condition $\gamma = 0^\circ$ the spin operators of (12) become, after a little manipulation:-

$$\begin{aligned}
S_x{}^2 = {} & \cos^2\alpha\cos^2\beta S_x{}'^2 + \sin^2\beta S_y{}'^2 + \sin^2\alpha\cos^2\beta S_z{}'^2 \\
& - \cos\alpha\cos\beta\sin\beta(S_x{}'S_y{}' + S_y{}'S_x{}') + \cos\alpha\sin\alpha\cos^2\beta(S_x{}'S_z{}' + S_z{}'S_x{}') \\
& - \sin\alpha\sin\beta\cos\beta(S_y{}'S_z{}' + S_z{}'S_y{}')
\end{aligned}$$

$$\begin{aligned}
S_y{}^2 = {} & \cos^2\alpha\sin^2\beta S_x{}'^2 + \cos^2\beta S_y{}'^2 + \sin^2\alpha\sin^2\beta S_z{}'^2 \\
& + \cos\alpha\sin\beta\cos\beta(S_x{}'S_y{}' + S_y{}'S_x{}') + \sin\alpha\cos\alpha\sin^2\beta(S_x{}'S_z{}' + S_z{}'S_x{}') \\
& + \sin\alpha\sin\beta\cos\beta(S_z{}'S_y{}' + S_y{}'S_z{}')
\end{aligned}$$

$$S_z{}^2 = \sin^2\alpha S_x{}'^2 + \cos^2\alpha S_z{}'^2 - \sin\alpha\cos\alpha(S_x{}'S_z{}' + S_z{}'S_x{}')$$

$$\begin{aligned}
(S_xS_y + S_yS_x) = {} & \cos^2\alpha\sin2\beta S_x{}'^2 - \sin2\beta S_y{}'^2 + \sin^2\alpha\sin2\beta S_z{}'^2 \\
& + \frac{\sin2\alpha\sin2\beta}{2}(S_x{}'S_z{}' + S_z{}'S_x{}') + \cos\alpha\cos2\beta(S_y{}'S_x{}' + S_x{}'S_y{}') \\
& + \sin\alpha\cos2\beta(S_y{}'S_z{}' + S_z{}'S_y{}')
\end{aligned}$$

$$\begin{aligned}
(S_xS_z + S_zS_x) = {} & - \sin2\alpha\cos\beta S_x{}'^2 + \sin2\alpha\cos\beta S_z{}'^2 + \cos2\alpha\cos\beta(S_x{}'S_z{}' + S_z{}'S_x{}') \\
& + \sin\alpha\sin\beta(S_x{}'S_y{}' + S_y{}'S_x{}') - \cos\alpha\sin\beta(S_y{}'S_z{}' + S_z{}'S_y{}')
\end{aligned}$$

$$\begin{aligned}
(S_yS_z + S_zS_y) = {} & - \sin2\alpha\sin\beta S_x{}'^2 + \sin2\alpha\sin\beta S_z{}'^2 + \cos2\alpha\sin\beta(S_x{}'S_z{}' + S_z{}'S_x{}') \\
& - \sin\alpha\cos\beta(S_y{}'S_x{}' + S_x{}'S_y{}') + \cos\alpha\cos\beta(S_y{}'S_z{}' + S_z{}'S_y{}')
\end{aligned} \tag{13}$$

By substituting these expressions into (12) and making use of the relationships between the two axis systems (9) we can, after collecting up like Spin Operators, express the D tensor in the magnetic axis system as:-

$$
\begin{aligned}
\underline{S}.\underline{D}.\underline{S} = {} & \Bigg(D_{xx}\frac{g_x{}^2\sin^2\theta\cos^2\phi}{g^2} + D_{yy}\frac{g_y{}^2\sin^2\theta\sin^2\phi}{g^2} + D_{zz}\frac{g_z{}^2\cos^2\theta}{g^2} \\
& + D_{xy}\frac{g_xg_y\sin2\phi\sin^2\theta}{g^2} + D_{xz}\frac{g_xg_z\cos\phi\sin2\theta}{g^2} + D_{yz}\frac{g_yg_z\sin\phi\sin2\theta}{g^2} \Bigg) S_z{}'^2 \\
& + \Bigg(D_{xx}\frac{g_z{}^2g_x{}^2\cos^2\phi\cos^2\theta}{g^2g_\perp{}^2} + D_{yy}\frac{g_z{}^2g_y{}^2\sin^2\phi\cos^2\theta}{g^2g_\perp{}^2} + D_{zz}\frac{g_\perp{}^2\sin^2\theta}{g^2} \\
& + D_{xy}\frac{g_z{}^2g_xg_y\sin2\phi\cos^2\theta}{g^2g_\perp{}^2} - D_{xz}\frac{g_xg_z\cos\phi\sin2\theta}{g^2} - D_{yz}\frac{g_yg_z\sin\phi\sin2\theta}{g^2} \Bigg) S_x{}'^2 \\
& + \Bigg(D_{xx}\frac{g_y{}^2\sin^2\phi}{g_\perp{}^2} + D_{yy}\frac{g_x{}^2\cos^2\phi}{g_\perp{}^2} - D_{xy}\frac{g_xg_y\sin^2\phi}{g_\perp{}^2} \Bigg) S_y{}'^2 \\
& + \Bigg(- D_{xx}\frac{g_zg_xg_y\sin2\phi\cos\theta}{2.gg_\perp{}^2} + D_{yy}\frac{g_zg_xg_y\sin2\phi\cos\theta}{2.gg_\perp{}^2} \\
& + D_{xy}\frac{g_z(g_x{}^2\cos^2\phi-g_y{}^2\sin^2\phi)\cos\theta}{gg_\perp{}^2} + D_{xz}\frac{g_y\sin\phi\sin\theta}{g} \\
& - D_{yz}\frac{g_x\cos\phi\sin\theta}{g} \Bigg) \Big(S_x{}'S_y{}' + S_y{}'S_x{}' \Big) \\
& + \Bigg(D_{xx}\frac{g_zg_x{}^2\cos^2\phi\sin2\theta}{2g^2g_\perp} + D_{yy}\frac{g_zg_y{}^2\sin^2\phi\sin2\theta}{2g^2g_\perp} - D_{zz}\frac{g_\perp g_z\sin2\theta}{2g^2} \\
& + D_{xy}\frac{g_zg_xg_y\sin2\phi\sin2\theta}{2g^2g_\perp} + D_{xz}\frac{g_x(g_z{}^2\cos^2\theta-g_\perp{}^2\sin^2\theta)\cos\phi}{g_\perp g^2} \\
& + D_{yz}\frac{g_y(g_z{}^2\cos^2\theta-g_\perp{}^2\sin^2\theta)\sin\phi}{g_\perp g^2} \Bigg) \Big(S_x{}'S_z{}' + S_z{}'S_x{}' \Big) \\
& + \Bigg(- D_{xx}\frac{g_xg_y\sin2\phi\sin\theta}{2gg_\perp} + D_{yy}\frac{g_xg_y\sin2\phi\sin\theta}{2gg_\perp} + D_{xy}\frac{(g_x{}^2\cos^2\phi-g_y{}^2\sin^2\phi)\sin\theta}{gg_\perp} \\
& - D_{xz}\frac{g_zg_y\sin\phi\cos\theta}{gg_\perp} + D_{yz}\frac{g_zg_x\cos\phi\cos\theta}{gg_\perp} \Bigg) \Big(S_y{}'S_z{}' + S_z{}'S_y{}' \Big)
\end{aligned}
\tag{14}
$$

or, summarising the coefficients of the spin operators

$$\underline{S}.\underline{D}.\underline{S} = A\ S_z{}'^2 + B\ S_x{}'^2 + C\ S_y{}'^2 + D(S_x{}'S_y{}' + S_y{}'S_x{}') + E(S_x{}'S_z{}' + S_z{}'S_x{}') + F(S_y{}'S_z{}' + S_z{}'S_y{}') \qquad (15)$$

Thus combining (10) and (15) the total hamiltonian (1), after making use of the operator relations of Appendix I, may be written as:-

$$\begin{aligned}\mathcal{H} = {} & g\beta H\ \underline{S}_z{}' + A\underline{S}_z{}'^2 + \frac{B}{4}(S_+^2 - 2S_z^2 + S_-^2) - \frac{C}{4}(S_+^2 + 2S_z^2 + S_-^2) \\ & + \frac{D}{2i}(S_+{}'^2 - S_-{}'^2) + \frac{E}{2}(S_+{}'S_z{}' + S_-{}'S_z{}' + S_z{}'S_+{}' + S_z{}'S_-{}') \\ & + \frac{F}{2i}(S_+{}'S_z{}' - S_-{}'S_z{}' + S_z{}'S_+{}' - S_z{}'S_-{}') \qquad (16)\end{aligned}$$

which is to be evaluated between the spin states $\langle +\frac{3}{2}|$ $\langle +\frac{1}{2}|$ $\langle -\frac{1}{2}|$ and $\langle -\frac{3}{2}|$. Restricting the perturbation theory treatment to first order we require matrix elements $\langle M_S|\mathcal{H}|M_S\rangle$ and the energy of the eigen states of (16) will be

$$E_{M_S} = g\beta H M_S + A M_S^2 + \frac{(B+C)}{2}\{S(S+1) - M_S^2\} \qquad (17)$$

By use of the selection rule $M_S = 1$, the e.p.r. transitions can be seen to occur at

$$H_{M_S} = H_o - \frac{(M_S - \frac{1}{2})}{g\beta}(2A - B - C) \qquad (18)$$

which, upon substituting back from (14) for A, B and C, can be shown to reduce to:

$$H_{M_S} = H_o - \frac{(M_S - \frac{1}{2})}{g\beta} \left(D_{xx}\left(\frac{3g_x{}^2\sin^2\theta\cos^2\phi}{g^2} - 1 \right) + D_{yy}\left(\frac{3g_y{}^2\sin^2\theta\sin^2\phi}{g^2} - 1 \right) + D_{zz}\left(\frac{3g_z{}^2\cos^2\theta}{g^2} - 1 \right) + D_{xy}\frac{3g_xg_y\sin2\phi\sin^2\theta}{g^2} + D_{xz}\frac{3g_xg_z\cos\phi\sin2\theta}{g^2} + D_{yz}\frac{3g_yg_z\sin\phi\sin2\theta}{g^2} \right) \tag{19}$$

where $H_o = \frac{h\nu}{g\beta}$.

This expression describes the angular variation of the spectrum observed from non-coincident g and D tensors with respect to the direction of the applied field H to the g tensor axes. The alternative way of treating this problem, using basis functions which refer to the g tensor axes as coordinate axes, leads of course to the same result (Dugdale 1970).

References

Bleaney, B., Phil. Mag. 42, 441 (1951).

Dugdale, D.E., Private Communication (1970).

Rutherford, D.E., 'Classical Mechanics' (Oliver and Boyd) 1960.